FUNCTIONALIZED GRAPHENE MATERIALS FOR HIGH PERFORMANCE SUPERCAPACITORS

A Dissertation
Presented to
The Academic Faculty

by

Bo Song

In Partial Fulfillment
of the Requirements for the Degree
Doctor of Philosophy in the
School of Chemistry and Biochemistry

Georgia Institute of Technology
August 2018

FUNCTIONALIZED GRAPHENE MATERIALS FOR HIGH PERFORMANCE SUPERCAPACITORS

Approved by:

Dr. C. P. Wong, Advisor
School of Materials Science and Engineering
Georgia Institute of Technology

Dr. David Collard
School of Chemistry and Biochemistry
Georgia Institute of Technology

Dr. Z. John Zhang
School of Chemistry and Biochemistry
Georgia Institute of Technology

Dr. Thomas Orlando
School of Chemistry and Biochemistry
Georgia Institute of Technology

Dr. Meilin Liu
School of Materials Science and Engineering
Georgia Institute of Technology

Date Approved: April 25, 2018

To my parents and my fiancée for their endless love, support and encouragement.

ACKNOWLEDGEMENTS

I would like to express my sincere gratitude to my advisor, Prof. C. P. Wong, for his guidance, support, and encouragement during my PhD study. His dedications to research and innovations significantly inspire me. I would like to extend my gratitude to Prof. David Collard, Prof. John Zhang, Prof. Thomas Orlando, and Prof. Meilin Liu, for serving as my thesis committee and providing valuable comments and suggestions.

I would like to acknowledge the help and discussion from my colleagues: Dr. Kyoung-Sik Moon, Dr. Ziyin Lin, Dr. Zhuo Li, Dr. Liyi Li, Dr. Chia-chi Tuan, Dr. Zhenkun Wu, Dr. Yagang Yao, Ms. Fan Wu, Mr. Jiaxiong Li, Mr. Jinho Hah, Dr. Yanqing Ma, Dr. Guoyun Zhou, Dr. Guoping Zhang, Dr. Lixi Wang, Dr. Yun Chen, Dr. Weimin Yang, Dr. Xiaogu Huang, Dr. Xin Fang, Dr. Xiangning Lu, Dr. Gang Jian, Dr. Ning Zhao, Dr. Tianchi Wang, Dr. Yi Lu, Dr. Zhaoxia Hou, Dr. Mingjun Wang, Mr. Cheng Zhang, Ms. Lin Chen, Dr. Xiaona Wang, and Dr. Rongli Zhang. I would also like to thank the undergraduate students who worked hard with me, Ms. Yuntong Zhu, Ms. Chelsea Sizemore, Mr. Luke Maurer, Mr. Jeffrey Mullavey, Ms. Sammi Riemann, Mr. Ruoyu Liu, Mr. Long Qian, Mr. Shiv Patel, Ms. Xueqiao Wang, Mr. Wanchen He, and Ms. Mengting Cheng.

I would like to express my appreciation to my collaborators: Dr. Ji Il Choi, Dr. Pengli Zhu, Dr. Xiaoliang Zeng, Prof. Manos Tentzeris, Dr. Taoran Le, Mr. Ryan Bahr, Dr. Dongchang Chen, Dr. Bote Zhao, Mr. Zhishuai Geng, Dr. Jingxiang Zhao, Dr. Yongdong Jiang, Dr. Michael Hu, Dr. Gyoung Gug Jang, and Mr. Vincent Desmaris. My appreciation is extended to the staff in Institute of Electronics and Nanotechnology at Georgia Tech for their training and guidance: Dr. Yong Ding, Ms. Yolande Berta, Mr. Eric Woods, Mr. David Tavakoli, Mr. Chris Yang, Mr. Charlie Suh, Mr. Charles Turgeon, Mr. Tran-vinh

Nguyen, and Ms. Rebhadevi Monikandan, and Dr. Johannes Leisen from Gerogia Tech NMR center.

I would also acknowledge Advanced Research Projects Agency-Energy (ARPAE) and Boeing Company for their financial support. I would also like to thank nGimat Corporation, Asbury Carbon Incorporation, Ames Goldsmith Corporation, Wacker Chemie AG corporation, and Shenzhen Institute of Advanced Technology for their supply of materials.

TABLE OF CONTENTS

LIST OF TABLES

LIST OF FIGURES

LIST OF SYMBOLS AND ABBREVIATIONS

SC	Supercapacitor
EDLC	Electrical double layer capacitor
MSC	Micro-supercapacitor
C_{cell}	Cell capacitance
C_s	Specific capacitance
E	Energy density
P	Power density
R_s	Equivalent series resistance
R_{ct}	Charge transfer resistance
τ_0	Relaxation time constant
GO	Graphene oxide
rGO	Reduced graphene oxide
SPANI	Sulfonated polyaniline
PPD	p-Phenylene diamine
MPD	m-Phenylene diamine
OPD	o-Phenylene diamine
EDA	Ethylenediamine
BDA	1,4-Butanediamine
HDA	1,6-Hexanediamine
CHDA	1,4-Cyclohexanediamine
Tris	Tris(2-aminoethyl)amine
EA148	Etheramine
TEA	Triethanolamine

PTFE	Polytetrafluoroethylene
PVDF	Polyvinylidene
PVP	Polyvinylpyrrolidone
CMS/SBR	Carboxymethylcellulose/styrene-butadiene rubber
SSA	Specific surface area
MD	Molecular dynamic
DFT	Density functional theory
CV	Cyclic voltammetry
CD	Charge/discharge
EIS	Electrochemical impedance spectroscopy
TGA	Thermal gravimetric analysis
DSC	Differential scanning calorimetry
XPS	X-ray photoelectron spectroscopy
FTIR	Fourier-transform infrared spectroscopy
UV-Vis	Ultraviolet-visible
XRD	X-ray diffraction
SEM	Scanning electron microscopy
TEM	Transmission electron microscopy
AFM	Atomic force microscopy

SUMMARY

Supercapacitors (SCs) have attracted tremendous attention as clean and sustainable energy storage sources in recent years. Graphene, as an atom-thick carbon form, has been considered as a promising electrode material for SCs due to its outstanding electrical conductivity, high surface area, chemical stability and mechanical flexibility. For scalable and cost effective production of graphene, reduced graphene oxide (rGO) is prepared by reduction of graphene oxide (GO). However, the reduction process can induce the restacking of graphene layers, which decreases the effective surface area and porosity for ion diffusion and storage. This dissertation aims to solve this problem through chemical functionalization of graphene and provide an in-depth understanding on the structure-property relationship of graphene-based electrodes.

The first part of this dissertation introduces the utilization of designed "molecular spacers" to create 3D graphene covalent organic frameworks. Taking advantage of the diverse functionalities on GO surface, multifunctional "molecular spacers" were selected to react with GO to form covalent bonds followed by the reduction to tune the interlayer spacing and specific surface area (SSA) of graphene at molecular level. The negligible structural change before and after GO reduction demonstrates the effectiveness and stability of the "molecular spacers". The use of aliphatic molecules serves to reveal SSA-dependent double layer (EDL) capacitance, and the use of organic and ionic liquid electrolytes dramatically increases the energy density of the electrodes. The interlayer spacing and the band gap energies of the functionalized graphene network were predicted using theoretical models complementary to the experimental results.

Organic pseudocapacitive materials, such as aromatic structures with nitrogen-containing groups, have also been incorporated into graphene networks to from larger conjugated networks with enhanced conductivity and pronounced redox charge transfer characteristics. The chemical reaction mechanism and the evidence of crosslinked graphene structures were further elucidated by thermal and rheological analyses. The systematic investigation on various conjugated graphene networks suggested that the physical structures and redox transitions are two critical factors affecting the electrochemical properties of the electrodes. Molecular dynamic (MD) and density function theory (DFT) calculations were performed to verify the experimental findings.

From material design to device fabrication, this dissertation also describes the development of micro-supercapacitors (MSCs), as miniaturized energy storage units, with excellent electrical and mechanical compatibilities. An aqueous dispersible graphene/sulfonated polyaniline (rG/SP) composite was synthesized and adopted as micro-electrode by direct thin film deposition. The high-resolution interdigitated patterns were created by well-controlled shadow masking and plasma etching processes. The in-plane design of interdigitated patterns and the highly conductive electrodes with porous edges greatly facilitated the ionic diffusion, leading to an ultrafast charge/discharge process within milliseconds. The as-fabricated MSC device presented a comparable energy density with thin film batteries and comparable power density with electrolytic capacitors. The design of the MSC architecture can be further extended to make flexible or even foldable MSC arrays with tunable operation potential window and much higher areal capacitance.

Moreover, polymer binder is an essential component to fabricate thin film electrodes. The effect of polymer binders on graphene-based free-standing electrodes were

discussed. Several quality metrics of the electrodes, including adhesion, hydrophilicity, conductivity, flexibility, and toxicity have been considered for the binder evaluation. The formulated graphene films with high conductivity and good electrolyte wettability generally rendered high capacitance, high power delivery, fast frequency response, and excellent cycling stability.

CHAPTER 1. INTRODUCTION

1.1 Overview of Supercapacitors

The increasing energy consumption and the reduction in fossil fuels have driven the development of sustainable energy technologies. Recently, we have witnessed rapid growth of energy production from wind and solar radiation, as well as the emergence of electric, hybrid, and low-emission vehicles [1]. One issue for these renewable energy sources is that they generate electricity in an intermittent manner. Therefore, efficient and reliable energy storage systems are required to provide long-term energy at any time of the day. Currently, batteries and electrochemical capacitors are two forefront technologies for energy storage [2, 3]. Typically, batteries can offer high energy density, but they suffer from low power density and they can take hours to be recharged. For example, lithium ions batteries rely on the intercalation of Li ions to enable redox reactions in bulk electrode materials, which is a diffusion controlled process and can be slow [4]. For higher power delivery, electrochemical capacitors (ECs), also known as supercapacitors (SCs), have been developed as an alternative energy storage solution [5]. Rather than chemical reactions, supercapacitors rely on physical charge storage process to achieve faster charge/discharge rates, longer cycle life, more efficient and environmentally friendly operations.

1.1.1 Energy storage mechanism

Supercapacitors can be classified into electrical double layer capacitors (EDLCs) and pseudocapacitors depending on the charge storage mechanism [6]. EDLCs store energy via reversible adsorption/desorption of electrolyte ions onto the surface of active electrode

materials. By applying bias to the electrodes, two layers of polarized ions are formed at the electrode/electrolyte interface, which is defined as the electrical double layer by Helmholtz in 1853 [7]. This model is in analogy to conventional parallel plate capacitor, in which the double layer capacitance can be expressed as Equation (1)

$$C = \frac{\varepsilon_r \varepsilon_0 A}{d} \tag{1}$$

where ε_r is the electrolyte dielectric constant, ε_0 is the dielectric constant of the vacuum, d is the effective thickness of the double layer, and A is the electrode surface area. If d is sufficiently small compared to the other dimension, on the order of Debye length (0.3-0.8 nm) [8] in this case, the capacitance can be approximated as

$$C = \frac{\varepsilon A}{4\pi d} \tag{2}$$

where ε is the dielectric constant of the medium (electrolyte). The Helmholtz model predicted a differential capacitance about 5-20 μF/cm^2, depending on the electrolyte used [9]. Based on Equation (1) and (2), the key factor to reach high capacitance is to select electrode materials with high surface area and porosity.

The Helmholtz model was later refined by Gouy and Chapman [10, 11]. Their model proposed the presence of "diffuse layer" considering the fact that ion distribution in electrolyte solution should be continuous. The motion of ions in electrolyte is controlled by the synergistic effect of ionic diffusion due to concentration gradient and electromigration due to the electric field. One drawback for the Guoy-Chapman model is that they overestimated the electrical double layer (EDL) capacitance [12]. Since the

capacitance increases dramatically with the decrease of charge separation distance, an unrealistic high capacitance will arise when the point charge ions are close to the electrode surface.

In 1924, Stern combined the Helmholtz model with the Guoy-Chapman model to describe two distinctive regions of ion distribution, the Stern layer and the diffuse layer [13]. The Stern layer consist of specifically absorbed ions (covalent forces) and non-specifically absorbed counter-ions (electrostatic forces). The inner Helmholtz plane (IHP) and outer Helmholtz plane (OHP) are used to distinguish two types of adsorbed ions [14]. Electrolyte ions are mostly hydrated, so a monolayer of solvent molecules exist between two layers of polarized ions, serving as IHP. The schematic illustration of electrical double layers structures for the aforementioned three models is shown in Figure 1.1.

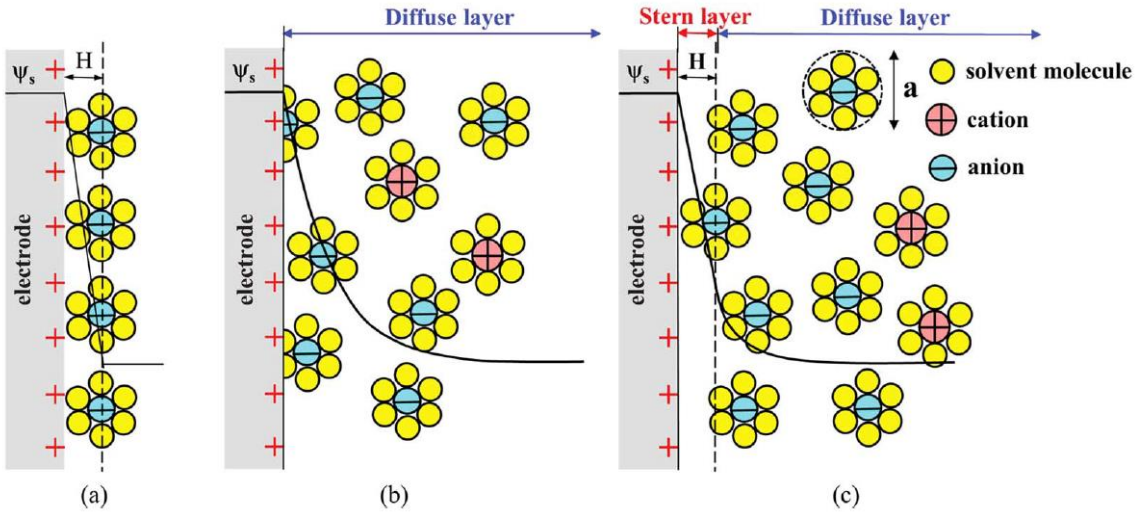

Figure 1.1 Schematic representation of electrical double layer structures according to (a) the Helmholtz model, (b) the Gouy-Chapman model, and (c) the Gouy-Chapman-Stern model. The double layer distance in the Helmholtz model and the Stern layer thickness are denoted by H while ψ_s is the potential at the electrode surface. Reprinted with permission from [14]. Copyright 2015, ECS.

Pseudocapacitors differ from EDLCs in that they utilize reversible Faradaic reactions (redox reactions) that take place at the active materials [15]. There are three types of Faradaic processes with electrochemical features: (1) underpotential deposition of metals, (2) surface redox reactions of transition metal oxides, or reversible electrochemical doping/dedoping in conducting polymers, and (3) ion intercalation without crystallographic phase change [16]. Materials that can undergo redox reactions include metal oxides/hydroxides, such as RuO_2, MnO_2, $Co3O_4$, $Ni(OH)_2$ and various electrically conducting polymers, such as polyaniline, polypyrrole, and poly(3,4-ethylenedioxythiophene) polystyrene sulfonate (PEDOT:PSS) [17-20]. The charge/discharge process involves the transition of charges across the double layers, resulting in the passage of Faradaic current through supercapacitor cells. Generally, pseudocapacitors exhibit far larger capacitance and energy density than carbon based EDLCs since the electrochemical processes occur at the surface as well as the bulk near surface of the electrode [2]. However, similar to batteries, pseudocapacitors relying on redox reactions have relatively lower power density and poor cycling stability. Hybrid capacitors, combining a supercapacitor electrode with a battery electrode, are also developed to possess the benefits of both capacitor and battery properties [21, 22].

1.1.2 Capacitance, energy and power densities

A conventional supercapacitor cell consists of two electrodes that are electrically isolated by a membrane as separator. Current collectors made of metal thin films, foils, foams, and carbon based templates are used to carry electrical current to the electrodes. The separator and electrodes are immersed into liquid or solid-state electrolyte to allow the ionic transport while prohibiting the current flow between two electrodes. As illustrated in

Figure 1.2, a typical SC cell can be considered as two capacitors (C_1 and C_2) connected in series, and the overall capacitance (C_{cell}) can be expresses as Equation (3)

$$\frac{1}{C_{cell}} = \frac{1}{C_n} + \frac{1}{C_p} \tag{3}$$

where C_n and C_p are the capacitance of C_1 and C_2. If the two electrodes are identical, namely, $C_n = C_p = C_s$ (specific capacitance), the cell capacitance is half of the specific capacitance.

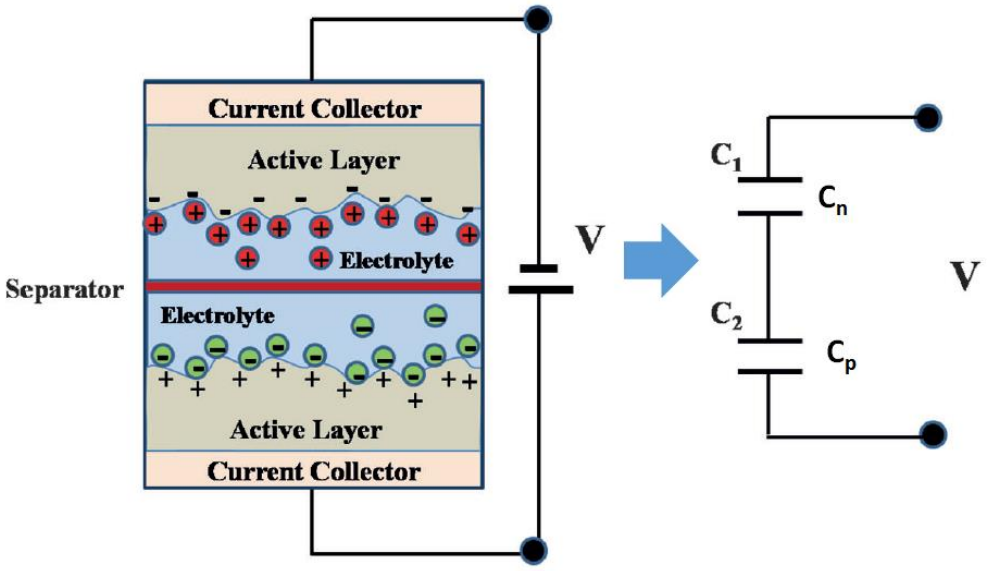

Figure 1.2 Schematic representation of a supercapacitor cell. Reprinted with permission from [23]. Copyright 2014, John Wiley & Sons.

Energy and power densities are another two critical parameters to evaluate the electrochemical performance of supercapacitors. The maximum energy (E_{max}) and power density (P_{max}) are calculated according to Equation (4) and (5)

$$E_{max} = \frac{1}{2} C_{cell} V^2 = \frac{1}{2} QV \tag{4}$$

$$P_{max} = \frac{1}{4R_s} V^2 \tag{5}$$

where Q is the total stored charges, V is the operation voltage, which is controlled by the electrochemical stability of the electrolyte and electrode, and R_s is the equivalent series resistance. It can be seen that C_{cell}, V, and R_s are three important variables, in which higher energy and power densities can be achieved by increasing C_{cell} and V while reducing R_s. Particularly, both energy and power densities are proportional to the square of voltage, thus the voltage increase plays a bigger role in raising energy and power densities.

The Ragone plot, with the power density versus energy density, for various energy storage devices are presented in Figure 1.3. It can be seen that electrochemical capacitors fill the gap between batteries and electrolytic capacitors. Due to the energy storage nature of the supercapacitors, they have high power density over 10 kW/kg, which make them fully charged or discharged in a seconds. However, for EDLCs, the charges are confined to the electrode surface, which limits their energy at around 5-10 Wh/kg. In contrast, the energy density is much higher for lead-acid (20-35 Wh/kg), Ni metal hydride (40-100 Wh/kg), and lithium ion batteries (120-170 Wh/kg).

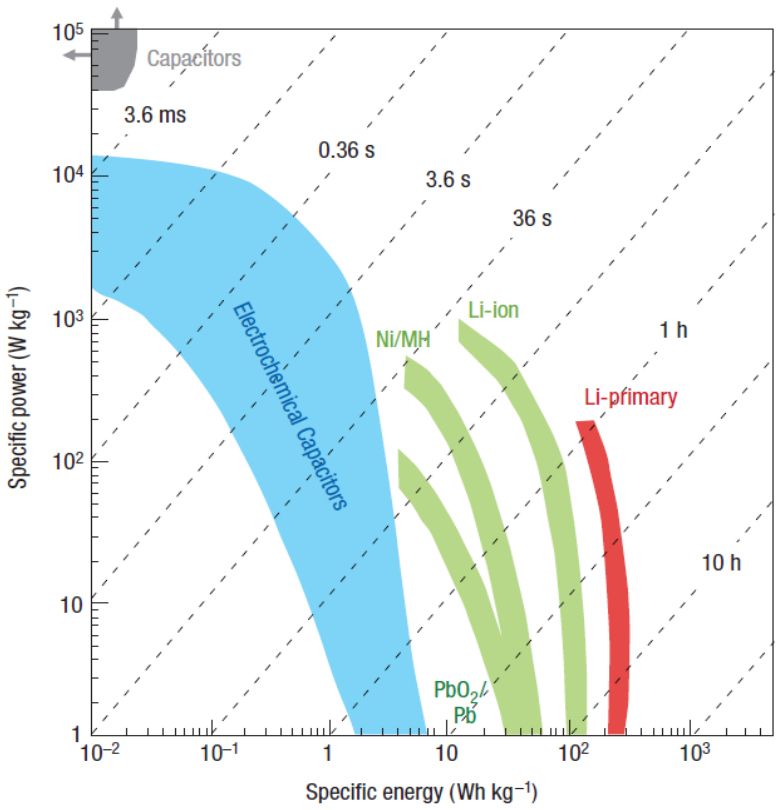

Figure 1.3 Ragone plots for different energy storage devices. Reprinted with permission from [1]. Copyright 2008, Macmillan Publishers Limited.

1.1.3 Applications

Supercapacitors have become an attractive power sources with high power density and exceptionally long cycle life. They show great potential for application when high power operation is demanded, including power buffer and saving units, as well as for energy recovery [24]. Specifically, supercapacitors are of great interest for electric vehicles, cameras, video recorders, mobile phones, laser tools featuring pulse power, uninterruptible power supplies, and energy storage from solar cells [25, 26]. For example, EDLCs have been widely used to perform power buffer and memory back-up functions in portable consumer electronic devices. As another example, the Airbus A380 jumbo jets utilizes EDLC technology to control the opening of emergency doors. The modules contain

an in series/parallel assembly of 100 F/2.7 V cells that are integrated into the doors to limit the use of heavy copper cables [1].

The main market for the EDLC manufacturers for the next years is the transportation industry, such as hybrid electric vehicles, metro trains, and tram ways [27, 28]. For automobiles, supercapacitors can be coupled with batteries to deliver high power during acceleration and recover the energy during braking. The increasing hybridization level in engines also serves to ensure smooth starting in cold weather and elongate battery life. It was reported that $205.9 million in revenue was generated for supercapacitor industry by 2014, and it is expected that the industry can further expand at an average of 10.9% annual growth rate in next decades [29].

1.2 Materials for Supercapacitors

The design and selection of materials, including electrodes, electrolytes, separators and current collectors, have a profound effect on the performance of SCs. While current collector and separator materials are significant to the internal and charge transport resistance, the focus of this study is on the development of electrode materials and evaluation of their electrochemical properties in different electrolytes.

In order to achieve high capacitance for EDLCs, the key is to use materials with high specific surface area to store charges and high electrical conductivity to transfer charges. Carbon materials with graphitic structures, including activated carbon, carbon derived carbons, carbon nanotubes (CNTs), and graphene can well meet these requirements with high conductivity, high electrochemical stability, and open porosity [9]. Carbon

materials are also coupled with conducting polymers and metal oxides/hydroxides to form composite electrodes to boost capacitance and energy density [20, 30].

1.2.1 Graphene

1.2.1.1 Structures and properties of graphene

Graphene is a monolayer of sp^2 carbon atoms arranged into a 2D hexagonal lattice [31]. Graphene was first isolated into an atom-thick carbon form by Novoselov and co-workers in 2004 [32]. Since then, graphene has gained increasing research interest due to outstanding structural, chemical, electronic, and mechanical properties. Intrinsic single layer graphene is a zero-gap semiconductor, and the electronic band structure of graphene results in both semiconducting and metallic characteristics [33]. The carrier mobility of graphene at room temperature is 1.5×10^4 V^{-1} s^{-1}, and charges carriers can be modulated between electrons and holes [34]. By minimizing the impurity scattering, the intrinsic carrier mobility can be as high as 2×10^5 cm^2 V^{-1} s^{-1} [35]. The electronic properties of graphene vary with the number of layers and the stacking order. In addition to the high conductivity, graphene has an ultrahigh theoretical specific surface area of 2630 m^2 g^{-1}, which makes it a promising candidate for electrochemical energy storage applications. Material properties of graphene and other forms of carbons are compared and summarized in Table 1.1.

Table 1.1 Materials properties of graphene and other carbon forms. Reproduced with permission from [36]. Copyright 2015, Macmillan Publishers Limited.

	Graphene	CNT	Fullerene	Graphite
Dimensions	2	1	0	3
Hybridization	sp^2	Mostly sp^2	Mostly sp^2	sp^2
Hardness	Highest (for single layer)	High	High	High
Tenacity	Flexible, elastic	Flexible, elastic	Elastic	Flexible, non-elastic
Experimental SSA ($m^2 s^{-1}$)	~1500	~1300	80-90	~10-20
Electrical Conductivity (S cm^{-1})	~2000	Structure-dependent	10-10	Anisotropic: 2–3 × 10^4*, 6†
Thermal conductivity (W m^{-1} K^{-1})	4840-5300	3500	0.4	Anisotropic: 1,500–2,000*, 5–10†

*a direction, †c direction

Graphene also demonstrates excellent thermal conductivity of ~ 5000 W m^{-1} k^{-1}, higher than the values measured for CNTs and diamonds [37]. The optical transmittance of graphene is ~97.7% [38]. Conductive and transparent graphene electrode can be a potential substitute for the expensive indium tin oxide (ITO) based electrodes in solar cells, displays, windows, and light emitting diodes. The mechanical flexibility of graphene electrodes show great advantages over rigid structures in designing flexible, portable, and wearable electronics [39-41].

1.2.1.2 Preparation methods

The methods for graphene synthesis play a critical role in determining the properties of the final product. Figure 1.4 shows the commonly adopted methods for graphene preparation [36]. The first approach to make graphene was achieved by a layer by layer technique using a scotch tape. Graphene layers were peeled off from a highly oriented pyrolytic graphite (HOPG), followed by the deposition on a silicon substrate using an organic solvent [32]. High quality graphene can be produced, but the yield and efficiency are low. Graphene can also be prepared by mechanical exfoliation, synthesis on SiC, and bottom-up approach through a total synthesis route from simple organic precursors [42]. However, the limited scalability and high cost constrains their widespread usage.

Chemical vapour deposition (CVD) produces graphene via the pyrolysis of hydrocarbon compounds on the surface of a metal catalyst at high temperature [43]. There are two types of graphene formation mechanisms, the precipitation mechanism and the surface growth mechanism [44]. The first mechanism is applied to the metal catalyst with high solubility of carbons (e.g. Ni). At high temperatures, hydrocarbon decomposes into smaller species that diffuses into the metal catalyst. During cooling, carbon species precipitate from the metal surface, undergo a nucleation and growth process to form graphene. For the second mechanism, a carbon precursor can absorb onto the surface of a metal catalyst (e.g. Cu), followed by the continuous nucleation and growth steps to from a large graphene domain. Although the CVD method has been well established, high production cost and low yield are not satisfactory for scalable production of graphene. In addition, the transfer of graphene from metal substrate is complicated and time consuming.

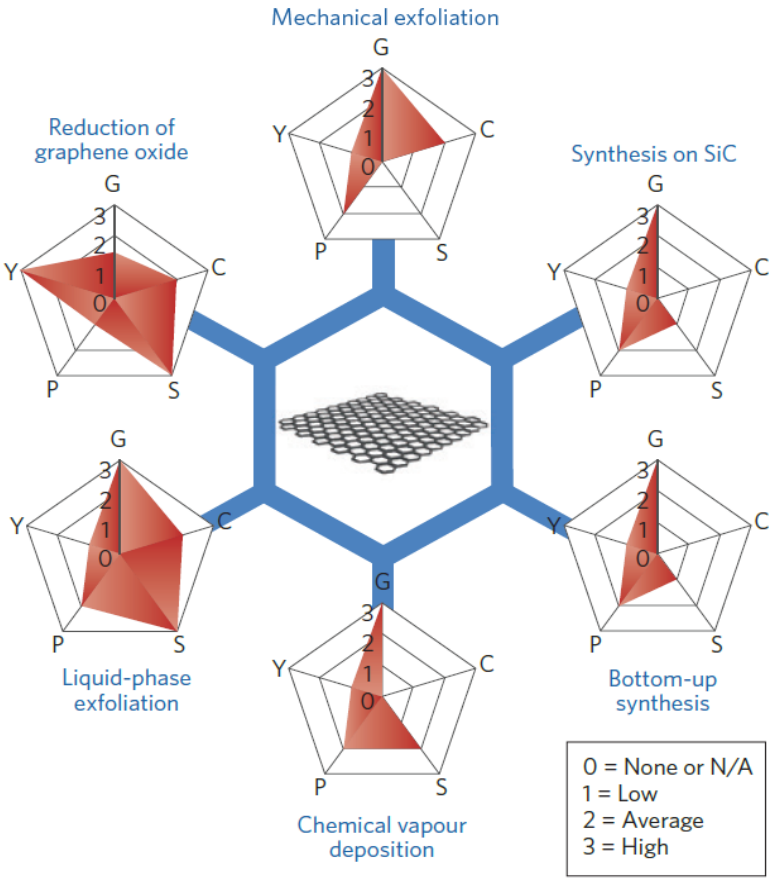

Figure 1.4 Schematic illustration of commonly adopted methods for graphene production. Several factors are considered for evaluation, including graphene quality (G), cost (C), scalability (S), purity (P), and yield (Y). Reprinted with permission from [36]. Copyright 2015, Macmillan Publishers Limited.

Solvent-assisted exfoliation is an effective method to prepare high quality graphene [45]. Graphite powders or expandable graphite are first dispersed in a suitable solvent to reduce the van der Waals interactions between graphene layers. Then a strong external power, such as ultrasonication, electric filed, or mechanical force, is imposed to fragment and exfoliate graphite into graphene sheets [36]. However, it remains a challenge for scalable production with reasonably low cost.

Reduction of graphene oxide (GO) is considered as a large-scale and low cost method to produce graphene with high yield [46]. GO is an oxidized and defective form of

graphene with disruptive sp^2 carbon network [47]. It is synthesized by strong oxidation of graphite, with subsequent dispersion and exfoliation in water or appropriate organic solvents [36]. During the oxidation process, many oxygen-containing functional groups are covalently bonded to graphene surface, including hydroxyl and epoxide groups on the basal plane, and smaller quantity of carboxyl and carbonyl group at the edges [48]. The presence of these functional groups provide obvious benefits for energy storage applications. First, GO containing rich polar oxygen functionalities are highly hydrophilic and can be well dispersed in water, which facilitates easy coating and processing of GO to make thin film electrodes by drop-casting, layer-by-layer assembly, and spin coating [49]. In addition, these reactive functional groups can serve as reaction sites for chemical modifications of GO, which can be used to anchor electroactive species via covalent bonds or non-covalent interactions for the design of graphene-based materials [39].

GO must be reduced to restore the conjugated π network to be used as SC electrode materials [50]. Thermal, chemical and hydrothermal reduction are generally used methods for reduction of GO to produce reduced graphene oxide (rGO) [46]. Thermal reduction (thermal annealing) utilizes heat treatment to expand graphene layers. Upon dramatic increase of temperature (thermal shock), oxygen functional groups are decomposed into CO_2 or CO that can generate large pressure to exfoliate the stacked graphene layers [51, 52]. In addition to thermal annealing, thermal reduction can also be achieved via microwave or photo-irradiation at a shorter processing time [46, 53].

Chemical reduction processes can be realized at room temperature or upon moderate heating. Hydrazine has been recognized as an efficient reducing agent for mass production of graphene. These chemically converted graphene can achieve good

conductivity with high C/O ratio, indicating a high reduction degree [54-56]. Sodium borohydride ($NaBH_4$) and hydroiodic acid (HI), are also strong reducing agent that can be used for GO reduction [57, 58]. Hydrothermal process is considered to be another simple, low energy-consuming and environmentally friendly approach to produce graphene in bulk quantities because it typically operates at low temperatures (<200°C) and requires no hazardous reducing agents.[59, 60] In addition, by adjusting the reaction time and temperature, the surface morphology and functionalities of the graphene nanostructure can be easily controlled.[61] Due to the incomplete removal of oxygen function groups (external defects) and the presence of fragmented edges (intrinsic defects), only medium quality graphene can be produced using chemical/hydrothermal reduction methods. However, the high yield, mass-production capability, and low cost raises considerable interest for the manufacture of graphene for supercapacitors. Moreover, the effect of structural defects can be minimized via delicate design of graphene networks. In some cases, the external defects of graphene can also be utilized and tailored to contribute to the overall charge storage capability.

1.2.1.3 Functionalization of graphene

It was reported that the intrinsic capacitance of graphene reach 21 $\mu F/cm^2$ (550 F/g) if the SSA of graphene (2630 m^2/g) can be fully utilized [62]. However, graphene made from reduction of GO tends to be restacked due to the loss of oxygen functional groups and van der Waals interaction between sheets. Therefore, reduced graphene oxide needs to be functionalized to tune the chemical and electrical structures of graphene for better electrochemical performance.

Various methodologies have been proposed and explored for graphene functionalization, which can be classified into three aspects:

(1) creating defect sites (e.g. pores) on graphene basal planes or edges;

(2) constructing three-dimensional (3D) graphene framework by using designed templates or incorporating cross-linkers between two-dimensional (2D) sheets;

(3) decorating graphene with nanoparticles, conducting polymers, and metal oxides/hydroxides, etc.

These approaches serve to modify graphene properties from several perspectives, including creating open pores, enlarging SSA, utilizing reversible Faradaic reactions, and modulating the conductivity and band gap structures. For example, activated graphene and holely graphene framework have been prepared by etching graphene with KOH and H_2O_2 respectively [63, 64]. The formation of interconnected meso- and micropores dramatically increase the SSA while offering open channels for efficient ion transfer through the entire network. It was reported that a 3D graphene network was synthesized using vertically aligned CNT as pillars using a controlled CVD method [65]. The intercalation of CNT is effective to reduce the aggregation of rGO sheets and provide additional conductive pathways of graphene network.

Generally speaking, the majority of graphene functionalization methodologies fall into the category of chemical functionalization. Typically, chemical functionalization can be achieved by covalent bonding or non-covalent interactions. The non-covalent interactions include van der Waals force, electrostatic interaction, hydrogen bonding, coordination bonding, and π-π interaction [66, 67]. For example, Wu *et al*. employed three types of surfactants, tetrabutylammonium hydroxide (TBAOH), cetyltrimethylammonium

bromide (CTAB), and sodium dodecylbenzene sulfonate (SDBS), to modify graphene for SC electrodes [68]. Specifically, the ammonium cations can interact with the negatively charged GO, and SDBS molecules with benzene ring can assembly on graphene surface via π-π stacking interactions. After the reduction, the surfactant-intercalated rGO electrodes, with structural stability and electrolyte wettability, achieved higher capacitance in both aqueous and ionic liquid electrolytes. Graphene has also been coupled with PEDOT:PSS, as an aqueous soluble and conducting polymer, via π-π stacking interactions to achieve high conductivity and capacity. The non-covalent interactions are relatively weak compared to covalent bonding [69]. They may trigger less defects to graphene network, but the limited structural stability may influence the long-term cycling performance of the electrode.

Covalent functionalization of graphene has aroused intense attention since more durable graphene network are formed at the presence of stronger covalent bonds. Taking advantage of the diverse functional groups on GO, versatile synthetic chemistry can be designed using a variety of candidate molecules. For instance, carboxylic acids in GO can be converted to highly reactive acyl halide groups, which can lead to the formation of anhydrides, esters, or amides by corresponding condensation reactions [70]; epoxide groups can undergo ring-opening reactions using alcohols, thiols, amines, and other reagents as nucleophiles [71]; hydroxyl groups can react with isocyanate groups to form carbamate esters [72]. While most reactions take place via oxygen groups, covalent bonds can also be generated through spontaneous reaction of an aryl diazonium salt with carbon atoms on graphene at room temperature [73]. Due to the excellent solution processability of GO, the covalent functionalization is typically performed at the GO stage first followed

by the reduction and other treatments. Multi-step reactions can be carried out to control the covalent grating of specific molecules. In addition, graphene-based polymer nanocomposites are prepared by grafting a monomer unit on GO followed by the *in-situ* polymerization. In particular, various graphene/polyaniline nanostructures have been developed by different synthetic routes to demonstrate improved electrochemical properties [74, 75]. The selection of dopants, doping degree, and the loading ratios to graphene all influence the conductivity and the pseudocapacitive behavior of the composite electrodes [76, 77]. Furthermore, heteroatoms, such as boron (B), nitrogen (N), oxygen (O), and phosphorous (P) can be doped into graphene lattice at elevated temperature [78, 79]. These dopants can tune the band gap structures of graphene to exhibit n-type or p-type behavior with modulated electrochemical activities. Chemical functionalization can not only tune the surface chemistry of graphene, but also modify the physical geometries of the graphene framework. Specifically, organic molecules with multi-functional groups can covalently bond to GO surface and crosslink between adjacent graphene sheets [80]. In this sense, these organic modifiers act as "spacers" to enlarge graphene interlayer spacing and create 3D graphene covalent organic frameworks (COFs).

1.2.2 Electrolytes

Electrolyte is an essential components in SC to provide sources of cations and anions. The requirements for electrolytes includes high ionic conductivity, fast ionic transfer, wide potential window, high electrochemical stability, high purity, moderate viscosity, low volatility, and low toxicity. The electrolyte used for SC can be categorized into three groups: (a) aqueous electrolyte, (2) organic electrolyte, and (3) ionic liquid (IL) electrolyte.

Aqueous electrolytes can be acidic, basic and neutral, such as H_2SO_4, KOH, LiCl, Na_2SO_4, etc. These electrolytes have relatively high ionic conductivity and small ionic sizes, which can achieve higher specific capacitance compared to organic and IL electrolytes. The disadvantage of the aqueous electrolytes is their narrow potential window, typically lower than 1 V, which limit their capability for high energy output. Moving from aqueous to organic electrolyte increases the cell voltage to 2.5-2.7 V [1]. According to Equation 4, a higher operation voltage offers dramatically improved energy density. Acetonitrile (AN) and propylene carbonate (PC) are two widely used solvents. While AN generally shows higher solubility for organic salts, PC electrolyte are gaining increasing popularity because of lower flash point, lower toxicity, and wider operating temperature [81]. Commonly used organic salts include tetraethylammonium tetrafluoroborate ($TEABF_4$), tetrabutylphosphonium tetrafluoroborate ($TBPBF_4$), and triethylmethylammonium tetrafluoroborate ($TEMABF_4$).

Ionic liquids are solvent-free and liquid form of organic salts at room temperature. Their voltage window is solely dependent on the electrochemical stability of the ions [82]. The main cations for ILs are imidazolium, pyrrolidinium, and quaternary ammonium salts, while the anions are tetrafluoroborate, trifluoromethanesulfonate (triflate), bis(trifluoromethanesulfonyl)imide (TFSI), and hexafluorophosphate (PF_6). The chemical structures of anions and cations in IL are illustrated in Figure 1.5. Although IL based SC device has demonstrated high working voltage (> 3V) and high energy density, the insufficient ionic conductivity at a practical working temperature range (-30 to 60°C) remains an issue [83]. By delicate design of cation and anion combinations, the ionic conductivity can be increased to 10^{-2} S/cm level with operating voltage over 4 V [84]. Apart

from the liquid electrolytes, solid-state gel electrolytes have been explored by incorporating polymer or fumed silica gels [85].

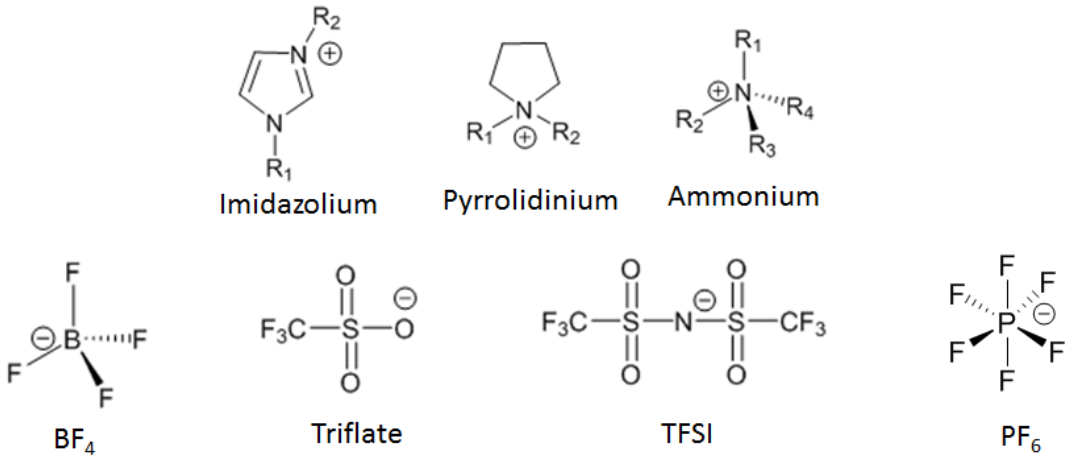

Figure 1.5 Chemical structures of cations and anions of ILs.

1.2.3 Binders and other additives

Electrode materials must be fabricated into free-standing thin films or cast uniformly onto current collectors to be used as SC electrodes. A high performance electrodes must have high capacitance, low internal and low contact resistance with current collectors, good wettability by electrolyte ions, low electroactive impurity, good chemical and mechanical stability. In this sense, electrode powders must be closely and neatly packed together to reduce the contact resistance and improve the density of the electrodes. Polymer binders are used in this regard to provide excellent mechanical integrity with strong bonding between particles as well as good adhesion to current collectors. Polymer binders are chemically and electrochemically inert, and they are used in small amount for effective bonding while not disrupting the porosity of the active electrode materials [86]. While most polymer binders are electrically insulating, conducting polymer binders have

been developed with improved conductivity and adhesion strength. The addition of polymer binders with specific functional groups can also tune the surface energy of the electrode, thus affecting the electrode wetting and the accessibility of electrolyte ions [87]. Processing methods for binder-free electrodes have also been reported in literature [88]. In addition to polymer binders, various conductive additives have been investigated to optimize the electrode formulation. The most frequently used conductive additives belong to the family of carbon black (CB) with widely accepted amount about 5 wt% [89]. The typical particle size of CB is between 30-50 nm with a SSA below 100 m^2 g^{-1}. In some case, graphite is also used for conductivity or lubrication purpose.

1.3 Micro-Supercapacitors

1.3.1 Design merits

The rapid growth of portable electronics, such as biomedical sensors, remote control systems, radio frequency detectors, and microelectromechanical systems (MEMS), have significantly increased the need for miniaturized energy storage units [90-92]. These smaller-scale energy storage units have become particularly essential in many self-powered systems, where the power supply from an external source is not easily accessible [93]. Currently, microbatteries have been mostly used as miniaturized power sources. However, problems with microbatteries include limited power supply, short working lifetime, and toxicity, which hinder their application in many areas [94]. As a novel type of micro/nano-scale supercapacitors, a micro-supercapacitor (MSC) has been developed [95, 96]. Unlike conventional sandwich-typed supercapacitors, MSCs typically adopt a 2D planar configuration with interdigitally patterned electrodes and exhibit comparable energy

density with lithium thin film battery and comparable power density with electrolytic capacitor (Figure 1.6).

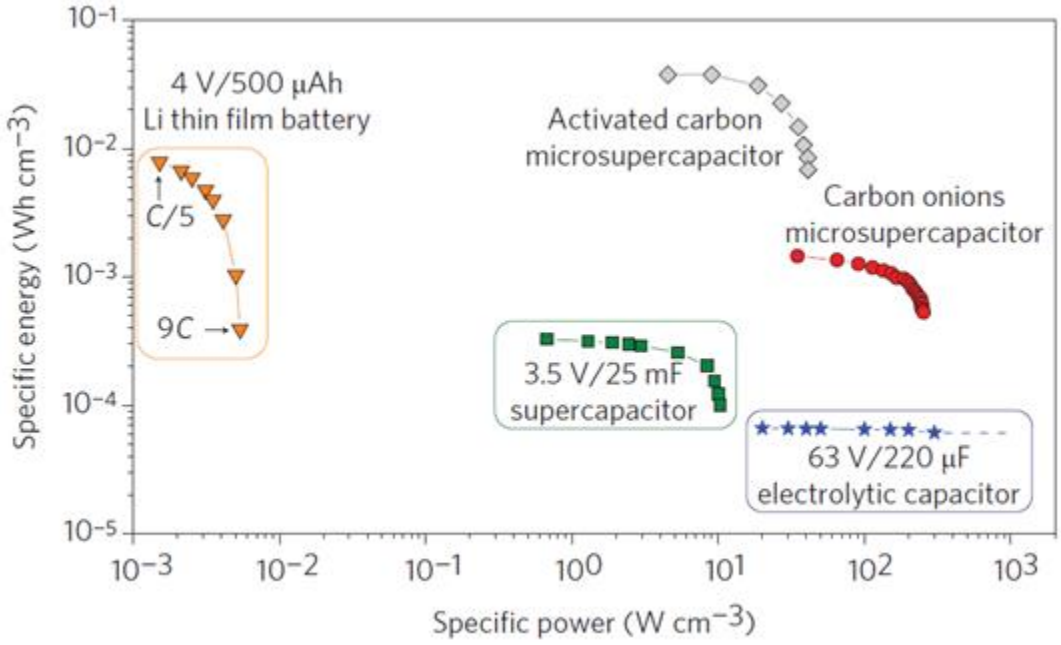

Figure 1.6 Ragone plots for various micro-devices for energy storage. Reprinted with permission from [85]. Copyright 2010, Macmillan Publishers Limited.

It was defined by Gogotsi *et al.* that the footprint of the MSC is generally in the millimeter or centimeter scale, consisting of micrometer scale thin film electrodes with thickness less than 10 µm [97]. Having the in-plane electrode structure has obvious technical advantages over the conventional sandwich structure (Figure 1.7). First, the mean ionic diffusion length is significantly reduced when the micro-scale electrode patterns (tens to a few hundred micrometers) are in the same plane, in which the electrolyte ions can easily transfer in the parallel direction of the electrode layers. The interdigitated fingers of microelectrodes offer large amount of open edges for the electrolyte ions to diffuse into the inner areas of the electrodes, which greatly enhances the utilization of the electrode surface area. By reducing the width of the microelectrodes and gap spacing, the diffusion pathway

of the electrolyte ions can be further shortened, resulting in larger power densities and faster frequency response. In the case of a sandwich structure, the electrolyte ions have to diffuse through the depth of each electrode film (~100 µm in thickness) and the separator (e.g. 250 µm, glass microfiber), which elongate the ionic diffusion pathway. In addition, the ionic transport perpendicular to electrode film can also be interrupted due to the stacked electrode structure, leading to poor capacitive properties. Second, the planar design enables the integration of MSC on various substrates for practical applications. For example, MSCs show great potential to be coupled with complementary metal-oxide semiconductor (CMOS) or MEMS on chip, and the functional chips can be further packaged into self-powered systems as sensors. Since the weight of the electrodes is small in MSCs, the areal or volumetric stack capacitance, rather than gravimetric capacitance, is more frequently used to evaluate the electrochemical performance [98].

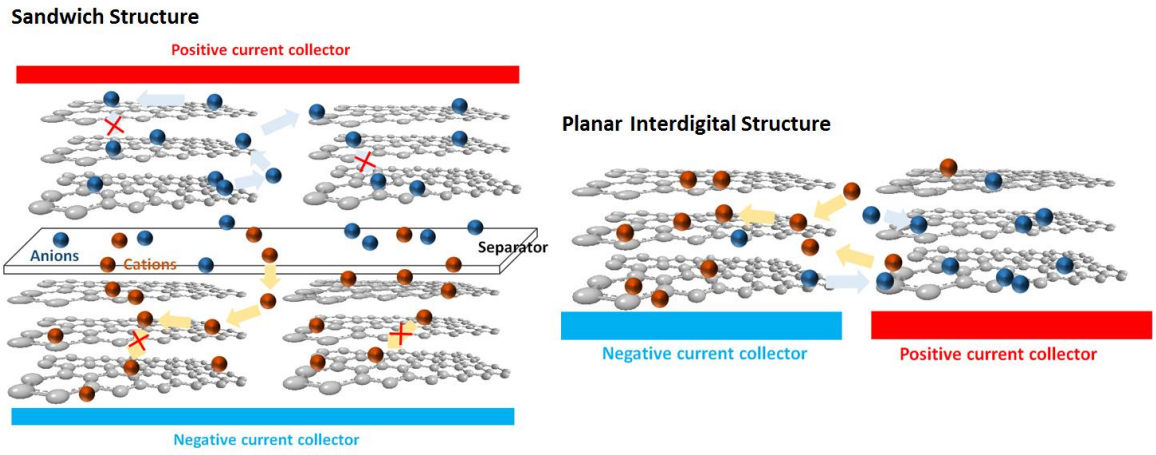

Figure 1.7 Schematic illustration of the supercapacitors in sandwich and interdigitated structures. Reprinted with permission from [85]. Copyright 2010, IEEE.

1.3.2 Fabrication processes

Advanced semiconductor fabrication technologies have facilitated the processing of thin-film microelectrodes. In 2010, Gogotsi's group designed a thin film carbon based (carbide-derived carbon e.g., TiC-CDC) MSC on a silicon wafer by chlorination, gold sputtering and selective etching techniques [99]. At the same time, Brunet and coworkers constructed an in-plane MSC by electrophoretic deposition of onion-like carbon (OLC, 6-7 nm in dimeter) with layer thickness of several micrometers [100]. The MSC architecture with high surface-to-volume ratios was made without the use of a binder and a separator, which significantly promote ionic diffusion through the thin-layer nanostructure. As a result, the MSC device achieves an ultrahigh power density and excellent frequency response. Later, a variety of fabrication methods have been employed for material deposition, including, sputtering, chemical vapor deposition, layer-by-layer (LBL) assembly, sol-gel methods, ink-jet printing, electrochemistry-based deposition, spray coating, and other related methods [101-106]. In an attempt to achieve fast and large-scale production of MSCs, direct laser writing methods have been employed to achieve synchronous reduction and patterning of GO films. In accordance with the growing interest for flexible and wearable electronics, flexible energy storage devices have been intensively studied. Particularly, two strategies have been proposed to make the flexible MSC arrays, (1) selection of flexible substrates that is compatible with material and device fabrication, (2) design of innovative MSC architecture that can relieve mechanical strains under deformation.

1.3.3 Solid-state electrolytes

Many researchers have used aqueous polymeric gels as solid-state electrolyte for MSCs with a voltage window around 0-1 V, such as polyvinyl alcohol/sulfuric acid (PVA/H_2SO_4), polyvinyl alcohol/phosphoric acid (PVA/H_3PO_4), and polyvinyl alcohol/lithium chloride (PVA/LiCl) electrolytes [107-109]. These solid-state electrolytes have exhibited high ionic conductivity, good mechanical strength, long cycling life, and low leakage current [110, 111, 109]. As proton conducting polymer blends, the ionic conductivity of PVA/H_3PO_4 is in the range of 10^{-5}-10^{-3} S/cm, and the ionic conductivity of PVA/H_2SO_4 can reach as high as 7×10^{-3} S/cm at room temperature [112, 113]. Ionic liquid-based solid state electrolyte have also been reported with operation voltage higher than 2V, which dramatically improves the energy density of MSC devices [114]. Two examples of non-aqueous gel electrolytes used in MSCs are PVA/1-butyl-3-methylimidazolium tetrafluoroborate ($BMIBF_4$) and 1-ethyl-3-methylimididazolium bis(trifluoromethylsulfonyl) imide (EMI TFSI)/ fumed silica (FS) [115, 116]. Compared with liquid electrolytes, the use of solid-state electrolytes not only reduces the possibility of internal shorting and electrolyte leakage, but also decreases the device thickness by alleviating the need for additional encapsulation layers. All these merits enable the easy packaging of MSC devices for miniaturized, portable and flexible electronic applications.

1.4 Research Objectives and Organization of the Dissertation

This research aims to study the chemical functionalization of graphene network and utilize the designed materials as electrodes for supercapacitor applications. The detailed research objective of this dissertation are:

(1) To rationally design the functionalized graphene materials as supercapacitor electrodes based on the fundamental understanding of the energy storage mechanisms

(2) To develop reliable methods for molecular level functionalization of graphene networks with controlled chemical, physical and electronic properties

(3) To systematically investigate the effect of graphene structures and formulations on the electrochemical performance via both experimental results and theoretical modeling

(4) To employ the optimized electrode materials and microfabrication technologies to make miniaturized energy storage devises

This dissertation is further organized into the following chapters. Chapter 2 introduces the design of graphene-based covalent organic framework by using various aliphatic and multi-functional "molecular spacers". These "molecular spacers" can be covalently grafted onto graphene surface, which dramatically reduces the restacking of graphene layers after reduction. Due to the structural benefits, the modified graphene demonstrates high EDL capacitance, high energy density, and excellent cycling stability in various electrolyte systems. Chapter 3 describes the incorporation of aromatic amines into graphene to boost the capacitance by reversible Faradaic reactions. Material structures, including reaction mechanism, chemical compositions, crosslinking and conjugated network, and electrochemical properties, including specific capacitance, charge transfer resistance, and redox transition states of the electrodes were comprehensively investigated to reveal the structure-property relationship. In conjugation with experimental results, molecular dynamic simulations and density function theory calculations were used to

predict the structural and charge transfer behavior of the electrode materials. Chapter 4 reports the development of a novel micro-scale supercapacitors, micro-supercapacitors (MSCs). A solution processable micro-electrode material and a compatible fabrication process were developed to achieve device miniaturization as well as high areal capacitance and fast frequency response. The architecture of MSCs were also designed to fabricate flexible and foldable energy storage devices. Chapter 5 describes the effect of polymer binders for graphene-based thin film electrodes. The conductivity, capacity, and wettability of the graphene electrodes with different binders in aqueous and organic electrolytes were explored and discussed. Chapter 6 presents the research summary and proposes future work.

CHAPTER 2. SYSTEMATIC INVESTIGATION ON GRAPHENE NETWORKS FUNCTIONALIZED BY ALIPHATIC MOLECULES

2.1 Introduction

Large-scale production of graphene can be realized by chemical reduction of GO, but the aggregated rGO structure results in significant loss of surface area and porosity [46, 117]. To overcome the problem, various modification approaches have been introduced to enlarge the interlayer spacing of graphene sheets and ensure the utilization of large surface area graphene derivatives. For example, exfoliated and few-layer graphene was obtained by assembling CNTs, carbon and SiO_2 nanospheres on graphene sheets with porous and hierarchical nanostructures [118-120]. However, the self-assembly process driven by π-π or electrostatic interactions is not strong enough to achieve uniform and consistent intercalation of spacers. In this sense, molecular spacers that rely on chemical bonds, rather than intermolecular interactions, can be used to effectively enhance the interlayer spacing and surface area of graphene and create a three-dimensional (3D) conductive graphene network. Although some synthesis methods have been proposed, few reports have performed a systematic study on graphene-based covalent organic framework (COF) in various electrolyte systems [121, 122]. In addition, the chemical and structural evolution from functionalized GO to rGO stage has not been elucidated. Moreover, the effect of chain size, chain conformation, degree of functionalization and hydrophilicity should be considered in tuning the functionalized graphene nanostructures.

In this chapter, chemical functionalization of graphene by various amines were investigated. Specifically, six types of aliphatic amines with different chain structures were

employed, namely, ethylene diamine (EDA), butane-1,4-diamine (BDA), hexane-1,6-diamine (HDA), 1,4-cyclohexane diamine (CHDA), ether diamine (EA148), and tris(2-aminoethyl) amine (Tris). These amine molecules can be covalently grafted on graphene, generating a 3D graphene network with more exfoliated layers and larger specific surface area. The chemical composition and the interlayer spacing before and after the complete reduction of GO were studied to illustrate the structural evolution. With these unique features, the as-fabricated graphene structure demonstrated an improved charge storage capability in aqueous electrolyte. In addition, larger energy density of the materials were obtained in 1 M tetraethylammonium tetrafluoroborate/acetonitrile (1 M $TEABF_4$/AN) as organic electrolyte and 1-butyl-3-methylamidazolium tetrafluoroborate ($BMIMBF_4$) as ionic liquid (IL) electrolyte. In conjugation with experiment results, computational methods were used to study the structural and electrical properties of the functionalized graphene. Moreover, a tertiary amine based spacer with multi-hydroxyl groups, trimethylamine (TEA), has been used to study and tune the wettability of the electrolyte surface. Due to the synergistic effect of enlarged surface area, stabilized 3D graphene structure and enhanced electrolyte wettability, the TEA/rGO electrode also presented improved specific capacitance with excellent rate performance and cycling stability.

2.2 Experimental

2.2.1 Materials preparation

Graphene oxide (GO) was prepared by a modified Hummers' method. Typically, 2 g of graphite flake (Asbury 230U) was put into 200 mL of concentrated H_2SO_4 (98%) containing 2 g of $NaNO_3$ in an ice bath. Then 9 g of $KnMnO_4$ was slowly added to the

solution and the temperature was kept below 10°C. The mixture was stirred in an ice bath for 2 h and in a water bath at 35°C for another 0.5 h. Then 92 mL of 70°C water was added dropwise to the solution while maintaining the temperature below 90°C. Afterwards, 280 mL of 70°C water was added into the solution, followed by the addition of 40 mL hydrogen peroxide (30 wt%) to terminate the reaction. Finally, the mixture was washed with 20 mL of 1 M HCl solution and copious amount of water until the pH of the GO solution was 6.

The amine/GO aerogel was prepared by ultrasonicating an aqueous solution containing 0.25 mmol of diamines (0.167 mmol of Tris) and 50 mg of GO (50 mL, 1 mg/mL) and heating hydrothermally in Teflon autoclaves at 90°C for 3 h. To make amine/rGO materials, same amount of amines and GO solutions were transferred to autoclaves to perform a two-step hydrothermal process at 90°C for 3 h and 180°C for 12 h. The amine/GO aerogels and amine/rGOs were rinsed with DI water under vacuum and dried in oven. To prepare TEA/rGO samples, viscous triethanolamine liquid was first diluted 10 times by deionized (DI) water and used as stock solution. Afterwards, 30 mg GO was dispersed in 60 mL followed by slow addition of 1.5 mL of TEA stock solution. The homogenously mixed dispersion was transferred to a 100 mL Teflon-lined autoclave for hydrothermal reaction at 105°C for 5 h and 180°C for 10 h.

2.2.2 Characterization

Solid-state ^{13}C magic-angle spinning (MAS) NMR spectrum was obtained on a Bruker DSX-300 spectrometer operating at a ^{1}H frequency of 300 MHz. ^{13}C direct polarization with ^{1}H high power decoupling was achieved at a 90° pulse of 5 ms with relaxation delay of 4 s for 2048 scans. A field-emission scanning electron microscope (FESEM, Hitachi

SU8010), a transmission electron microscope (TEM, JEOL 100 CX), and a Veeco Dimension Edge atomic force microscope (AFM) were used to image the morphology of amine/rGO materials. High resolution TEM (HRTEM) image of graphene nanostructure and the selected area electron diffraction (SAED) were acquired on a FEI Tecnai F30 TEM. The chemical structures were recorded on an attenuated total reflectance-Fourier transform infrared spectroscopy (ATR-FTIR, Nicolet 6700, Smart Performer single-bounce ATR module) or a transmission mode FTIR (Magma IR 560, Nicolet) spectrophotometer. X-ray photoelectron spectroscopy (XPS) was characterized by a Thermo K-Alpha spectrometer. Raman spectroscopy was taken by a Thermo Nicolet Almega XR Dispersive Raman spectrometer. X-ray diffraction (XRD) patterns were recorded from an X'Pert Alpha-1 diffractometer using Cu Kα radiation. Thermal profiles during heating were monitored by differential scanning calorimetry (DSC, TA Instrument Q 2000) at a heating rate of 10°C/min. Surface area and pore size distribution were analyzed using Micromeritics ASAP 2000 via Brunauer–Emmett–Teller (BET) and Barrett-Joyner-Halenda (BJH) methods. Contact angle measurements were conducted on a Rame-Hart goniometer. The electrochemical properties of the amine/rGO films were tested in symmetric coin cells using two-electrode system in 1 M H_2SO_4, 1 M $TEABF_4$/AN, and $BMIMBF_4$ electrolytes. The cyclic voltammetry (CV), galvanostatic charge/discharge (CD), and electrochemical impedance (EIS) tests were performed on Versastat 2-channel system (Princeton Applied Research). The specific capacitance (C_s) of the active materials was calculated from CV curves by

$$C_s = \frac{2\int IdV}{vmV} \tag{6}$$

where I is the applied current, V is voltage range, v is the scan rates, and m is the weight of two electrodes. Based on the cell capacitance, the energy density (E) was calculated based on Equation (4), and the power (P) was determined according to

$$P = \frac{E}{\Delta t} \tag{7}$$

where Δt is the discharge time.

2.2.3 Theoretical calculations

All the spin–polarized DFT computations were carried out by employing the PBE functional [123] and the double numerical plus polarization (DNP) basis set, as implemented in the DMol^3 code [124]. The accuracy of the DNP basis set was comparable to that of Pople's 6–31G** basis set. The convergence criteria applied for geometry optimizations were 2.0×10^{-5} au, 4.0×10^{-3} au/Å , and 5.0×10^{-3} Å for energy change, maximum force and maximum displacement, respectively. A vacuum space of 30 Å was adopted between adjacent layers to avoid mirror interactions. The Brillouin zone was sampled with the Γ−point only in geometry optimizations, whereas a $12 \times 12 \times 1$ grid was used for the electronic structure calculations.

2.3 Results and Discussion

2.3.1 Amine functionalized graphene

2.3.1.1 Chemical reactions and compositions

The chemical structures of amines and their reaction scheme with GO were shown in Figure 2.1. A two-step hydrothermal reaction was performed, in which the first step at 90°C for 3h served to enable the chemical reaction between GO and amines to form the covalent bonding, while the second step at 180°C for 12h served to reduce the amine-modified GO and restore the sp^2 hybridized graphene network. Notably, all the amines used in this study can be dissolved in water, enabling them to be processed with well-dispersed GO in aqueous solutions. In addition, the molar ratios of amine molecules to GO were controlled to ensure the efficient functionalization while the unreacted amines were rinsed off by water. Moreover, these amine molecules are of aliphatic structures, which provides another two advantages for the study of spacing effect. First, amino groups with aliphatic chains have higher chemical reactivity (nucleophilicity) since the lone pair electrons are closer to N atoms; whereas the lone pair electrons are delocalized when amino groups were connected to a benzene ring. Second, it avoids any possible pseudocapacitive charge transfer process when used as supercapacitor electrodes compared with aromatic-based amines. In this study, the molarity of the amino functional groups to GO was kept constant: 0.5 mmol of amino groups was reacted with 50 mg of GO.

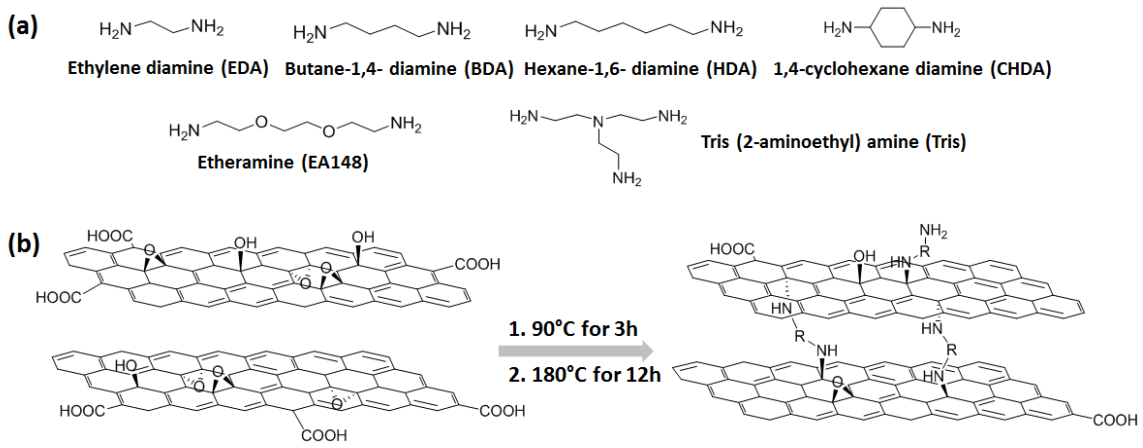

Figure 2.1 (a) Chemical structures of six amines used in this work; (b) schematic illustration of the chemical reactions between GO and amines.

Solid-state NMR was carried out to evaluate the functionalization degree of GO. According to the direct ^{13}C pulse spectrum (Figure 2.2), the characteristic GO peaks, namely, C-O-C at 63 ppm, C-OH at 71 ppm, O=C-O at 167 ppm, C=O at 193 ppm, and C=C at 132 ppm can be clearly visualized [125]. Peak integration results indicated that GO was well oxidized with largest amount of epoxide groups.

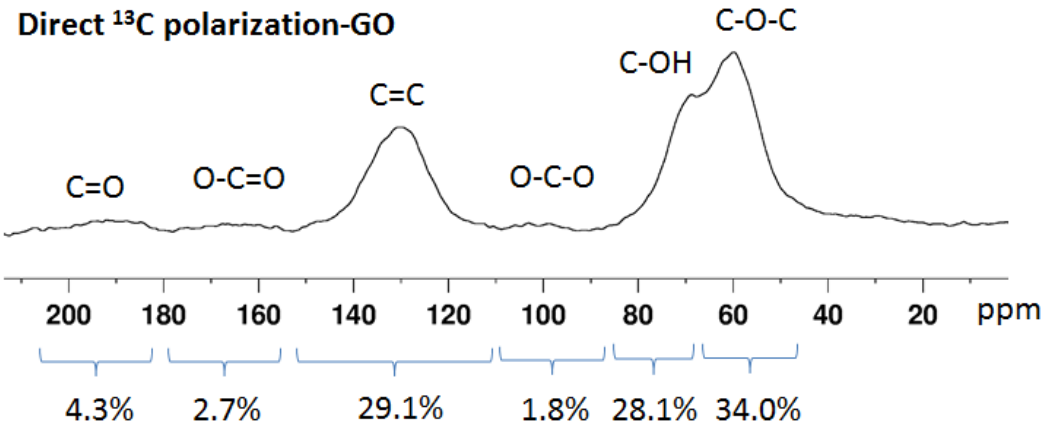

Figure 2.2 ^{13}C MAS NMR spectrum of GO with the percentage of the functional groups calculated by peak integration. Figure courtesy of Dr. Johannes Leisen.

The chemical structures of the GO, rGO and amine/rGOs were characterized by ATR-FTIR. As shown in Figure 2.3a, the characteristic peaks of GO appearing at 1730, 1230 and 1070 cm^{-1} corresponded to the carbonyl (C=O), epoxy (C-O-C), and alkoxyl (C-O) groups at GO surface, respectively. The broad peak at around 3400 cm^{-1} and the sharp peak at 1630 cm^{-1} were assigned to the hydroxyl (O-H) stretching and the physisorbed water [126]. After chemical functionalization and reduction, the peak for carbonyl groups diminished and a new peak appeared at 1551 cm^{-1}, which came from the vibration of –NH stretching in C-NH- group [122]. This chemical bonding indicate that these aliphatic amines, as highly reactive nucleophiles, could attack the epoxide groups on GO via nucleophilic substitution. It was also noticed that the alkoxyl and epoxy peaks shifted to higher wavenumbers (1112 and 1264 cm^{-1}) after the chemical reaction, which possibly arose from the change of neighboring environments when the amino groups were introduced into graphene structure.

Figure 2.3b shows the Raman spectra of rGO and amine/rGO, and all spectra had the typical D, G, 2D, and D+G bands for graphene-based materials. Generally, the I_D/I_G ratio was used to study the disorder in graphitic structures. It was found that the I_D/I_G ratio was in the range of 1.02-1.10 for functionalized rGO, which was slightly higher than that of rGO. The increase in I_D/I_G ratio was attributed to the incorporation of N heteroatoms and the possible formation of smaller-size graphitic domains [127].

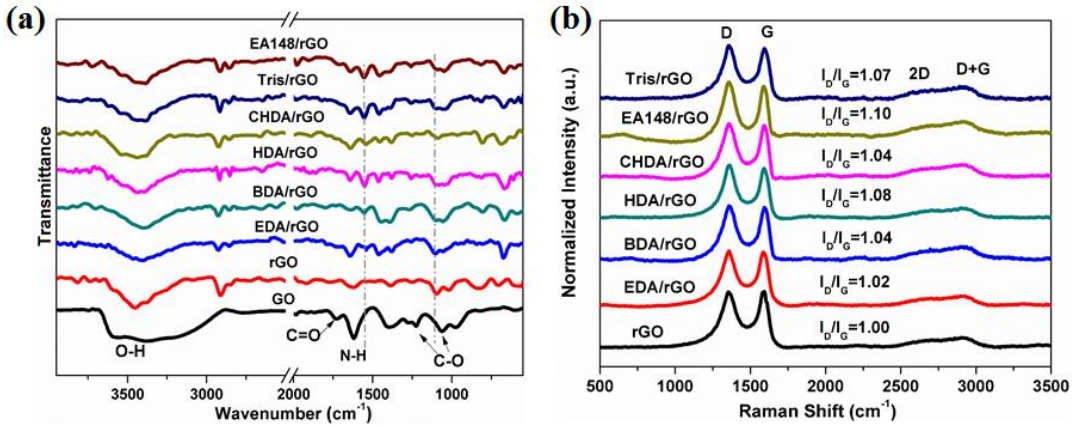

Figure 2.3 (a) ATR-FITR spectra of GO, rGO and amine/rGO; (b) Raman spectra of rGO and amine/rGO structures.

XPS was used to further examine the chemical composition. Based on XPS survey spectra, the atomic ratios of C, N and O were determined and listed in Table 2.1 and Table 2.2 . The carbon-to-oxygen (C/O) ratio only increased slightly from 2.1 of GO [128] to 2.4 of GOA, suggesting that GO was barely reduced during this step. After the process at 180°C, the significant decrease of O content (partial reduction) was accompanied by the increase of C content. It was found that the percentage of amino groups (N content) had a small change compared to amine/GO before reduction, which suggested the strong bonding nature of the amine spacers. The highest N percentage of ~8.15% was determined for Tris/GO. The high O percentage in EA148/rGO came from ether groups on the chain, which made the materials more hydrophilic. The high resolution C 1s and N 1s spectra of the BDA/rGO are shown in Figure 2.4a as an example to illustrate the chemical bonding. The C1s peak can be deconvoluted into four peaks at binding energies of 284.7 eV (C=C), 285.9 eV (C-O), 287.2 eV (C-N), and 288.7 eV (C=O) respectively. Peak integration revealed that there was a large quantity (13.4%) of C-N groups, which corresponded to the covalently grafting of amino groups on rGO. In N 1s spectrum (Figure 2.4b), the single –

NH- peak at 399.6 eV with the high level of fitting indicated that most amino groups were covalently bonded in the form of C-N-C [129], which is consistent with the FTIR results and the peak analysis of C 1s spectrum.

Table 2.1 Atomic ratios of C, N, and O in GOA and amine/GO

Samples	GOA	EDA	BDA	HDA	CHDA	EA148	Tris
C	70.88	73.20	74.20	74.91	76.34	70.87	75.99
N	-	6.37	6.48	4.65	5.39	5.51	8.15
O	29.12	20.43	19.32	20.44	18.27	23.62	15.86

Table 2.2 Atomic ratios of C, N, and O in rGO and amine/rGO

Samples	rGO	EDA	BDA	HDA	CHDA	EA148	Tris
C	87.36	85.66	85.48	86.39	86.76	83.15	86.17
N	-	6.33	6.37	3.93	4.53	5.24	7.79
O	12.64	8.02	8.15	9.68	8.71	11.61	6.04

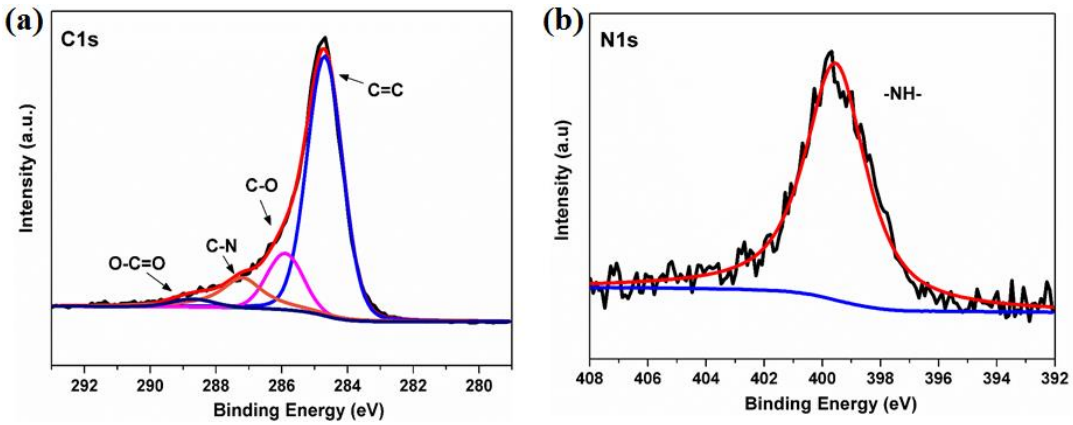

Figure 2.4 XPS (a) C 1s and (b) N 1s spectra of BDA/rGO with peak deconvolution to show the chemical bonding.

2.3.1.2 Physical properties

Surface morphology of rGO and amine/rGO were characterized. As shown in Figure 2.5 (a-b), rGO had stacked graphene sheets whereas the functionalized rGO showed crumpled morphology due to the intercalation of molecular spacers. The wrinkled and exfoliated form of the graphene sheets was also observed under TEM (Figure 2.5c), and the low contrast image indicated a small thickness of the specimen. From the HRTEM image (Figure 2.5d), the subnanometer scale of the edge thickness indicated the few-layer (1~2 layers) character of the graphene sheets. Selected area electron diffraction (SAED) pattern (Figure 2.5e) was obtained along the zone axis. The clear spots corresponded to the crystalline structure of graphene. For monolayer pristine graphene, the diffraction pattern typically shows a hexagonal symmetry. The functionalized graphene showed deviated hexagonal symmetry with twelve spots, which could be attributed to the twisting of graphene planes and clustered defects including the unreduced oxygen-containing functional groups and the molecular spacers decorated on graphene surface [130]. Figure 1f shows the AFM image of the functionalized graphene sheets with measured single-layer

thickness of 1.5 nm. The increased interlayer thickness, in comparison to GO (1.1 nm) [131], was attributed to the molecular level grafting of amine molecules, and the ultra-thin layer characteristic further confirmed the good exfoliation of graphene. The wrinkled feature of the graphene sheets were also observed by the high-contrast lines.

XRD was employed to investigate the effect of chain structures on graphene interlayer spacing. Figure 2.6a shows the XRD patterns of the amine/GO films after the first-step reaction. The GO aerogel (GOA) control sample displayed a 2θ peak at 10.9°, corresponding to an interlayer spacing of 0.82 nm. The 2θ angle of EDA/GO appearing at 10.0° was due to the intercalation of EDA. As the chain length increased, the 2θ shifted to smaller angles at 9.3° and 8.4° for BDA/GO and HDA/GO, respectively. In analogy to HDA, CHDA also exhibited 2θ at 8.5° with the calculated d spacing of 1.04 nm. For the bulkier-size molecules, the complicated inter/intra molecular interactions could affect the interlayer spacing. In the case of EA148/GO, the molecular chain with hydrophilic ether groups tended to be in a helix or coil configuration rather than a stretched form to be thermodynamically stable [132]. Therefore, the interlayer spacing for EA148 did not increase accordingly with chain length. The largest d spacing of 1.22 nm was observed for Tris/GO, which increased by 48.8% compared to that of GOA. It is believed that the tri-functional Tris molecules can form more chemical linkages on graphene surfaces than diamine molecules, leading to a more stabilized 3D network.

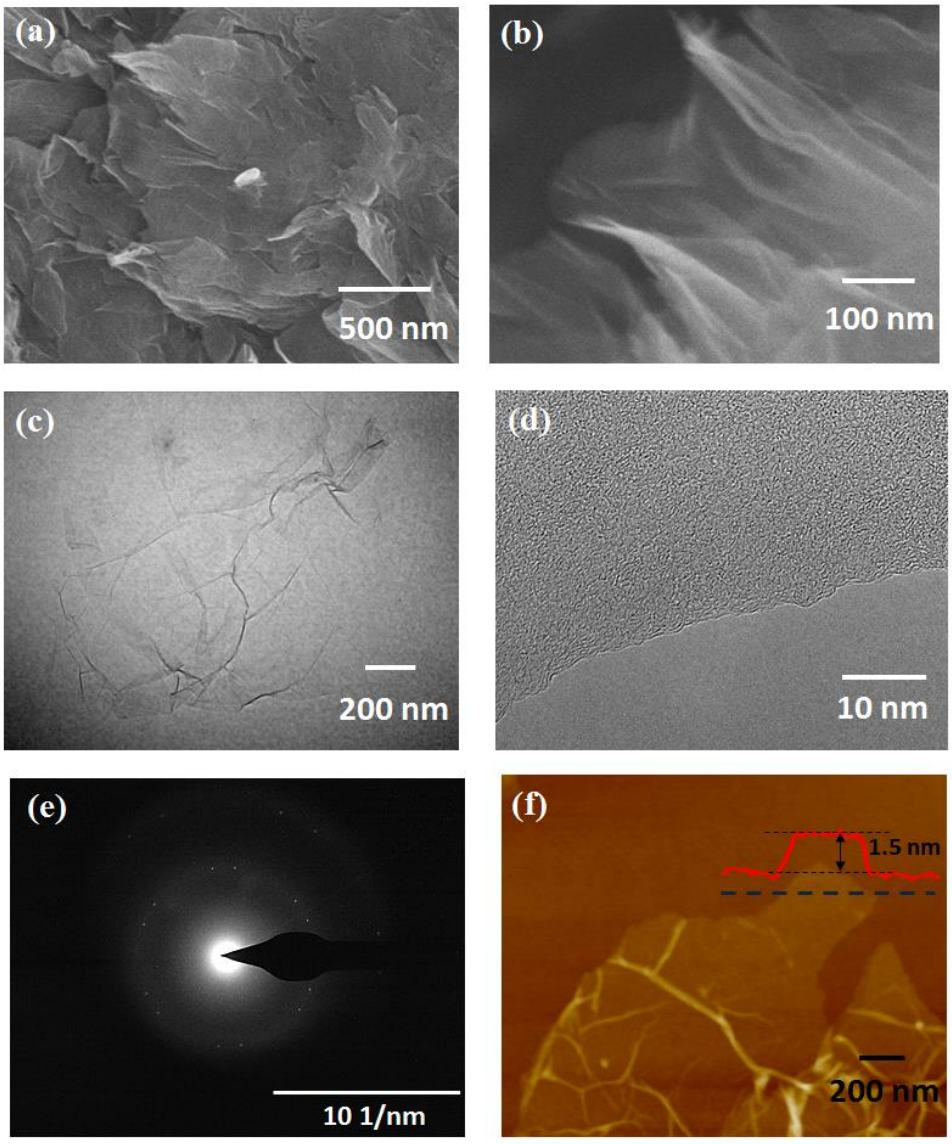

Figure 2.5 SEM images of (a) rGO and BDA/rGO; (c) TEM and (d) HRTEM image of the BDA/rGO; (e) SAED patterns of BDA/rGO; (f) AFM image of a single-layer BDA/rGO sheet with height profile showing the layer thickness.

To take advantage of the structural benefits for electrochemical energy storage, it was required to maintain the spaced graphene nanostructures in thin film electrodes. XRD patterns of the free-standing amine/rGO films were shown in Figure 2.6b. The sharp peak at 18° corresponded to the PTFE binder. For rGO control sample, a broad peak appeared at 24.8° (d=0.36 nm), which was assigned to the stacking of graphene sheets. In

comparison, the new peaks occurring below 11° indicated the increased graphene interlayer spacing due to the grafting of spacers with oriented molecular configuration. The 2θ of EDA, BDA, HDA, and CHDA functionalized rGO followed the same trend as in their GO forms, in which smaller 2θ (larger *d* spacing) values were observed for diamine molecules with longer chain lengths. The peak at around 24° could be explained as the wavy nature of the modified graphene structure with partial restacking at some areas. For HDA/rGO and EA148/rGO, the low-intensity or even the absence of the characteristic peak implied the disordered molecular structure. Tris/rGO had a prominent peak at 7.2° with the largest *d* spacing of 1.2 nm. The values of interlayer spacing before and after the reduction of GO were summarized in Figure 2.6c. The results showed that EDA, BDA, HDA, and CHDA functionalized graphene had a minor change in *d* spacing before and after the reduction, which demonstrated the formation of 3D crystalline graphene nanostructures. The small decrease in spacing could be attributed to the intrinsic shrinkage of graphene sheets driven by intermolecular interactions and electrostatic repulsions.

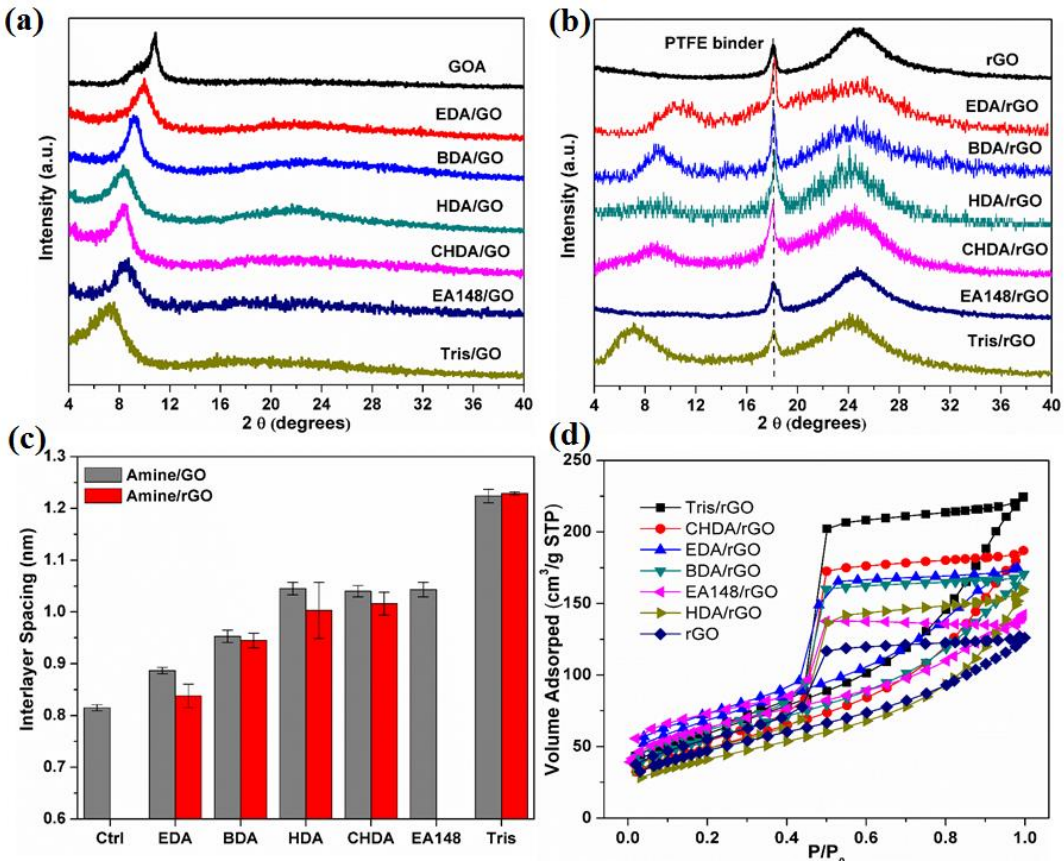

Figure 2.6 XRD spectra of (a) amine/GO and (b) amine/rGO; (c) comparison of *d* spacing values between amine/GO and amine/rGO (before and after the reduction); (d) nitrogen adsorption-desorption isotherms of the amine/rGO structures. The control samples were included in all the plots.

Nitrogen adsorption-desorption isotherms were used to provide more information on the spacing effect and the porous structure of the functionalized graphene. As shown in Figure 2.6d, all samples displayed a type IV isotherm, which indicated the formation of mesoporous structure. Table 2.3 summarized BET specific surface area (SSA) and pore size distribution by BJH method. It can be seen that the SSA increased from 129 m^2/g (rGO) to 327 m^2/g (Tris/rGO) due to the amine-based spacers. The values of SSA were basically consistent with the *d* spacing from XRD patterns, where a longer interlayer distance generally created a larger surface area. According to BJH adsorption analysis, the

average pore width (w) varied between 5.28 and 6.76 nm, and the pore size typically decreased with the increase of SSA. For amine/rGO structures, the wide distribution of pore sizes are beneficial for energy storage in that mesopores supply fast ion transport pathways and micropores provide large surface area to accommodate electrolyte ions.

Table 2.3 Specific surface area (SSA) and pore size of rGO and various amine/rGO

Samples	rGO	EDA	BDA	HDA	CHDA	EA148	Tris
SSA (m^2/g)	149	263	266	188	285	192	327
Pore diameter (nm)	6.76	5.88	5.94	6.68	5.41	6.62	5.28

The functional groups introduced to the graphene can also be effective in tuning the surface energy. The contact angles of water on rGO and amine/rGO films were shown in Figure 2.7. The hydrophilic amino groups rendered stronger water affinity to amine/rGOs through hydrogen bonding. Among the functionalized graphene, EA148/rGO had the lowest contact angle of 86.0° due to the presence of large amount of O-containing functional groups; whereas CHDA/rGO and HDA/rGO showed large contact angles of 107.4° and 110.8° due to the presence of relatively long and hydrophobic chains.

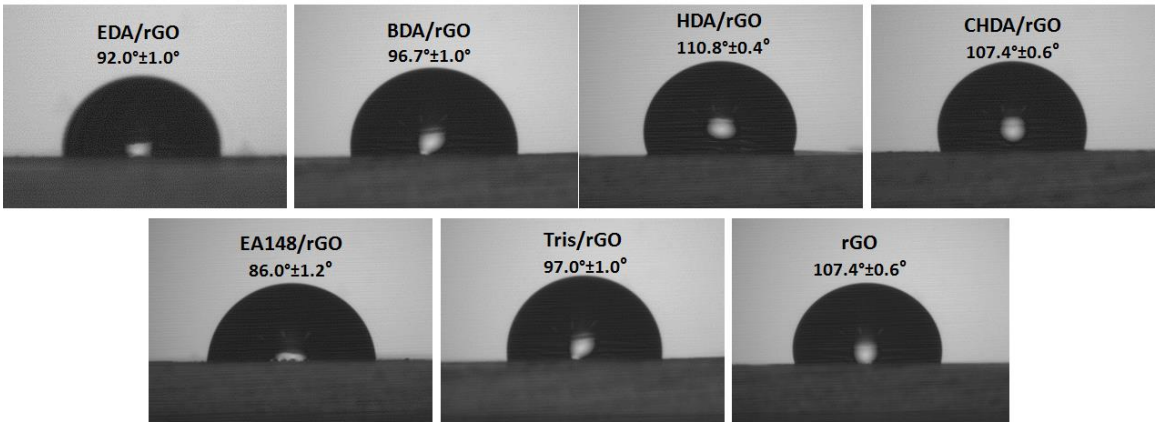

Figure 2.7 Static water contact angle of amine/rGO and rGO films.

2.3.1.3 Electrochemical analysis

To determine the electrochemical properties of the amine/rGO electrodes, two-electrode symmetric coin cells were used. Figure 2.8 (a-c) show the cyclic voltammetry curves of three amine/rGO samples in 1 M H_2SO_4 electrolyte with scan rates from 2 to 200 mV/s at a voltage range of 0-1 V. The near rectangular-shaped curves implied a strong EDLC character. Particularly, these aliphatic amines are unlikely to get involved in any redox reactions, so the capacitance was directly associated with the spacing effect of graphene structures. The amine/rGO provided enlarged interlayer spacing and ion accessible surface area, thus achieving obvious increase in capacitance values compared with rGO. As scan rates increased from 2 to 200 mV/s, most amine/rGO electrode (except for CHDA/rGO) retained over 75% of the capacitance value. This result demonstrated the high power handling capability of the materials, resulting from the rapid propagation of electrolyte ions. The BDA/rGO electrode exhibited a maximum specific capacitance of 216 F/g at 2 mV/s, which are almost double the value as that of rGO [131]. With well-spaced graphene structure, EDA/rGO and CHDA/rGO electrodes also delivered high specific capacitance values of 203 F/g and 214 F/g, respectively. Unlike the other amine/rGO

electrodes, the capacitance of CHDA/rGO declined quickly as scan rates increased. The reason can be explained that cyclohexane rings typically adopted the chair conformation to keep them thermodynamically stable, which could hinder efficient charge transfer through graphene layers and lead to relatively poor rate performance. As shown in Figure 2.8b, the CV curve of CHDA/rGO displayed a tilted shape at high scan rates, indicating the resistive behavior of charge transport. The slightly lower capacitance (189 F/g) of Tris/rGO might arise from the reduced conductivity when large Tris molecules were introduced. HDA/rGO and EA148/rGO, with a less obvious spacing effect, had the smallest capacitance improvement compared to other amine/rGOs. For EA148/rGO, the higher hydrophilicity could potentially enhance the wetting of aqueous electrolyte, but the poor capacitance values indicated that spacing effect and electrical conductivity outweighed the effect of surface hydrophilicity. Overall, the highest capacitance achieved by EDA/rGO, BDA/rGO and CHDA/rGO electrodes were comparable to other structurally modified graphene electrodes without the use of any pseudocapacitive materials (conducive polymers or metal oxides) [133-135].

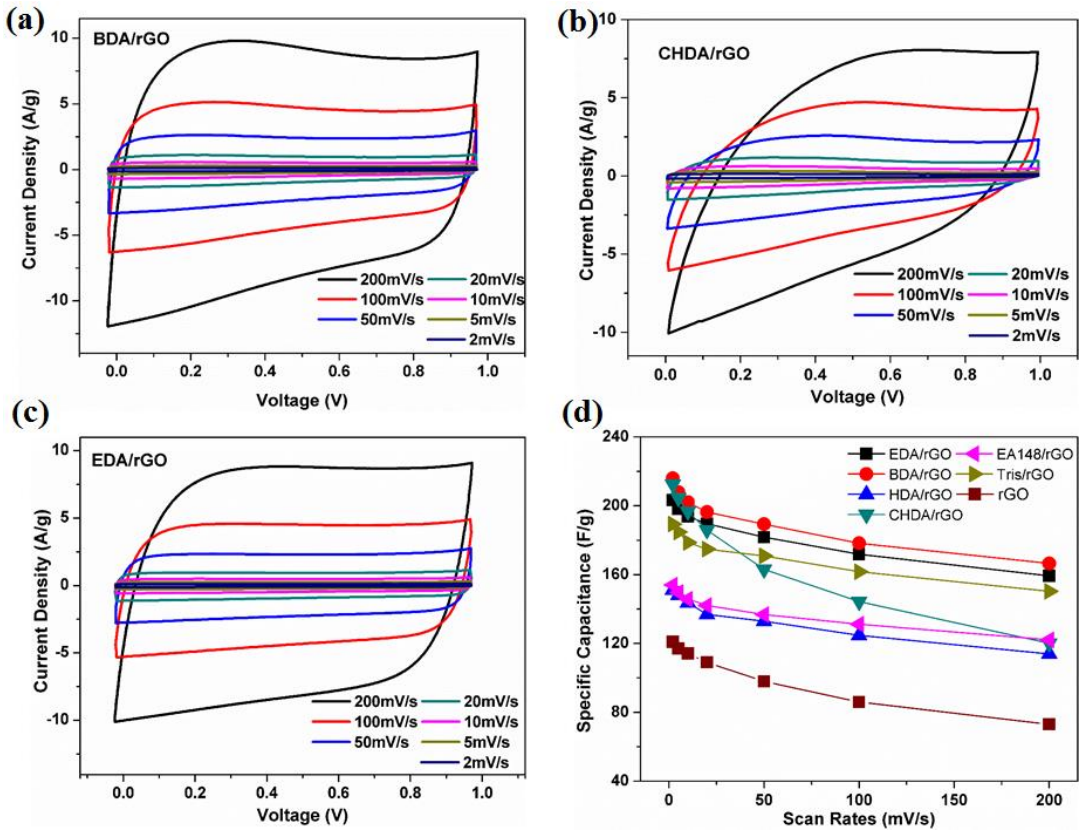

Figure 2.8 Electrochemical tests in 1 M H_2SO_4 electrolyte. CV curves of the (a) BDA/rGO, (b) CHDA/rGO and (c) EDA/rGO at various scan rates; (c) plots of specific capacitance values at different scan rates.

Galvanostatic charge-discharge measurements were also taken to evaluate the electrochemical performance. As shown in Figure 2.9a, charge/discharge curves exhibit an almost linear and symmetric triangle shape, which reflects the EDLC storage mechanism. At current density of 1 A/g, BDA/rGO showed the maximum capacitance of 208 F/g, which agreed well with the values calculated from CV curves at similar discharge time. The cycling stability of these functionalized graphene was investigated by 10,000 charge/discharge cycles. It can be seen that all the amine/rGOs exhibited over 92% capacitance retention over 10,000 cycles (Figure 2.9b). This remarkable cycling durability further verified the stability of the 3D graphene structure. Particularly, the Tris/rGO

electrode was able to retain 96.8% of initial capacitance after long-term cycling. The robust graphene network could efficiently buffer the possible structural change induced by the uptake and release of electrolyte ions.

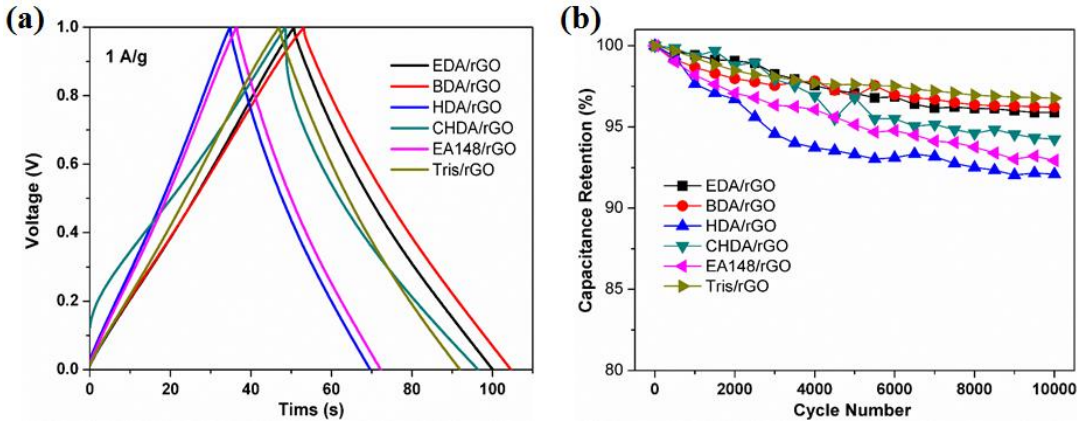

Figure 2.9 Charge/discharge curves at current density of 1 A/g; (e) cycling stability of the electrodes for 10000 cycles at 1 A/g.

Electrochemical impedance spectroscopy (EIS) was used to evaluate the resistive and charge transfer behavior of the electrodes. As shown in Figure 2.10, Nyquist plots of the amine/rGOs showed a nearly perpendicular line at low frequency regions, indicating an almost ideal capacitive behavior. The first intersection points to the real axis, defined as the equivalent series resistance (R_s), was in the range of 0.25-0.60 Ω [136]. The small R_s implied good conductivity of the electrode material and good electrical contact at the electrode/current collector interfaces. The charge transfer resistance (R_{ct}) reflected the total resistance at electrode/electrolyte interface.[136] Generally, graphene modified by shorter-chain amine, such as EDA/rGO (R_s: 0.25 Ω, R_{ct}: 1.86 Ω), exhibited lower intrinsic and interfacial resistance than those with larger amine spacers, including HDA/rGO (R_s: 0.58 Ω, R_{ct}: 5.87 Ω) and CHDA/rGO (R_s: 0.57 Ω, R_{ct}: 7.11 Ω). For CHDA/rGO, the high R_{ct}, together with the large Warburg region at medium frequency region, provided further

evidence that bulky cyclohexane ring could hinder the ionic transport/diffusion between graphene layers.

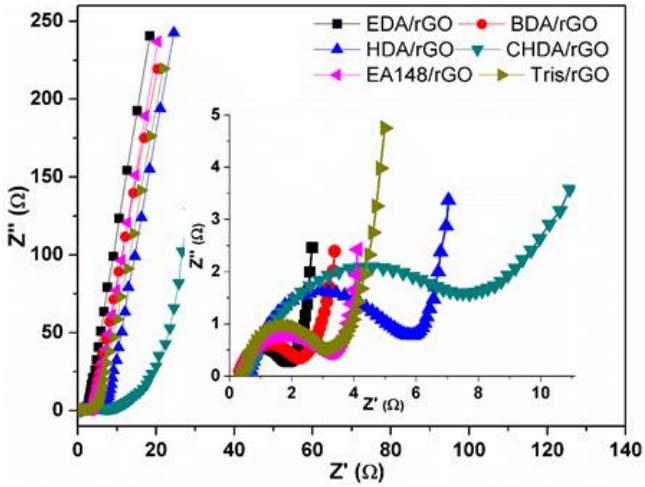

Figure 2.10 Nyquist plots of the electrodes with a magnified view for the high-frequency region.

To investigate the capacitive properties in organic electrolyte, amine/rGO electrodes were tested in 1 M $TEABF_4$/AN with a wider potential window from 0-2.7 V. Figure 2.11a and b show the CV curves of BDA/rGO and specific capacitance values of different electrodes. The EDLC charge storage characteristic was verified by the quasi-rectangular curves at various scan rates. The largest specific capacitance of 134 F/g was obtained at 10mV/s for BDA/rGO electrodes, and the capacitance values decreased to 124 F/g at 50 mV/s, and 107 F/g at 200 mV/s. It was noted that the capacitance only dropped by 20% at high scan rates, indicating a good accessibility for organic electrolyte ions to the inner area of the electrodes. In acetonitrile, the size of the solvated cations (NEt_4^+) and anions (BF_4^-) was 1.35 and 1.40 nm respectively [137], which have a good match with the pore size of electrode materials for charge transport and storage. The Tris/rGO and EDA/rGO delivered a high capacitance of 131 F/g and 119 F/g respectively at 2 mV/s. and

both electrodes had excellent rate performance as well due to the porous structure. Similar to the results acquired in H_2SO_4 electrolyte, the CHDA/rGO also showed large decay of capacitance values upon increasing the scan rates, suggesting obstructed charge transfer processes. As shown in Figure 2.11c, the symmetric triangles of the curves with small IR drop implied a nearly ideal capacitive behavior. In organic electrolyte, the electrodes also exhibited excellent cycling stability with slight decline of specific capacitance over 10,000 cycles (Figure 2.11d).

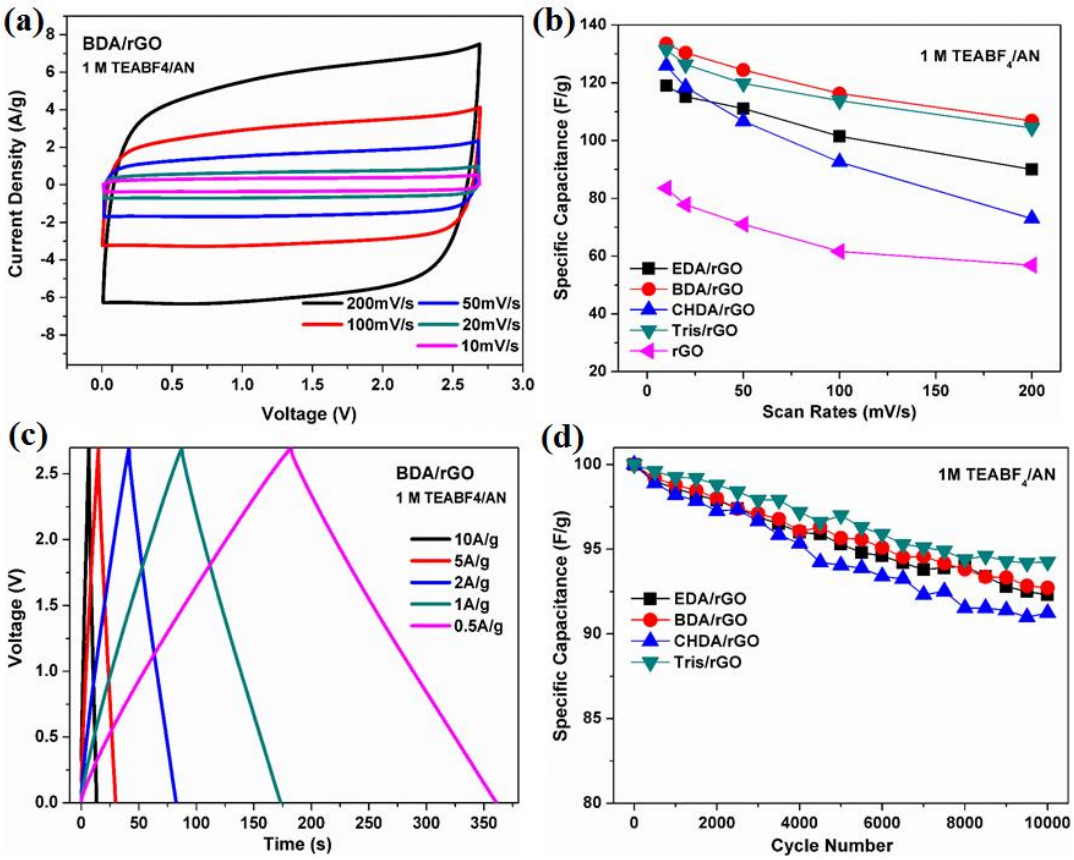

Figure 2.11 Electrochemical tests in 1 M $TEABF_4$/AN electrolyte. (a) CV curves of the BDA/rGO electrode; (b) plots of the specific capacitance values as a function of scan rates; (c) charge/discharge curves of BDA/rGO at various current densities; (d) capacitance retention of different electrodes over 10,000 cycling tests.

Figure 2.12a shows the Nyquist plots of the electrodes in organic electrolyte. It was observed that all electrodes exhibited incomplete semicircles at high frequency region due to the charge transfer process and nearly vertical lines at low frequency regions due to fast ionic diffusion within the graphene nanostructure. In spite of the low ionic conductivity and high viscosity of the organic electrolyte, the graphene-based electrodes showed small R_s (< 0.8 Ω) and R_{ct} (<6.5 Ω) values (except for CHDA/rGO). The Ragone plot (Figure 2.12b) compared the energy density and power density for different electrodes. BDA/rGO electrode displayed the highest energy density of 34 Wh/kg at power density of 425 W/kg, which was larger than some reported graphene-based materials in organic electrolyte [138, 139].

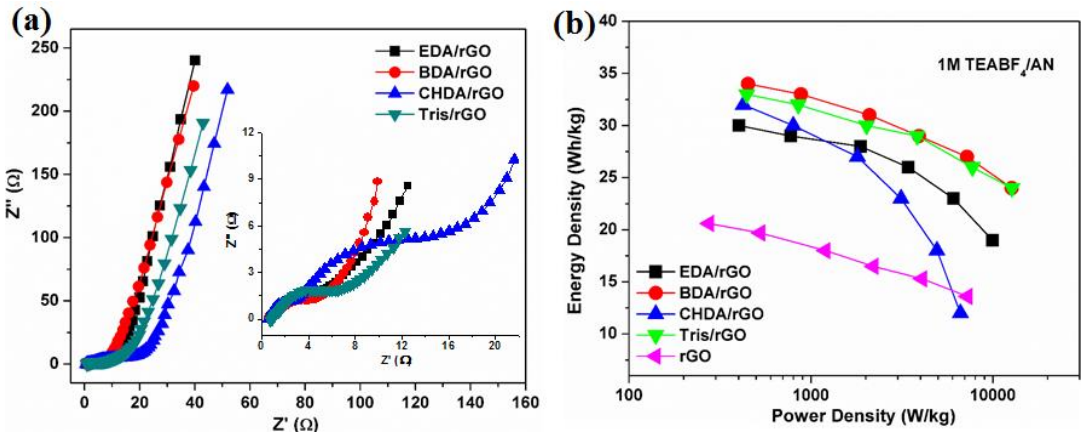

Figure 2.12 (a) Nyquist plots of the amine/rGO with a magnified view at high frequency region; (b) Ragone plots of rGO and amine/rGO electrodes in organic electrolyte.

For the amine/rGO electrodes, an ionic liquid electrolyte ($BMIMBF_4$) was also used to extend the potential window to 3.5 V. Among all electrodes, Tris/rGO showed a maximum specific capacitance of 119 F/g at 10 mV/s (Figure 2.13a-b), as a result of the larger surface area and optimal pore sizes. Generally, the inert IL electrolytes ions are not

involved in any redox processes, which makes Tris/rGO, with larger surface area and better pore size distribution, superior in accumulating charges at the electrolyte/electrode interface. The specific capacitance of other functionalized graphene samples were also obtained at 10 mV/s, which was much higher than that of 65 F/g for rGO control sample. In contrast to the capacitive performance in aqueous and organic electrolytes, the relatively poor rate performance can be attributed to the high viscosity and slow ionic transport features of the IL electrolyte.

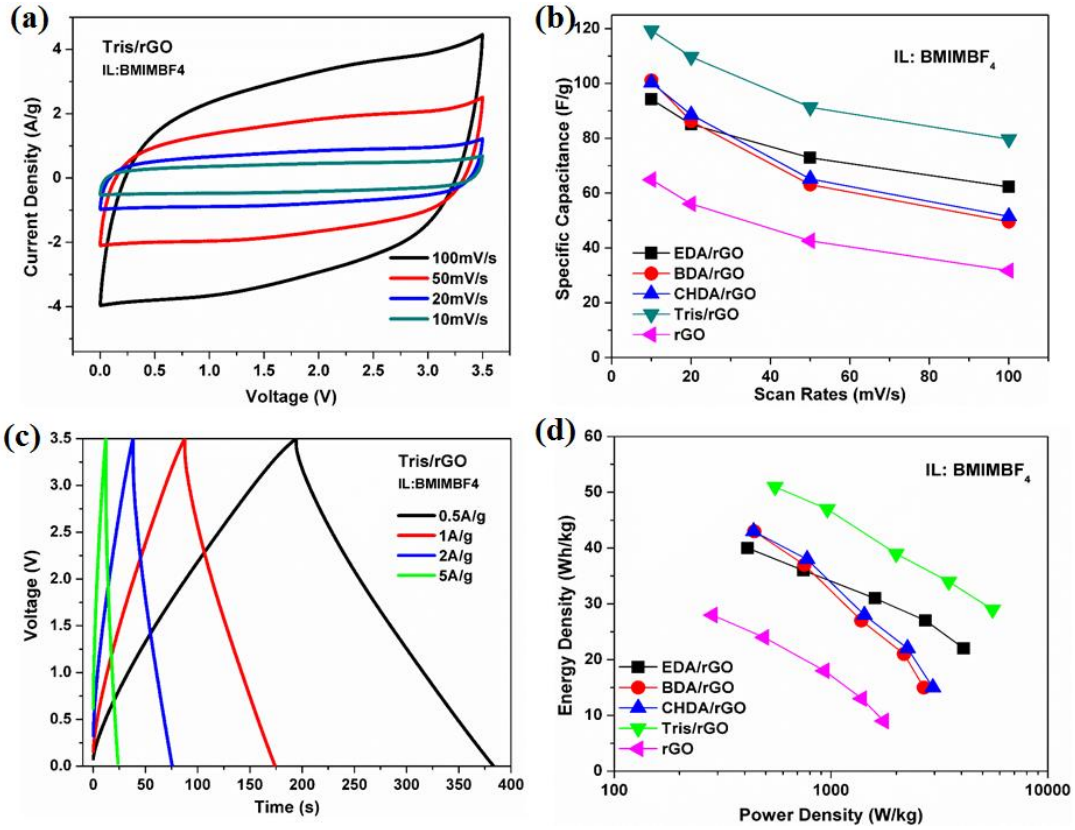

Figure 2.13 Electrochemical tests in $BMIMBF_4$ IL electrolyte. (a) CV curves of the Tris/rGO electrode; (b) specific capacitance values as a function of scan rates; (c) charge/discharge curves of Tris/rGO at various current densities; (d) Ragone plots of rGO and amine/rGO electrodes.

The charge/discharge profiles (Figure 2.13c) exhibited linear and symmetric curves at various current densities, but a larger IR drop corresponded to the lower ionic conductivity of the IL. Figure 2.13d shows the Ragone plots of the samples in IL electrolyte. For Tris/rGO, a considerably high energy density of 51 Wh/kg was achieved at power density of 552 W/kg, while the energy was still as high as 30 Wh/kg as the power density increased to 6 kW/kg. The state-of-the-art electrochemical performance of graphene-based supercapacitors in IL electrolytes and the amine/rGO materials in this work are listed in Table 2.4 for comparison.

Table 2.4 Comparison of the start-of-art electrochemical performance for graphene-based supercapacitors in ionic liquid electrolyte

Electrode Materials	Electrolyte	Voltage (V)	Specific Capacitance (F/g)	Energy Density (Wh/kg)	Self-Discharge
Exfoliated graphene**[140]**	$PYR_{14}TFSI$	3.5	75	31.9	N/A
Graphene/AC**[141]**	$EMIMBF_4$	4	94	52.2	N/A
Mesoporous graphene**[6]**	$EMIMBF_4$	4	154	85.6	N/A
Sponge-like graphene**[142]**	BMPY TFSI	3	68.5	21.4	N/A
Nitrogen-doped graphene**[143]**	$EMIMBF_4$	3	130	41	50% V drop, 4.3 h
This work (Tri/rGO)	$BMIMBF_4$	3.5	119	51	45% V drop, 24 h

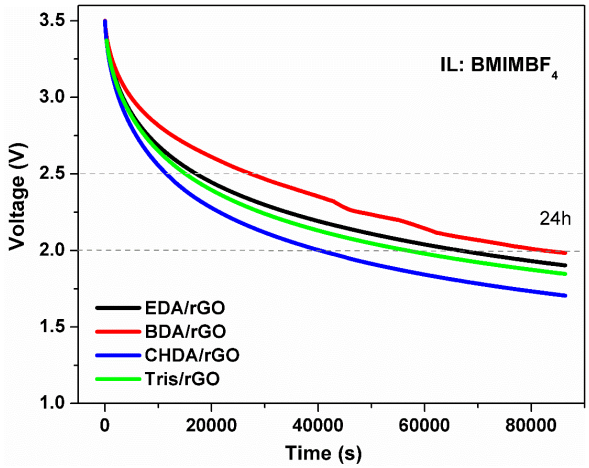

Figure 2.14 Self-discharge curves of rGO and amine/rGO in $BMIMBF_4$ IL electrolyte over a period of 24 h.

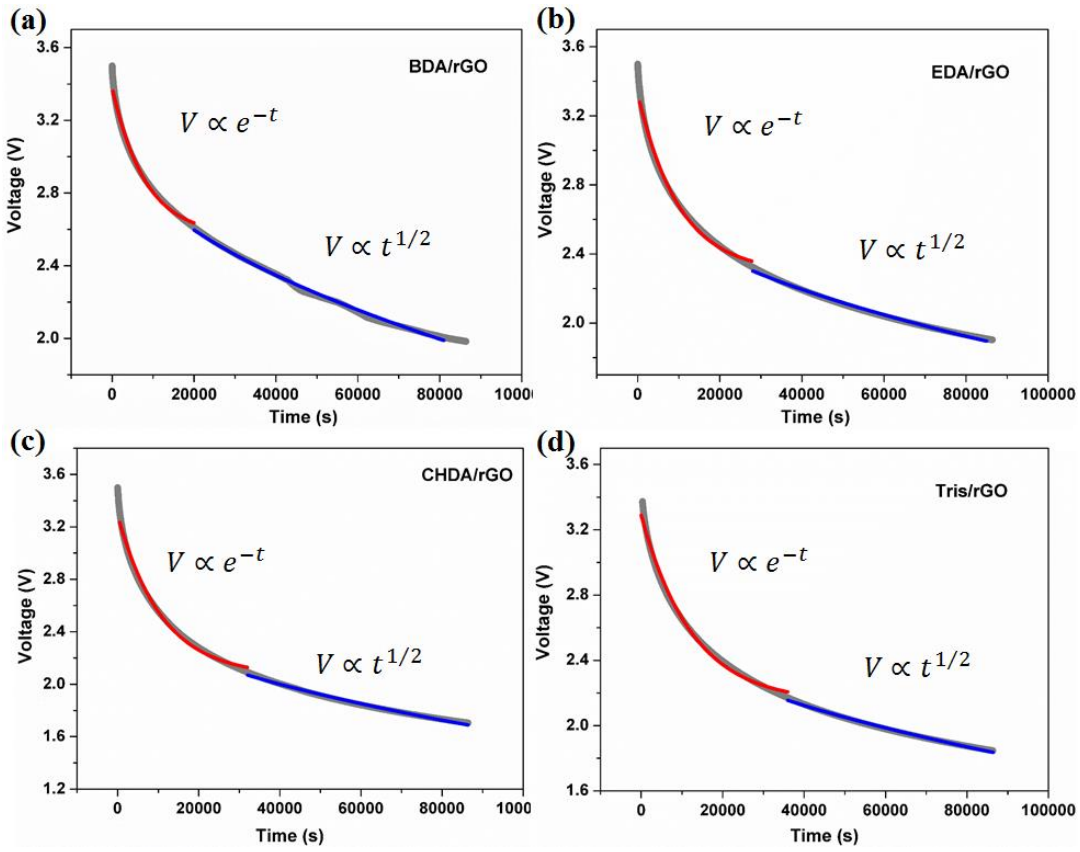

Figure 2.15 Simulation of the self-discharge curves by a combination of potential driving model and diffusion control model for (a) BDA/rGO, (b) EDA/rGO, (c) CHDA/rGO, and (d) Tris/rGO in $BMIMBF_4$ IL electrolyte.

Self-discharge process was investigated to evaluate the energy retention capability of the as-fabricated supercapacitors. Self-discharge is defined as the decay of voltage with time in open-circuit condition. Generally, two self-discharge models were proposed for EDLCs, namely, diffusion control model and potential driving model [144, 145]. In diffusion control model, the driving force is the ionic concentration gradient with varied distance from the electrode/electrolyte interface, denoted as $V = V_{initial} - m * t^{1/2}$, where *m* represents the diffusion factor and *t* represents the self-discharge time; while the potential driving model relies on the potential field difference, denoted as $V = V_{initial} * e^{-t/\tau}$, where τ is the time constant of capacitor. Figure 2.14 shows the self-discharge curves of the functionalized graphene electrodes in ionic liquid electrolyte after precharging to 3.5 V. It can be seen that BDA/rGO exhibited remarkable self-discharge performance with the final voltage kept at around 2 V over a period of 24 h. For EDA/rGO and Tri/rGO, more than 55% of voltage was also preserved after 24 h, which was superior to other self-discharge results reported for supercapacitors [146-149]. The relatively faster self-discharge rate for CHDA and Tris/rGO might be due to the bulky amine structures and large surface heterogeneity. The defective areas on electrode surface can generate weak bonding with electrolyte ions due to the interference of large CHDA/Tris structures, leading to easier leakage of ions from the double layer [146]. The self-discharge curves of the graphene-based materials were also fitted into the potential driving model and diffusion control model for better understanding of the processes [144]. As shown in Figure 2.15, the red and blue curves signified the fitting of the potential driving model ($V \propto e^{-t}$) and diffusion control model ($V \propto t^{1/2}$), respectively. At the beginning stage of the self-discharge, the driving force came from the electric field scaled by the potential difference.

Then, the self-discharge process was governed by the ionic diffusion and the voltage drop became much slower.

2.3.1.4 Theoretical calculations

Complementary to experimental studies, computational simulations were performed to explain the structural and electronic properties of the amine/rGOs. The interlayer distance of these graphene derivatives was calculated using the periodic model (Figure 2.16). The calculation was based on the assumption that these molecules stably crosslinked between graphene layers via C-N bonds. Given the C-N bond length of 1.47 Å, the interlayer distance for EDA/rGO, BDA/rGO, and HDA/rGO were calculated to be 0.67 nm, 0.91 nm, and 1.18 nm, which were consistent with the experimental results. The large HDA and EA148 molecules might adopt bent conformation due to the flexible hydrocarbon chains, which made the experimental data smaller than calculated values. For Tris/rGO and CHDA/rGO, the theoretical and experimental results also showed good agreements (variation < 0.25 nm), and the discrepancy might result from the complicated intra/intermolecular interactions due to their branched or ring structures.

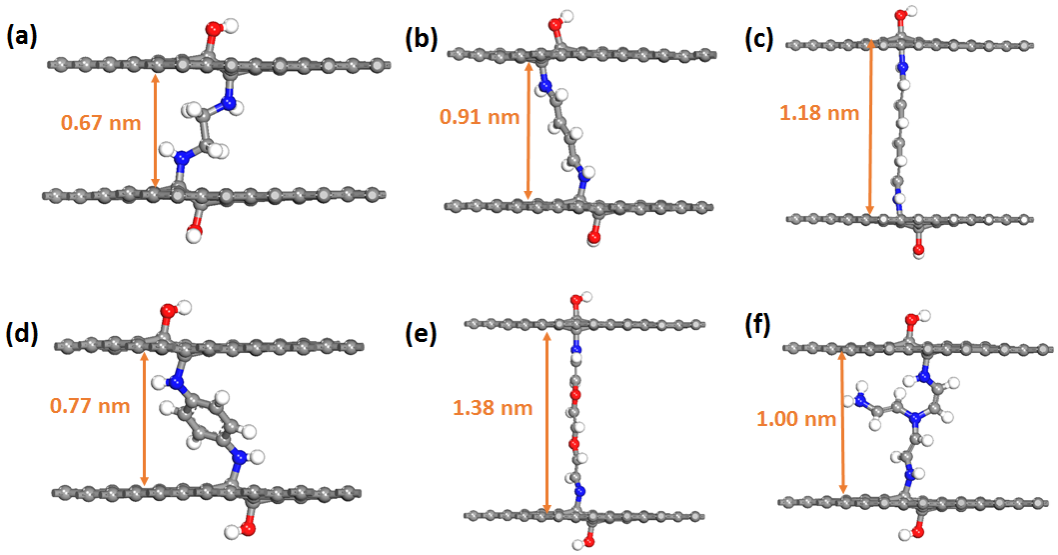

Figure 2.16 Simulated molecular geometries of (a) EDA/rGO, (b) BDA/rGO, (c) HDA/rGO, (d) CHDA/rGO, (e) EA148/rGO, and (f) Tris/rGO. Figure courtesy of Dr. Jingxiang Zhao.

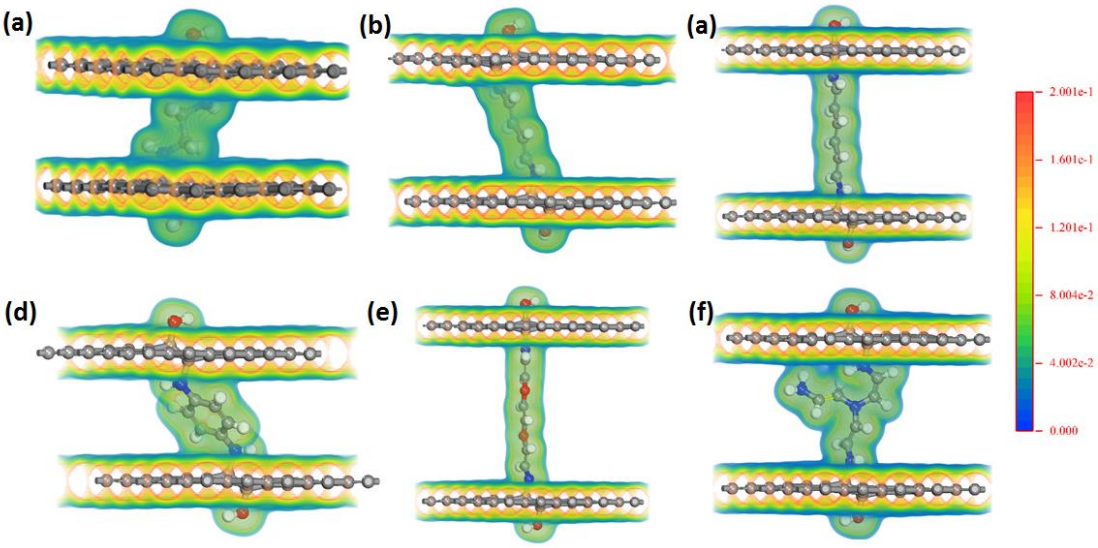

Figure 2.17 Total electron energy maps of (a) EDA/rGO, (b) BDA/rGO, (c) HDA/rGO, (d) CHDA/rGO, (e) EA148/rGO, and (f) Tris/rGO. Figure courtesy of Dr. Jingxiang Zhao.

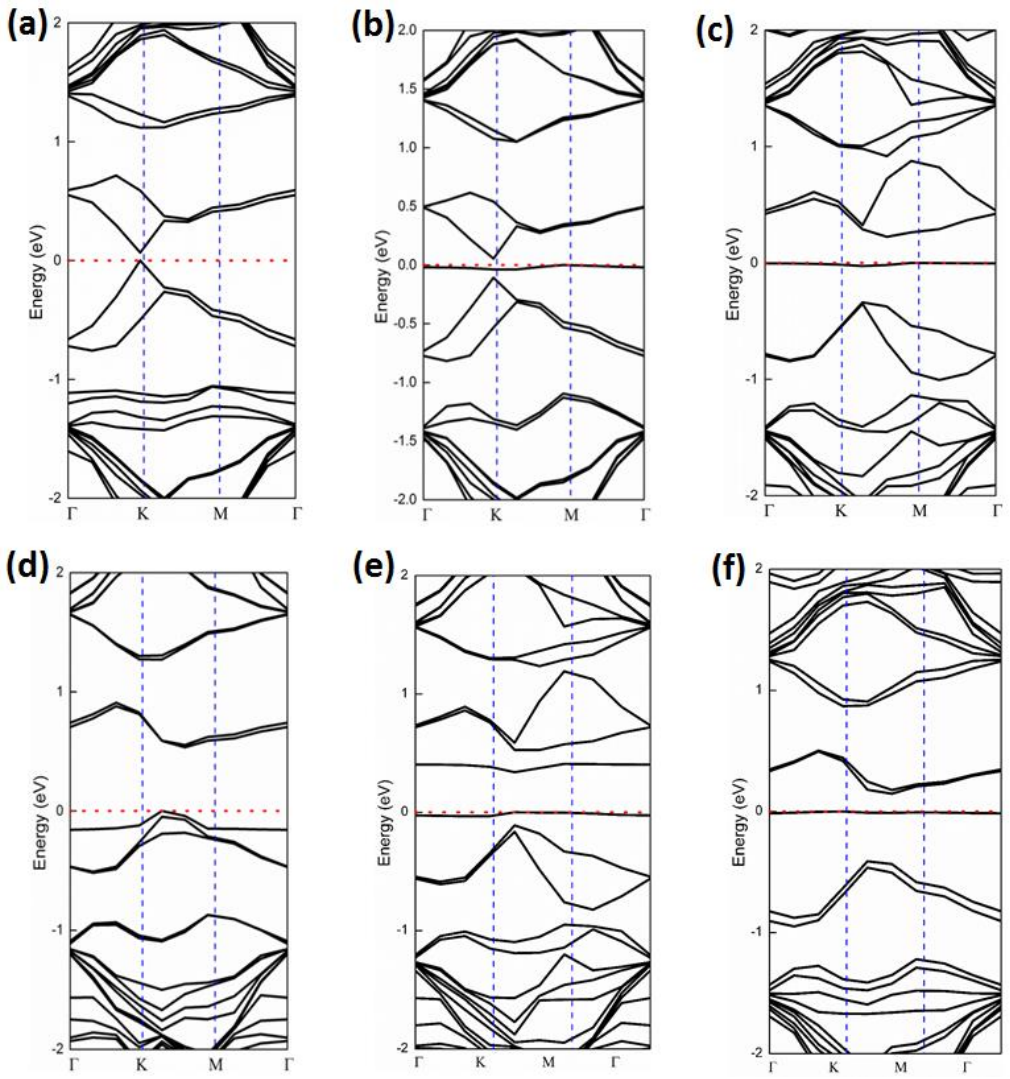

Figure 2.18 Simulated band gap structures of (a) EDA/rGO, (b) BDA/rGO, (c) HDA/rGO, (d) CHDA/rGO, (e) EA148/rGO, and (f) Tris/rGO using periodic model. Figure courtesy of Dr. Jingxiang Zhao.

DFT calculations were employed to theoretically examine the electron density and band gap of the amine/rGO. The introduction of electron-rich amino groups led to the charge redistribution and delocalization at the amine/rGO interfaces. The phenomena were verified by the total electron density map (Figure 2.17) that the charges concentrated at the C-N covalent bonds were further distributed to the conductive graphene networks. The band structure were simulated to evaluate the charge transfer characteristic between

graphene layers. The bandgap of the functionalized graphene was calculated to be in the range of 0.05 eV to 0.54 eV (Figure 2.18). For EDA/rGO and BDA/rGO, the band gaps were as small as 0.07 and 0.05 eV, which suggested the strong charge carrier mobility between graphene layers. The better electron mobility of the BDA/rGO also correlated well with the larger capacitance values acquired from the electrochemical tests. The highest band gap for CHDA/rGO (0.54 eV) indicated that the cyclohexane ring could hinder the charge propagation through graphene layers, resulting in poor specific capacitance as the increase of scan rates.

2.3.2 Triol functionalized graphene

2.3.2.1 Chemical and thermal analysis

The schematic illustration of the chemical reaction and the as-formed graphene-framework was shown in Figure 2.19. At 105°C, TEA molecule can be grafted on graphene surface to exfoliate the stacked graphene sheets. The hydrothermal treatment at 180°C serves to ensure more complete reduction of GO.

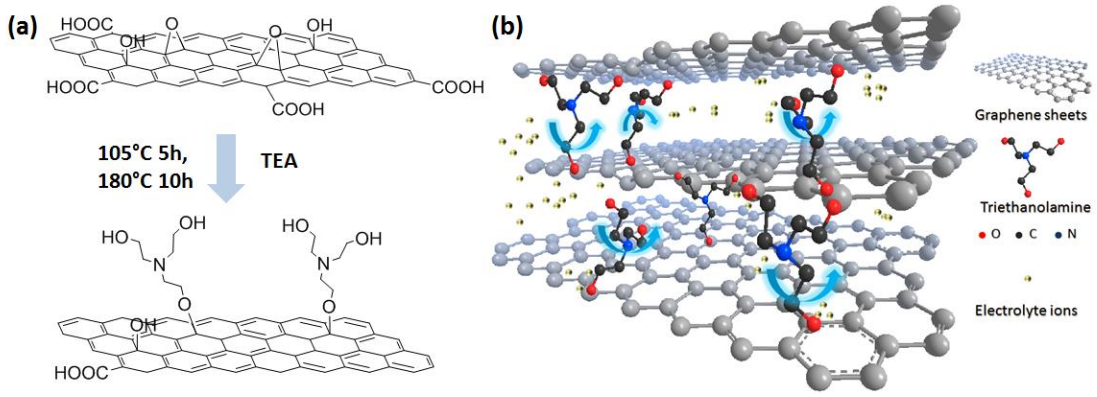

Figure 2.19 Schematics of (a) the chemical reaction between TEA and GO and (b) the as-formed 3D TEA/rGO nanostructure with charge transfer characteristics (the residue oxygen-containing groups on graphene sheets are omitted for clarity.

Chemical structures of TEA/rGO were measured by FTIR, DSC, Raman and XPS. FTIR was used to elucidate the formation of chemical bonds between GO and TEA. As shown in Figure 2.20a, TEA/rGO presented two strong bands at 1260 cm^{-1} and 1066 cm^{-1}, which are ascribed to the epoxy and alkoxyl groups respectively. These enhanced C-O characteristics suggests an obvious covalent linkage of TEA onto graphene sheets. Furthermore, two emerging peaks at 1468 and 715 cm^{-1} ($–CH_2$ bending modes), together with the intensified peaks at 2925 and 2854 cm^{-1} (stretching modes of $–CH_2$ units), all confirms the existence of the TEA molecules in the graphene structure. The FTIR spectrum of pure TEA is also presented in Figure 2.20b as a reference.

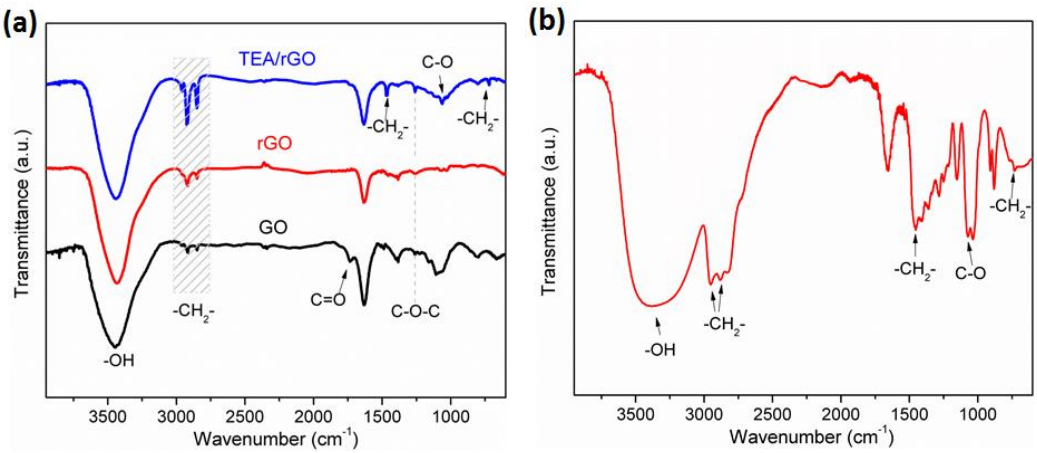

Figure 2.20 FTIR spectra of (a) GO, rGO, TEA/rGO, and (b) TEA.

Figure 2.21a shows DSC profiles of GO/TEA mixture, which is used to monitor the in-situ reaction process. From 105°C to 173°C, a prominent exothermic peak was observed with a calculated enthalpy of 975 J/g, which provides an evidence for the exothermic reactions between GO and TEA. It is believed that the ring opening of epoxide groups or the condensation of hydroxyl groups are mostly likely to occur at the temperature range with strong exothermic features. The resulting material with higher content of C-O functionalities was also confirmed by FTIR. The reaction onset temperature, 105°C, was used as the first step temperature for the molecular grafting. This low-temperature treatment can maximize the degree of chemical reactions before GO was further reduced at 180°C. Raman spectroscopy was used to illustrate the graphitic crystalline structure. In Figure 2.21b, the D band at 1340 cm^{-1} represents structural defects while the G band 1590 cm^{-1} corresponds to the ordered sp^2 hybridized graphene network [150]. It was found that I_D/I_G ratio was 0.97 for GO, increased slightly to 1.09 for rGO and 1.13 for TEA/rGO. The small increase of the I_D/I_G ratio between rGO and TEA/rGO is due to the TEA incorporation, in which the grafting of TEA molecule on graphene surface replaces some

of the sp^2 carbon sites and generates more sp^3 carbon forms. In addition, the 2D peak was observed at around 2700 cm^{-1} after GO reduction, which is caused by the second order vibration of two phonons with opposite wavevectors [151]. For TEA/rGO, the pronounced intensity of the 2D peak relative to rGO indicates the improved exfoliation of graphene sheets to fewer layers upon molecular functionalization [152].

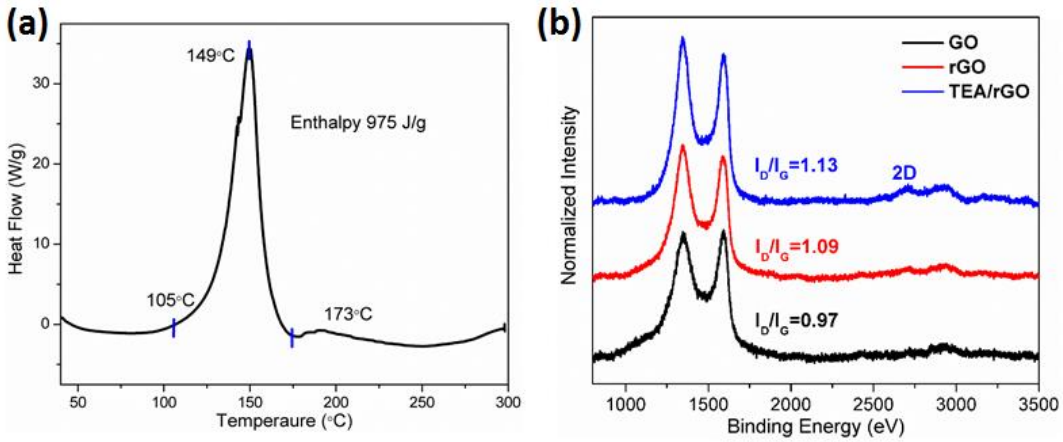

Figure 2.21 (a) DSC curves of GO/TEA mixture in N_2 atmosphere with heating rate of 10°C/min; (b) Raman spectra of GO, rGO and TEA/rGO.

XPS was used to provide further insight on the TEA/rGO nanostructure. From the survey spectrum (Figure 2.22a), the N content was quantified to be ~2.05%, which provides an estimated percentage of 20.5 wt% of TEA spacer in the functionalized graphene (atomic ratios C:O:N=6:1:3). Figure 2.22b shows the high resolution C1s spectrum of TEA/rGO. Peak deconvolution reveals that there is 69.6% C=C, 16.1% C-O, 8.4% C-N & C=O, and 5.9% O-C=O.[153, 154] Among the oxygen-containing groups, the largest fraction of C-O bonds indicates covalent linkage between TEA and graphene, as complementary to FTIR [61]. Compared with rGO (Figure 2.22a), O content increases from 9.95% to 15.75% via upon TEA modification. The surface functionalities, specifically O-containing groups, can effectively tune the surface energy of the materials.

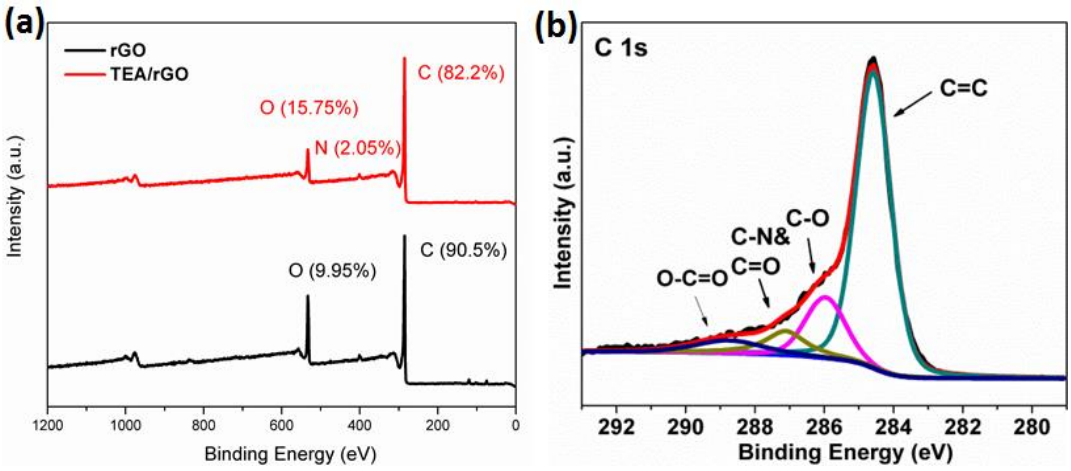

Figure 2.22 XPS (a) survey spectra of rGO and TEA/rGO; (b) high resolution C 1s spectra of TEA/rGO.

2.3.2.2 Physical properties

Figure 2.23a shows the SEM image of the TEA/rGO with well-exfoliated thin layer features. The TEM image (Figure 2.23b) reveals the wrinkled form of functionalized rGO with no obvious aggregation. An individual TEA/rGO flake with slightly wrinkled surfaces was observed by AFM (Figure 2.24a). The average thickness of the flake is determined to be ~ 1.96 nm from the height profile (Figure 2.24b). The AFM image of a single layer GO flake with an average depth of 1.10 nm is shown in Figure 2.24(c-d) as a comparison. In the absence of layer-by-layer aggregation, we believe that the increased thickness of the TEA/rGO nanostructure is mainly attributed to the presence of TEA molecules grafted between graphene layers.

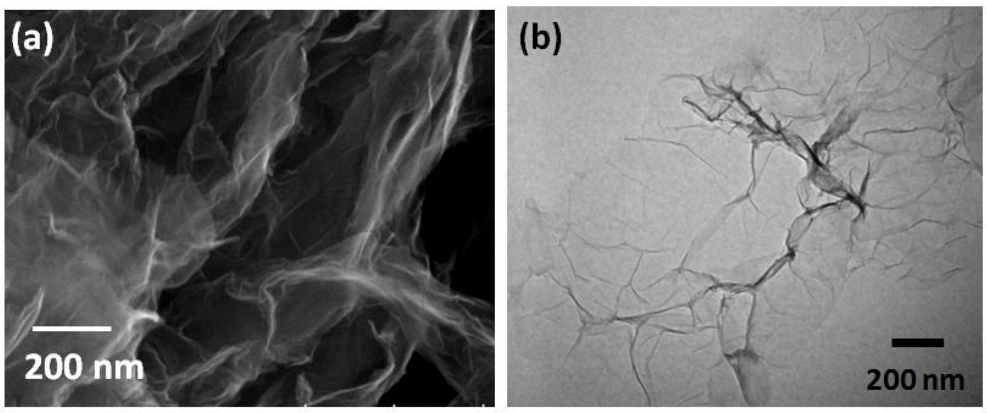

Figure 2.23 (a) Cross-section SEM and (b) TEM images of the TEA/rGO.

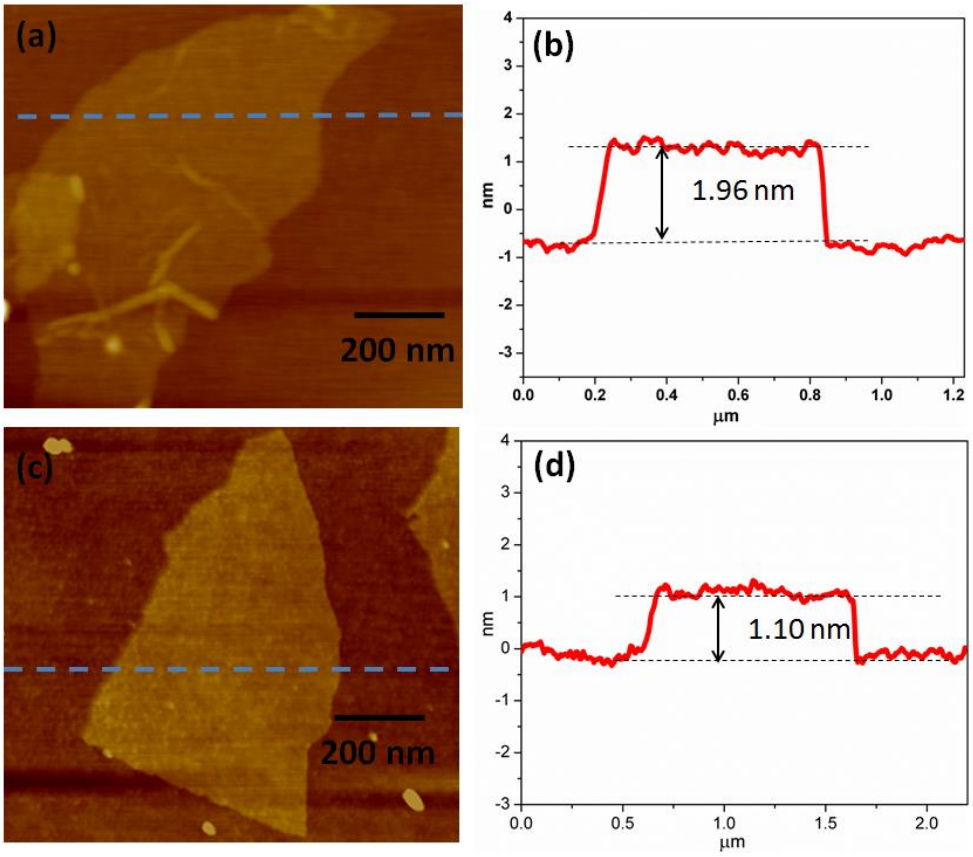

Figure 2.24 AFM image of the (a-b) individual TEA/rGO and (c-d) GO sheet with corresponding height profiles showing the average thickness.

Figure 2.25 shows the XRD patterns of GO, rGO and TEA/rGO. GO displays a characteristic diffraction peak at 9.9°, corresponding to an interlayer spacing of 0.90 nm. Upon the hydrothermal reduction, rGO became restacked due to the loss of considerable oxygen-containing groups, which reduces the interlayer spacing to ~.35 nm. Upon the grafting of TEA, a new diffraction peak was observed at 5.1°. The broadened interlayer spacing (1.75 nm) was attributed to the intercalation of TEA as molecular spacer, which serves to reduce the agglomeration of curved graphene sheets to some extent. Particularly, TEA molecule with highly branched structure, is more likely to form a 3D graphene network with stabilized interlayer spacing and enhanced surface area. Moreover, the interlayer thickness calculated by Bragg's law is consistent with that measured by AFM.

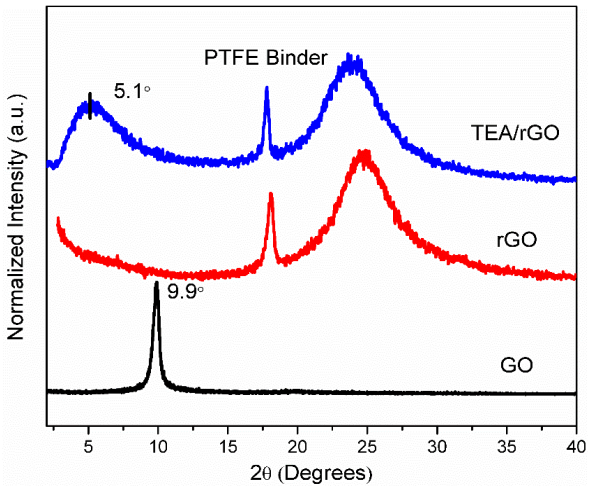

Figure 2.25 XRD patterns of GO, rGO and TEA/rGO.

In conjugation with XRD, N_2 adsorption-desorption isotherms was used to examine the spacing effect of TEA/rGO. As shown in Figure 2.26a, TEA/rGO displays a type-IV isotherm with SSA up to 527.8 m^2/g, which has a three-fold improvement compared with rGO (189.8 m^2/g). The dramatic raise in the adsorption curve at low relative pressure indicates a large content of micropores, while the clear hysteresis loop at the relative

pressure of (0.4~0.85) corresponds to the capillary condensation of mesopores between graphene layers [155]. Figure 2.26b presents the pore size distribution plots of TEA/rGO with an average pore width of 2.96 nm. The TEA/rGO containing different pore sizes ensures the efficient charge transfer through mesopores and provides the sufficient surface area for charge storage within micropores.

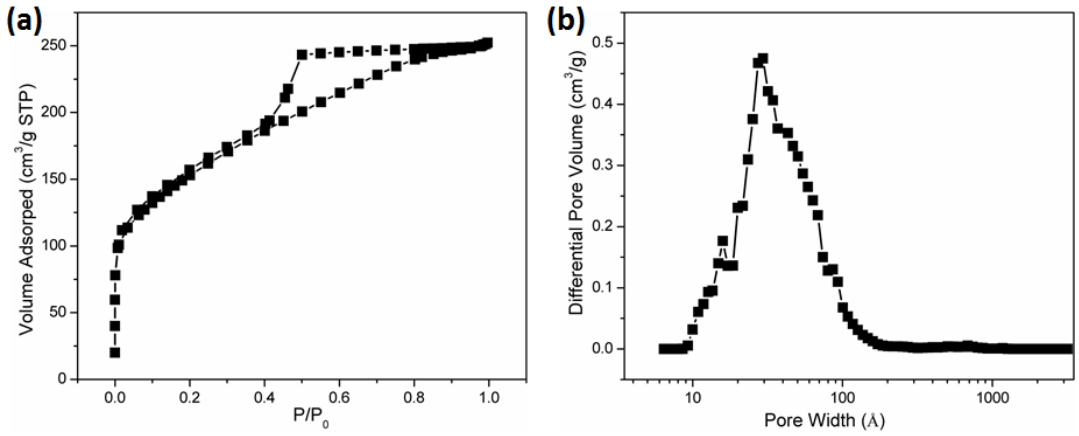

Figure 2.26 (a) Nitrogen adsorption/desorption isotherm and (b) pore size distribution plots of TEA/rGO.

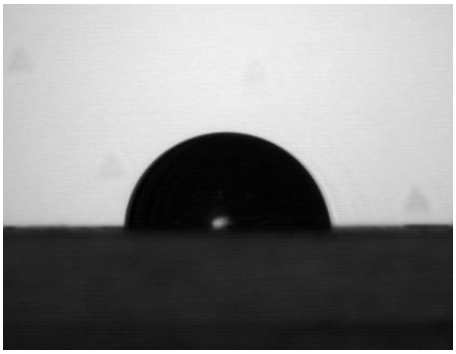

Figure 2.27 Contact angle measurement of the (a) TEA/rGO film.

As shown in Figure 2.27, the contact angle of 78.9±2.0° was obtained with a water droplet on a TEA/rGO film. The hydrophilic nature of the modified electrode is mainly attributed to the sufficient amount of C-O groups in TEA/rGO.

2.3.2.3 Electrochemical properties

The electrochemical performance of TEA/rGO films was measured by cyclic voltammetry (CV) using a two-electrode symmetrical coin cell in both 1 M H_2SO_4 and 1 M TEA/BF_4 electrolytes. The rate-dependent capacitance results calculated from CV curves is shown in Figure 2.28a. In H_2SO_4 electrolyte, the maximum specific capacitance was as high as 210 F/g at 2 mV/s, which can be attributed to the synergistic effect of large ionic accessible surface area and good wettability of the electrolyte, as discussed above. As the increase of scan rates, the specific capacitance was kept as high as 156 and 143 F/g at 100 and 200 mV/s, which retained 74.3% and 68.1% of the capacitance from the capacitance value at 2 mV/s, respectively. The TEA/rGO thin film electrodes were also tested in organic electrolytes (1 M TEABF_4/AN). As shown in Figure 2.28a, the highest specific capacitance of 118 F/g was achieved for TEA/rGO at 10mV/s. The enhanced interlayer spacing of TEA/rGO can facilitate the bulkier-sized electrolyte ions to penetrate through the inner pores, thus resulting in more charge accumulation at the electrode/electrolyte interface for energy storage. Generally, graphene derivatives decorated by conductive polymers or metal oxide shows a high energy density, but the relatively slow charge/discharge rates and the poor cycling stability limit their usage. As for the TEA/rGO that possesses strong EDLC characteristic, the highest energy density is determined to be 25.7 Wh/kg at 2.5 V in organic electrolyte. The compatibility of the

electrode materials in organic electrolyte provides the feasibility for high energy-density applications.

Figure 2.28b shows the galvanostatic charge/discharge (CD) profiles at different current densities. The symmetric lines of the curves indicate capacitive features of the charge propagation in a reversible manner. Cycling stability of the TEA/rGO electrodes were investigated at current densities of 2 A/g. It can be seen from Figure 2.28c that ~91.7% of capacitance is retained after 10,000 cycling tests. The outstanding cycling durability, together with excellent rate performance and electrolyte wettability, demonstrates the unique nanostructure of TEA/rGO for charge storage, which shows apparent advantages over other types of molecular spacer functionalized graphene materials [75, 156, 134, 119]. Figure 2.28d shows the Nyquist plots at a frequency range from 100 kHz to 0.01 Hz. The small R_s value (0.38 Ω) indicates the excellent electrical conductivity provided by the electrode material. The extrapolated low charge transfer resistance (R_{ct}: 1.37 Ω) represents the small interfacial resistance between electrode and electrolyte, which further demonstrates the superior wettability of the electrodes by introducing O-containing functionalities on graphene surface.

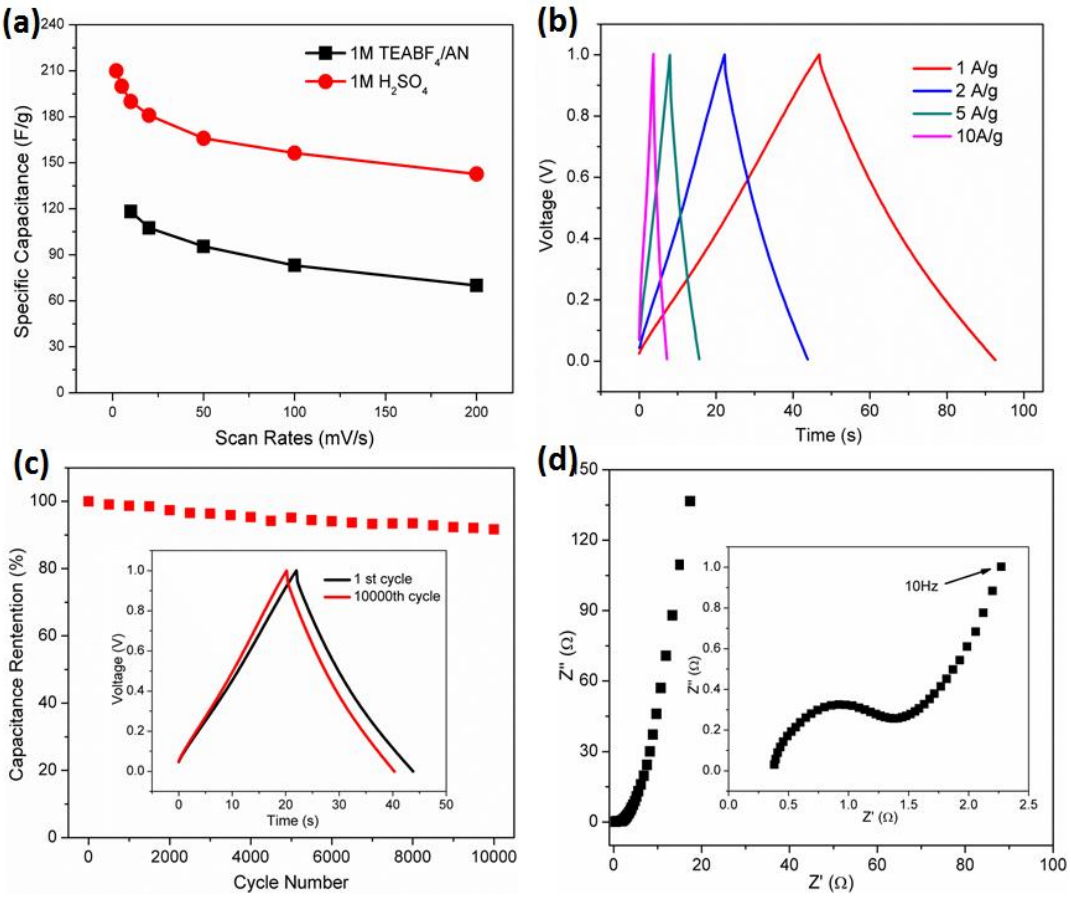

Figure 2.28 Electrochemical test results of TEA/rGO electrodes. (a) Rate-dependent plot of the specific capacitance values ; (b) galvanostatic CD curves at various current densities; (c) capacitance retention at 10,000 cycles at 2 A/g with first and 10000th CD plots in the inset; (d) Nyquist plot with a magnified view at high-frequency region.

2.4 Conclusions

In summary, various aliphatic amine molecules were used to functionalize graphene via a two-step hydrothermal method. These highly reactive amine molecules could form covalent linkages on graphene that effectively suppress the aggregation of graphene sheets. The controllable interlayer spacing with varied pore sizes significantly promotes the diffusion and anchoring of electrolyte ions. In addition, the interlayer spacing was found to have small change before and after the GO reduction, indicating the

generation of stabilized 3D graphene networks. The incorporation of amino and hydroxyl groups can also adjust the surface energy of graphene, which serves to dramatically enhance the ion accessibility to the electrode. With remarkable structural features, amine/rGO electrodes achieved an enlarged capacitance in aqueous and organic electrolytes with excellent cycling stability and charge transport capability. Furthermore, an ultrahigh specific capacitance of 119 F/g was obtained in ionic liquid electrolyte with ultrahigh energy density of 51 Wh/kg and slow self-discharge rate. Moreover, the DFT calculations revealed the electron distribution at the amine/graphene interfaces and overall good conductivity of these modified graphene.

CHAPTER 3. MOLECULAR LEVEL STUDY OF CONJUGATED GRAPHENE FRAMEWORK

3.1 Introduction

Introducing heteroatom-containing components (N, B, S) to graphene is an effective way to tune the graphene structure and enhance the capacitive values [78, 157, 158]. The active functional groups on GO open up various chemical routes for the surface modification. For example, Lee *et al.* have used a diazonium salt to prepare modified graphene electrodes with specific capacitance of 210 F/g [159]. Yu's group has utilized the acid-catalyzed cyclization chemistry to produce benzobisoxazole functionalized graphene networks [128]. Moreover, *in situ* oxidative polymerization processes have been reported to produce conductive polymers (polyaniline or polypyrrole) decorated graphene composites with a relatively high capacitance [160-162]. Nevertheless, conductive polymer chains are prone to structural breakdown during multiple redox processes, resulting in poor cycling stability [163].

Phenylene diamines (PDs), also called "amino anilines", have been widely employed in the field of electroanalytical detection, chemical synthesis and catalysis, and energy storage.[164-166]. Similar to aniline, phenylene diamines can also be oxidized chemically or electrochemically to corresponding oligomers or polymers, but their conductivity is several orders of magnitude lower than that of polyaniline [167]. Kuang *et al.* have reported a rGO/poly(p-phenylene diamine) composite with a specific capacitance of 347 F/g. The composite was prepared by grafting a monomer to chlorinated GO through amidation, followed by *in situ* polymerization and reduction.[168] Lee *et al.* also adopted

PDs as part of redox active electrolytes to study the electron transfer in nitrogen-doped (ND) graphene electrode [166]. Despite the simple synthesis of PD polymers and ND graphene from PDs, the chain length of polymers and the distributions of dopants are difficult to control. Therefore, it is of great significance to comparatively study the molecular level functionalization of graphene layers by PD molecules, taking advantage of the GO surface chemistry. PDs (donor) can serve as surface modifying agent to GO (acceptor) to facilitate the electron delocalization and enable electron transport at the donor-acceptor junction. By utilizing these PD isomers with different molecular geometries and electrochemical activities, the structure of graphene network and the effect of reversible redox processes can be better elucidated.

Complementary to experimental characterizations, multiscale computational studies using molecular dynamics (MD) and density functional theory (DFT) calculations play a crucial role in the investigation of functionalized graphene system. Specifically, the molecular configurations under the given thermodynamic conditions can be characterized by classical force field (FF) based MD simulations, and the electronic structures can be explored by the quantum mechanical DFT calculations. For the functionalized graphene, the electronic interactions serve to reveal the electronic density distribution, and the electron density difference between isomers informs molecular interaction features in the atomic level.

In this work, phenylene diamine isomers, o-phenylene diamine (OPD), m-phenylene diamine (MPD), and p-phenylene diamine (PPD), were selected as the molecular spacers to experimentally and computationally study the chemical interactions and electrochemical properties of different PD/rGO networks. The binding of molecules to

GO was *in situ* monitored by thermal analysis. Combining XRD characterization and MD simulation, the interlayer spacing affected by PD geometries were investigated. The dynamic rheological study was performed to record the change of storage modulus, which provided evidence for the formation of stabilized graphene structure. The optimal loadings for each PD to obtain the highest capacitance values were determined. The redox transitions and the charge transport kinetics were also discussed based on electrochemical analysis and theoretical models to explain the large capacitance variation of the three PD/rGO electrodes.

3.2 Experimental

3.2.1 Materials synthesis

GO was synthesized through a modified Hummers' method. To prepare functionalized graphene, three phenylene diamine molecules, OPD, MPD, and PPD were used as the molecular spacers. 50 mg of GO was dispersed in 30 mL of water by sonication, and mixed with 0.1, 0.2, 0.5, 1, 2, and 4 mmol of diamine in 20 mL of water. Then the diamine/GO solutions were heated in a Teflon autoclave liner (80 mL volume) at 90°C for 3 h, followed by 180°C for another 12 h. Afterwards, the diamine/rGO hydrogel was filtered, washed with water multiple times and dried in an oven at 55°C overnight. The rGO control sample was prepared by dispersing 50 mg of GO in 50 mL of water and reacted in an autoclave at the same condition as for PD/rGOs. The OPD/rGO, MPD/rGO, and PPD/rGO materials for characterization were made from 0.5 mmol of diamine with 50 mg of GO unless otherwise noted.

3.2.2 Materials characterization

The morphology was visualized by SEM (Hitachi 8010) and TEM (JEOL 100 CX). Elemental analysis and electron energy loss spectroscopy (EELS) were carried out on a Tecnai F30 TEM. ATR-FTIR was performed on a Nicolet 6700 spectrometer, XPS was characterized by a Thermo K-Alpha XPS. The chemical reactions was monitored by DSC (TA Instrument Q 2000). UV-Visible (UV-Vis) spectra were obtained from a UV-2450 spectrometer (Shimadzu), and X-ray diffraction patterns were acquired on an X'Pert Alpha-1 diffractometer. The dynamic rheological study of the materials were conducted on a Discovery Hybrid rheometer (TA Instruments), and the storage modulus was measured at 90°C under an oscillation mode.

3.2.3 Electrochemical characterization

The electrochemical measurements were performed on a Versastat electrochemical station (Princeton Applied Research) by using both two-electrode and three-electrode systems. For two-electrode testing, free-standing electrodes were prepared by mixing 90 wt% of active materials with 5 wt% of carbon black and 5 wt% of PTFE binder in a few droplets of DI water. After homogenization, the resultant paste was cast into a film by high pressure rolling. Each electrode film had an average weight of (1 ± 0.2) mg with a size of 6 mm in diameter, and the normalized density for the active material in each electrode was around 3.2 mg/cm^2. In the three electrode system, a Pt wire and Ag/AgCl electrode in saturated KCl solution were used as the counter and reference electrodes respectively. To prepare the working electrodes, the active materials and PVDF binder were mixed at the same ratio as in two-electrode preparation and dispersed in NMP solution. The concentration of the active materials was kept at 0.25 mg/mL. A 2 µL dispersion was

transferred onto a glassy carbon (GC, 0.07065 cm^2 geometric area) and dried at 80°C before testing. For two electrode system, the specific capacitance was calculated from both CV and CD curves using Equation (6) and (8),

$$C_s = \frac{4It}{mV} \tag{8}$$

where *I* is the current, *V* is the potential range, *m* is the total mass of two electrodes, and *t* is the discharge time. The specific capacitance in the three-electrode system was determined based on Equation (9)

$$C_s = \frac{\int IdV}{2vmV} \tag{9}$$

3.2.4 Computational model

The computational models were configured to include the OPD, MPD, and PPD molecules with hydroxide adatoms on the reduced graphene surface so as to reflect the experimental assumption that the functionalization was accompanied by donating a hydrogen to neighboring oxygen atom on the reduced graphene. The concentrations of the PD isomers were determined to be 29.41 wt% for PPD and MPD, and 13.63 wt% ~ 20.44 wt% for the OPD. In MD simulations, the dimension of the cell was determined to be 25.56 Å × 22.14 Å for PPD and MPD, and 39.18 Å × 34.30 Å for OPD. Each slab structure was separated by ~40 Å vacuum space (Figure 3.1a-c). The phenyl ring of OPD tended to be placed in parallel to the graphene surface due to the disorderly bonded or non-bonded character.

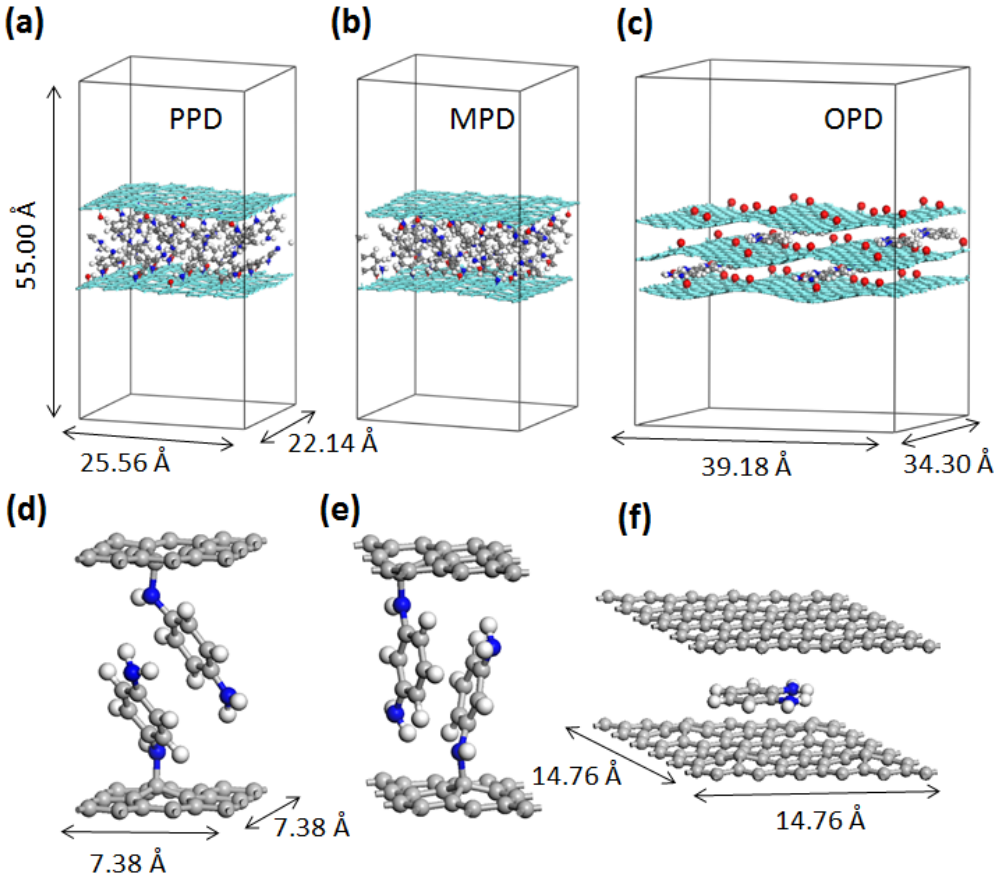

Figure 3.1 Computational models of (a) PPD/rGO, (b) MPD/rGO, and (c) OPD/rGO for the molecular dynamics simulations; unit models of (d) PPD/rGO, (e) MPD, and (f) OPD for the DFT calculations. Figure courtesy of Dr. Ji Il Choi.

To describe the sp^2 hybridized carbon form in graphene, we adopted an sp^2 graphite carbon force field.[169] The van der Waals interactions between heterogeneous atomic pairs were calculated from the geometric mean of associated parameters provided by an universal force field (UFF) [170]. The molecular dynamics simulations were performed in a canonical ensemble (NVT) type in which Nose-Hoover thermostat [171, 172] was used to control the temperature, and a particle-particle particle-mesh Ewald (PPPM) method was used in periodic cells for long-range interactions. Required atomic partial charges for electrostatic interactions were calculated using a charge equilibration (QEq) method [173].

LAMMPS package [174] was used for the simulations. To obtain simulated XRD patterns, we removed the vacuum space from each model and optimized the geometries.

DFT calculations was used to investigate the electron density difference and electron density of states (DOS) of the PD/rGO structures. We used a projector augmented wave method (PAW) [175, 176] within the plane wave basis set to describe the interaction between ion cores and valence electrons. The Perdew-Burke-Ernzerhof (PBE)[177] exchange correlation function was used, as implemented in Vienna Ab-initio Simulation Package (VASP) [178, 179]. The Brillouin zone was sampled for the 3×3×1 k-point mesh for the geometry optimizations within the Monkhorst-Pack scheme[180] with plane-wave energy cutoff of 450 eV. As shown in Figure 3.1(d-e), optimized geometries of the PPD and MPD/rGO systems had an equivalent surface dimension of 7.38 Å × 7.38 Å with a 20 Å vacuum space introduced between graphene stacks though the periodic boundaries; whereas the optimized equivalent surface dimension for OPD/rGO was 14.76 Å × 14.76 Å. Refined 6×6×1 Monkhorst-Pack k-point mesh was adopted to compute the electronic density of states. The pairwise dispersions were corrected by the DFT-D3 method by Grimme *et al* [181].

3.3 Results and Discussion

3.3.1 Surface analysis

As shown in Figure 3.2(a-c), functionalized graphene had wrinkled/wavy form of sheets with 3D porous structures upon molecular level modification. Particularly, the MPD/rGO and PPD/rGO exhibited thin graphene layers with low contrast images, indicating the effective exfoliation of the graphene sheets; while the OPD/rGO exhibited

thicker graphene sheets, showing the possible stacking of OPD molecules. The TEM images (Figure 3.2(d-e)) also reflected the ultra-small thickness of the graphene samples due to the semi-transparent images. The uniform distribution of the amino groups on graphene was visualized by elemental mapping of N and C atoms in an energy-filtered TEM (Figure 3.3). According to the electron energy loss spectroscopy (EELS), the atomic composition of N atoms were estimated to be 7.5~8.6%.

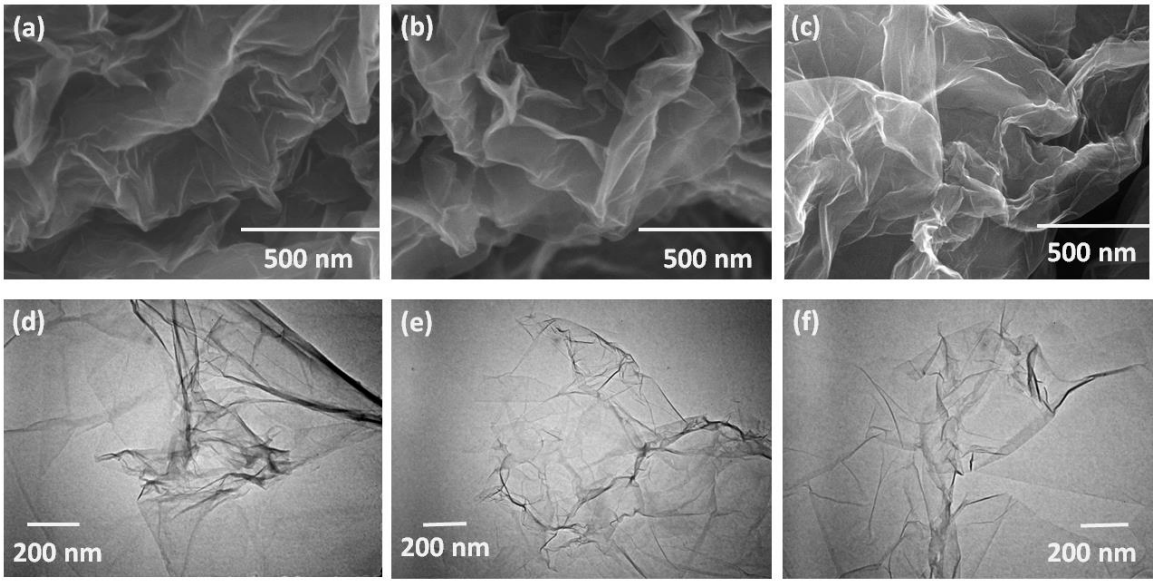

Figure 3.2 (a-c) SEM images and (d-f) TEM images of the OPD/rGO, MPD/rGO, and PPD/rGO materials, respectively.

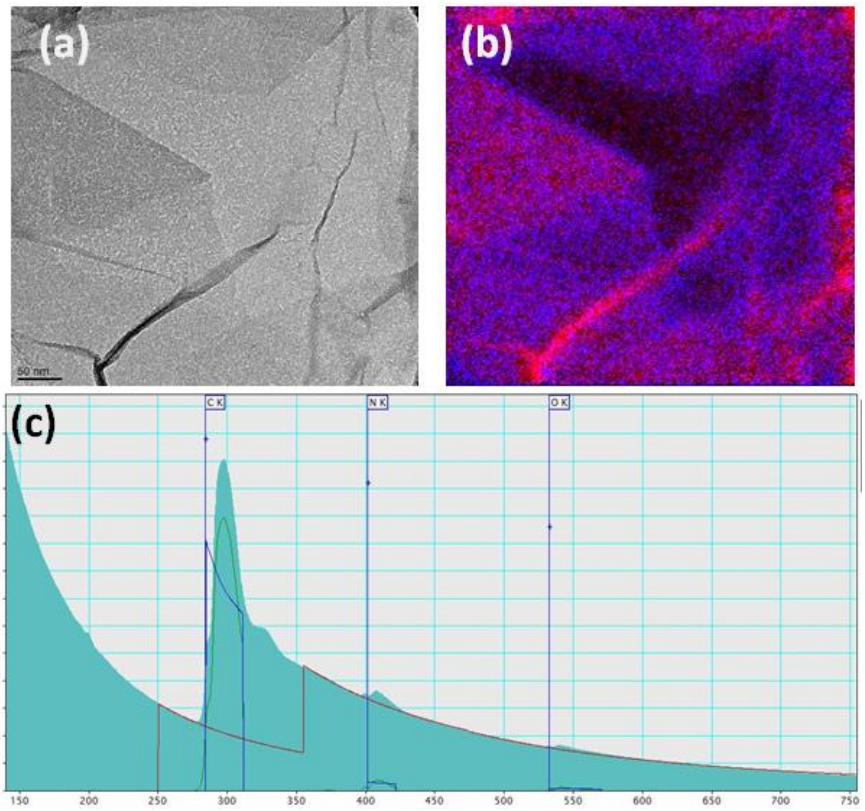

Figure 3.3 (a) Bright field TEM image and (b) energy-filtered TEM image of PPD/rGO. Red dots and blue dots represent the C and N respectively. Black area is the background; (c) EELS spectrum obtained from the area shown in (a).

3.3.2 Reaction mechanism and chemical bonding

Based on previous literatures, three possible reactions between GO and amines were proposed: (1) condensation reaction between amines and carboxylic acids to form amides (-CONH-); (2) acid-base reaction of amines and carboxylic acids to form ammonium salts ($-COO^{-}NH_3^{+}$) ; (3) nucleophilic substitution between amino groups and epoxy groups.[122] However, FTIR and XPS results were insufficient to explain the reaction mechanism [122, 182, 183]. Therefore, DSC was used to *in-situ* monitor the heat profile accompanied by the chemical reaction. All the three reactions listed above were exothermic, in which exothermic profiles are expected to appear in DSC curves. Biphenyl

4,4’-dicarboxylic acid and an epoxy resin (bisphenol A type, Hexion Specialty Chemicals) were selected as reference materials with bi-functional carboxylic acid and epoxide groups. These materials were mixed with PPD molecules at 1:1 stoichiometric ratios of the functional groups and heated from 40°C to 250°C. In Figure 3.4a, the PPD/BDA mixture presented only a sharp endothermic peak at 142°C, which corresponded to the melting of the PPD molecules. This indicated that PPD molecules simply underwent a phase change and did not react chemically with the carboxylic acid. On the contrary, the PPD/epoxy mixture showed a broad exothermic peak from 90°C to 150°C (Figure 3.4b), which can be attributed to the reaction between amino groups and epoxide groups. Moreover, the melting behavior of PPD was not observed since the molecules already reacted with epoxy groups before the melting point. These results provided a clear evidence that aromatic amines prefer to react with epoxide groups via nucleophilic substitution. The mixture of aromatic amines and GO were also tested by DSC, and similar exothermic peaks were observed due to the ring-opening reaction of the epoxide groups (Figure 3.4c). The endothermic peaks at 58°C and 85°C refer to the melting of MPD and OPD molecules before the reaction. The exothermic peaks were centered at 102°C, 109°C, and 123°C for PPD, OPD, and MPD functionalized rGOs, respectively, which suggested that the chemical reactivity towards epoxide groups on GO be in the sequence of PPD>OPD>MPD. 90°C, the onset temperature for the exothermic reaction, was used as the temperature for the first step hydrothermal process, which enabled the covalent grafting of amino groups while minimizing the reduction degree of GO. The sharp endothermic peaks at ~ 150°C might arise from the decomposition of unreacted oxygen groups on GO. The prominent endothermic profile was also observed for pure GO, as shown in Figure 3.4d.

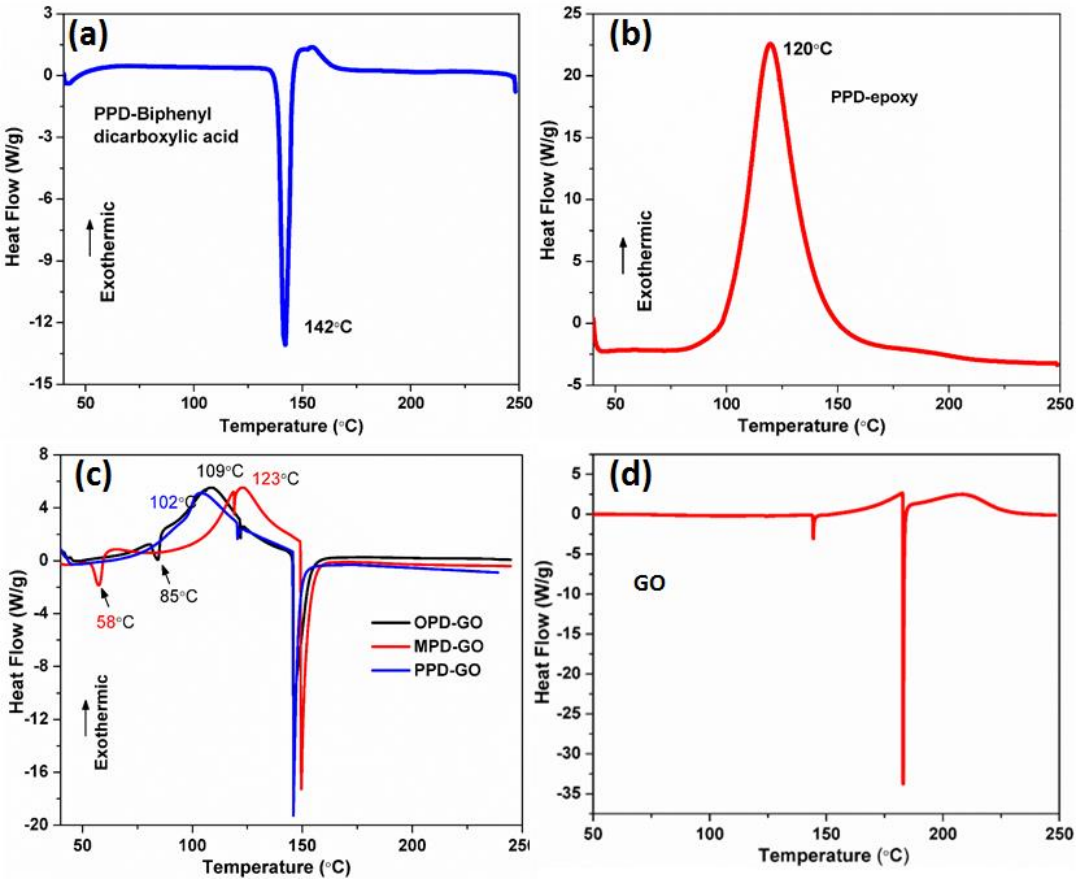

Figure 3.4 DSC curves of (a) PPD/biphenyl di-carboxylic acid mixture, (b) PPD/epoxy mixture, (c) OPD/GO, MPD/GO, and PPD/GO mixtures, and (d) GO in N_2 at heating rate of 10°C/min.

The chemical bonding of PD/rGO was verified by ATR-FTIR (Figure 3a). The peak at 1543 and 896 cm^{-1} corresponded to the stretching and wagging modes of –NH group in the C-NH chemical bonds [184, 122]. In addition, the peak intensity of the epoxy group reduced after functionalization, implying the possible reaction of amino groups at epoxide sites on GO surfaces.

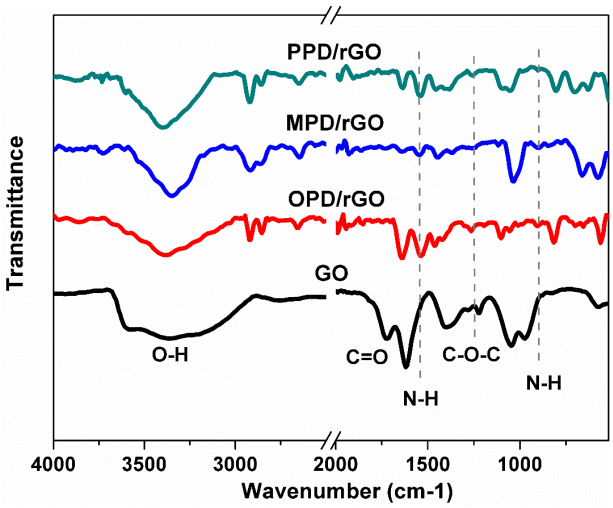

Figure 3.5 ATR-FTIR spectra of GO and PD/rGOs.

XPS was used to further characterize the degree of functionalization. From the survey spectra (Figure 3.6a), the atomic percentage of N was determined to be 7.6% for PPD/rGO, which was consistent with the results obtained from elemental mapping. The N contents for OPD/rGO and MPD/rGO were found to be 9.2% and 7.2% respectively. Considering an average 8% of N and 10% of O (atomic percentage) in PD/rGO, the weight percentage of PD was around 32% at 0.5 mmol of molecular loading. These values provided an estimation on the degree of functionalization on graphene. The N content at different PD loading levels were also determined (Figure 4b). It can be seen that the N percentage increased sharply as the initial addition of PDs and gradually slowed down above 1 mmol. At high molecular loadings, the majority of the epoxide groups were reacted and the residual PD molecules were stacked within graphene network via non-covalent $\pi - \pi$ interaction [185, 68, 186]. It was found that the N percentage in OPD/rGO was higher than that in MPD/rGO and PPD/rGO at high molar ratios, which can be probably explained by the following two reasons. First, for three types of PD isomers, it required different molarities of each PD molecule to fully react with same amount of GO to reach

an equilibrium state. Specifically, the PPD and MPD were likely to crosslink between graphene sheets with both amino groups reacted, while only one amino group in OPD molecules could possibly react due to the large steric hindrance. In this sense, larger quantity of OPD molecules was needed to consume all the epoxide groups than PPD and MPD. Second, OPD molecules tended to lie down on (align more horizontal to) graphene sheets to increase the likelihood of $\pi - \pi$ interactions by having more effective *p* orbitals overlapping. At high molar loadings, additional OPD molecules can be further stacked within graphene sheets to stabilize the molecular orbitals. Nevertheless, it is thermodynamically favorable for PPD and MPD molecules to bond perpendicularly to graphene sheets, making it difficult for the accumulation of PPD or MPD molecules via $\pi - \pi$ interactions between aromatic amines and grapheme sheets. These explanations will be further discussed in later section.

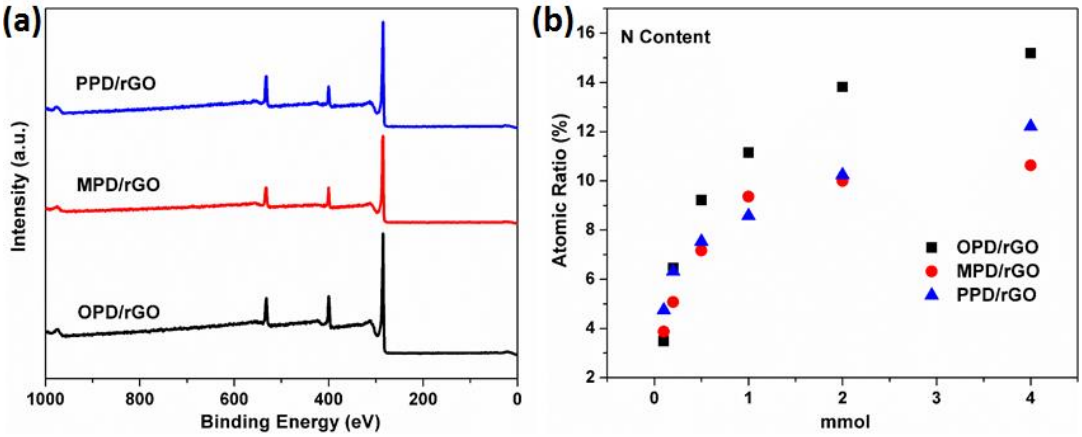

Figure 3.6 (a) XPS survey spectra of OPD/rGO, MPD/rGO, and PPD/rGO at the molar loading of 0.5 mmol; (b) N percentage of the PD/rGO composites made from different PD loadings.

For high resolution C1s spectra (Figure 3.7a), the high-intensity peak centered at 284.8 eV represented the sp^2 hybridized graphitic carbon. Three peaks located at 286.1,

287.7 and 289.2 eV were assigned to C=N/C-O, C-N, and O-C=C groups, respectively. Complementary to FTIR, the presence of C=N/C-N bonds implied the covalent linkage of amino groups on graphene. The nature of N-containing functionalities was illustrated by N 1s spectra, and the spectra can be deconvoluted into three peaks: the benzoid amine (-NH-) at 399.6 eV, the quinoid amine (-N=) at 398.6 eV, and cationic radical ($-N^{+}=$) at 401 eV [129]. These aromatic structures can be associated with multiple electronic states that change the charge transfer efficiency. Integration of these peaks revealed that 52.9% of N was in the form of benzoid amine, 19.6% in quinoid amine, and 27.5% in cationic radical for PPD/rGO; while smaller portions of quinoid amine (15.1%) and cationic radical (14.9%) were found for MPD/rGO. PPD molecules covalently bonded to graphene can be seen as an analogy to a short segment of polyaniline, and an increasing amount of N cationic radicals and quinoid-to-benzoid ratio led to a higher conductivity of polyaniline [187, 188, 129]. Similarly, larger portions of the quinoid imines and cationic radicals implied that PPD/rGO could be more electrochemically active and electrically conductive than MPD/rGO.

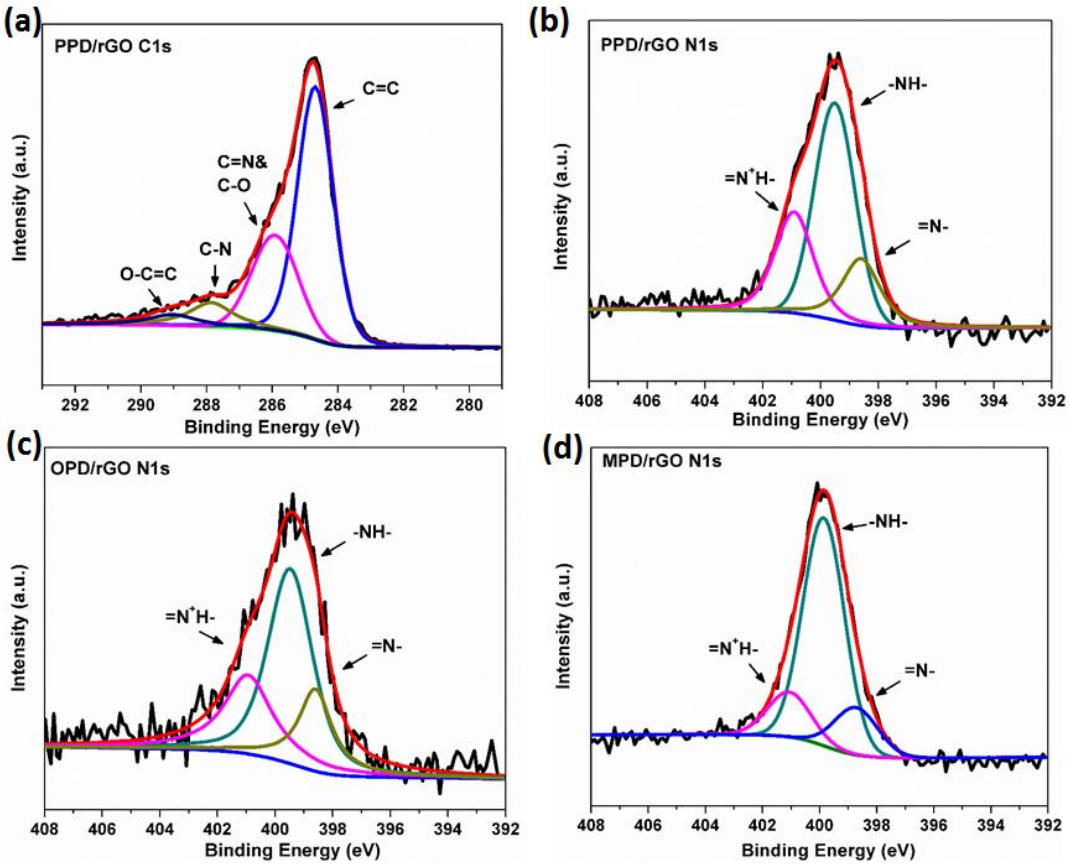

Figure 3.7 High resolution (a) C1s for PPD/rGO; deconvoluted N1s spectra for (b) PPD/rGO, (c) OPD/rGO, and (d) MPD/rGO.

UV-Vis absorption spectroscopy was used to study the conjugated network (Figure 3.8). For GO, two characteristic peaks showed up with a maximum at 229 nm due to $\pi - \pi^*$ transition of aromatic structure and a shoulder peak at 305 nm due to the $n - \pi^*$ transition of C=O bonds [189]. The absorption maximum shifted to 259 nm for rGO as the conjugated graphene backbone was restored. The absorption features appeared at 279 nm, 265 nm, and 267 nm for PPD, MPD and OPD functionalized graphene, respectively. The red-shift of the $\pi - \pi^*$ transition peaks indicated that the aromatic amines covalently interacted with graphene sheets to form larger π conjugated networks. Upon the formation of covalent linkage, the electron lone pairs on amino groups can be delocalized into the

graphene sheets, thus increasing the overall electron density in the conjugated system. The PPD/rGO, with the biggest red-shifted value, reflected the highest degree of the electronic conjugation among the modified graphene, which has also been evidenced by the rich quinoid imine and cationic radical structures in XPS. For the PD/rGO materials, broad shoulder peaks were observed at wavelengths above 400nm, which can be explained by the charge transfer between the electron donors (aromatic amines) and electron acceptors (graphene) when the molecules are in close proximity (≤4 Å) [190].

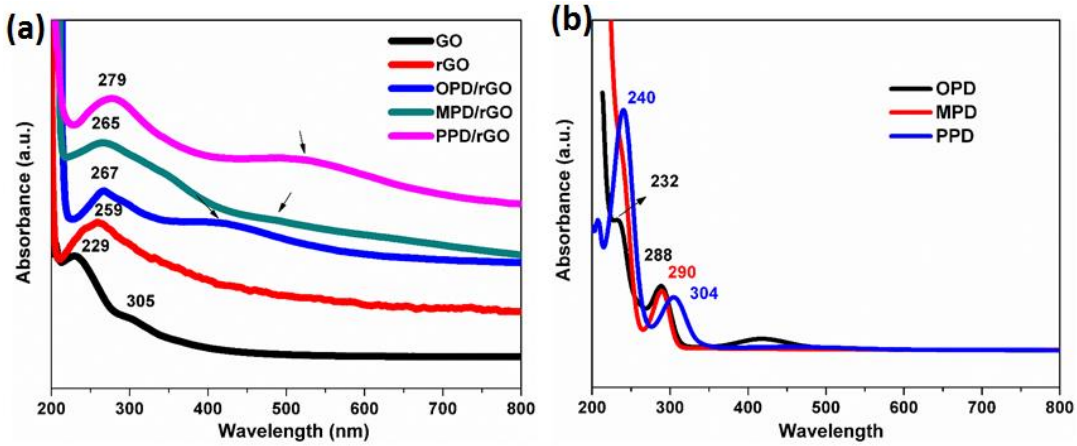

Figure 3.8 UV-vis absorption spectra of (a) GO, rGO, and PD/rGOs, (b) OPD, MPD and PPD isomers.

3.3.3 Crystalline structure analysis with MD simulation

Structural evolution of the PD modified graphene was investigated by the change of storage modulus, which provided an evidence on the formation of cross-linked graphene structures. The storage moduli of the GO and PD/GO mixtures were obtained upon isothermal treatment at 90°C (Figure 3.9). GO solution had a negligible change of storage modulus (~10 Pa), while the addition of PD molecules resulted in a dramatic increase of storage modulus. After 5 min, the maximum modulus of 13,680 Pa was obtained for

PPD/rGO, which was three orders of magnitude higher than that of GO. MPD molecules could also adjust its orientation to partially crosslink graphene sheets, leading to storage modulus over 6000 Pa; while OPD was likely to bond onto one side of graphene or intercalated between stacked graphene sheets in non-bonding form, thus having the smallest modulus increase.

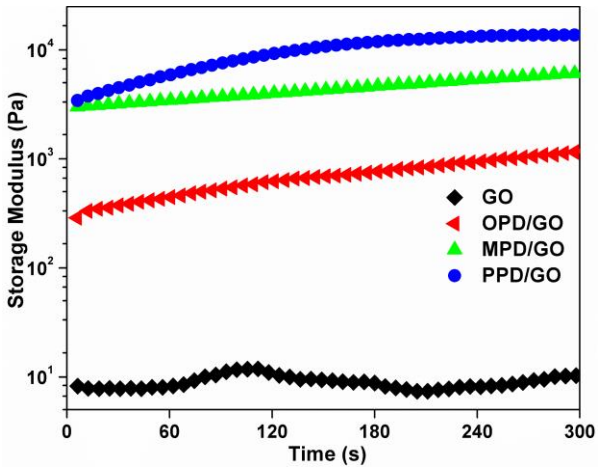

Figure 3.9 Dynamic rheological measurements of GO and PD/GO mixtures with storage modulus vs time.

XRD patterns were obtained to study the effect of the molecular spacers on interlayer *d*-spacing (Figure 3.10). As for rGO, only one peak appeared at ~25.9°, which was attributed to the restacking of the graphene sheets. The diffraction peaks of PPD/rGO and MPD/rGO occurred at smaller angles of 6.3° and 6.8°, which can be converted to *d* spacing of 1.41 nm and 1.30 nm, respectively. The significant enhancement of interlayer spacing was achieved due to the covalent grafting of PPD and MPD as molecular spacers. The emergence of low-angle (<11°) 2θ peaks, in conjugation with the enlarged storage modulus, implied the formation of crystalline and partially crosslinked graphene structure. For OPD/rGO, two new peaks were observed at 14.5° and 20.7°, corresponding to *d*

spacing of 0.61 nm and 0.43 nm. It is believed that OPD was disorderly bonded or physically adsorbed to the graphene surface, leading to irregular and variable interlayer spacing.

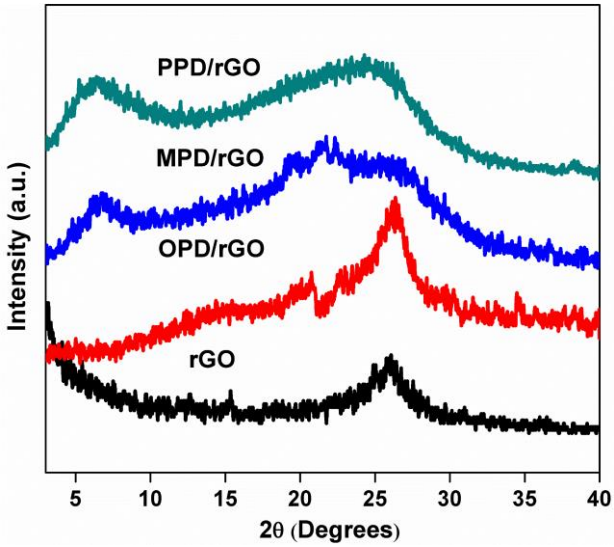

Figure 3.10 Experimental XRD patterns of rGO and PD/rGOs.

Molecular dynamic (MD) simulations were performed to theoretically elaborate the molecular geometries of the functionalized graphene. The computational models were based on the assumption that PD isomers were uniformly distributed on graphene (Figure 3.11a). Therefore, only characteristic XRD peaks showing the inter-layer dependence of the peaks were considered. As shown in Figure 3.11b, the simulated *d* spacing of 1.47 *nm* (PPD/rGO) and 1.39 *nm* (MPD/rGO) agreed well with the experimental data, which confirmed the highly stable graphene nanostructure. In addition, the simulation revealed that molecular density of 25 wt% or higher was necessary to secure the *d* spacing of 1.47 *nm* for PPD/rGO (consistent with the weight percentage quantified by XPS). Reducing the PPD loading to 22 wt% would decrease the *d* spacing to less than 1.35 *nm*. According to the simulated OPD/rGO pattern, two major peaks at 12.95° and 19.5° corresponded to *d*-

spacing of 0.63 *nm* and 0.37 *nm*, respectively, which matched experimental results well. The existence of multiple XRD peaks of the OPD/rGO particularly stemmed from the disorderly bonded or non-bonded OPD molecules to graphene, which led to variable interlayer distances with a fluctuating surface morphology.

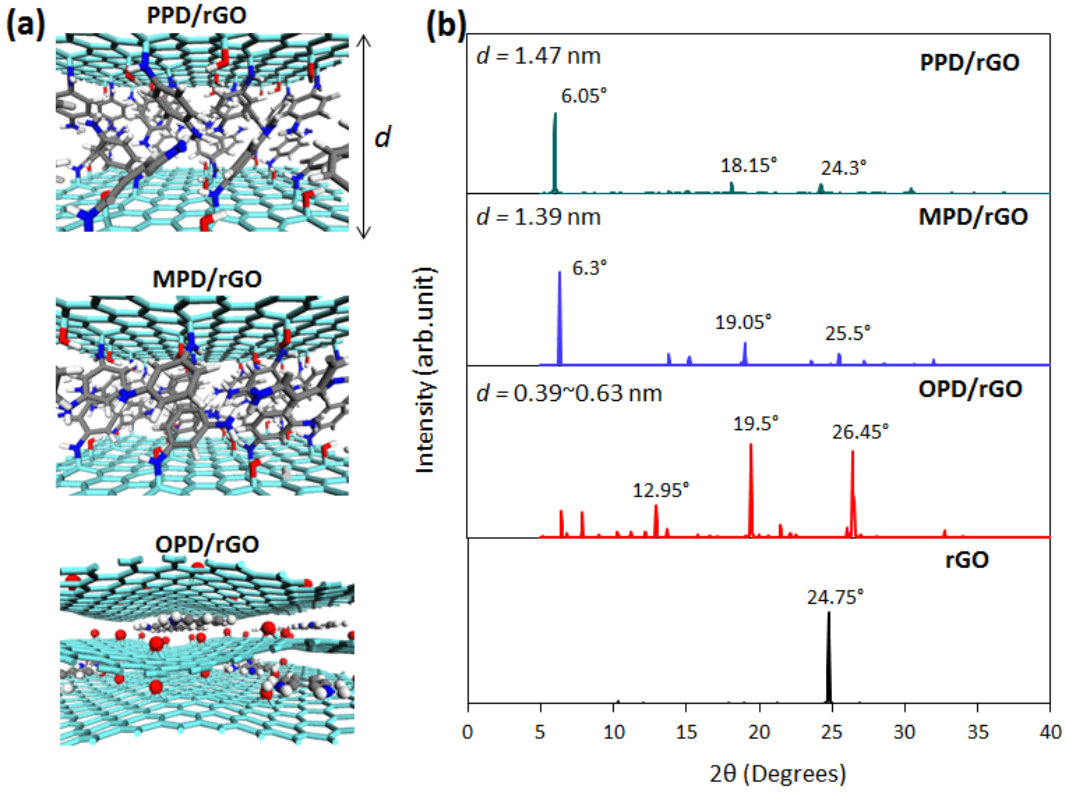

Figure 3.11 (a) Simulated configurations of the PD/rGO networks; (b) simulated XRD patterns of rGO and PD/rGOs. Figure courtesy of Dr. Ji Il Choi.

The formation energy of the PD/rGO structures was evaluated and compared using DFT, as shown in Figure 3.12. The relative energy values were referenced to that of PPD/rGO and calculated by the following equation,

$$E_{formation} = E_{total} - E_{isomer} - E_{graphene} + \mu(H) \quad (10)$$

where E_{total} represents the total energy of PD/rGOs, E_{isomer} and $E_{graphene}$ represent the energy of individual PD isomer in a vacuum and the pristine graphene surface, respectively. The chemical potential of atomic hydrogen, $\mu(H)$, was obtained from hydrogen molecules in vacuum. The formation energy plot confirmed that the PPD/rGO was the most thermodynamically stable form, while the formation of stabilized OPD/rGO required the highest amount of energy.

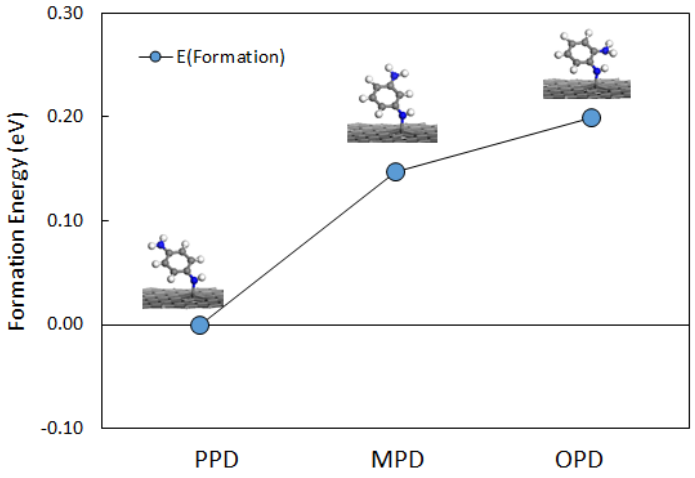

Figure 3.12 Relative formation energy plot of the PD/rGO structures. The energy level of PPD/rGO was set to the reference. Figure courtesy of Dr. Ji Il Choi.

3.3.4 Structure-dependent electrochemical properties

Electrochemical properties of the OPD, MPD and PPD/rGO thin film electrodes were evaluated in two-electrode coin cells. To achieve the best electrochemical performance, the effect of molecular loading was systematically studied. It was determined that the composites made from 50 mg of GO with 0.5 mmol (54 mg) of PDs had the highest specific capacitance values. Figure 3.13 (a-c) showed the CV curves of PD/rGO (optimized ratio) electrodes in 1 M H_2SO_4 electrolyte at scan rates from 2 mV/s to 100 mV/s. It can be seen that all the electrodes exhibited a distinct hump due to reversible redox transitions of

the grafted aromatic amines, indicating strong pseudocapacitive characteristics in addition to EDL capacitance.

For the PD/rGO electrodes, the calculated capacitances at different scan rates were shown in Figure 3.13 (d-f). For all three types of electrodes, the capacitance variation followed a similar trend: a gradual increase as the initial addition of amines, reaching a maximum at 0.5 mmol loading and declining upon further loading. At the optimized PPD loading, the maximum capacitance of 422 F/g was achieved at 2 mV/s, which had more than 3-fold increase in comparison to rGO control electrode. As scan rates increased, the specific capacitance dropped to 412 F/g at 10mV/s and 374 F/g at 50 mV/s. At fast scan rates of 100 mV/s, the capacitance (339 F/g) maintained 80% of the maximum values at slow scan rates, demonstrating its capability to handle high-power output. These outstanding capacitive properties can be explained by the synergistic effect of the enlarged interlayer spacing facilitating the fast ionic diffusion and pseudocapacitive redox transitions. When the PPD loading exceeded 0.5 mmol, most of the epoxide groups were consumed by PPD. The residual PPD molecules might be physically attached onto graphene surfaces, or possibly reacted with themselves to form PD oligomers, causing the aggregation at interlayer spaces [167]. The excessive loading of the PPD might destroy the structural integrity of the graphene network, leading to a large decrease of capacitance values. In spite of the capacitance drop, it is interesting to note that an improved capacitive rate performance was obtained at 2 mmol and 4mmol PPD loadings (only 15% of capacitance loss as the scan rates increased from 2 mV/s to 100 mV/s). It is proposed that stacking of residual PPD or its derivatives might provide extra ion transfer channels, promoting the charge propagation at high scan rates.

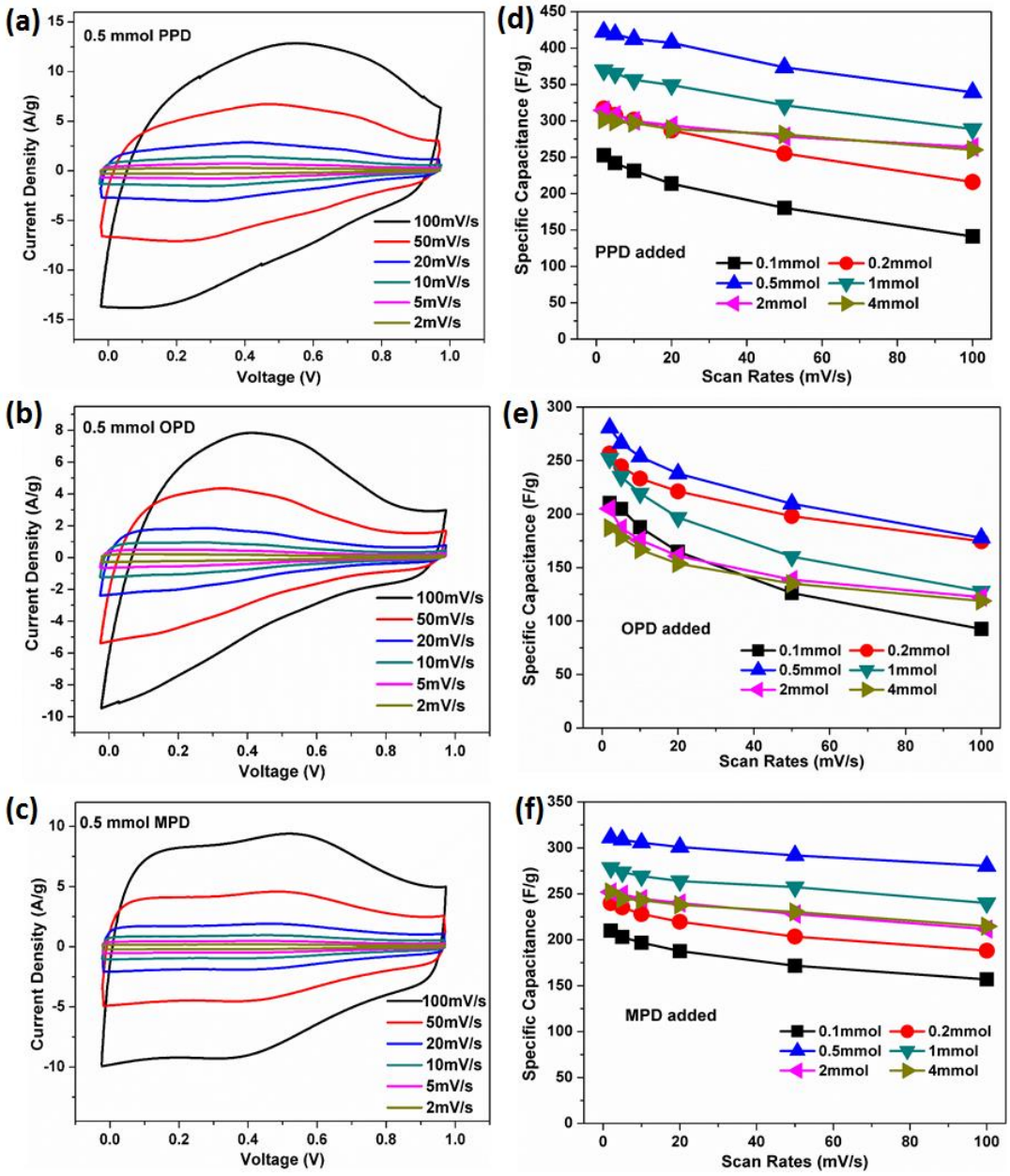

Figure 3.13 CV curves of (a) PPD/rGO, (b) OPD/rGO, and (b) MPD/rGO electrodes at optimized PD loading at scan rates from 2 to 100 mV/s; plots of specific capacitance of (d) PPD/rGO, (e) OPD/rGO, and (f) MPD/rGO electrodes with different PD loadings at various scan rates.

Similar to PPD/rGO electrodes, the CV curves of OPD/rGO exhibited broad redox peaks at the OPD loading below 1 mmol, indicating the reversible redox transitions of the OPD molecules. At 0.5 mmol OPD loading, OPD/rGO electrode delivered the largest capacitance of 281 F/g at 2 mV/s, and 63% of the capacitance (178 F/g) was maintained as the scan rate increased to 100 mV/s, both of which were much smaller than those of PPD/rGO. These results implied that fast charge transfer pathways were not established since most OPD molecules laid down on graphene sheets rather than functioned as molecular spacers. As the continuous addition of OPD (2 mmol and 4 mmol), the electrode became increasingly disordered due to the aggregation of OPD molecules and their derivatives. The disorderly bonded OPD and possible OPD derivatives might be responsible for the multiple redox peaks observed in CV curves [167, 191]. From Figure 3.13e, it can be seen that MPD/rGO electrodes presented more rectangular-shaped CV curves than those of PPD/rGO and OPD/rGO, indicating the significant capacitance contribution from EDL capacitance. A pair of redox peaks were observed for all MPD/rGO electrodes as well. At an optimized MPD loading, the maximum capacitance was determined to be 311 F/g, which was higher than that of OPD/rGO, but much lower than that of PPD/rGO. Although MPD/rGO demonstrated enlarged interlayer spacing, the lower electrochemical activity of the 1,3 substituted MPD molecules resulted in weaker redox transitions. The capacitance of PD/rGO electrodes were compared with other amine functionalized graphene electrodes in literature and summarized in Table 3.1.

Table 3.1 Comparison of the specific capacitance of PD/rGO electrodes with other amine functionalized graphene electrodes reported in literature

Electrode Materials	Amines	Testing Configuration	Electrolyte	Specific Capacitance (F/g)
NH_2-G [192]	NH_3	Three-electrode	0.5 M H_2SO_4	218
rGH [119]	Ethylene diamine	Two-electrode	2 M KOH	232
ADS-G [159]	Aminoazobenzene sulfonate	Three-electrode (on Pt foil)	1 M H_2SO_4	210
GOBIN [193]	Benzenetetraamine	Two-electrode (coated on gold	1 M H_2SO_4	370
RGO-p-PPD [168]	Poly(p-phenylene diamine)	Three-electrode (on glassy carbon)	0.5 M H_2SO_4	347
NH_2-RGO/PANI	Aniline	Two-electrode film	1 M H_2SO_4	395
rGO-Naph [189]	1,5-Diaminonaphthalen	Two-electrode film	1 M H_2SO_4	450
OPD/rGO	o-Phenylene diamine	Two-electrode film	1 M H_2SO_4	281
MPD/RGO	m-Phenylene diamine	Two-electrode film	1 M H_2SO_4	311
PPD/rGO	p-Phenylene diamine	Two-electrode film	1 M H_2SO_4	422

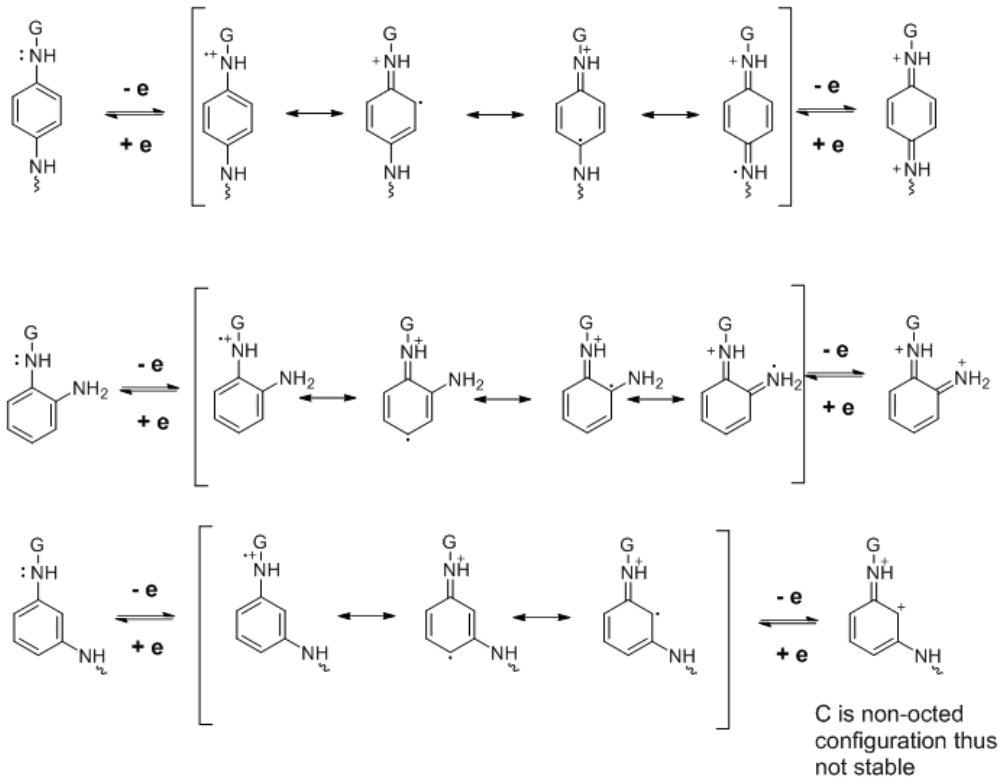

Figure 3.14 Illustration of the possible charge transition states for three PD/rGO electrodes.

Figure 3.14 shows the chemical structures of the reversible charge transfer states when PD molecules were bonded to graphene. In acidic electrolyte, OPD and PPD can undergo reversible charge transfer between benzoid diamine and quinoid diimine with four resonance structures coexisted in the intermediate state. In contrast, the conjugated diimine structure cannot be formed for MPD, and fewer stable intermediate states were involved during the charge transfer processes.

To validate the charge transfer characteristic, electrochemical tests were conducted in 1M H_2SO_4 electrolyte at 50mV/s in three-electrode set-up. In Figure 3.15a, rGO electrode exhibited near rectangular CV curves, whereas multiple redox peaks were

observed for PD/rGO electrodes, indicative of the pseudocapacitive transitions. A weak redox peak at 0.7 V was in common for all PD/rGO. For MPD/rGO, the prominent redox peak appeared at ~0.58 V. In comparison, two obvious redox peaks were observed in PPD/rGO and OPD/rGO. The results indicated that PPD/rGO and OPD/rGO electrodes, with larger number of charge transition states, might contribute to greater pseudocapacitance. The specific capacitance was calculated to be 367 F/g, 372 F/g, and 473 F/g at 50 mV/s for OPD, MPD and PPD functionalized rGOs, which followed the same trend as two-electrode test: PPD/rGO≫MPD/rGO>OPD/rGO. The higher capacitance values were due to the nature of the three-electrode system. As a reference, the CV curves of the pure PD molecules were shown in Figure 3.15b. Similarly, two pairs of redox peaks were observed in PPD/rGO while only one pair of redox peaks were seen in MPD/rGO. The results from three-electrode tests were in accordance with the possible charge transfer states in Figure 3.14. In summary, the highest capacitance values of PPD/rGO electrode can be attributed to the well-interspaced graphene network for EDL capacitance and multiple reversible charge transitions for pseudocapacitance. The MPD/rGO electrodes provided an enlarged graphene interlayer spacing, but the limited charge transition states brought down the pseudocapacitive charge storage. Although OPD molecules had multiple charge transition states, the disorderly bonded or non-bonded structures would hinder the mobility of the charges due to aggregation of the molecules between graphene layers, resulting in lower capacitive values.

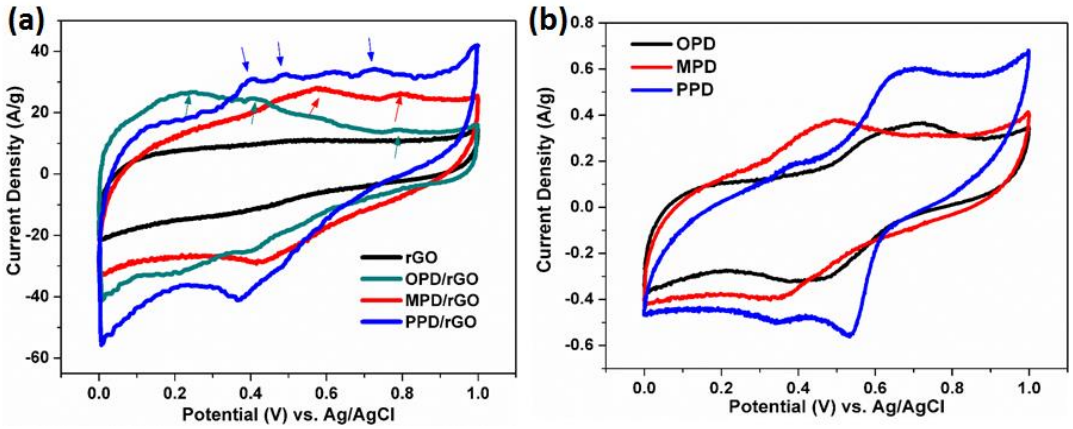

Figure 3.15 CV curves of (a) rGO and PD/rGO electrodes, and (b) PD isomers tested in 1M H_2SO_4 electrolyte at scan rate of 50 mV/s in three-electrode system.

Figure 3.16 (a-c) shows the galvanostatic charge/discharge profiles of PD/rGO electrodes at current densities from 0.5 A/g to 10 A/g. The quasi-linear curves corresponded to the reversible pseudocapacitive redox reactions [194]. Based on CD curves, the specific capacitance was calculated to be 252 F/g, 300 F/g, and 416 F/g at 0.5 A/g for OPD, MPD, and PPD modified rGO, which agreed well with the values obtained from CV curves at similar discharge time (Figure 3.16d).

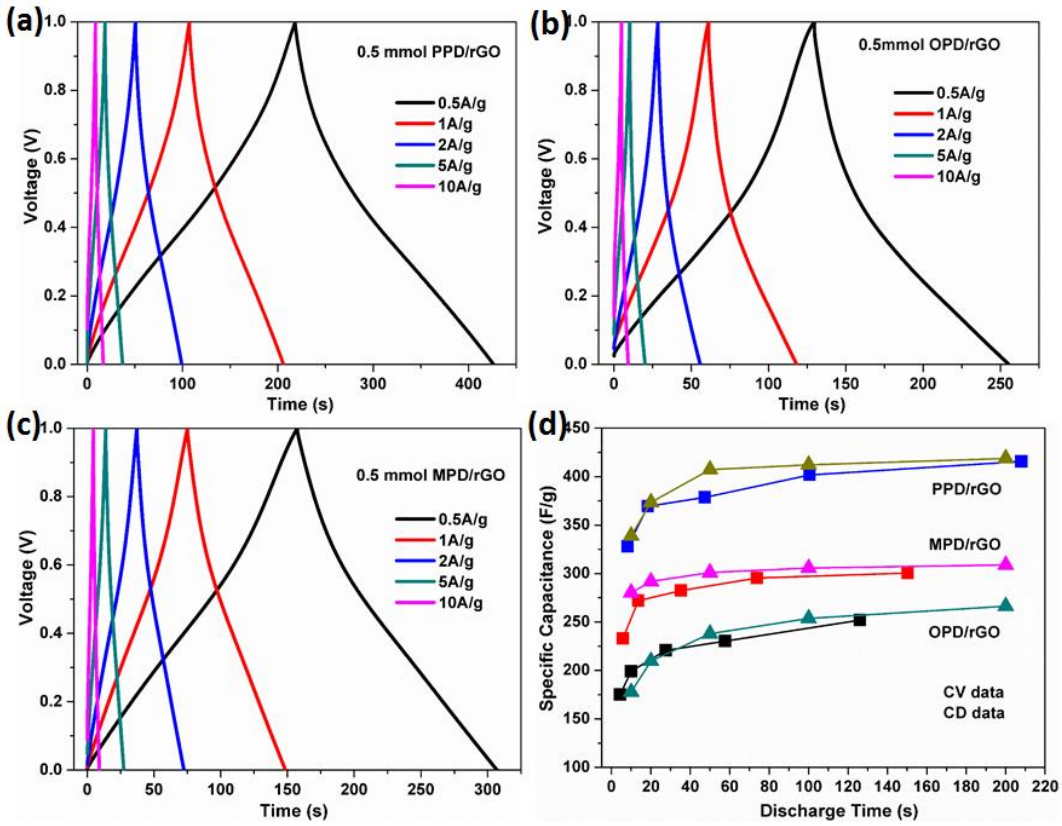

Figure 3.16 Galvanostatic charge/discharge curves of (a) PPD/rGO, OPD/rGO, and MPD/rGO at current densities from 0.5 to 10 A/g; (d) plots of the specific capacitance of PD/rGO electrodes (0.5 mmol PD loading) calculated from both CV and charge/discharge curves.

The cycling stability tests of the electrodes were performed at current density of 2 A/g (Figure 3.17). It is known that pseudocapacitive materials typically have a poor cycling stability due to structural degradation during the redox processes. For PPD/rGO and MPD/rGO electrodes, the molecular spacers grafted (partially crosslinked) between graphene layers can effectively strengthen the structural stability of the graphene network while ensuring the fast charge transport. Therefore, both electrodes achieved high cycling stability with over 89% capacitance retention after 10,000 cycles, which showed better performance compared with graphene/polyaniline composites [129, 74, 160]. In contrast,

the OPD/rGO had a larger decay of capacitance after long-term cycling tests due to the disordered graphene nanostructure.

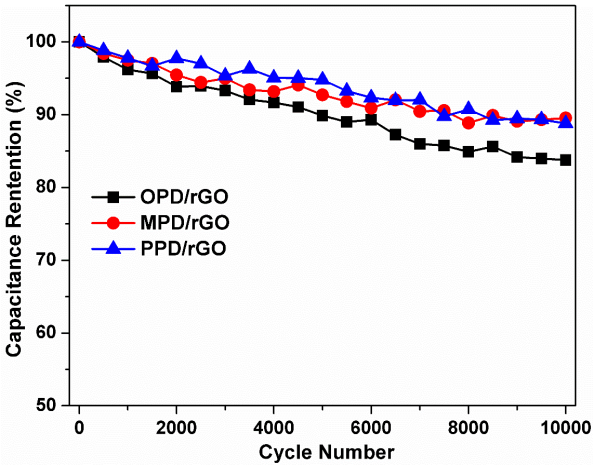

Figure 3.17 Cycling stability of the PD/rGO electrodes under 10000 charge/discharge cycles.

EIS was employed to study the resistive behavior and charge transfer kinetics of the electrode. As shown in Figure 3.18(a-c), the semicircle at high-frequency region of Nyquist plots represented the charge transfer resistance at the electrode/electrolyte interface, and the almost vertical lines at a low frequency region reflected the ionic diffusion within the electrodes [195, 131]. The series resistance, R_s, was found to be below 0.6 Ω for almost all electrodes, indicating high conductivity of the electrodes and the low contact resistance between electrodes and current collectors. The charge transfer resistance, R_{ct}, represents the total resistance at the electrode/electrolyte interface [136]. At 0.5 mmol loading, the R_{ct} was as low as 2.0 Ω and 2.3 Ω for PPD/rGO and MPD/rGO, and a higher R_{ct} value of 3.9 Ω was recorded for OPD/rGO. In particular, the OPD/rGO electrodes displayed an extended Warburg impedance region, which resulted from the slow ionic diffusion at the electrode/electrolyte interfaces [136]. The smaller R_{ct} values at high

molecular loadings of PPD and MPD can be explained by the formation of more charge transfer pathways. The Nyquist plot of rGO was also presented in Figure 3.18d, and the larger R_{ct} further demonstrated the improved charge transfer features of the PD/rGO.

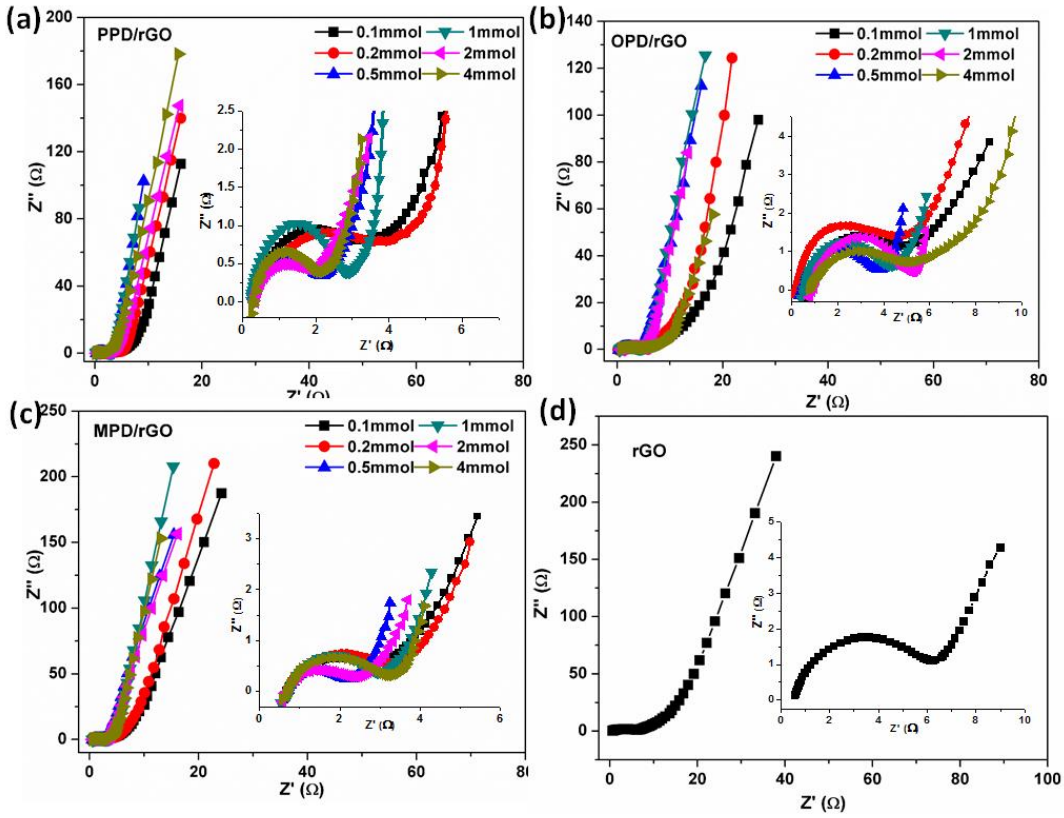

Figure 3.18 Nyquist plots of (a) PPD/rGO, (b) OPD/rGO, (c) MPD/rGO, and (d) rGO electrodes in the frequency range from 100 kHz to 10 mHz; inset is the magnified plots at high frequency region.

3.3.5 DFT calculations

In conjugation with the electrochemical analysis, DFT calculations were carried out for the PD/rGO at given molecular density to investigate electronic structures and charge transfer features. During the DFT calculation, the configuration of the graphene networks was based on the simulated results (Figure 3.11), keeping the interlayer distance constant.

Figure 3.19(a-c) illustrated the electron density difference of the PD functionalized graphene networks. It was found that the electronic interactions of the PD molecules were closely associated with the molecular geometries. For PPD/rGO, a prominent feature was obtained that the net electron density was preferably distributed on the interaction region connecting the PPD molecules through the π-π interactions of the phenylene rings. The existence of this electron rich region could provide a fast charge transfer pathway between graphene layers. In contrast, the electron density was primarily distributed on individual molecule in MPD and OPD/rGO. The localized electronic distribution on MPD or OPD molecules implied a different electronic interaction features compared to that of PPD/rGO. To investigate the interacting atomic orbitals, the distribution of the highest occupied molecular orbitals (HOMOs) of the PD/rGO was calculated, as shown in Figure 3.19(d-f). The results revealed that the grafted PPD and MPD molecules presented a similar atomic origin with different symmetries in HOMO distribution. Anisotropic distribution of the HOMO energy levels in grafted MPD led to a different molecular alignment in comparison to grafted PPD, which further explained the discrepancy in electronic interaction features. The most preferable geometries of the grafted PPD and MPD in molecular interactions are displayed in Figure 3.20. It should be mentioned that this model was obtained by the energy miniaturization using DFT calculation, and geometries could vary when other thermodynamic factors were considered.

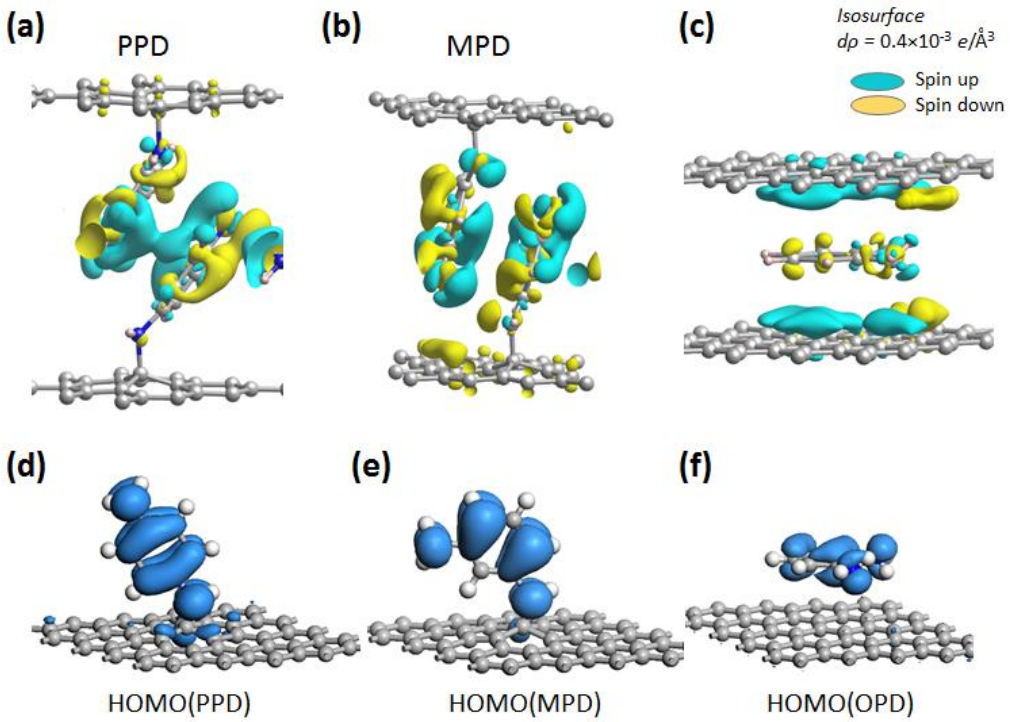

Figure 3.19 Electron density difference calculated for (a) PPD/rGO, (b) MPD/rGO, and (c) OPD/rGO. PPD/rGO shows unique density linkage between the PPD molecules. HOMO levels are illustrated at (d) ~ (f) for the PPD/rGO, MPD/rGO, and OPD/rGO, respectively. Figure courtesy of Dr. Ji Il Choi.

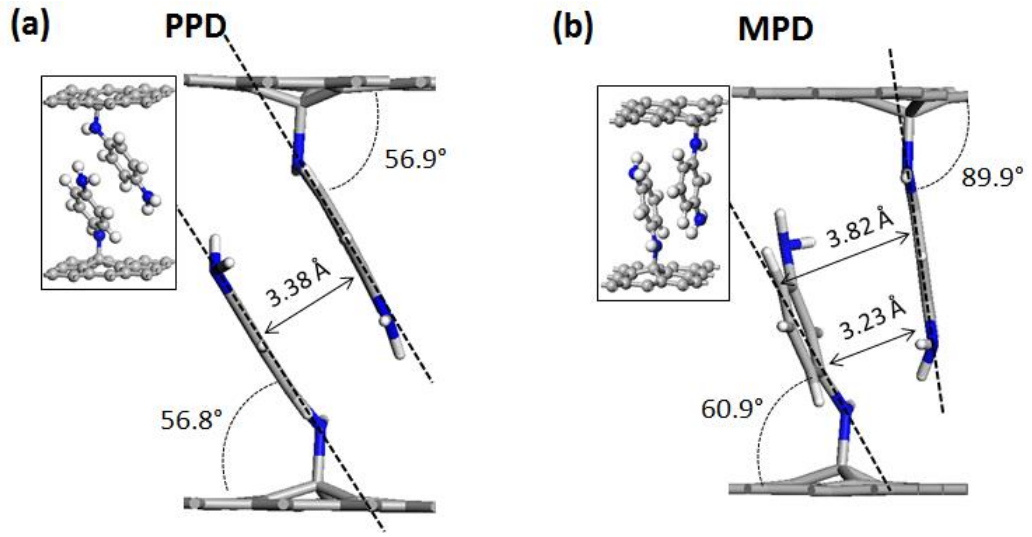

Figure 3.20 Interaction geometries of (a) PPD and (b) MPD. The PPD shows highly symmetric configuration compared to that of MPD. The insets illustrate the optimized atomic geometries, and the distance and angles were measured from the snapshots. Figure courtesy of Dr. Ji Il Choi.

The electronic density of states (DOS) were studied to further elucidate the electronic structure of PPD/rGO and MPD/rGO systems. Projected electron density of states (PDOS) provided information about the electronic DOS at given energy levels, or the specific energy level of contributing atoms, particularly at the Fermi level in this study. As depicted in Figure 3.21, total DOS of PPD and MPD/rGO presented an identical feature in the DOS near the Fermi level. However, it was found that nitrogen 2*p* orbital of the PPD molecule contributed to a higher electron density at the Fermi level compared to that of MPD. The results also indicated that electronic energy levels were dependent on the position of amine groups on PD molecules.

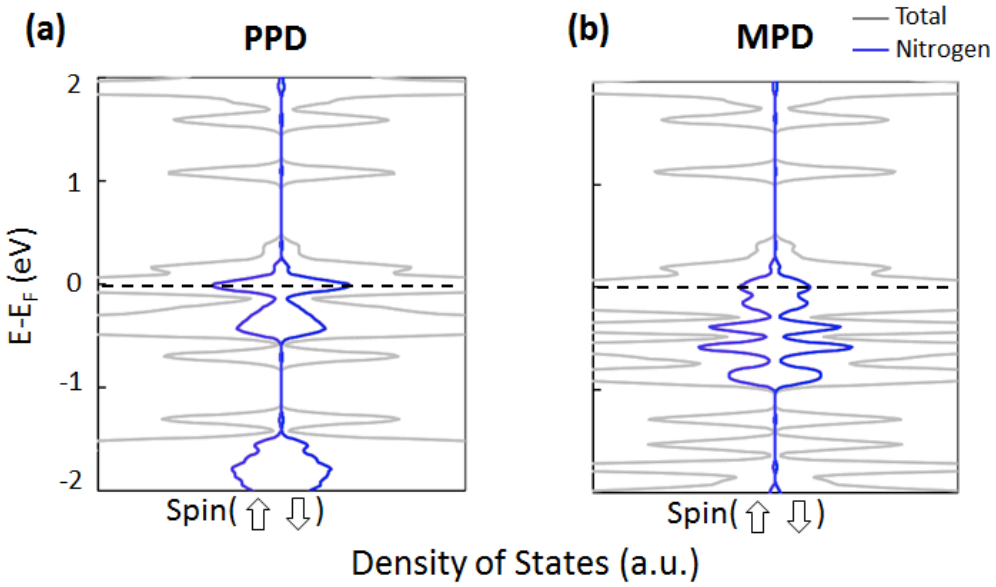

Figure 3.21 Electron density of states near the Fermi level for the (a) PPD/rGO and (b) MPD/rGO. Nitrogen 2*p* orbital of PPD shows well-developed DOS at the Fermi level compared to that of MPD. The Fermi level is adjusted to zero. Figure courtesy of Dr. Ji Il Choi.

3.4 Conclusions

Three phenylene diamine isomers were used to fabricate chemically modified graphene networks with various structural and electrochemical features. With different molecular geometries, PPD and MPD molecules could efficiently enlarge graphene interlayer spacing to 1.41 nm and 1.30 nm respectively; while OPD molecules showed disorderly bonded or non-covalently bonded structures. Simulated XRD analysis was in good agreement with the experimental measurements and predicted the prominent curved surface morphology of OPD/rGO. Among the three PD/rGO structures, PPD/rGO presented the highest specific capacitance of 422 F/g, which can be attributed to the synergistic effect of well-spaced graphene configuration, multiple redox transitions and rapid charge transport through the graphene networks. In comparison, the lower

capacitance of MPD/rGO could be explained by the limited number of redox transitions for pseudocapacitance, and the disordered/aggregated structure led to the poor capacitive properties of OPD/rGO. DFT calculations were performed to further investigate the electronic structures of PD/rGOs. The unit binding geometry study showed that the interactions of the PPD molecules within graphene networks produced a continuous electron density distribution, while interaction of MPD molecules produced anisotropic binding geometries showing weak interaction features. In addition, electron density of states for nitrogen 2*p* orbitals showed that more amplified electron density states existed at the Fermi level of PPD/rGO compared to those of MPD/rGO. The comprehensive understanding of conjugated PD/rGO networks will be beneficial for the design of graphene-based covalent organic frameworks (COFs) for energy storage applications.

CHAPTER 4. FLEXIBLE MICRO-SUPERCAPACITORS AS MINIATURIZED ENERGY STORAGE DEVICES

4.1 Introduction

In an attempt to miniaturize the energy storage units for flexible and portable electronics, micro-supercapacitors (MSCs) have been recently developed with excellent electrical and mechanical compatibilities [196, 99, 100, 197]. In contrast to traditional sandwich assembled supercapacitors, MSCs are based on two-dimensional interdigitated patterns. The unique design of microelectrode patterns in planar geometry has achieved significant size reduction and superior charge transfer characteristics, which enables the direct integration of MSCs into other electronic devices for high energy and power supplies.

Recently, several fabrication methods have been reported to make micro-supercapacitors using graphene-based materials. El-Gao and Katy et. al. have developed a laser scribing approach to convert graphene oxide (GO) film into interdigitated graphene patterns [198, 149]. Lin *et. al.* have used a combination of chemical vapor deposition (CVD) and lithographic techniques to fabricate graphene/CNT composite [199]. To make bendable and wearable energy storage devices, patterned graphene materials have also been made on a flexible polyethylene terephthalate (PET) substrate [200]. However, the substrate transfer process is complex and difficult to control. Moreover, for some of the aforementioned approaches, the high temperature requirement and photolithographic processing are not cost effective for large-scale production. Therefore, a facile solution-

processible approach at low temperature is highly desirable for cost-effective and scalable MSC fabrication [201].

To achieve the desirable electrochemical properties of the MSCs, a variety of nanostructured materials have been studied. Different carbon structures including onion-like carbon, carbide-derived carbon, carbon nanotubes have been used for EDLCs, while conductive polymers such as polyaniline (PANI) and polypyrrole have been used for pseudocapacitors [99, 100, 202-204]. Graphene has been regarded as an excellent electrode material for EDLCs owing to its superior charge carrier mobility, mechanical strength and large surface area [205, 206, 61]. In addition, a pseudocapacitive material, particularly polyaniline (PANI), has been incorporated into graphene network to form composite materials with improved specific capacitance [207, 208, 129, 209]. For example, it has been reported the covalent grafting of amino groups onto graphene oxide (GO) followed by an *in-situ* polymerization of PANI achieved a maximum specific capacitance of 500 F/g [162, 70]. Non-covalent treatment has also been used to exfoliate graphene sheets via π-π interactions and electrostatic forces between negatively charged conductive polymer and graphene. [210] Despite the unique structural and electrical properties of these graphene/PANI composites, the poor dispersion in aqueous solution poses limitations for its application in MSC fabrication through stencil printing and spin coating. The stable aqueous dispersion is the prerequisite to achieve thin-layer deposition with high uniformity. In this sense, a water-soluble graphene/polyaniline composite will be of great importance for the practical application of the electrode materials in MSC.

In this study, a water-dispersible graphene/sulfonated polyaniline (SPANI) structure (rG/SP) was developed as the electrode material to fabricate flexible micro-

supercapacitors with high energy density using a combination of spin coating, shadow masking, and plasma etching methods. The hydrophilic nature of the rG/SP allows the direct thin-film deposition on a flexible substrate by spin coating without further chemical or thermal treatment, which provides the possibility for fast and large-scale fabrication. Moreover, pre-designed shadow mask was used for the formation of interdigital patterns, which presents obvious advantages over traditional multiple-step photolithography processes. The as-fabricated rG/SP-MSC delivered an ultrahigh volumetric capacitance of 16.55 F/cm^3 with excellent cycling performance. Remarkably, the flexible MSC device also demonstrated exceptional electrochemical stability under multiple bending and twisting cycles, which presents tremendous suitability for flexible and portable energy storage.

4.2 Experimental

4.2.1 Materials preparation

GO was prepared using the Hummers' method. SPANI was synthesized by sulfonation of emeraldine salts as previously reported [211, 212]. In a typical process, emeraldine salts were prepared by oxidizing aniline monomer in 1.2 M hydrochloric acid. The resulting emeraldine salts (3g) were sulfonated by 7.27 g chlorosulfonic acid in 100 ml 1,2-dichloroethane at 80°C for 5 h followed by hydrolysis in 150 ml water at 100°C for 4 h. Finally, the concentrated precipitates were washed by acetone and water, and dried under at 55°C overnight. For the rG/SP composite, 100 mg GO and 200 mg SPANI were dispersed in 100 ml DI water by sonication. Thereafter, 1 ml of hydrazine monohydrate was added to the water suspension of GO and SPANI and the suspension was stirred at 80

°C for 12 h. After cooling to room temperature, the rG/SP composite was obtained by vacuum filtration, washed repeatedly with water, and dried in oven at 55°C overnight. The effect of SPANI loadings into graphene structures was also investigated to optimize the electrochemical performance.

Carboxylated graphene with good dispersion stability in aqueous solution was also prepared and used as the thin film materials for MSC. Highly conductive graphene powders were purchased from Institute of Coal Chemistry, Chinese Academy of Science. For carboxylated graphene (C/G) synthesis, 100 mg of graphene were added into an oxidizing solution containing 6 ml of concentrated sulfuric acid (98%) and 2 ml of nitric acid (70%), and stirred at room temperature for 1 h. The resultant C/G was washed repeatedly with copious amount of water by filtration and dispersed in water as stock solution before use. The fabrication processes to make C/G-MSC were the same as described previously.

4.2.2 Fabrication of interdigitated patterns

Kapton® FPC (flexible printed circuit) film (125 μm) was used as the flexible substrate, and treated in UV-Ozone (Novascan) chamber for 30 min before use. The rG/SP dispersion was sonicated for 1 h and spin coated (1000 rpm, 30s; MTI Corp.) on a UV treated Kapton substrate. A stainless steel stencil with a 10-finger interdigital pattern (250 μm finger width, 350 μm interspacing, MiniMicroStencil Inc.) was used as a shadow mask. To fabricate the current collector, 10 nm Ti (adhesion layer) and 200 nm Au were subsequently deposited on the rG/SP film by a Denton Explorer electron-beam evaporator at a rate of 3 Å/s. Then the remaining films uncovered with Au were etched away by O_2-plasma in a Plasma-Therm RIE system for 10 min (250 W, 100 mTorr). Finally, 10 wt%

H_2SO_4/PVA electrolyte was drop-casted on the microelectrodes and dried overnight to form the gel.

4.2.3 Materials and electrochemical characterizations

SEM (Leo 1550), TEM (Joel 1000) and AFM (Veeco Dimension Edge) were used to image the morphology of rG/SP. Optical images of the interdigital patterns were taken from LEICA DC 3000 microscope. Raman and FTIR spectra were obtained from LabRAM ARAMIS, HORIBA JOBIN YVON with 532 nm laser and Nicolet, Magna IR 560, respectively. XPS was conducted using Thermo K-Alpha XPS. Thermogravimetric analysis (TGA) was carried out on TGA-2050 analyzer (TA Instruments Co). Conductivity measurement was performed using Lucas Labs S302 four probe system. Cyclic voltammetry (CV), charging/discharging (CD), and electrochemical impedance spectroscopy (EIS) were measured on a Versastat 2-channel system (Princeton Applied Research). CV tests were conducted at scan rates from 2mV/s to 5000mV/s and EIS was examined at a frequency range from 100 kHz to 10 mHz.

The device capacitance (C_{device}) of the MSC was calculated from CV data according to

$$C_{device} = \frac{\int IdV}{2vV} \tag{11}$$

where v is the scan rate, V is the voltage range, and I is the current. The specific areal capacitance (C_{area}) and volumetric stack capacitance (C_{volume}) were calculated based on

$$C_{area} = \frac{C_{device}}{A} \tag{12}$$

$$C_{volume} = \frac{C_{device}}{V} \tag{13}$$

where *A* is the entire surface area of the device including the area of the microelectrodes and the gap between them, and *V* is the volume of the device considering the thickness of microelectrodes and current collectors. The energy and power densities were calculated according to Equation (4) and (7), where C_{volume} was used instead C_{cell}.

4.3 Results and Discussion

4.3.1 Deposition and patterning of microelectrodes

Figure 4.1 illustrates the fabrication process of micro-supercapacitors on a flexible Kapton substrate. Due to the hydrophilic nature of the sulfonated polymer, highly conductive rG/SP composite can be directly spin-coated on the UV-Ozone treated substrate to form uniform thin film electrodes. This process does not require further reduction or heat treatment, being low-temperature processable. Furthermore, the use of water to disperse electrode materials is more environmentally friendly than volatile organic solvents. For the interdigital patterns, a gold current collector was deposited on top of rG/SP electrode materials via a specifically designed stencil. The use of a stencil as a shadow mask eliminates the need for the expensive photolithographic operation and avoids the contamination of the electrodes materials in a developer solution during the lift-off process. Finally, the remaining rG/SP thin films at the gaps between gold current collectors were removed by oxygen plasma etching to generate high resolution interdigitated patterns.

The optical and digital images of the patterns with clear edges are shown in Figure 4.2. The conformal and thin layer coating ensures the effective plasma etching and electrical interconnect with the gold interdigits. The thickness of the electrodes can be easily tuned by changing solution concentrations and spin coating speeds. A four-probe test reveals the rG/SP film had a high electrical conductivity of 1100 S/m, which is comparable to reported graphene materials for MSCs [213, 199]. A solution containing 10 wt% of sulfuric acid and polyvinyl alcohol (H_2SO_4/PVA) was used as gel electrolyte by drop casting onto the entire device area. Taking advantages of the 2D porous structures of graphene electrodes, electrolyte ions can easily diffuse into graphene layers and wet the electrodes through the capillary force. After the solvent was evaporated, the electrolyte was solidified and formed into a gel. Notably, the use of all-solid state gel electrolyte reduces the overall packaging size of the in-plane MSC architecture, and enables direct integration into flexible electronic devices, which has superior strengths over liquid electrolytes for manufacturing.

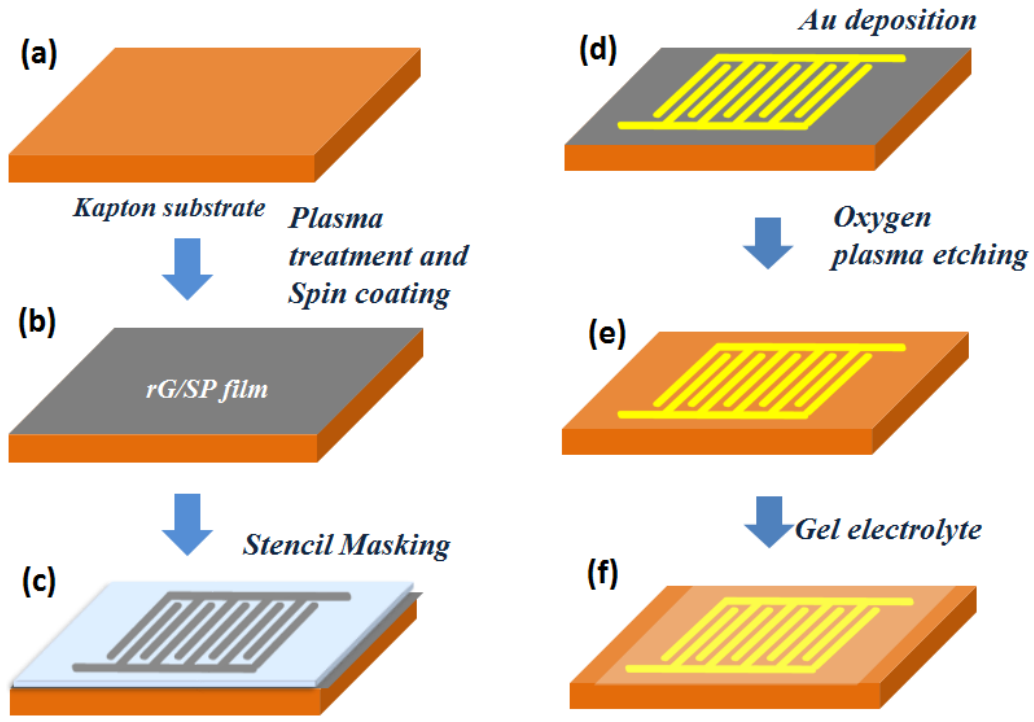

Figure 4.1 Schematic illustration of the fabrication processes of rG/SP micro-supercapacitor. The fabrication procedure includes (a) UV-ozone surface treatment of flexible Kapton substrate, (b) spin coating of rG/SP suspension to form thin film on substrate, (c-d) shadow masking and electron-beam evaporation to deposit gold-current collectors; (e) plasma etching, and (f) drop casting of PVA/H_2SO_4 gel electrolyte.

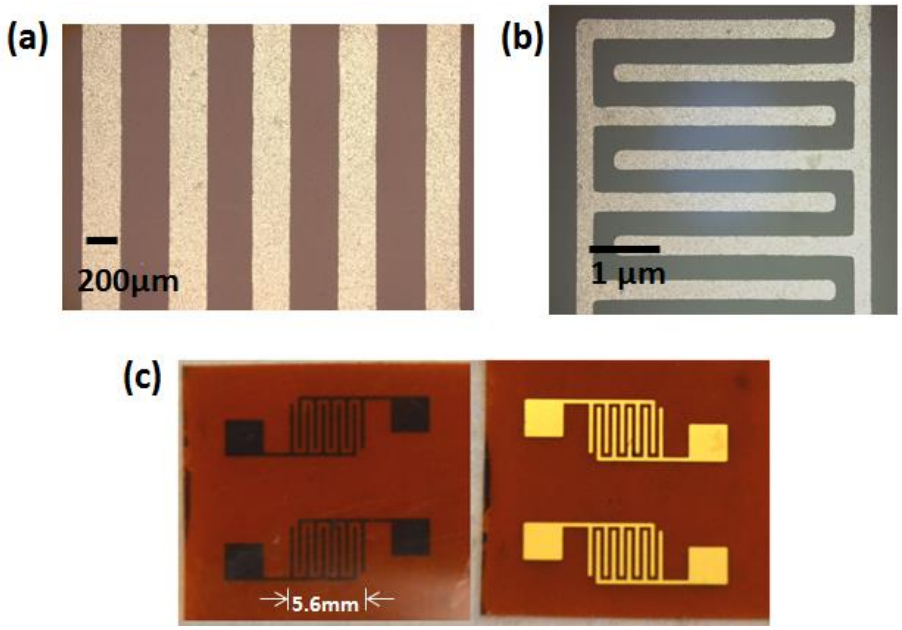

Figure 4.2 (a-b) Optical images of the interdigital patterns; (c) digital image of the back side (left) and front side (right) of the as-fabricated rG/SP-MSC.

4.3.2 Material properties

The morphology of the rG/SP microelectrode materials was characterized by SEM, TEM and AFM. As shown in Figure 4.3a, the cross-section image clearly reveals the uniform deposition of rG/SP thin film electrodes with highly porous structure at edges (magnified view in inset). The intercalation of SPANI can tune the curvature of rGO sheets and increase the degree of porosity. The average thickness of the microelectrodes (including gold current collector) is (2±0.5) µm, estimated from the cross-sectional SEM image. Under TEM (Figure 4.3b), the darker area covering the entire sample area can be clearly visualized, which is attributed to the intercalation of SPANI nanostructure between graphene sheets. The relatively low contrast image implies small thickness and efficient exfoliation of graphene structure upon modification.

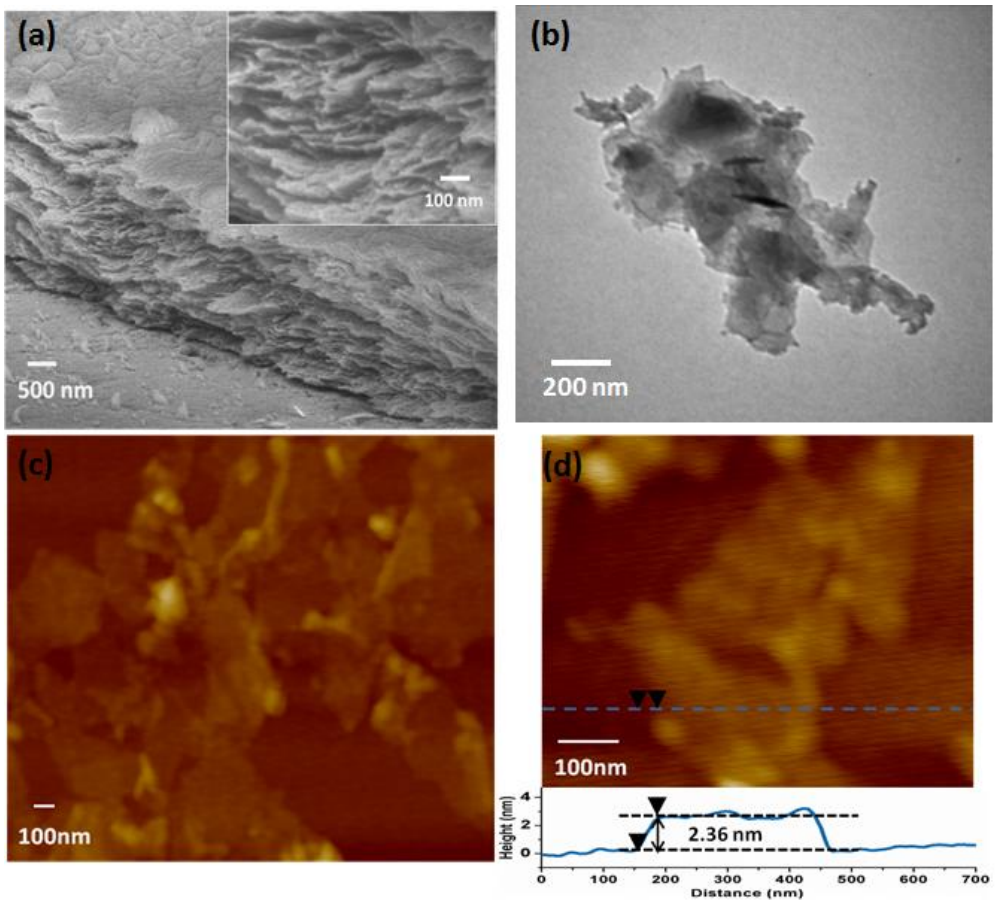

Figure 4.3 (a) Cross-section SEM images of the deposited rG/SP microelectrodes on Kapton susbstrate with a magnified image in the inset; (b) TEM image of the rG/SP composite; (c-d) AFM images of the rG/SP composite and the height profile of an individual rG/SP flake.

Surface texture of the rG/SP is investigated by AFM (Figure 4.3c), which exhibited individual and stacked layers of graphene sheets with sharp edges. The SPANI nanostructures was found to be uniformly distributed on graphene layers and no phase separation was observed. The stabilizing effect of the strong π-π interaction between SPANI and graphene mainly accounts for the homogeneous distribution of polymer intercalated within graphitic layers. A typical single rG/SP flake was shown in Figure 4.3d. From the corresponding height profiles, the SPANI coated graphene had an average thickness of 2.36 nm, which had a two-fold increase compared to that of GO flake. The

increased thickness of the rG/SP sheets is mainly due to the incorporation of SPANI polymer structures, which serves to expand the graphene interlayer spacing between graphene sheets and provide more surface area to facilitate ion diffusion and storage.

Figure 4.4a shows the thermal profiles of GO, rGO and rG/SP in N_2 at a heating rate of 10°C/min. The weight derivative values as a function of temperature was also obtained (Figure 4.4b) to display the transition temperatures. It can be seen that GO was thermally unstable and a significant weight loss was observed at 200°C due to the release of liable oxygen-containing functional groups [214, 215]. For a pure SPANI, the initial structural deposition occurred at ~ 180°C. In comparison, the rG/SP composite showed higher thermal stability with only 10% weight loss at temperatures between 230°C and 350°C, which corresponds to typical decomposition of the SPANI polymer chains. The higher degradation onset temperature indicates the improved structural stability of the SPANI when intercalated into the graphene network. For the graphene-based materials, the gradual weight loss above 600°C is attributed to the decomposition of graphene structure.

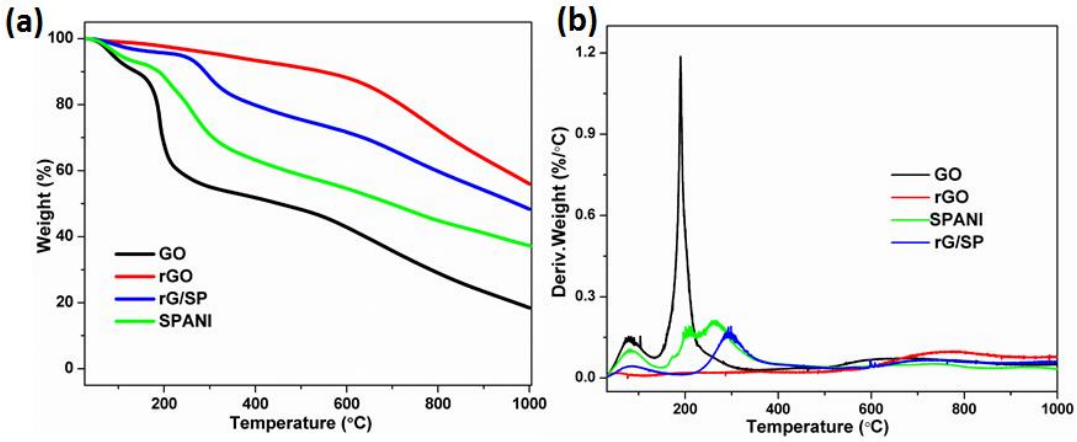

Figure 4.4 (a) TGA and (b) derivative weight curves of GO, rGO, SPANI, and rG/SP in N_2 at a heating rate of 10°C/min.

Figure 4.5a shows the Raman spectrum of GO, rGO and rG/SP. It can be seen that all these materials exhibited a prominent D peak at 1350 and G peak at 1590 cm^{-1} [216, 70]. The intensity ratio, I_D/I_G, is commonly used to evaluate the level of disorder in graphene materials. The small difference in I_D/I_G ratio between rG/SP and rGO indicates that the incorporation of SPANI structure through non-covalent functionalization triggers a negligible structural change to graphene [217, 153]. FTIR spectra are presented in Figure 4.5b to illustrate the chemical bonding. After the hydrazine reduction and SPANI functionalization, the peak for carbonyl groups diminished and three distinctive peaks appeared. The sharp C-N stretching band at 1300cm^{-1}, the benzoid and quinoid ring vibrations at 1465 and 1564 cm^{-1} confirms the presence of polyaniline in the composite [74].

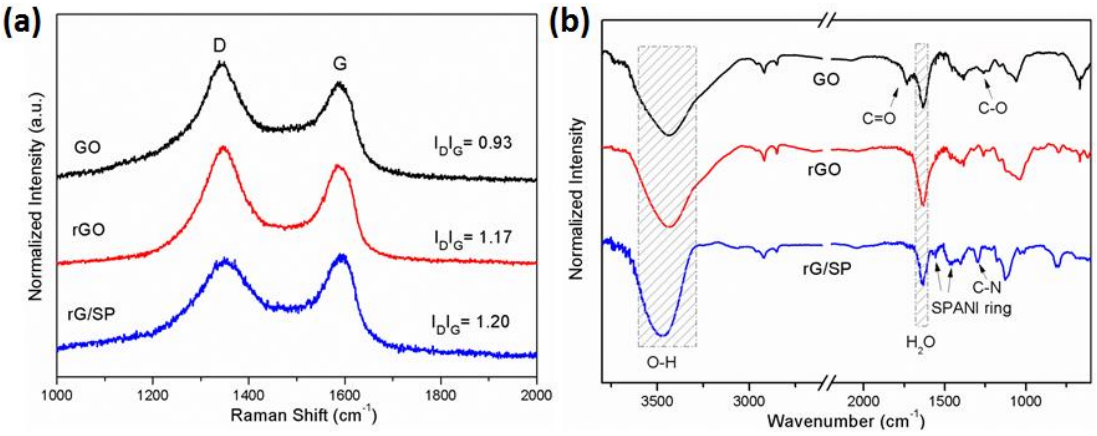

Figure 4.5 (a) Raman spectra and (b) FTIR spectra of GO, rGO, and rG/SP.

XPS was used to further characterize chemical structure and composition of rG/SP composite. From a survey spectrum (Figure 4.6a), the nitrogen content was determined to be 5.37%, which gives an estimated ~42% mass loadings of SPANI nanostructure in the overall composite. In Figure 4.6b, peak deconvolution of C1s spectrum shows a dominant

peak at 284.5 eV (C-C), with three oxygen and nitrogen containing functional groups at higher binding energies. The N 1s spectrum (Figure 4.6c) was also deconvoluted to illustrate the oxidation states of the doped polyaniline, with 69.4% benzoid amine (-NH-) at 399.7 eV, 20.5% quinioid amine (=N-) at 398.5 eV and 10.1% cationic radicals (=N^{+}H-) at 401.1 eV. Considerable amount of the quinoid amine structure enhances the electrical conductivity of the conductive polymer. In addition, the electroactive N cations, stabilized by the negatively charged graphene scaffold, can serve to create more efficient electron transfer pathways between graphene sheets. The small amount of S2p peak, with an atomic percentage of 1.79%, confirms the sulfonation of emeraldine salts. The elemental analysis provided a quantitative degree of sulfonation with a sulfonated group per three monomer units. As shown in Figure 4.6d, the S2p spectra can be split into two spin-orbit components, $S2p_{3/2}$ and $S2p_{1/2}$, at binding energies of 167.8 and 168.8 eV respectively, which can be assigned to sulfur elements in sulfonate groups [218].

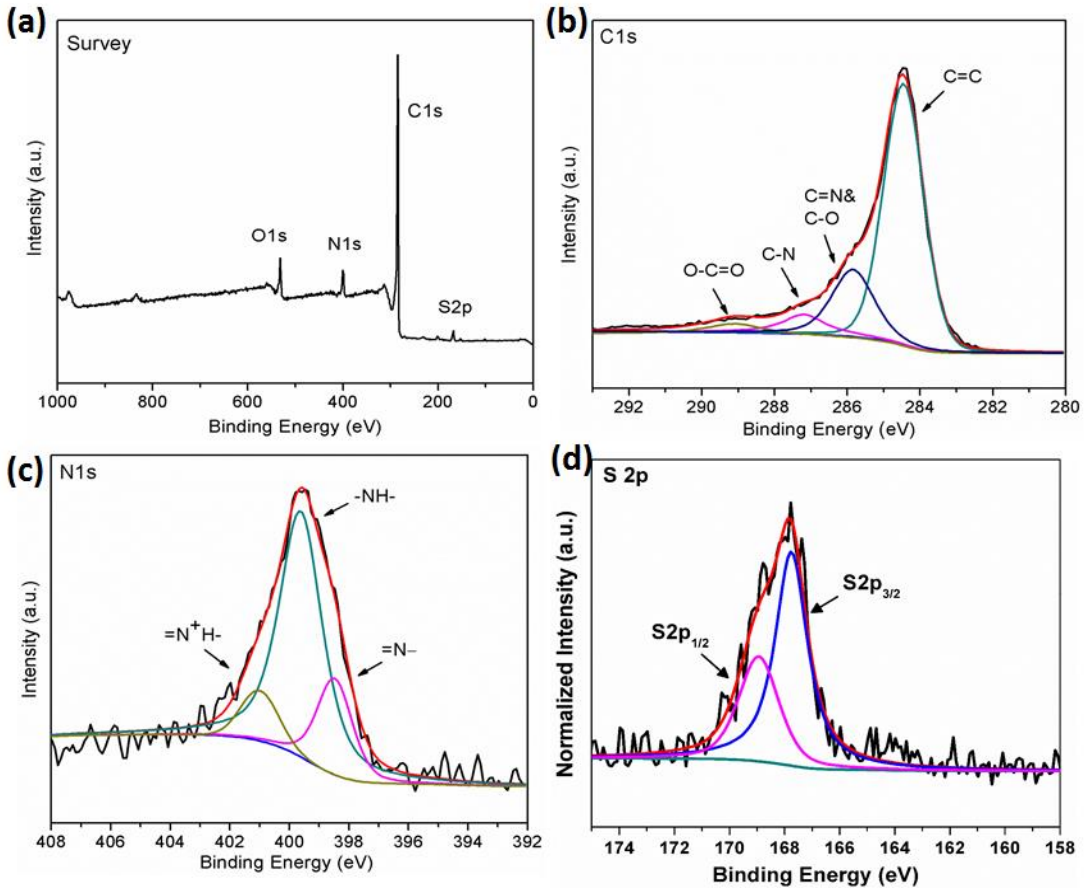

Figure 4.6 XPS (a) survey, high resolution (b) C1s, (c) N1s, and (d) S2p spectra of rG/SP.

4.3.3 Electrochemical properties

To optimize the compositions of rG/SP structures for best capacitive properties, the loadings of SPANI was tuned by varying the precursor ratios between SPANI and GO. The specific capacitance of different rG/SP thin film electrodes in 1 M H_2SO_4 electrolyte is shown in Figure 4.7. The maximum capacitance of 262 F/g was achieved at scan rate of 2 mV/s when the initial SPANI to GO ratio was 2:1. At this optimized precursor ratio, SPANI nanostructure intercalated within rGO sheets not only enhanced the interlayer spacing to accommodate charges, but also provided multiple charge transfer pathways between graphene layers to maximize the capacitance. Additional loadings of SPANI may cause

agglomeration of the conductive polymer, thus reducing ion accessible surface area of the active materials and impairing charge transfer process at the graphene/SPANI interface.

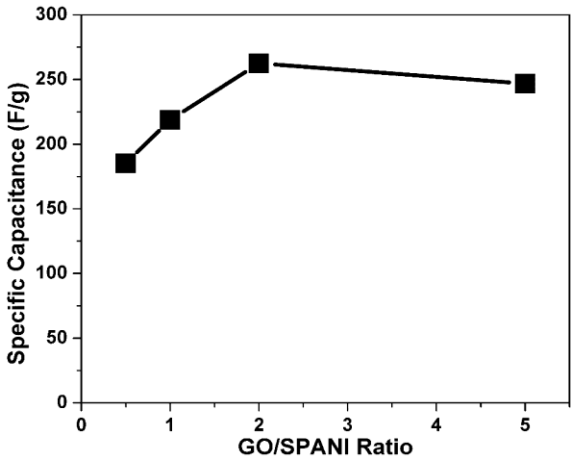

Figure 4.7 Specific capacitance of the rG/SP structures made from different precursor ratios in 1 M H_2SO_4 electrolyte.

The rG/SP electrode was also tested in 6 M KOH electrolyte for electrochemical study. As shown in Figure 4.8, the redox peaks associated with the N-containing functionalities become less obvious compared with that in acidic medium. In addition, the maximum specific capacitance was 228 F/g at 2mV/s, lower than the value in H_2SO_4 electrolyte. The phenomenon can be explained as the SPANI changes from doped emeraldine salts to undoped emeraldine base form in basic electrolyte, and the deprotonation process traps the free charge carrier for energy storage [219].

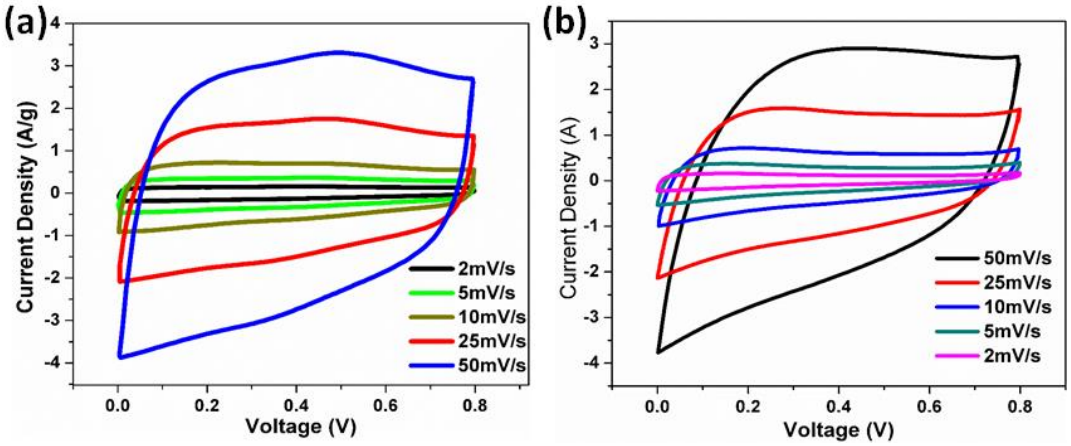

Figure 4.8 CV curves of rGO/SP thin film electrodes (optimize ratio) in (a) 1 M H_2SO_4 and (b) 6 M KOH electrolytes.

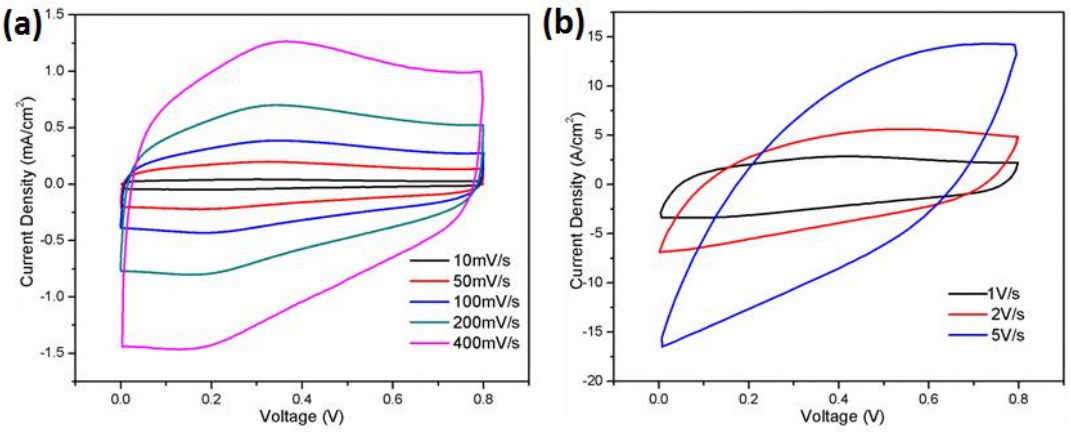

Figure 4.9 CV profiles of rG/SP-MSC at scan rates of (a) 10 - 400 mV/s and (b) 1, 2, 5 V/s in PVA/ H_2SO_4 gelled electrolyte.

The electrochemical performance of the rG/SP-MSC devices using 10 wt% H_2SO_4/PVA as gel electrolyte was evaluated by cyclic voltammetry. Figure 4.9 (a-b) show the CV curves with scan rates ranging from 10 to 5000 mV/s. The near rectangular CV curves at different rates imply the EDLC characteristics of the active electrodes. Pseudocapacitive behavior also contributes to the specific capacitance due to the presence of conductive SPANI, which is manifested by a pair of redox peaks at ~0.35V (cathodic) and ~ 0.18V (anodic) in a CV profile. The transformation between emeraldine to

pernigraniline forms of SPANI upon anionic doping/dedoping accounts for the major pseudocapacitive charge transfer in the acidic electrolyte [162]. The reversible Faradaic reactions of SPANI in acidic electrolyte is illustrated in Figure 4.10. The SPANI nanostructure between graphene sheets can provide additional charge transfer pathways and improve the overall conductivity of the thin film electrodes. Moreover, the existence of hydrophilic sulfonated groups also improves electrolyte wetting of the bulk materials. Compared to the traditional supercapacitors in a sandwiched structure, the interdigitated MSC has shorter ionic transport distance between electrodes, thus having the capability to operate at faster charge/discharge rates for instant power delivery.

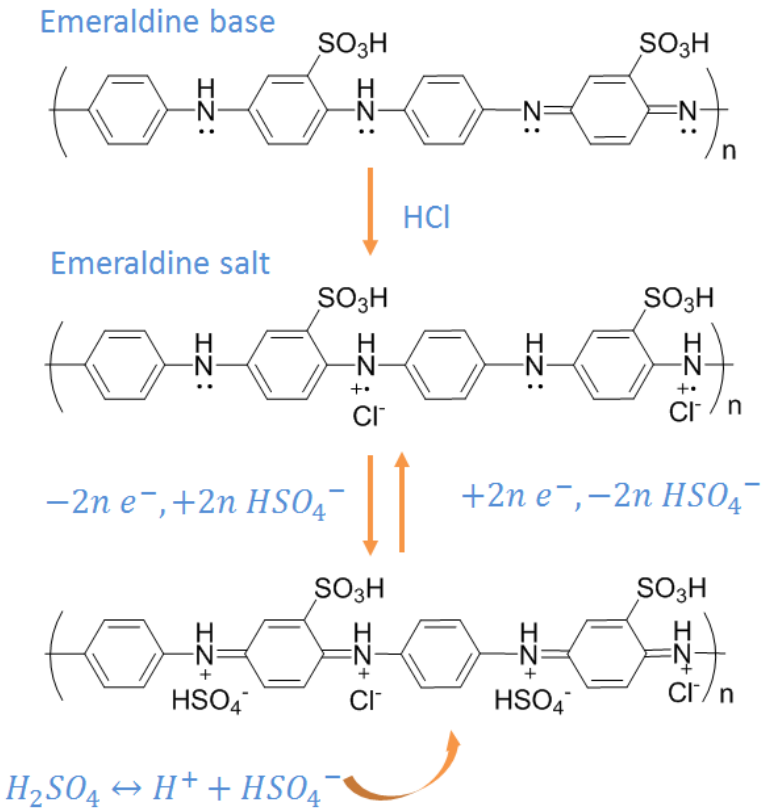

Figure 4.10 Faradaic reactions of SPANI in sulfuric acid electrolyte.

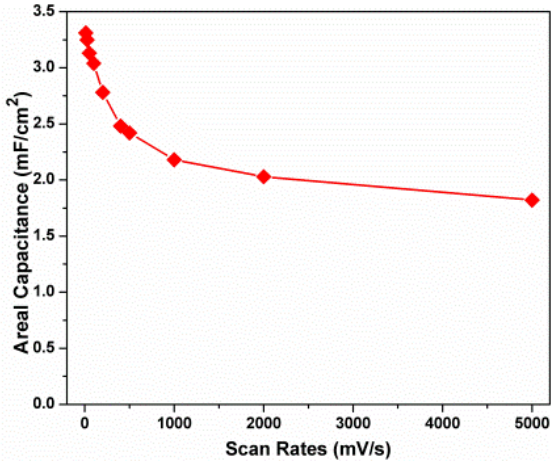

Figure 4.11 Plot of areal capacitance calculated from CV curves at different scan rates.

For in-plane MSCs, the areal and volumetric capacitance values are more frequently used than a gravimetric capacitance to assess its performance. The scan rate dependent areal capacitance is shown in Figure 4.11. It can be seen that the rG/SP-MSC exhibited an ultrahigh areal capacitance of 3.31 mF/cm^2 at 10mV/s. Upon increasing the scan rates, the capacitance values only slightly decreased to 3.13 mF/cm^2 at 50 mV/s, 2.78 mF/cm^2 at 200 mV/s, and 2.03 mF/cm^2 at high scan rates of 2 V/s. The areal capacitance of 2.18 F/cm^2 at a scan rate of 1000 mV/s is greater than the previously reported values at same scan rates, such as 1.7 mF/cm^2 for onion like carbon, 1.6 mF/cm^2 for laser scribed graphene, and 0.87mF/cm^2 for Cu-templated graphene aerogel [100, 149, 128]. Considering the small thickness of the deposited rG/SP microelectrodes, the rG/SP MSC in this study presented ultrahigh volumetric capacitance values of 16.55 F/cm^3 and 10.90 F/cm^3 at 10mV/s and 1000mV/s respectively. The large areal and volumetric capacitance values implies the superior charge storage capability of the composite materials and the structural integrity of the fabricated devices. The rG/SP MSC was also tested in a 1M

H_2SO_4 aqueous electrolyte to verify the similar functionality of the device as in a gelled electrolyte (Figure 4.12).

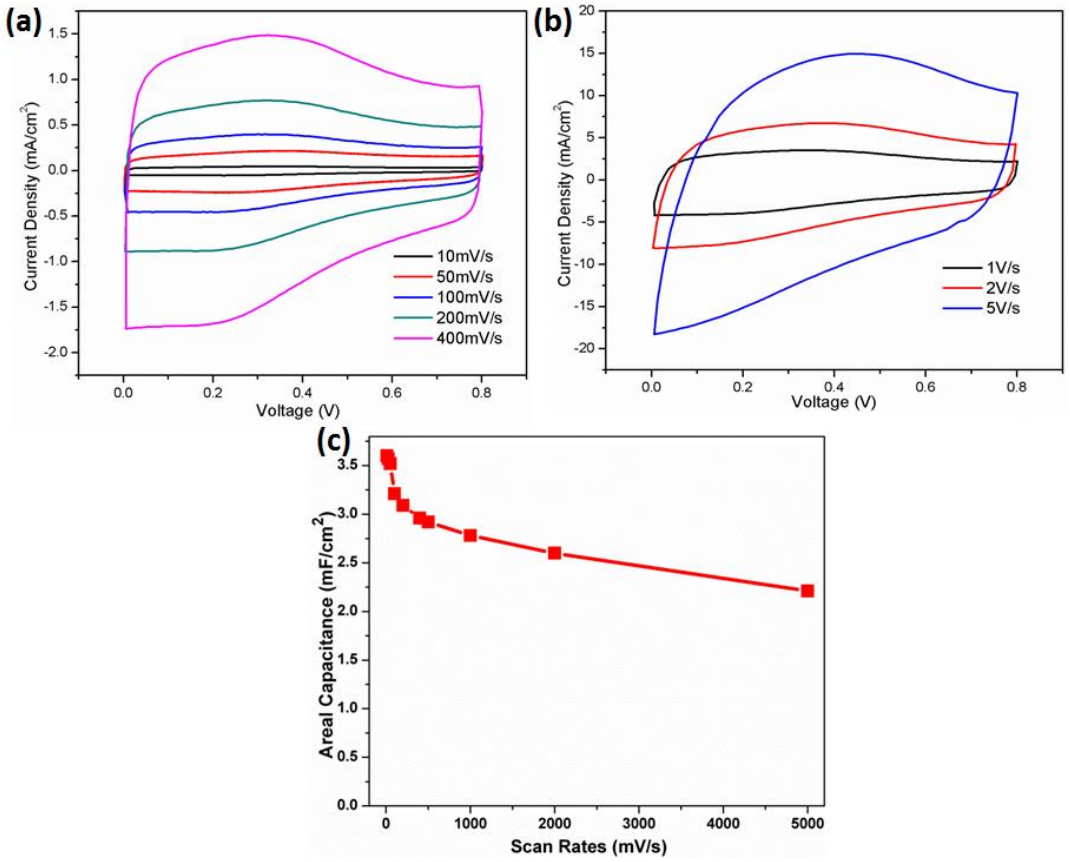

Figure 4.12 (a-b) CV curves of the rG/SP-MSC tested at 1M H_2SO_4 electrolyte and (c) specific areal capacitance values at scan rates from 10mV/s to 5V/s.

Figure 4.13a shows the galvanostatic charge/discharge curves at different current densities. The linear lines and symmetric triangles of the curves reflect the reversible EDL capacitance characteristics of the rG/SP electrodes. The relative low voltage drops at the start of discharging process indicates a small internal resistance of the electrode/electrolyte system. PANI based supercapacitor electrodes often shows rapid capacitance degradation duinrg cycling due to structural instability. For the rG/SP structure, the superior mechanical strength and flexibility of graphene network serve as a robust template to anchor

conductive polymers and tolerate their structural changes. Cycling stability of the rG/SP-MSC electrodes were tested in same electrolyte at 2 mA/cm^2. Figure 4.13b shows that more than 85.4% of the capacitance was retained after 10,000 cycles, which demonstrated improved cycling performance compared with other graphene/PANI composite materials. [129, 220, 221]

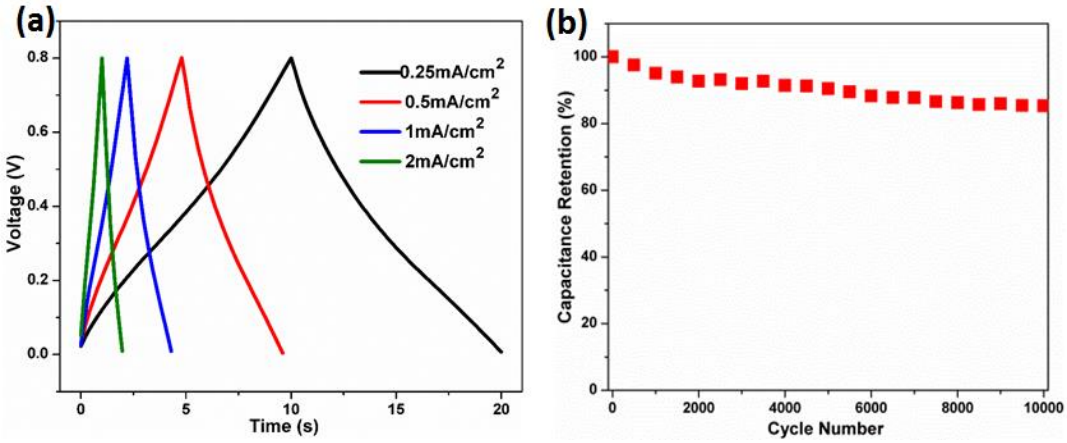

Figure 4.13 (a) Galvanostatic charge/discharge curves at current densities from 0.25mA/cm^2 to 2mA/cm^2; (b) capacitance retention for 10k charge/discharge cycles.

Electrochemical impedance spectroscopy was used to study the internal resistance and charge transfer behavior of rG/SP-MSC in a frequency range from 100,000 Hz to 0.01 Hz. According to the Nyquist plot in Figure 4.14a, the series resistance obtained from the intercept on a real axis is 14.17 Ω, which was smaller than rGO-based MSC reported in literature.[200, 128, 108] This low ESR implies the high conductivity of the composite and excellent electrical contact at the electrode/current collector interface. At the mid-to-low frequency region of the plot, the near vertical line with regards to the Z' axis corresponds to an almost ideal capacitive behavior of the device. At a high frequency range (inset Figure 4.14a), the lacking of semicircular shape for rG/SP-MSC verifies the short ionic diffusion pathway in the interdigital structure [222]. The efficient charge transfer process is also

attributed to the intercalation of conductive SPANI nanostructures between graphene sheets. The frequency response of the rG/SP-MSC is illustrated in Figure 4.14b. According to the Bode phase plot, the characteristic frequency f_0 at phase angle of -45° was found to be 12.6 Hz. The corresponding time constant τ_0 was determined to be 79.4 ms ($\tau_0 = \frac{1}{f_0}$), which indicates that MSC device can be fully discharged to deliver power within an ultrashort period.

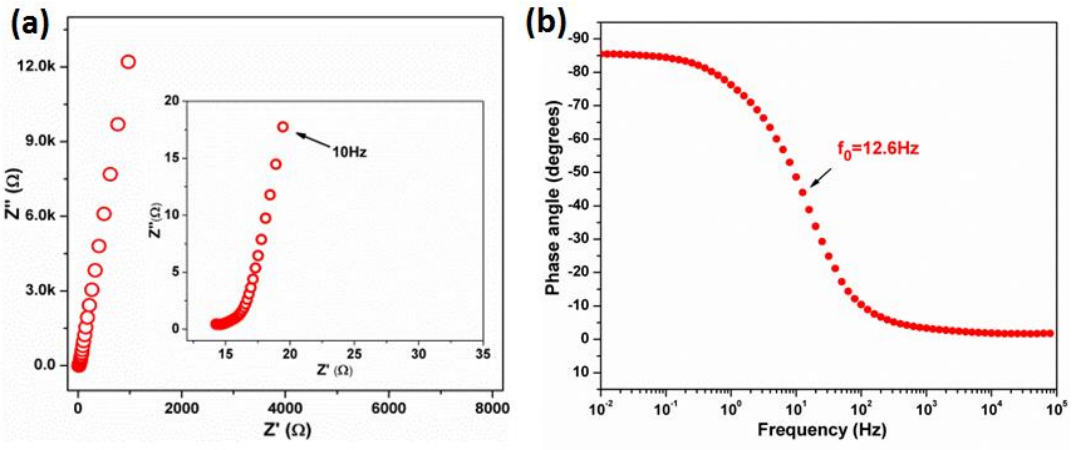

Figure 4.14 (a) Nyquist plots of the electrochemical impedance behavior with a magnification of high frequency region in the inset; (b) bode phase plot as a function of frequency for the rG/SP-MSC. The f_0 represents the frequency at phase angle of -45°.

Figure 4.15 shows the Ragone plot comparing the energy and power densities of various energy storage devices for microelectronic applications, including commercial lithium thin-film batteries (4 V/500 mAh), electrolytic capacitor (63V/220μF), and other types of micro-supercapacitors [213, 100, 200]. Remarkably, the rG/SP-MSC in this study delivered a maximum volumetric energy density of 1.51 mWh/cm^3, which is 20 times higher than that of electrolytic capacitors and 5 times higher than that of conventional supercapacitors (3.5V/25mF). In addition, rG/SP-MSC showed superior energy density in

comparison with other MSC devices fabricated via laser scribing (LSG-MSC, PVA/H_2SO_4) and electrospray deposition (rGO-CNT, 3M KCl) [199, 149]. Moreover, rG/SP micro-device also exhibited a considerably higher power density (3 orders of magnitude) than that of lithium-ion batteries. With extraordinary energy and power densities, MSC devices have become promising energy storage solutions for miniaturized consumer electronic devices.

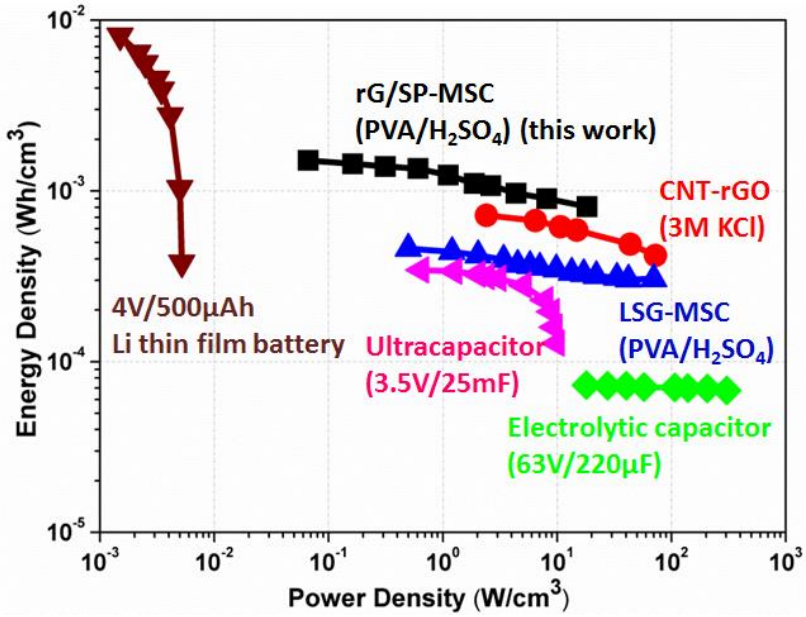

Figure 4.15 Ragone plots of the rG/SP-MSC compared with other energy storage systems, including commercially available lithium-ion batteries, electrolytic capacitors, conventional ultracapacitors, and micro-supercapacitor devices based on CNT-rGO and laser scribed graphene.

4.3.4 Flexible and foldable energy storage devices

For flexible energy storage device applications, the performance of rG/SP-MSC under mechanical strains was presented. The selected Kapton substrate was specifically designed for flexible printed circuits with strong adhesion and high resilience. Figure 4.16a shows the CV curves of our MSC device examined at different bending angles at 50mV/s.

The device showed a remarkably high electrochemical stability with 98.5% and 98.3% of the capacitance retention at 60° and 180° bending angles, respectively. A photograph of the rG/SP- MSC device under bending is shown in Figure 4.16b (inset). The mechanical durability of the devices was also studied under bending and twisting at 90° for 2000 cycles. In Figure 4.16b, it can be seen that 96.5% of the initial capacitance was retained after 2000 bending and twisting cycles. The strong physical adhesion of the microelectrodes to the flexible substrate and the robust SPANI-intercalated graphene network both serve to ensure the high electrochemical performance of the device upon mechanical deformations.

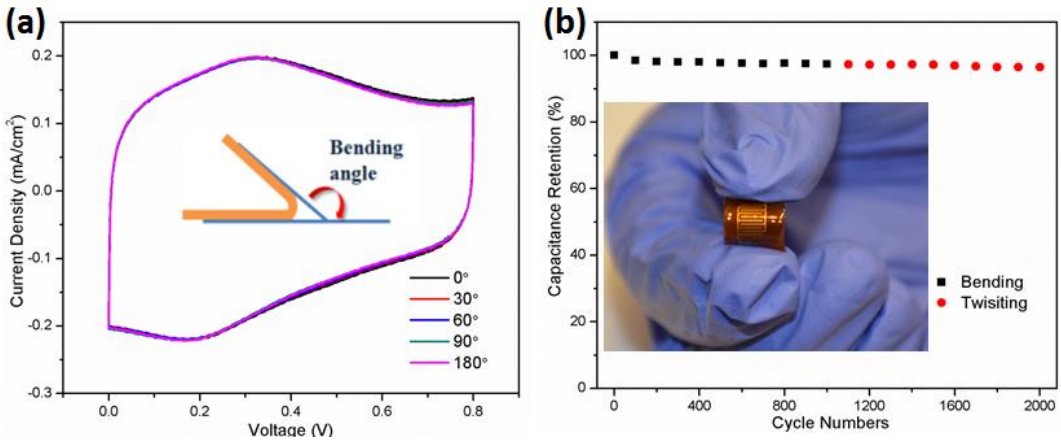

Figure 4.16 (a) CV performance of the device with different bending angles tested at 50mV/s; (b) capacitance retention of the devices under 2000 cycles of bending and twisting tests (a photograph rG/SP-MSC at bent condition shown in inset).

The development of flexible energy storage devices can be extended to make deformable and foldable components at systematic level. Inspired by the paper origami (Miura folding) technique, a foldable MSC prototype was fabricated as a proof-of-concept [223]. Conventionally, Miura-origami patterns were used to design telescope lenses, solar cell arrays, surgical devices, and other functional structures [224-227]. Using Miura

folding, a flat surface can be made into various deformable three-dimensional structures by folding along the designed creases [228]. The MSC units can be attached onto the smaller-area parallelograms and electrically connected for operation. The art of Miura folding can enable the MSC devices with increasing areal energy density under folding conditions.

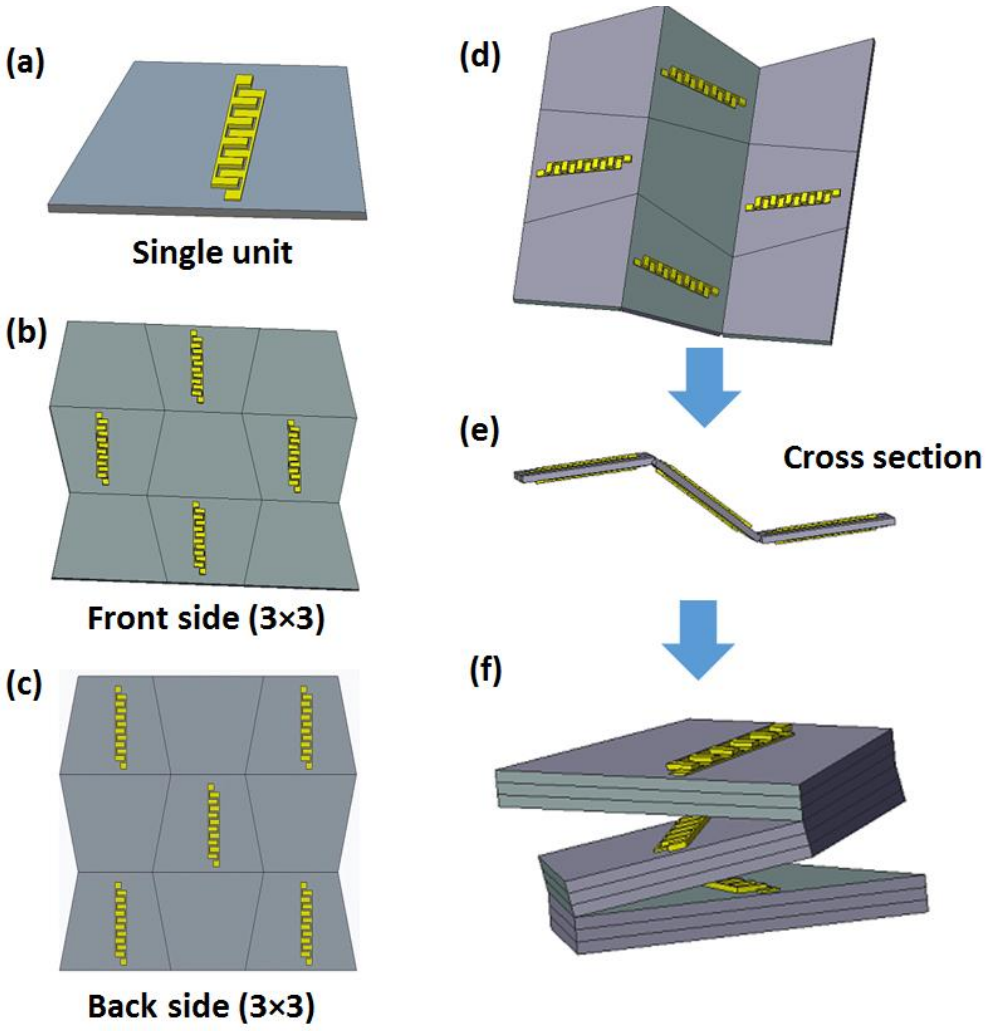

Figure 4.17 Schematic illustration of a 3×3 foldable MSC arrays designed by Miura folding (electrical connection is omitted here for clarity).

The schematic illustration of a foldable MSC array design (3 by 3) is shown in Figure 4.17. In the Miura folding pattern, identical trapezoids were connected by creases

and became compressible under the folding. The foldable MSC arrays were constructed by placing single MSC device on a flat paper surface comprised of Miura folds, and connected in series/parallel combinations. It was noted that MSC patterns were placed in the diagonal direction on one side (front side) with the other patterns on the other side (back side) to avoid the direct contact of adjacent MSC units upon folding. Individual MSC unit was electrically connected by flexible silver paste.

Figure 9 shows the charge/discharge profiles of a 3×2 and 3×3 tandem MSC arrays with 3 in series and 3 in parallel configurations by Miura folding. The near triangular curves indicated that the excellent capacitive properties were maintained as in single MSC unit. In addition, the series connection tripled the operation voltage up to 2.4 V while the parallel connection tripled the discharge time. More importantly, the foldable design allowed a dramatic increase in specific areal capacitance. For single MSC unit based on C/G microelectrodes, the areal capacitance calculated from charge/discharge curves was 2.17 mF/cm^2 at 0.25 mA/cm^2 and 1.69 mF/cm^2 at 1 mA/cm^2. The areal capacitance of MSC arrays with 3×2 and 3×3 Miura folds was 9.33 mF/cm^2 and 13.24 mF/cm^2 respectively at same scan rate, which increased by a factor of 4.3 and 6.1 compared with the MSC units built in a flat substrate. Moreover, the foldable MSC arrays delivered much higher energy density with tunable control on charging/discharging rates. The foldable MSC arrays (3×3) delivered a high energy density of 8.3 μWh/cm2 at a power density of 22.1 mW/cm^2.

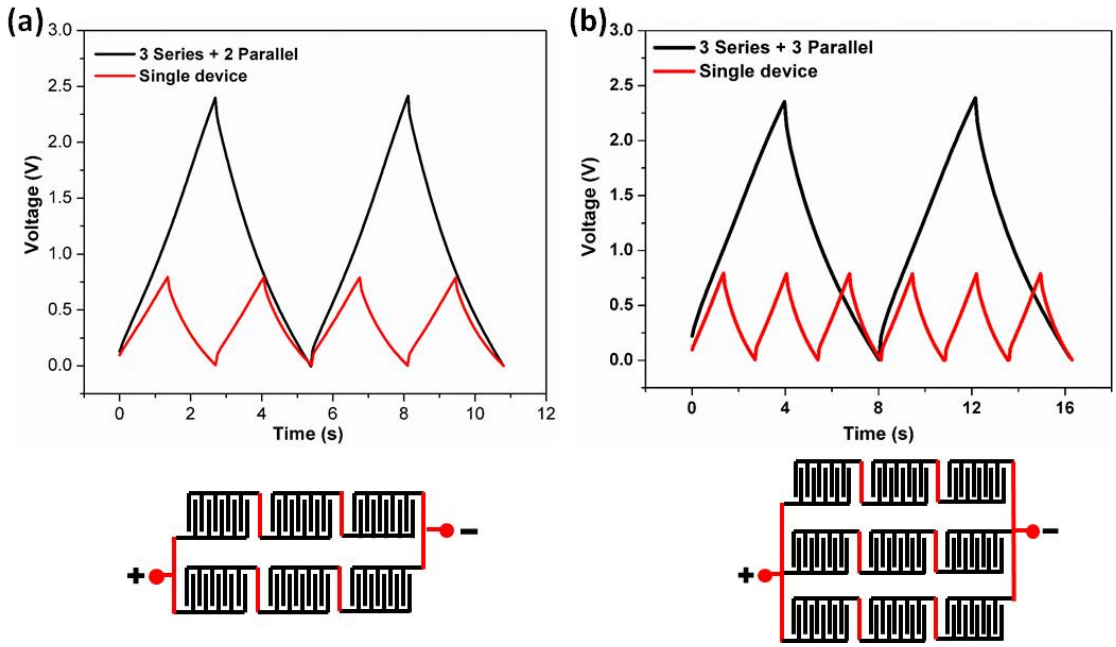

Figure 4.18 Charge/discharge curves for MSC arrays constructed by (a) 3×2 and (b) 3×3 Miura folding pattern connected in a combination of in series and in parallel configurations.

4.4 Conclusions

In summary, flexible solid-state MSCS have been successfully fabricated based on highly conductive and aqueous dispersible rG/SP and C/G as microelectrode materials. The newly developed fabrication processes included the utilization of a microstencil for interdigital patterning, which obviates the need for complicated photolithography and presents great prospect for large-scale fabrication. The as-fabricated micro-device has shown a maximum electrical conductivity and ultrahigh volumetric capacitance of 16.55 F/cm^3. Remarkably, the excellent structural and electrochemical integrity under mechanical deformations brings the micro-devices more promising for wearable electronic applications. Moreover, the concept of Miura folding has be used to make foldable MSC arrays. The preliminary results indicated that the foldable MSC arrays have delivered

higher areal capacitance and energy density with tunable operation voltage and charging/discharging rates. For further improvement of the foldable structure, optimizations should be made on electrode and interconnection materials to enhance the conductivity and reliability of the interdigitated circuits under folding.

CHAPTER 5. EFFECT OF POLYMER BINDERS ON GRAPHENE-BASED FREE-STANDING ELECTRODES

5.1 Introduction

Carbon nanomaterials, such as activated carbon (AC), carbon nanotube (CNTs), and graphene, have been applied as electrode materials for EDLCs to accommodate large ion adsorption on electrode surface [229]. To fabricate high density thin film electrodes, carbon particles or graphene sheets have to be bridged together by polymer binders to form compact and mechanically stable films. In addition, binders must be inert to electrolytes, be electrochemically stable over wide potential window, and must not impose any degradations to internal structures of electrodes [230]. Generally, polymer binders are electrically insulating and their concentrations are kept at around 5~10 wt%. Excessive amount of binder added can increase the internal resistance and block the open pores of the electrodes for ionic transport, thus lowering down the electrochemical performance of the device [231, 232].

Several quality metrics have been considered for the selection of appropriate binders, such as adhesion strength, hydrophilicity, toxicity, mechanical flexibility and electrical conductivity. Polytetrafluoroethylene (PTFE) and polyvinylidene fluoride (PVDF) are two commonly used inert binders. PTFE has a high operating temperature up to 270 °C, while PVDF can provide strong adhesion to metal current collectors with improved chemical and mechanical stability in carbon pastes [230, 233]. However, problems remain for PVDF including their electrically insulating nature and the necessity to use the toxic organic solvent, N-methyl-2-pyrrolidone (NMP). Therefore, it is of great

advantage to introduce some water-soluble, conductive and environmentally friendly binder for electrode fabrication. Recently, several aqueous dispersible binders have been developed, such as polyvinyl alcohol (PVA), poly (3,4-ethylenedioxythiophene) (PEDOT:PSS), and carboxymethyl cellulose (CMC) [234-237]. Particularly, an elastomeric binder can be made by mixing the stiff CMC with a styrene butadiene rubber (SBR) as thickening agent [238, 239]. In CMC/SBR, the ratio of these two components can be tuned to make the electrodes flexible and compatible with various electrode processing configurations. As a conductive and water-dispersible binder, commercial Eletrodag binder has been formulated containing PVP (primary binder), carbon black, graphite and other additives (detailed compositions listed in Table 5.1) [240]. The introduction of conductive components in binder slurries can improve the conductivity of electrodes while facilitating the electrode mixing process. However, for this multi-component binder, the amount of binder should be carefully adjusted to ensure the best capacitive performance.

Table 5.1 Compositions of Electrodag binder

Components	Water	PVP	Carbon black	Graphite	Additives
wt%	60	5	5	20	10

Previous reports on the binder study have mainly focused on the AC-based electrodes cast on current collectors [241-245]. Due to the unique nanostructures of 2D graphene sheets [246], it is necessary to select optimal binders to make large scale thin film graphene electrodes for supercapacitor applications. In this work, chemically reduced

graphene oxide (rGO) was used as a benchmark material. Four types of binders, PTFE, PVDF, Electrodag and CMC/SBR (Figure 5.1), were employed to fabricate free-standing thin film graphene electrodes and their corresponding structural and electrochemical properties were discussed. Specifically, the effect of binders on surface morphology, crystalline structures, thermal stability, and surface energy of these graphene electrodes were investigated. The electrochemical behavior of the electrodes using different binders were also compared and analyzed in both aqueous and organic electrolytes using a symmetric two-electrode coin cell configuration.

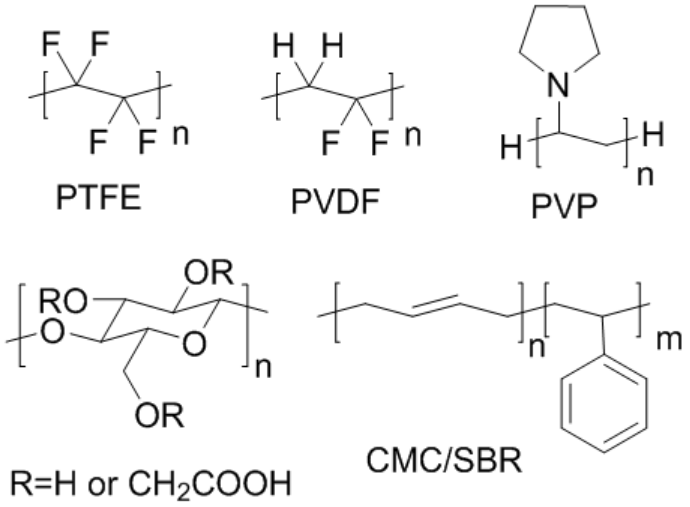

Figure 5.1 Chemical structures of the four types of polymer binders.

5.2 Experimental

5.2.1 Reagents

PTFE condensed liquid binder (PTFE solid content: 60%), PVDF powder, CMC powder, and SBR glue (solidity: 50%) were purchased from MTI Inc. Electrodag EB-012

binder was obtained from Ladd Research Industries Inc. The KOH pellets, tetraethylammonium tetrafluoroborate ($TEABF_4$), N-Methyl-2-pyrrolidone (NMP), and acetonitrile (AN) were purchased from Sigma Aldrich and used without further treatment. The salt and solvent for organic electrolyte ($TEABF_4$ and AN) were stored and processed in a glovebox.

5.2.2 Electrode preparation

To prepare the rGO powders, graphene oxide (GO) was first made by modified Hummers' method, followed by the chemical reduction of GO using hydrazine. Typically, 100 mg of GO was dispersed in 100 mL water and ultrasonicated for 1 h. The 1 mL of hydrazine monohydrate was added into solution. The solution was stirred at 90ºC for 24 h and purified by filtration. The collected powder was dried in oven at 75ºC overnight before use. The synthesized rGO powders had a bulk conductivity around 250 S/m with a few layers of stacking, and the specific surface area was determined to be 170 m^2/g based on BET measurements.

For the binder preparation, a 5 wt% PVDF solution was made by dissolving PVDF power into NMP. For CMC/SBR binder, the weight ratio of CMC: SBR was kept at 1:2 to ensure high binding efficiency and sufficient elasticity. Generally, CMC/SBR mixture were diluted in DI water to make 1.5 wt% aqueous solution. PTFE and Electrodag binder solutions were used without additional treatment. To prepare rGO films, rGO powders were mixed with different binders at 9:1 ratio with respect to the solid content of binders except Electrodag binder. The rGO/binder mixture was thoroughly blended until a uniform paste was formed (Figure 5.2).For Electrodag binder, different rGO to binder ratios were

studied: the best electrochemical performance was achieved for rGO films containing 25 wt% of solid binder content (3.1 wt% PVP). After homogeneous mixing, rGO pastes were sandwiched between two parallel plates and rolled through a rolling machine to make free-standing electrodes with an average thickness of 80 μm. After drying in a vacuum oven, thin film electrodes were punched into a round disk (6 mm in diameter, (2 ± 0.2) mg in mass) before assembled into coin cell for electrochemical testing.

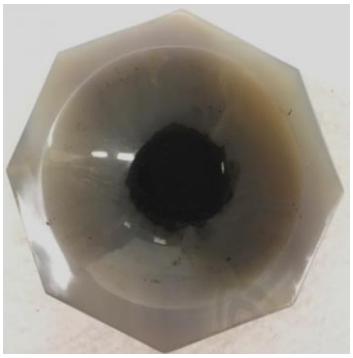

Figure 5.2 A photo image of the CMS/SBR-rGO slurry during electrode preparation.

5.2.3 Materials and electrochemical characterization

Surface morphology of the samples was studied using a Hitachi SU8010 field-emission SEM. XRD patterns were acquired from Panalytical X'Pert PRO Alpha-1 system using Cu Kα radiation (1.5418 Å). FTIR spectra were obtained from a Nicolet Magna IR 560 spectrometer. TGA was conducted with a TGA system (Q5000, TA Instrument) in air at a heating rate of 10°C/min. Contact angle measurements were carried out on a Rame-Hart goniometer. Electrochemical characterizations including cyclic voltammetry (CV), galvanostatic charge/discharge (CD), and electrochemical impedance spectroscopy (EIS) were performed on a 2-channel system (Princeton Applied Research) using symmetric two-electrode coin cells in both aqueous (2 M KOH) and organic (1 M $TEABF_4$/AN)

electrolytes. The coin cell consists of two pairs of symmetric current collectors and electrode films in sandwich structures with glass microfibers in between as separators. Electrolyte solutions were degassed by sonication for several times under vacuum to remove dissolved oxygen before use. The specific capacitance was calculated from CV curves using Equation (6). All the capacitance was normalized based on the content of active rGO materials. The frequency-dependent capacitance was derived based on

$$C = -\frac{1}{2\pi f Z''} \tag{14}$$

where f is the frequency, and Z'' is the imaginary part of the impedance.

5.3 Results and Discussion

5.3.1 Structural properties of the electrodes

The morphology of rGO films using different binders were visualized by SEM images. In Figure 5.3, all the four binders exhibited similar structural forms as thin fibrils. The binder fibrils spread out among graphene sheets and adhered over their edges and planes. The free-standing films with structural integrity demonstrate the excellent binding efficiency for all the binders, especially the Electrodag binder containing a smaller fraction of PVP.

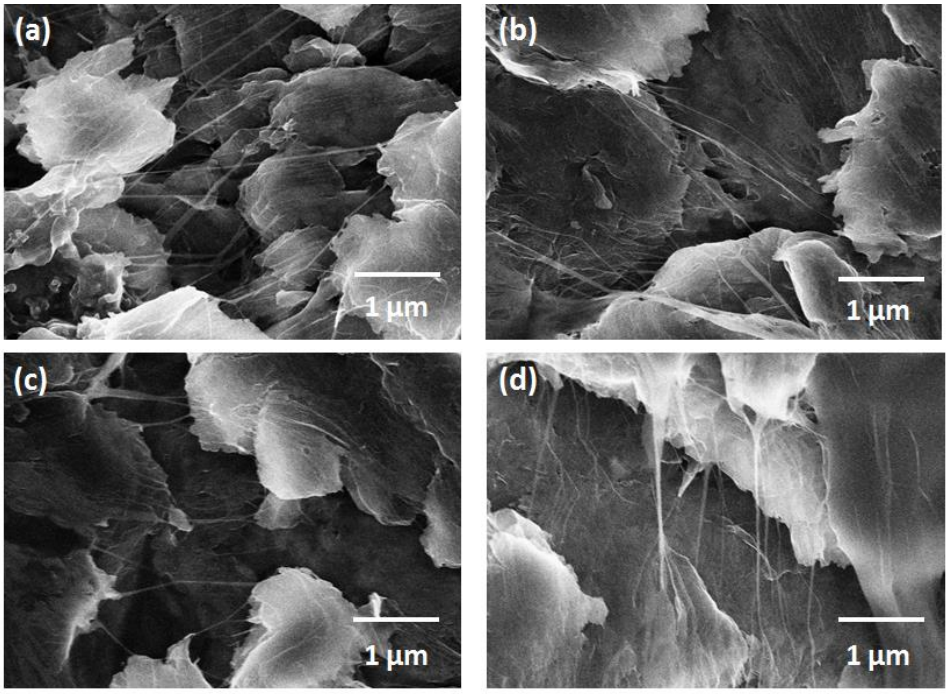

Figure 5.3 SEM images of the rGO electrodes with (a) PTFE, (b) PVDF, (c) Electrodag, and (d) CMC/SBR binders.

The mechanical flexibility of the electrodes was tested by rolling the films (18×18 cm^2) around a cylinder (12.9 mm in diameter) for 100 cycles (Figure 5.4). To demonstrate the mechanical robustness, surface morphology of different rGO films were taken after bending tests. As shown in Figure 5.5, binder fibrils still stuck to the surface and connected between graphene sheets without any obvious change of morphology, indicating the flexibility of the fabricated graphene films.

Figure 5.4 Image showing the bending of rGO films by rolling around a cylinder.

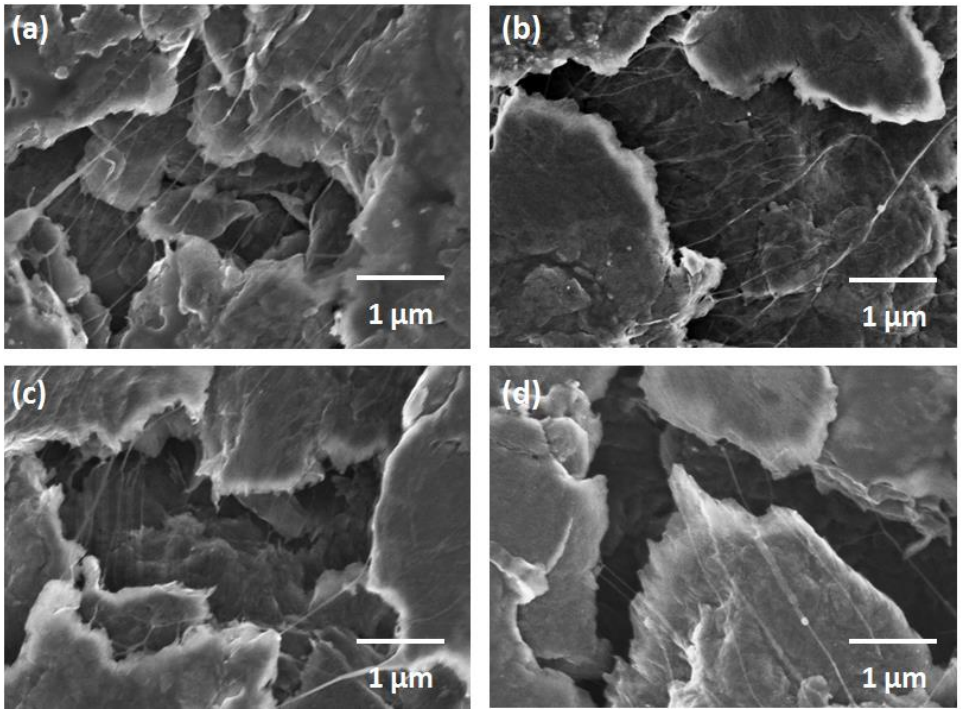

Figure 5.5 SEM images of the rGO electrodes with (a) PTFE, (b) PVDF, (c) Electrodag, and (d) CMC/SBR binders after bending tests.

The crystalline structures of the binders and as-formulated rGO films were studied by XRD (Figure 5.6). Both PTFE and PVDF are semi-crystalline polymers: the sharp peak at 18.6° corresponds to the crystalline domain of PTFE, and two sharp peaks at 18.6° and 20.1° reflect the crystalline regions of PVDF. For the corresponding rGO films, broad peaks appeared at around $2\theta = 25°$, which represent the stacked rGO structures [71]. The

characteristic binder peaks were also observed in rGO films with relatively low intensities, indicating that the binders remained some crystalline forms in the films. It has been reported that PVDF and PTFE polymer chains can be densely packed in crystal domains and form bundled or long-range ordered structures, which reduce the chances of physical binding to electrode materials [247]. In contrast to the fluoropolymers, PVP and CMC/SBR only exhibited broad peaks in XRD, implying highly amorphous nature of these binders. Crystalline peaks were not observed in rGO films with Electrodag and CMC/SBR. In particular, PVP and CMC/SBR tend to have stronger affinity to rGO materials due to the enhanced interactions between the reactive carbonyl and carboxylate groups in binders and the residue oxygen-containing functional groups in rGO. Moreover, the amorphous PVP and SBR structures with flexible polymer chains can provide flexibility to the overall electrodes, which are important for the development of flexible energy storage materials.

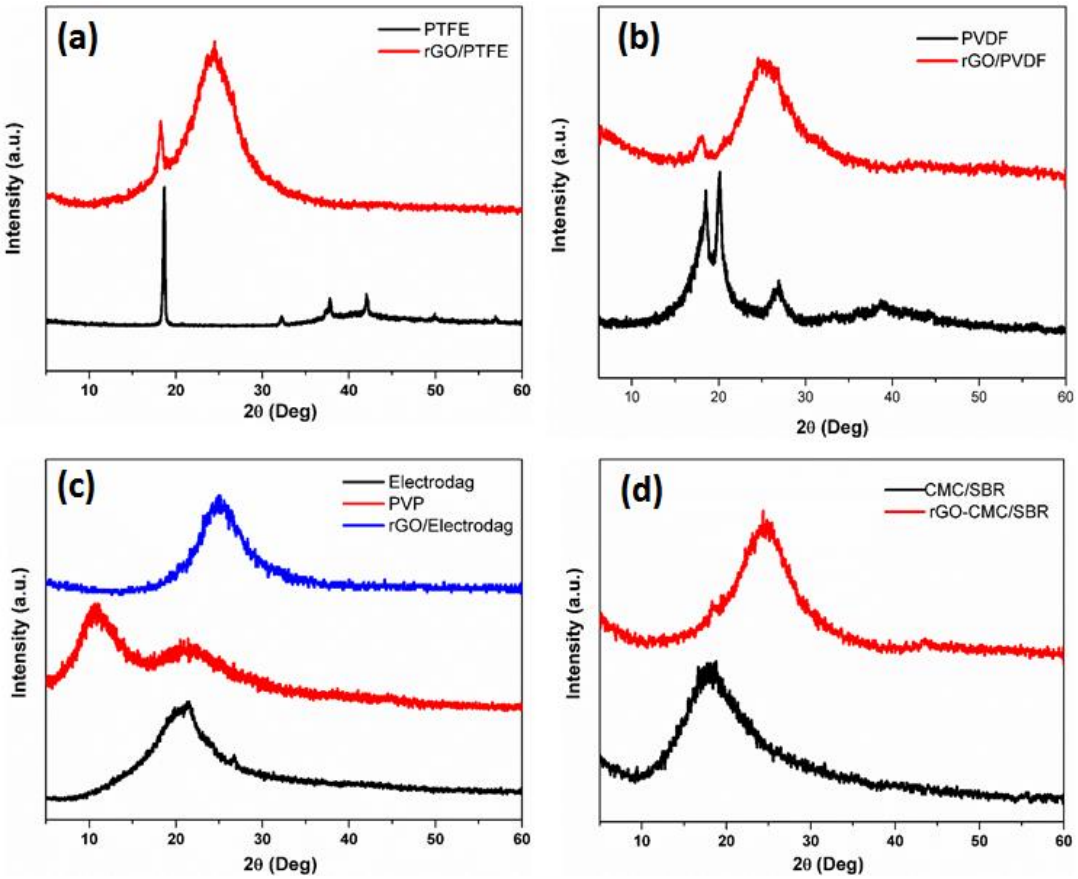

Figure 5.6 XRD patterns of (a) PTFE, (b) PVDF, (c) Electrodag, and (d) CMC/SBR binders and their corresponding rGO films.

Figure 5.7 shows the TGA curves of the binders (solid content) in air. It can be seen that fluorinated polymers are more thermally stable. The dramatic weight loss occurred at 425°C and 500°C for PVDF and PTFE, respectively. The 5% weight loss for PTFE at 200~300°C might come from the non-ionic surfactants that is included in the PTFE binder solution. The aqueous dispersible Electrodag and CMC/SBR binders are more susceptible to moisture absorption, which explains the weight loss up to 5% below 150°C. For Electrodag binder, the weight loss between 250~400°C is attributed to the degradation of PVP and other additives. For CMC/SBR binder, a multiple-step weight loss profile was

observed. The TGA curves of PVP powder, CMC powder, and dried SBR glues are shown in Figure 5.7b as reference.

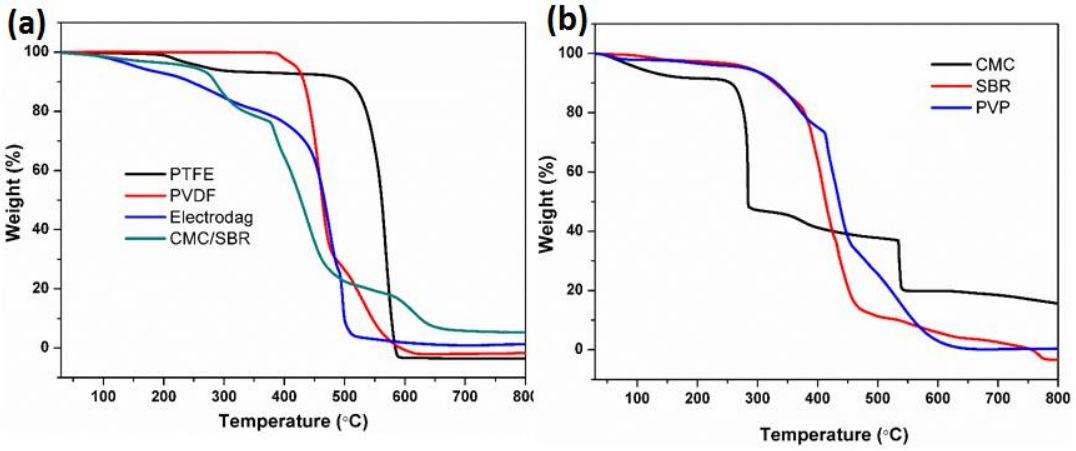

Figure 5.7 TGA curves of (a) four binders and (b) CMC, SBR and PVP in air at a heating rate of 10°C/min.

Among the four rGO electrodes, PTFE/rGO showed the highest thermal stability with its thermal profile similar to that of rGO powders, as shown in Figure 5.8. The onset temperature at around 475°C corresponds to the initial decomposition of graphene network. The Electrodag bonded rGO had ~ 4% weight loss at 280~360°C, which reflects the degradation of PVP components. The presence of carbon black and graphite in Electrodag binder renders it higher stability than CMC/SBR bonded rGO. The 10% weight loss difference between rGO and CMC/SBR/rGO from 350 to 450°C results from the decomposition of elastomeric binders.

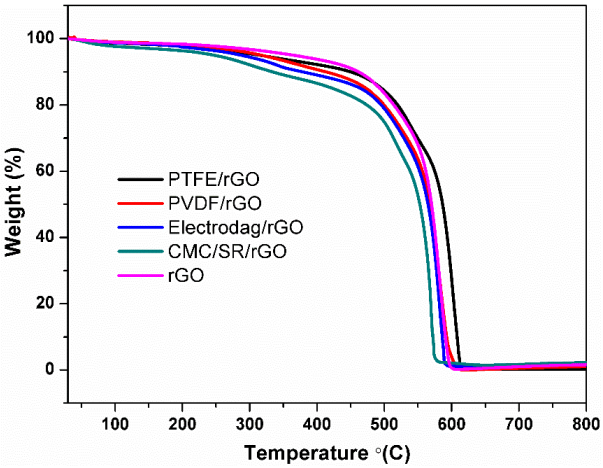

Figure 5.8 TGA curves of rGO films in air at a heating rate of 10°C/min.

Surface hydrophilicity of the electrodes were investigated by contact angle measurements. Figure 5.9 shows the contact angles of water droplet on four rGO electrodes with different binders. The average contact angles were determined to be PVDF (113.0°) > PTFE (110.2°) > Eletrodag (101.5°) > CMC/SBR (85.8°). The presence of substituted carboxylate anions, together with the water dispersible SBR glues, contributes to the high hydrophilicity of CMC/SBR-rGO films. As the active binding component in Electrodag, the small portion of PVP in Electrodag, as a water-soluble polymer binder, also serves to improve surface wetting. As expected, the low surface energy of the fluoropolymers makes PTFE and PVDF bonded rGO hydrophobic. Generally, the more hydrophilic are the rGO electrodes, the better wettability they can be achieved in an aqueous electrolyte.

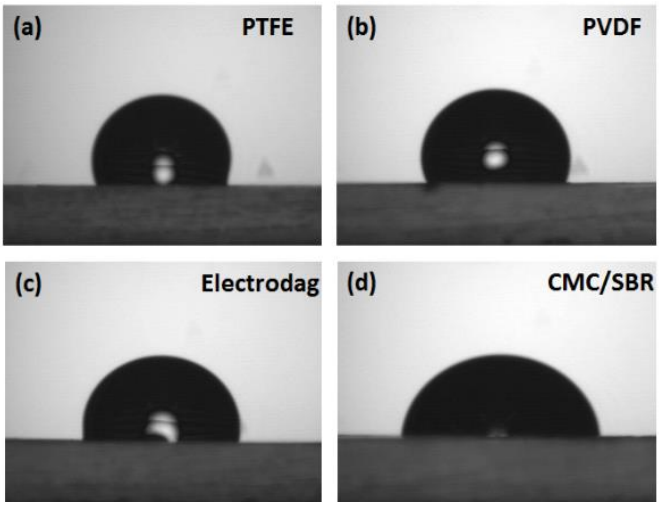

Figure 5.9 Contact angles of rGO films with four binders by water droplet.

5.3.2 Electrochemical analysis of the electrodes

The electrochemical properties of free-standing rGO electrodes with four different binders were studied in 2 M KOH and 1 M $TEABF_4$/AN electrolytes. Figure 5.10 show the CV curves of PTFE, PVDF, Electrodag, and CMC/SBR bonded rGO electrodes at scan rates from 10 to 200 mV/s. In KOH electrolyte, all electrodes displayed near rectangular profiles from 0-0.8 V, indicating the characteristics of EDL capacitance. As shown in Figure 5.11, rGO electrodes with PTFE and PVDF binders had specific capacitance values of 90 F/g and 80 F/g at 10 mV/s, respectively. The PTFE/rGO showed good capacitance retention as the increase of scan rates; while PVDF/rGO showed more tilted CV curves and a larger decay of capacitance as the scan rates increased. The PVDF binder, with strong hydrophobic nature, might have poor compatibility in the aqueous electrolyte because of the obstructed ionic diffusion.

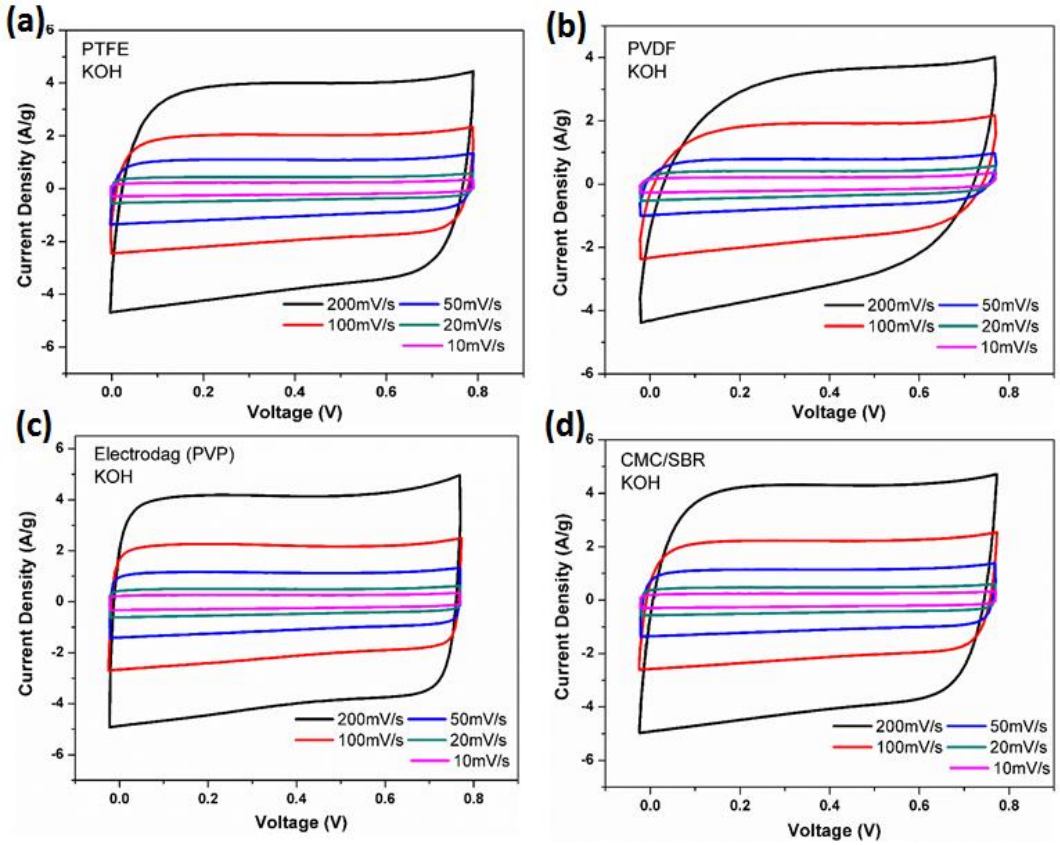

Figure 5.10 CV curves of (a) PTFE/rGO, (b) PVDF/rGO, (c) Electrodag/rGO, and (d) CMC/SBR-rGO in 2 M KOH electrolyte.

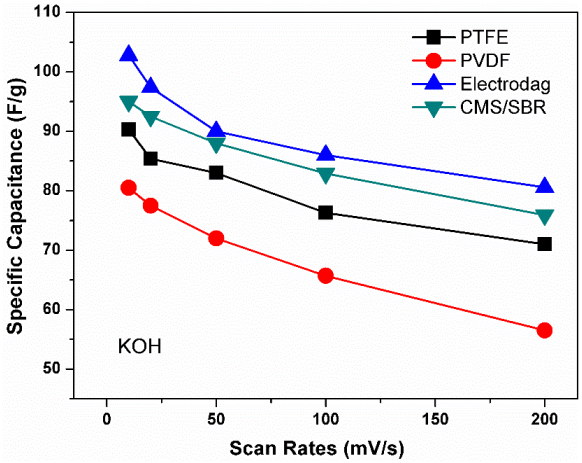

Figure 5.11 Specific capacitance of rGO electrodes vs scan rates in 2 M KOH electrolyte.

For rGO bonded with Electrodag binder, a maximum capacitance of 103 F/g was achieved at 10 mV/s, which is 28.7% and 14.4% improvements compared to PVDF and PTFE binders. Even with the increasing scan rate, the capacitance remained as high as 90 F/g and 80 F/g at 50 and 200 mV/s respectively. The excellent rate performance can be attributed to the highly conductive components in the binder, which induces faster charge transfer within the electrode. The Electrodag binder contains 30 wt% of graphite and only 5 wt% of PVP. Therefore, the addition of too much binder would significantly decrease the overall capacitance due to the large quantity of graphite; while insufficient amount of binder would result in a lower adhesion strength, making it difficult to form free-standing electrode films. When rGO to binder (solid content) ratio was 2:1, the specific capacitance decreased to 75.4 F/g at 10 mV/s (Figure 5.12); while the rGO powders could not be bound together to form thin film electrodes at rGO/binder ratio of 4:1. The optimum rGO to binder ratio was found to be 3:1, which contained 3.1% of active PVP binder.

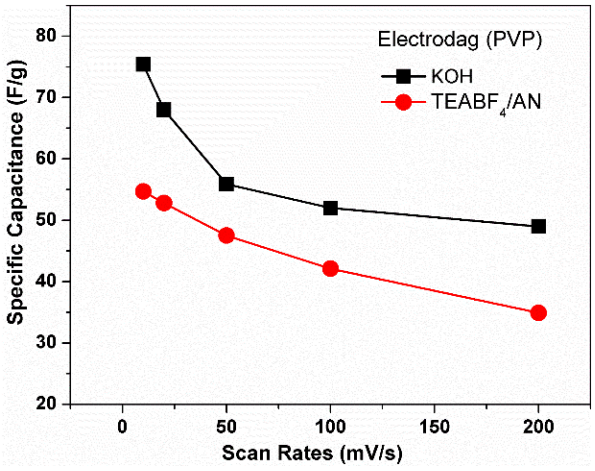

Figure 5.12 Specific capacitance of rGO electrodes with 33.3% Electrodag binder (4.17% PVP) in KOH and $TEABF_4$/AN electrolytes at different scan rates.

rGO with CMC/SBR demonstrated a specific capacitance of 95 F/g at 10 mV/s and a high degree of capacitance retention with increasing scan rates. The fabricated electrodes using hydrophilic CMC/SBR binder could have better surface wetting than PTFE and PVDF in aqueous electrolyte, thus leading to better capacitive performance. The electrical conductivity of the rGO films were measured and shown in Table 5.2. The addition of insulating binder slightly decreased the conductivity of rGO; while higher conductivity with Electrodag binder was achieved due to the synergistic effect of carbon additives to create additional electrical conduction pathways and PVP binder to increase the contact area between rGO flakes. The specific capacitance of pure binders were also calculated from CV curves (Figure 5.13) and summarized in Table 5.3. It can be seen that the capacitive contribution from most binders were miniscule; while the components in Electrodag binder can play a bigger role in enhancing the overall capacitance of graphene electrodes.

Table 5.2 Electrical conductivity of four rGO films

Electrodes	PTFE/rGO	PVDF/rGO	Electrodag/rGO	CMC/SBR-rGO
Conductivity (S/m)	196	210	285	220

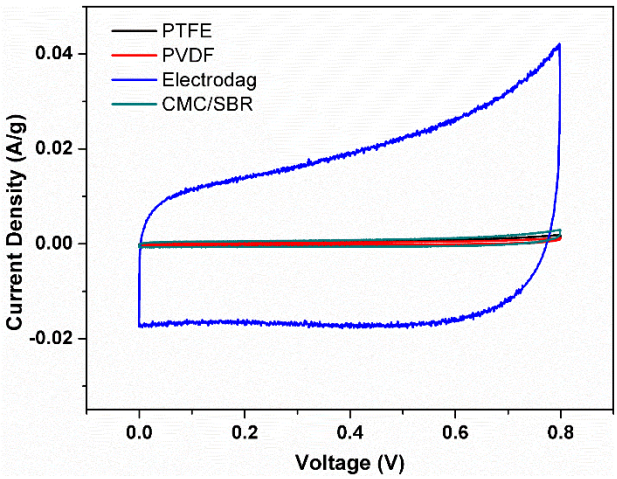

Figure 5.13 CV curves of the four binders at a scan rate of 50 mV/s in KOH electrolyte.

Table 5.3 Specific capacitance of four binders calculated from CV curves at 50 mV/s

Binders	PTFE	PVDF	Electrodag	CMC/SBR
Specific capacitance (F/g)	0.037	0.020	1.400	0.057

In organic electrolyte, the voltage window was extended to 2.7 V to achieve higher energy densities. However, the acquired specific capacitance decreased and the capacitance decay accelerated at higher scan rates as a result of larger ionic size and constrained ionic diffusion in $TEABF_4$/AN electrolyte. As shown in Figure 5.14, rGO with Electrodag had a maximum capacitance of 86 F/g, and rGO with PTFE and PVDF binders had capacitance values of 82 F/g at 10 mV/s. It is noted that PVDF/rGO even exhibited higher capacitance in $TEABF_4$/AN, which can be explained by the improved wetting of the electrode with hydrophobic PVDF binder. For CMC/SBR bonded rGO, the dramatically declined capacitance values with increasing scan rates correspond to the limited ionic diffusion process within the electrodes, which might be caused by poor electrolyte wetting.

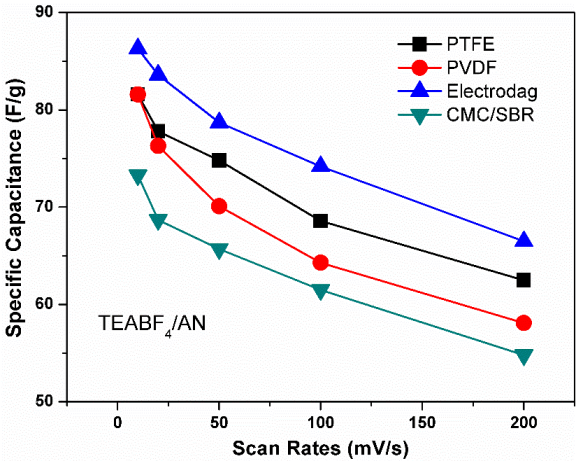

Figure 5.14 Specific capacitance of rGO electrodes vs scan rates in 1 M $TEABF_4$/AN electrolyte.

The galvanostatic charge/discharge curves of different rGO electrodes at current density of 1 A/g are shown in Figure 5.15(a-b). The IR drop in the discharge curves corresponds to the internal resistance of the electrode/electrolyte system. It can be seen that the trend for IR drop is consistent with the capacitive properties obtained from CV curves. The smallest IR drop was observed for Eletrodag/rGO, and rGOs with PVDF and CMC/SBR binders have the largest IR drop in aqueous and organic electrolytes respectively. The cycling stability of the electrodes was studied by charge/discharge tests (Figure 5.15c-d). In KOH electrolyte, rGO with CMC/SBR binder showed the best cycling performance with 95.1% capacitance retention after 10,000 cycles, while the capacitance decreased to below 88% for PVDF-bonded rGO. The faster decay of capacitance for PVDF/rGO in aqueous electrolyte can be explained by the low flexibility and high hydrophobicity of the PVDF binder. Whereas CMC/SBR binder combines the benefits of water solubility from CMC and high mechanical flexibility from SBR. In other words, the existence of elastomeric SBR rubbers can well accommodate the possible volume change of the electrode during charge/discharge cycles to provide excellent cycling stability [238].

In $TEABF_4$/AN, over 93% of initial capacitance was maintained after 5,000 cycles for all the electrodes.

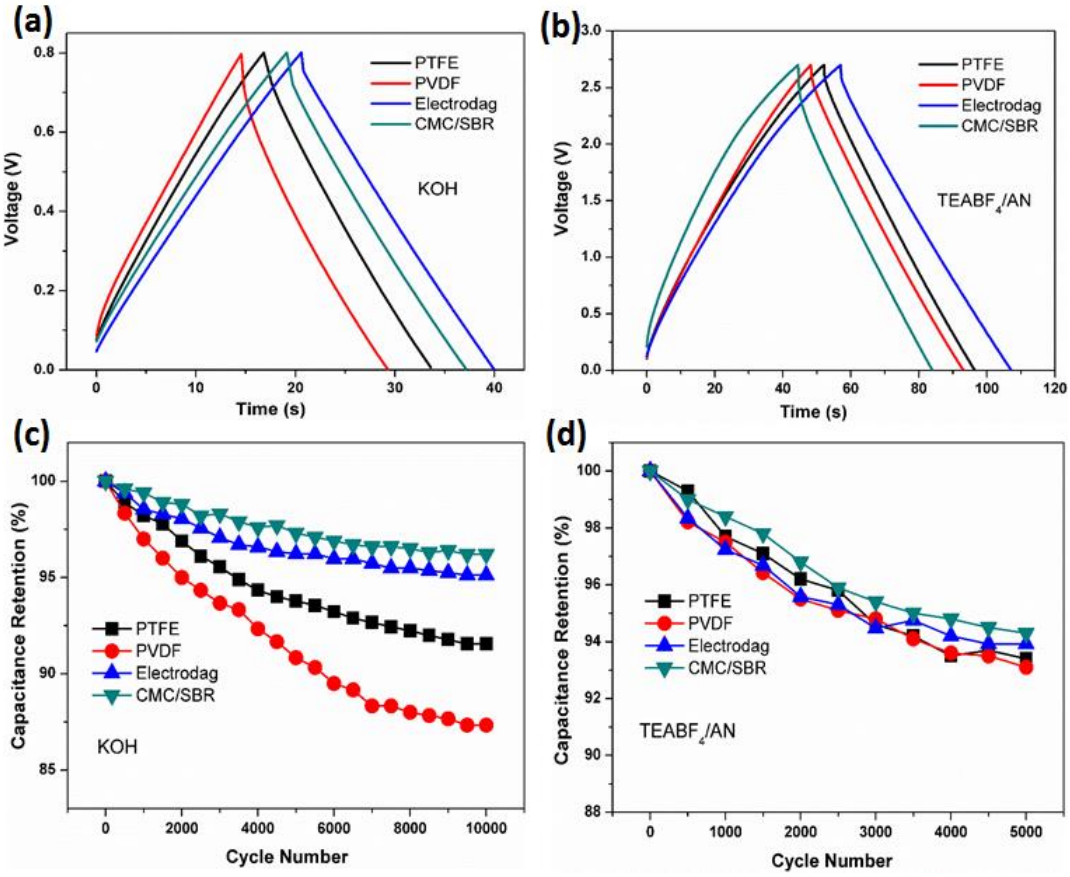

Figure 5.15 (a-b) Charge/discharge curves of the rGO electrodes at current density of 1 A/g in (a) 2 M KOH and (b) 1 M $TEABF_4$/AN electrolytes; cycling performance of the rGO electrodes in (c) 2 M KOH and (d) 1 M $TEABF_4$/AN electrolytes.

The resistive behavior and frequency response of the electrodes were studied by impedance spectroscopic techniques. Figure 5.16(a-b) show the Nyquist plots of the rGO electrodes in aqueous and organic electrolytes. At low frequency regions, the almost vertical lines suggest near ideal capacitive behavior. It was determined that the ESR was below 0.4 Ω for all electrodes except PVDF/rGO in KOH, indicative of the small internal resistance of the other three electrodes. The semicircle at the high frequency region

corresponds to the charge transfer process at the electrolyte/electrode interface. As shown in Figure 5.16a, the spectrum for PVDF/rGO displayed a larger Warburg impedance region as the slope of the curve changing from 45° to 90° at mid-to-low frequencies. This characteristic Warburg impedance implies the limited ionic diffusion and large ionic resistance within the electrode. In KOH electrolyte, the smallest R_{ct} was observed for CMC/SBR bonded rGO, indicating that the water soluble CMC/SBR could expedite the penetration of ions into the porous graphene structures. In $TEABF_4$/AN electrolyte, all electrodes showed similar ESR ~ 1.5 Ω. Among the four electrodes, Electrodag/rGO had the smallest R_{ct}, which denotes the high ionic conductivity at the electrode/electrolyte interface.

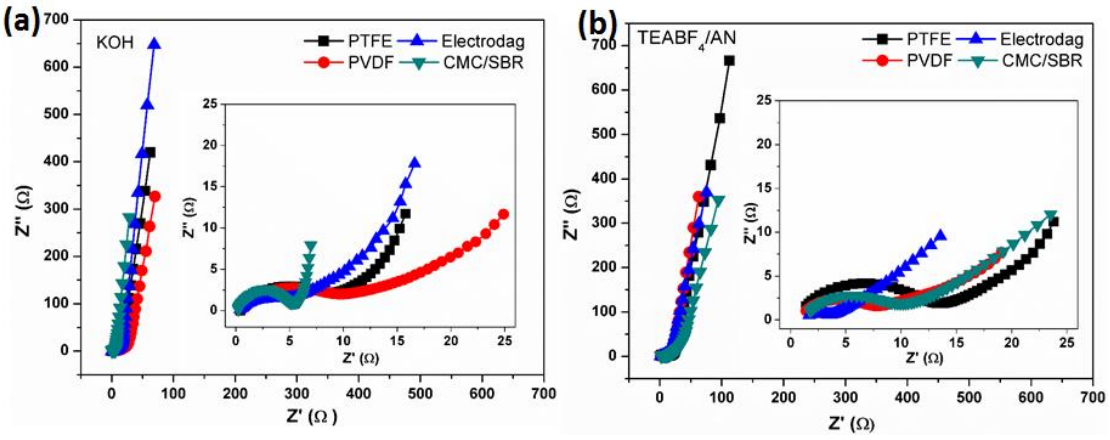

Figure 5.16 . Nyquist plots of the rGO electrodes with magnified view in the high frequency region in (a) 2 M KOH and (b) 1 M $TEABF_4$/AN electrolytes.

The specific capacitance variation as a function of frequency was further investigated. As shown in Figure 5.17(a-b), the characteristic relaxation time constant (τ_0) can be obtained from reciprocal of the frequency values when the imaginary capacitance (C″) reached the maximum. τ_0 denotes the minimum time needed to discharge all the energy from the supercapacitors with an efficiency over 50% [100, 248]. The τ_0

values for all electrodes in both electrolytes are listed in Table 5.4. Comparing the four electrodes in KOH electrolyte, CMC/SBR-rGO exhibited the smallest τ_0 of 2 s, while the PVDF/rGO had the largest τ_0 of 7.94 s. The trend for τ_0 agrees well with the resistive properties of the electrodes, in which lower charge transfer resistance leads to faster charge/discharge rates. In organic electrolyte, a similar trend was observed for τ_0, in which electrodes with larger capacitance and smaller impedance presented smaller τ_0. In contrast to aqueous electrolyte, τ_0 values was slightly higher due to a bulkier ionic size and slower ionic diffusion. One exception was seen for PVDF/rGO, the hydrophobic PVDF binder hindered charge transport within the inner surface area of rGO in aqueous electrolyte.

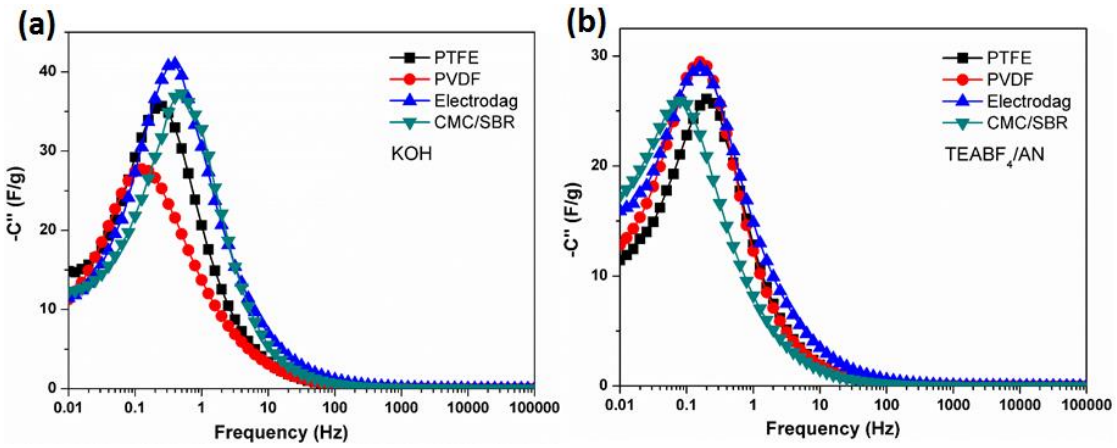

Figure 5.17 Imaginary part of capacitance as a function of frequency for rGO electrodes in (a) 2 M KOH and (b) 1 M $TEABF_4$/AN electrolytes.

Table 5.4 Relaxation time constant (τ_0) of rGO electrodes with different binders

	$\tau_{0\,PTFE}$ (s)	$\tau_{0\,PVDF}$ (s)	$\tau_{0\,Electrodag}$ (s)	$\tau_{0\,CMC/SBR}$ (s)
1 M KOH	3.98	7.94	2.51	2.00
1 M $TEABF_4$/AN	5.00	6.33	6.25	12.66

Figure 5.18 shows the frequency-dependent specific capacitance for all the electrodes. It can be seen that the capacitance first increased steeply with the decrease of frequency and then the increase of capacitance slowed down at lower frequency regions. The slow capacitance increase at low frequencies indicates the penetration of electrolyte ions into the inner pores of graphene electrodes [235]. For CMC/SBR-rGO, a high level of capacitance retention was achieved until 1 Hz in aqueous electrolyte, while dramatic capacitance drop occurred at below 0.1 Hz for PVDF/rGO. The results implies that hydrophilic CMC/SBR binder can handle high power at a wider frequency window in aqueous electrolyte. In organic electrolyte, a sharp decline in capacitance appeared at around 0.5 Hz for PTFE/rGO; whereas CMC/SBR-rGO showed almost continuous capacitance drop with increasing frequency.

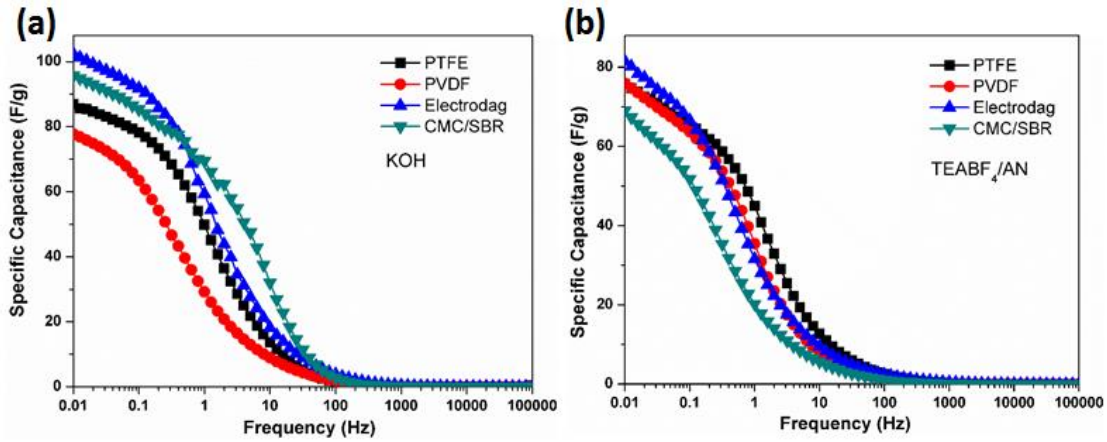

Figure 5.18 Specific capacitance as a function of frequency for rGO electrodes in (a) 2 M KOH and (b) 1 M $TEABF_4$/AN electrolytes.

5.4 Conclusions

In this work, free-standing graphene electrodes have been fabricated using PTFE, PVDF, Electrodag, and CMC/SBR binders. Surface morphology study confirms that

graphene sheets were efficiently held together by binder fibrils. XRD patterns indicates that PTFE and PVDF binders had some crystalline domains in rGO films, while Electrodag and CMC/SBR binders are highly amorphous within rGO films. The contact angle measurements verify the hydrophobic nature of the fluorinated binders, whereas CMC/SBR binder is more hydrophilic due to the carboxylate groups. Electrochemical study reveals that the improved electrolyte wettability and enhanced conductivity of the components are two essential factors for the capacitance increase. Using the conductive Electrodag binder, the rGO electrode exhibited the highest capacitance with low internal and charge transfer resistances in both aqueous and organic electrolytes; while the rGO electrode fabricated by water-soluble CMC/SBR showed the fastest frequency response in aqueous electrolyte due to a better wetting of the electrode surface. The CMC/SBR-rGO also demonstrated the best cycling stability as the elastic SBR could compensate for the volume change during charge/discharge cycles. Moreover, the poor wettability makes the PVDF-rGO and CMC/SBR-rGO not compatible in aqueous and organic electrolytes respectively. Further studies on various porous carbon nanomaterials are necessary to establish more comprehensive guidelines for the binder selection. Meanwhile, it is important to develop new binder formulations with high adhesion strength, structural flexibility, and electrical conductivity to meet the requirements for high performance electrodes in energy storage devices.

CHAPTER 6. CONCLUSIONS AND FUTURE WORK

6.1 Conclusions

In this dissertation, molecular level functionalization of graphene was achieved to prevent the aggregation of graphene layers after GO reduction. Upon functionalization, graphene-based 3D covalent organic frameworks have been established by selecting molecular spacers that can be covalently bonded between graphene sheets. A series of multifunctional molecules, such as diamines, triamines, triols, and polyanilines, have been employed as molecular spacers. The molecular spacers served as pillars to enlarge the interlayer spacing of graphene and generate more open pores to facilitate charge storage and transport. The functionalization process was realized via a two-step hydrothermal process, in which the chemical functionalization took place at the first step at moderate temperature, and the reduction process occurred in the second step at elevated temperature. Chemical analyses revealed that ring opening of epoxide groups on GO by molecular spacers (nucleophiles) was the main reaction for covalent grafting. Diffraction and surface analyses showed that interlayer distance (0.84-0.41 nm) and pore size distribution of the graphene network were correlated with chain length and functionalities of the spacer, which indicate the functionalization can be well controlled at molecular level. The negligible structural change before and after GO reduction demonstrated the stability of the 3D graphene network. In addition, the evidence of crosslinking was elucidated by the increase of modulus by dynamic rheological study.

The functionalized graphene materials have been fabricated into free-standing thin films using polymer binders. The effect of polymer binders on adhesion, hydrophobicity,

conductivity, flexibility, and toxicity of the electrodes have been studied. With improved chemical and structural features, the modified graphene by aliphatic amines achieved enhanced capacitance and excellent cycling stability in aqueous and organic electrolytes. Remarkably, a maximum capacitance of 119 F/g was obtained in ionic liquid electrolyte with ultrahigh energy density of 51 Wh/kg and slow self-discharge rate. Incorporation of aromatic amine structures into graphene network has led to the formation of conjugated graphene network with high conductivity and prominent Faradaic charge transfer characteristics. Phenylene diamine treated rGO electrodes delivered a high capacitance of 422 F/g with low equivalent and charge transfer resistance. Further investigation implied that the crosslinked graphene structures, multiple redox transition states, and rapid charge transport are the critical factors that determine the electrochemical properties of the conjugated graphene networks. Complementary to the experimental results, computational modeling, including molecular dynamic and density functional theory calculations, were adopted to verify the interlayer spacing, molecular geometries, band gap structures, formation energy, electron distribution, and HOMO energy levels of the functionalized graphene network. The systematic study of graphene functionalization can provide a generalized guidance for molecular engineering of graphene networks in the future.

The research on electrode design has also been extended to device level fabrication to make miniaturized, high efficient, and cost-effective micro-supercapacitors (MSCs) to meet the demands for small-form factor energy storage units in microelectronic field. A solid-state MSC has been successfully developed using highly conductive and aqueous dispersible graphene/sulfonated polymer composites as micro-electrodes. Well-defined interdigitated patterns were formed by a controlled process flow including surface

cleaning, thin film depositions, shadow masking, electron-beam evaporation, plasma etching, and electrolyte casting. The as-fabricated MSC presented a high conductivity of 1100 S/m, an ultrahigh stacking volumetric capacitance of 16.55 F/cm^3, and a superior energy density of 1.51mWh/cm^3, which is comparable to that of thin film batteries while providing much higher power density. The outstanding electrochemical performance can be attributed to the planar interdigitated architecture to decrease charge transfer distance and the material optimization to enlarge charge storage capability. Individual MSC units have been connected in series or parallel configurations to make MSC arrays to enlarge the operation voltage window and control the charge/discharge rates. Moreover, the prototypes of flexible and foldable MSC arrays have been made using compatible substrates and Miura folding concept. The dramatically improved areal energy density and mechanical compliancy of the foldable MSC arrays show great promise for foldable and wearable electronics.

6.2 Suggested Future Work

6.2.1 Graphene network co-functionalized by organic and inorganic species for hybrid supercapacitors

A high energy density supercapacitor with speedy charge/discharge rate and extremely long cycle life is considered as one of the critical enablers for next generation electric vehicle (EV) applications. However, current supercapacitor technology cannot meet the energy storage requirement for EV because of limited energy density. Pure carbon or chemically functionalized carbon materials can only deliver specific of around 100~500 F/g. Metal oxides based electrodes can achieve much higher specific capacitance over

2000F/g, but they are struggling with poor cyclic performance by a few thousands cycles [249]. The current carbon and metal oxides hybrid supercapacitors also suffer from severe stability issue. The reason can be explained that the nanostructures of metal oxides/hydroxides are subject to repeated swelling and shrinkage by accessing electrolyte ions, which causes the physical dimension change of the intrinsic crystal structures as well as the interfaces between metal oxides and carbon substrates. In particular, the deteriorating interface abruptly degrades the electrical conductivity [250]. Therefore, novel materials design are imperative to combine the benefits of graphene and transition metal oxides/hydroxides while elongating the working lifetime of the devices.

The proposed research includes the incorporation of both organic and inorganic species into graphene network. The organic spacers can be covalently crosslinked between graphene sheets to construct a 3D graphene architecture with large usable surface area and controlled surface chemistry; while nickel or cobalt based oxides/hydroxides/sulfides can be anchored within the interlayer space to offer high pseudocapacitance. Methods for the deposition of these inorganic materials include solution based crystal growth, hydrothermal synthesis and electrodeposition. The processing conditions at moderate temperature can ensure the chemical and physical stability of the functionalized graphene network. To further improve structural integrity and enable charge transport, a multifunctional molecular coupler will be used to provide chemical and electrical linkage between graphene and metal oxides. The chemical bonding and the charge transfer capability will be rationally designed and investigated. On one side, organic spacers can utilize coordination and electrostatic interactions to form bonds with metal oxides. On the other side, diazonium and azide groups can be easily grafted to graphene surface at room

temperature [251]. The backbone of the molecular can be decorated with conjugated aromatic structures, thus efficient charge transport can be realized through the overlapped π bonds. The molecular coupler will suppress the interface deterioration and dramatically enhance the cyclic performance of the inorganic nanomaterials on graphene nanosheets. The hybrid supercapacitors are promising to provide specific capacitance over 2000 F/g with extended lifetime.

6.2.2 Further developments for micro-supercapacitors

Despite the recent progress, research and development of MSC is still at an immature stage and has much room for advancement. First, current MSC devices have insufficient energy densities than those of electrochemical batteries, even though they demonstrate superior power handling capability. Since the capacitance is strongly dependent on microstructure of electrodes, key parameters such as surface morphology, pore size, and surface affinity to electrolyte ions should be continuously engineered. According to Equation (4), the operating voltage can increase the energy density with the square level. Therefore, ionic liquid based polymer electrolytes are favored to provide higher energy density. However, one problem of typical polymer gels (e.g. PVA) is the low ionic conductivity. In this regard, controlling electrolyte chemistry for better ionic conductivity while maintaining cycling stability at wider temperature range is highly necessary. Furthermore, asymmetric configuration of MSCs combines the features of increased capacitance and large potential window, which can boost the energy density without losing much power. Second, innovations in the structural design of MSCs are required. On one hand, by reducing the gap size between adjacent electrodes, a larger

number of interdigital patterns can be packed more efficiently on planar substrates with increasing amount of active materials and shortened ion diffusion pathways. On the other hand, MSC devices can be built in a 3D architecture through deposition of electrodes and electrolytes on 3D networks for higher energy storage per unit area [252]. The interpenetrated electrodes with conformal coating of thin-layer electrolytes can be loaded in a conductive 3D scaffold, and the 3D scaffold can either serve as current collectors or be part of the electrodes. Third, MSCs can be fabricated to perform energy storage as well as other functions in microelectronics. For example, MSC is regarded as a possible alternative to traditional aluminum electrolytic capacitors for alternating current (ac) line-filtering, where large capacitance and high level of miniaturization are preferred to meet future demands [253]. The MSC structure may also been applied in capacitive deionization (CDI) as a method to remove impurities in liquid coolant for thermal management of integrated circuit devices. As discussed earlier, foldable MSC architectures can be improved via optimization of materials and structure layout. Particularly, more complicated folding algorithms and mechanical analyses can be done via computational tools to construct more user-friendly designs at the system level for portable and wearable electronics devices. Primary quality metrics should be carefully considered and emphasized when using MSC for specific applications. For instance, the ultrafast frequency response is the key to ensure operation of alternating current (ac) line-filters and radio frequency devices, and electrochemical stability under mechanical strains are crucial for flexible devices. Moreover, MSCs are promising to become an integral component in futuristic self-powered bio-electronic/photonic devices coupling with energy harvesting element [254]. In order to meet such upcoming energy demands in bio-applications,

biocompatible packaging scheme and materials for MSC should be intensely studied as well. Finally, the capability for large-scale and low cost production is a prerequisite towards technology commercialization, which requires further efforts on process control and development.

APPENDIX A. AUTHOR'S PUBLICATIONS

A.1 Journal Publications

1. ***Song, B.***, Zhao, J., Wang, M., Mullavey, J., Zhu, Y., Geng, Z., Chen, D., Ding, Y., Moon, K.S., Liu, M., and Wong, C.P., Systematic study on structural and electronic properties of diamine/triamine functionalized graphene networks for supercapacitor application, *Nano Energy* 2017, 31, 183-193.

2. ***Song, B.***, Choi, J.I., Zhu, Y., Geng, Z., Zhang, L., Lin, Z., Tuan, C.C., Moon, K.S., and Wong, C.P., Molecular level study of graphene networks functionalized with phenylenediamine monomers for supercapacitor electrodes, *Chem. Mater.* 2016, 28, 9110-9121.

3. ***Song, B.***, Wu, F., Zhu, Y., Hou, Z., Moon, K.S. and Wong, C.P., Effect of polymer binders on graphene-based free-standing electrodes for supercapacitors. *Electrochim. Acta*, 2018, 267, 213-221.

4. ***Song, B.***, Li, L., Lin, Z., Wu, Z.K., Moon, K.S. and Wong, C.P., Water-dispersible graphene/polyaniline composites for flexible micro-supercapacitors with high energy densities, *Nano Energy* 2015, 16, 470-478.

5. ***Song, B.***, Sizemore, C., Li, L., Huang, X., Lin, Z., Moon, K.S. and Wong, C.P., Triethanolamine functionalized graphene-based composites for high performance supercapacitors. *J. Mater. Chem. A* 2015, 3, 21789-21796.

6. ***Song, B.***, Tuan, C.C., Huang, X., Li, L., Moon, K.S., and Wong, C.P., Sulfonated polyaniline decorated graphene nanocomposites as supercapacitor electrodes, *Mater. Lett.* 2016, 166, 12-15. (Citations: 16)

7. ***Song, B.***, Moon, K.S., and Wong, C.P., Recent developments in design and fabrication of graphene-based interdigital micro-supercapacitors for miniaturized energy storage devices, *IEEE Transactions on Components, Packaging and Manufacturing Technology* 2016, 6, 1752-1765.

8. Li, L.*, ***Song, B.****, Maurer, L., Lin, Z., Lian, G., Tuan, C.C., Moon, K.S. and Wong, C.P., Molecular engineering of aromatic amine spacers for high-performance graphene-based supercapacitors, *Nano Energy*, 2016, 21, 276-294. (*co-first author)

9. Jang, G.G., ***Song, B.***, Li, L., Keum, J.K., Jiang, Y., Hunt, A., Moon, K.S., Wong, C.P. and Hu, M.Z., Microscopic vertical orientation of nano-interspaced graphene architectures in deposit films as electrodes for enhanced supercapacitor performance, *Nano Energy* 2017, *32*, 88-95.

10. Jang, G.G., ***Song, B.***, Moon, K.S., Wong, C.P., Keum, J.K. and Hu, M.Z., 2017. Particle size effect in porous film electrodes of ligand-modified graphene for enhanced supercapacitor performance, *Carbon* 2017, 119, 296-304.

11. Li, Z., ***Song, B.***, Wu, Z., Lin, Z., Yao, Y., Moon, K.S. and Wong, C.P., 3D porous graphene with ultrahigh surface area for microscale capacitive deionization. *Nano Energy*, 2015, 11, 711-718.

12. Fang, X., Hao, P., ***Song, B.***, Tuan, C.C., Wong, C.P. and Yu, Z.T., Form-stable phase change material embedded with chitosan-derived carbon aerogel, *Mater. Letters* 2017, 195, 79-81.

13. Huang, X., Zhang, Z., ***Song, B.***, Deng, Y., Liu, S., Cui, Y., Wang, G. and Wong, C., Facile solvothermal way to synthesize CuIn 0.7 Ga 0.3 S 2 nanocrystals and their application in low-cost photovoltaic device, *J. Alloys Compd.* 2016, 656, 663-666.

14. Lu, X., Li, L., ***Song, B.***, Moon, K.S., Hu, N., Liao, G., Shi, T. and Wong, C., Mechanistic investigation of the graphene functionalization using p-phenylenediamine and its application for supercapacitors. *Nano Energy* 2015, 17, 160-170.

15. Wang, M., Song, X., ***Song, B.***, Liu, J., Hu, C., Wei, D. and Wong, C.P., 2017. Precisely quantified catalyst based on in situ growth of Cu 2 O nanoparticles on a graphene 3D network for highly sensitive glucose sensor. *Sens.Actuators B: Chem.*, 2017, *250*, pp.333-341.

16. Zhao, B., Chen, D., Xiong, X., ***Song, B.***, Hu, R., Zhang, Q., Rainwater, B.H., Waller, G.H., Zhen, D., Ding, Y. and Chen, Y., 2017. A high-energy, long cycle-life hybrid supercapacitor based on graphene composite electrodes. *Energy Storage Mater.* 2017, 7, 32-39.

17. Wang, L., Yang, X., Zhang, Q., ***Song, B.*** and Wong, C., Luminescence properties of La 2 O 2 S: Tb 3+ phosphors and phosphor-embedded polymethylmethacrylate films, *Mater. Design* 2017, 125, 100-108.

18. Wu, Z., Li, L., Lin, Z., ***Song, B.***, Li, Z., Moon, K.S., Wong, C.P. and Bai, S.L., Alternating current line-filter based on electrochemical capacitor utilizing template-patterned graphene. *Scientific Reports*, 2015, 5, 10983.

19. Wu, Z.K., Lin, Z., Li, L., ***Song, B.***, Tuan, C.C., Li, Z., Moon, K.S., Bai, S.L. and Wong, C.P., Capacitance enhancement by electrochemically active benzene derivatives for graphene-based supercapacitors, *RSC Adv.* 2015 *5*, 84113-84118.

20. Wu, Z.K., Lin, Z., Li, L., ***Song, B.***, Moon, K.S., Bai, S.L. and Wong, C.P., Flexible micro-supercapacitor based on in-situ assembled graphene on metal template at room temperature, *Nano Energy*, 2014, *10*, 222-228.

21. Yang, W., Tang, Y., Zhang, Q., Wang, L., ***Song, B.*** and Wong, C., Reducing Pb concentration in α-CsPbI3 based perovskite solar cell materials via alkaline-earth metal doping: A DFT computational study. *Ceramics International*, 2017, 43, 13101-13112.

22. Yang, W., Zhang, B., Zhang, Q., Wang, L., ***Song, B.***, Wu, F. and Wong, C.P., Different valence Sn doping–A simple way to detect oxygen concentration variation of ZnO quantum dots synthesized under ultrasonic irradiation, *Ultrasonics Sonochemistry*, 2017, 38, 29-37.

23. Yang, W., Zhang, B., Zhang, Q., Wang, L., ***Song, B.***, Ding, Y. and Wong, C.P., 2017. Adjusting the band structure and defects of ZnO quantum dots via tin doping, *RSC Adv.* 2017, 7, 11345-11354.

24. Huang, X., Zhang, J., Rao, W., Sang, T., ***Song, B.*** and Wong, C., Tunable electromagnetic properties and enhanced microwave absorption ability of flaky graphite/cobalt zinc ferrite composites, *J. Alloys Compd.*, 2016, 662, 409-414.

25. Huang, X., Zhang, J., Wang, W., Sang, T., ***Song, B.***, Zhu, H., Rao, W. and Wong, C., Effect of pH value on electromagnetic loss properties of Co–Zn ferrite prepared via coprecipitation method. *J. Magnetism Magnetic Mater*. 2016, 405, 36-41.

26. Huang, X., Zhang, J., Liu, Z., Sang, T., ***Song, B.***, Zhu, H. and Wong, C., Facile preparation and microwave absorption properties of porous hollow BaFe 12 O 19/CoFe 2 O 4 composite microrods. *J. Alloys Compd.* 2015, 648, 1072-1075.

27. Dai, S., Zhao, B., Qu, C., Chen, D., Dang, D., ***Song, B.***, Fu, J., Hu, C., Wong, C.P. and Liu, M., 2017. Controlled synthesis of three-phase Ni x S y/rGO nanoflake electrodes for hybrid supercapacitors with high energy and power density, *Nano Energy* 2017, 33, 522-531.

28. Zhang, L., Ben, Y., Chen, H., Tang, D., Fu, X., Sun, R., ***Song, B.*** and Wong, C.P., Low temperature-sintering and microstructure of highly transparent yttria ceramics. *J. Alloys Compd.* 2017 *695*, pp.2580-2586.

29. Wang, L., Yang, X., Yang, W., Zhang, J., Zhang, Q., ***Song, B.*** and Wong, C.P, Surface defect modification of ZnO quantum dots based on rare earth acetylacetonate and their impacts on optical performance. *Appl. Surf. Sci*. 2017, 398, 97-102.

30. Wang, L., Liu, Q., Shen, K., Zhang, Q., Zhang, L., ***Song, B.*** and Wong, C., A high quenching content red-emitting phosphor based on double perovskite host BaLaMgSbO 6 for white LEDs. *J. Alloys Compd.* 2017, 696, 443-449.

31. Jian, G., Shao, H., Zhang, C., Yan, C., Zhao, N., ***Song, B.*** and Wong, C.P., Orientation dependence of magnetoelectric coefficient in 1-3–type BaTiO3/CoFe2O4. *J. Magn. Magn. Mater*. 2018, 449, 263-270.

32. Zhang, R., Lv, J., Zhang, C., Yang, R., Sun, X., ***Song, B.*** and Wong, C.P., Alginate-based colloid particles from direct chemical self-assembly using as particulate emulsifiers. *Colloids Surf. A: Physicochemical and Engineering Aspects*, 2018, 542, 15-20.

33. Hu, J., Huang, Y., Yao, Y., Pan, G., Sun, J., Zeng, X., Sun, R., Xu, J.B., ***Song, B.*** and Wong, C.P., Polymer Composite with Improved Thermal Conductivity by Constructing a Hierarchically Ordered Three-Dimensional Interconnected Network of BN. *ACS Appl. Mater. Interfaces.* 2017, 9, 13544-13553.

34. Zhao, B., Zhang, L., Zhang, Q., Chen, D., Cheng, Y., Deng, X., Chen, Y., Murphy, R., Xiong, X., ***Song, B.*** and Wong, C.P., Rational Design of Nickel Hydroxide-Based Nanocrystals on Graphene for Ultrafast Energy Storage. *Adv. Energy Mater.* **2017**, 1702247.

35. Wu, F., Tuan, C.C., ***Song, B.***, Moon, K.S., Wong, C.P., Controlled Synthesis and Evaluation of Cyanate Ester/Epoxy Copolymer System for High Temperature Epoxy Molding Compounds, *J. Polym. Sci. Part A: Polym*. Chem. 2018. Accepted.

A.2 Conference Proceedings

1. ***Song, B.***, Chen, Y., Moon, K.S. and Wong, C.P., Design of Miura Folding-Based Micro-Supercapacitors as Foldable and Miniaturized Energy Storage Devices. *IEEE 67th Electronic Components and Technology Conference (ECTC)*, 2017, 2027-2032. IEEE.

2. ***Song, B.***, Moon, K.S. and Wong, C.P., Stretchable and Electrically Conductive Composites Fabricated from Polyurethane and Silver Nano/Microstructures. *67th IEEE Electronic Components and Technology Conference (ECTC)*, 2017, 2181-2186

3. ***Song, B.***, Li, L., Zhu, Y., Moon, K.S. and Wong, C.P., Miniaturized integrated micro-supercapacitors as efficient power sources for wearable and biocompatible electronic Devices. *IEEE 66th Electronic Components and Technology Conference (ECTC)*, **2016**, 2046-2050.

4. ***Song, B.***, Tuan, C.C., Li, L., Zhu, Y., Moon, K.S. and Wong, C.P., Highly conductive polyurethane/polyaniline-based composites for wearable electronic applications. *IEEE 66th Electronic Components and Technology Conference (ECTC)*, 2016, 2424-2429.

5. ***Song, B.***, Li, L., Wu, Z., Moon, K.S., Wu, J. and Wong, C.P., Solution-processed flexible solid-state micro-supercapacitors for on-chip energy storage devices.

IEEE 65th Electronic Components and Technology Conference (ECTC), 2015, 1483-1487.

6. ***Song, B.***, Wu, Z., Zhu, Y., Moon, K.S. and Wong, C.P., Three-dimensional graphene-based composite for flexible electronic applications, *IEEE 65th Electronic Components and Technology Conference (ECTC)*, 2015, 1803-1807.

7. ***Song, B.***, Wu. F., Moon, K.S., Bahr, R., Tentzeris, M., Wong, C.P., Stretchable, printable, and electrically conductive composites for wearable RF antennas, *68th IEEE Electronic Components and Technology Conference (ECTC)*, 2018. Accepted.

8. Saleem, A.M., Andersson, R., Desmaris, V., ***Song, B.*** and Wong, C.P., On-Chip Integrated Solid-State Micro-Supercapacitor. *67th IEEE Electronic Components and Technology Conference (ECTC)*, 2017, 173-178.

9. Le, T., ***Song, B.***, Liu, Q., Bahr, R.A., Moscato, S., Wong, C.P. and Tentzeris, M.M., A novel strain sensor based on 3D printing technology and 3D antenna design. *IEEE 65th Electronic Components and Technology Conference (ECTC)*, 2015, 981-986.

10. Le, T., Bahr, R.A., Tentzeris, M.M., ***Song, B.*** and Wong, C.P., A novel chipless RFID-based stretchable and wearable hand gesture sensor. *IEEE Microwave Conference (EuMC)*, 2015 *European*, 371-374.

11. Wu, F., ***Song, B.***, Moon, K.S., Wong, C.P., Cyanate Ester/Epoxy Co-Curing System with Thermal Stabilizers for High Temperature Stability, *68th IEEE Electronic Components and Technology Conference (ECTC)*, 2018. Accepted.

12. Hah, J., ***Song, B.***, Moon, K.S., Graham, S., Wong, C.P., Design and Surface Modification of PET Substrates using UV/Ozone Treatment for Roll-to-Roll Processed Solar Photovoltaic (PV) Module Packaging. *68th IEEE Electronic Components and Technology Conference (ECTC)*, 2018. Accepted.

13. Anderson, R., Saleem, A.M., Desmaris, V., ***Song, B.***, Wong, C.P., On-Chip Solid-State CMOS Compatible Micro-Supercapacitors, *68th IEEE Electronic Components and Technology Conference (ECTC)*, 2018. Accepted.

REFERENCES

[1] P. Simon and Y. Gogotsi, "Materials for electrochemical capacitors," *Nature materials,* vol. 7, p. 845, 2008.

[2] B. E. Conway, *Electrochemical supercapacitors: scientific fundamentals and technological applications*: Springer Science & Business Media, 2013.

[3] J. R. Miller and P. Simon, "Electrochemical capacitors for energy management," *Science Magazine,* vol. 321, pp. 651-652, 2008.

[4] J.-M. Tarascon and M. Armand, "Issues and challenges facing rechargeable lithium batteries," in *Materials For Sustainable Energy: A Collection of Peer-Reviewed Research and Review Articles from Nature Publishing Group*, ed: World Scientific, 2011, pp. 171-179.

[5] P. Simon, Y. Gogotsi, and B. Dunn, "Where do batteries end and supercapacitors begin?," *Science,* vol. 343, pp. 1210-1211, 2014.

[6] C. Liu, Z. Yu, D. Neff, A. Zhamu, and B. Z. Jang, "Graphene-based supercapacitor with an ultrahigh energy density," *Nano letters,* vol. 10, pp. 4863-4868, 2010.

[7] J. H. Masliyah and S. Bhattacharjee, *Electrokinetic and colloid transport phenomena*: John Wiley & Sons, 2006.

[8] M. S. Halper and J. C. Ellenbogen, "Supercapacitors: A brief overview," *The MITRE Corporation, McLean, Virginia, USA*, pp. 1-34, 2006.

[9] A. Pandolfo and A. Hollenkamp, "Carbon properties and their role in supercapacitors," *Journal of power sources,* vol. 157, pp. 11-27, 2006.

[10] M. Gouy, "Sur la constitution de la charge électrique à la surface d'un électrolyte," *J. Phys. Theor. Appl.,* vol. 9, pp. 457-468, 1910.

[11] D. L. Chapman, "LI. A contribution to the theory of electrocapillarity," *The London, Edinburgh, and Dublin philosophical magazine and journal of science,* vol. 25, pp. 475-481, 1913.

[12] L. L. Zhang and X. Zhao, "Carbon-based materials as supercapacitor electrodes," *Chemical Society Reviews,* vol. 38, pp. 2520-2531, 2009.

[13] O. Stern, "Zur theorie der elektrolytischen doppelschicht," *Berichte der Bunsengesellschaft für physikalische Chemie,* vol. 30, pp. 508-516, 1924.

[14] L. Pilon, H. Wang, and A. d'Entremont, "Recent advances in continuum modeling of interfacial and transport phenomena in electric double layer capacitors," *Journal of The Electrochemical Society,* vol. 162, pp. A5158-A5178, 2015.

[15] A. Rudge, J. Davey, I. Raistrick, S. Gottesfeld, and J. P. Ferraris, "Conducting polymers as active materials in electrochemical capacitors," *Journal of Power Sources,* vol. 47, pp. 89-107, 1994.

[16] V. Augustyn, P. Simon, and B. Dunn, "Pseudocapacitive oxide materials for high-rate electrochemical energy storage," *Energy & Environmental Science,* vol. 7, pp. 1597-1614, 2014.

[17] N.-L. Wu, "Nanocrystalline oxide supercapacitors," *Materials Chemistry and Physics,* vol. 75, pp. 6-11, 2002.

[18] A. M. Bryan, L. M. Santino, Y. Lu, S. Acharya, and J. M. D'Arcy, "Conducting polymers for pseudocapacitive energy storage," *Chemistry of Materials,* vol. 28, pp. 5989-5998, 2016.

[19] B. Zhao, L. Zhang, Q. Zhang, D. Chen, Y. Cheng, X. Deng, Y. Chen, R. Murphy, X. Xiong, and B. Song, "Rational Design of Nickel Hydroxide-Based Nanocrystals on Graphene for Ultrafast Energy Storage," *Advanced Energy Materials,* 2017.

[20] G. A. Snook, P. Kao, and A. S. Best, "Conducting-polymer-based supercapacitor devices and electrodes," *Journal of Power Sources,* vol. 196, pp. 1-12, 2011.

[21] Y. Zhang, H. Feng, X. Wu, L. Wang, A. Zhang, T. Xia, H. Dong, X. Li, and L. Zhang, "Progress of electrochemical capacitor electrode materials: A review," *International journal of hydrogen energy,* vol. 34, pp. 4889-4899, 2009.

[22] S. Dai, B. Zhao, C. Qu, D. Chen, D. Dang, B. Song, J. Fu, C. Hu, C.-P. Wong, and M. Liu, "Controlled synthesis of three-phase Ni x S y/rGO nanoflake electrodes for hybrid supercapacitors with high energy and power density," *Nano Energy,* vol. 33, pp. 522-531, 2017.

[23] G. Xiong, C. Meng, R. G. Reifenberger, P. P. Irazoqui, and T. S. Fisher, "A review of graphene-based electrochemical microsupercapacitors," *Electroanalysis,* vol. 26, pp. 30-51, 2014.

[24] E. Frackowiak and F. Beguin, "Carbon materials for the electrochemical storage of energy in capacitors," *Carbon,* vol. 39, pp. 937-950, 2001.

[25] J. R. Miller, "Electrochemical capacitor thermal management issues at high-rate cycling," *Electrochimica Acta,* vol. 52, pp. 1703-1708, 2006.

[26] Y. Jeong and A. Manthiram, "Nanocrystalline manganese oxides for electrochemical capacitors with neutral electrolytes," *Journal of the Electrochemical Society,* vol. 149, pp. A1419-A1422, 2002.

[27] J. Larminie and J. Lowry, *Electric vehicle technology explained*: John Wiley & Sons, 2012.

[28] R. Barrero, X. Tackoen, and J. Van Mierlo, "Analysis and configuration of supercapacitor based energy storage system on-board light rail vehicles," in *Power Electronics and Motion Control Conference, 2008. EPE-PEMC 2008. 13th*, 2008, pp. 1512-1517.

[29] J. R. Miller and A. F. Burke, "Electrochemical capacitors: challenges and opportunities for real-world applications," *The Electrochemical Society Interface*, vol. 17, p. 53, 2008.

[30] M. Zhi, C. Xiang, J. Li, M. Li, and N. Wu, "Nanostructured carbon–metal oxide composite electrodes for supercapacitors: a review," *Nanoscale*, vol. 5, pp. 72-88, 2013.

[31] A. K. Geim and K. S. Novoselov, "The rise of graphene," *Nature materials*, vol. 6, p. 183, 2007.

[32] K. S. Novoselov, A. K. Geim, S. V. Morozov, D. Jiang, Y. Zhang, S. V. Dubonos, I. V. Grigorieva, and A. A. Firsov, "Electric field effect in atomically thin carbon films," *science*, vol. 306, pp. 666-669, 2004.

[33] M. Terrones, A. R. Botello-Méndez, J. Campos-Delgado, F. López-Urías, Y. I. Vega-Cantú, F. J. Rodríguez-Macías, A. L. Elías, E. Munoz-Sandoval, A. G. Cano-Márquez, and J.-C. Charlier, "Graphene and graphite nanoribbons: Morphology, properties, synthesis, defects and applications," *Nano Today*, vol. 5, pp. 351-372, 2010.

[34] Y. Zhang, Y.-W. Tan, H. L. Stormer, and P. Kim, "Experimental observation of the quantum Hall effect and Berry's phase in graphene," *nature*, vol. 438, p. 201, 2005.

[35] J. C. Meyer, A. K. Geim, M. I. Katsnelson, K. S. Novoselov, T. J. Booth, and S. Roth, "The structure of suspended graphene sheets," *Nature*, vol. 446, p. 60, 2007.

[36] R. Raccichini, A. Varzi, S. Passerini, and B. Scrosati, "The role of graphene for electrochemical energy storage," *Nature materials*, vol. 14, p. 271, 2015.

[37] I. Calizo, A. Balandin, W. Bao, F. Miao, and C. Lau, "Temperature dependence of the Raman spectra of graphene and graphene multilayers," *Nano letters*, vol. 7, pp. 2645-2649, 2007.

[38] S. Bae, H. Kim, Y. Lee, X. Xu, J.-S. Park, Y. Zheng, J. Balakrishnan, T. Lei, H. R. Kim, and Y. I. Song, "Roll-to-roll production of 30-inch graphene films for transparent electrodes," *Nature nanotechnology*, vol. 5, p. 574, 2010.

[39] G. Eda, G. Fanchini, and M. Chhowalla, "Large-area ultrathin films of reduced graphene oxide as a transparent and flexible electronic material," *Nature nanotechnology*, vol. 3, p. 270, 2008.

[40] K. S. Kim, Y. Zhao, H. Jang, S. Y. Lee, J. M. Kim, K. S. Kim, J.-H. Ahn, P. Kim, J.-Y. Choi, and B. H. Hong, "Large-scale pattern growth of graphene films for stretchable transparent electrodes," *nature,* vol. 457, p. 706, 2009.

[41] B. Song, Z. Wu, Y. Zhu, K.-s. Moon, and C. Wong, "Three-dimensional graphene-based composite for flexible electronic applications," in *Electronic Components and Technology Conference (ECTC), 2015 IEEE 65th*, 2015, pp. 1803-1807.

[42] K. S. Novoselov, V. Fal, L. Colombo, P. Gellert, M. Schwab, and K. Kim, "A roadmap for graphene," *Nature,* vol. 490, p. 192, 2012.

[43] X. Li, W. Cai, J. An, S. Kim, J. Nah, D. Yang, R. Piner, A. Velamakanni, I. Jung, and E. Tutuc, "Large-area synthesis of high-quality and uniform graphene films on copper foils," *Science,* vol. 324, pp. 1312-1314, 2009.

[44] X. Li, W. Cai, L. Colombo, and R. S. Ruoff, "Evolution of graphene growth on Ni and Cu by carbon isotope labeling," *Nano letters,* vol. 9, pp. 4268-4272, 2009.

[45] J. N. Coleman, "Liquid exfoliation of defect-free graphene," *Accounts of chemical research,* vol. 46, pp. 14-22, 2012.

[46] S. Pei and H.-M. Cheng, "The reduction of graphene oxide," *Carbon,* vol. 50, pp. 3210-3228, 2012.

[47] D. Chen, H. Feng, and J. Li, "Graphene oxide: preparation, functionalization, and electrochemical applications," *Chemical reviews,* vol. 112, pp. 6027-6053, 2012.

[48] X. Li, G. Zhang, X. Bai, X. Sun, X. Wang, E. Wang, and H. Dai, "Highly conducting graphene sheets and Langmuir–Blodgett films," *Nature nanotechnology,* vol. 3, p. 538, 2008.

[49] F. Kim, L. J. Cote, and J. Huang, "Graphene Oxide: Surface Activity and Two-Dimensional Assembly," *Advanced Materials,* vol. 22, pp. 1954-1958, 2010.

[50] W. Gao, "The chemistry of graphene oxide," in *Graphene oxide*, ed: Springer, 2015, pp. 61-95.

[51] H. C. Schniepp, J.-L. Li, M. J. McAllister, H. Sai, M. Herrera-Alonso, D. H. Adamson, R. K. Prud'homme, R. Car, D. A. Saville, and I. A. Aksay, "Functionalized single graphene sheets derived from splitting graphite oxide," *The Journal of Physical Chemistry B,* vol. 110, pp. 8535-8539, 2006.

[52] M. J. McAllister, J.-L. Li, D. H. Adamson, H. C. Schniepp, A. A. Abdala, J. Liu, M. Herrera-Alonso, D. L. Milius, R. Car, and R. K. Prud'homme, "Single sheet functionalized graphene by oxidation and thermal expansion of graphite," *Chemistry of materials,* vol. 19, pp. 4396-4404, 2007.

[53] L. J. Cote, R. Cruz-Silva, and J. Huang, "Flash reduction and patterning of graphite oxide and its polymer composite," *Journal of the American Chemical Society,* vol. 131, pp. 11027-11032, 2009.

[54] S. Stankovich, D. A. Dikin, R. D. Piner, K. A. Kohlhaas, A. Kleinhammes, Y. Jia, Y. Wu, S. T. Nguyen, and R. S. Ruoff, "Synthesis of graphene-based nanosheets via chemical reduction of exfoliated graphite oxide," *carbon,* vol. 45, pp. 1558-1565, 2007.

[55] X. Lu, L. Li, B. Song, K.-s. Moon, N. Hu, G. Liao, T. Shi, and C. Wong, "Mechanistic investigation of the graphene functionalization using p-phenylenediamine and its application for supercapacitors," *Nano Energy,* vol. 17, pp. 160-170, 2015.

[56] G. G. Jang, B. Song, K.-s. Moon, C.-P. Wong, J. K. Keum, and M. Z. Hu, "Particle size effect in porous film electrodes of ligand-modified graphene for enhanced supercapacitor performance," *Carbon,* vol. 119, pp. 296-304, 2017.

[57] H. J. Shin, K. K. Kim, A. Benayad, S. M. Yoon, H. K. Park, I. S. Jung, M. H. Jin, H. K. Jeong, J. M. Kim, and J. Y. Choi, "Efficient reduction of graphite oxide by sodium borohydride and its effect on electrical conductance," *Advanced Functional Materials,* vol. 19, pp. 1987-1992, 2009.

[58] S. Pei, J. Zhao, J. Du, W. Ren, and H.-M. Cheng, "Direct reduction of graphene oxide films into highly conductive and flexible graphene films by hydrohalic acids," *Carbon,* vol. 48, pp. 4466-4474, 2010.

[59] Y. Xu, K. Sheng, C. Li, and G. Shi, "Self-assembled graphene hydrogel via a one-step hydrothermal process," *ACS nano,* vol. 4, pp. 4324-4330, 2010.

[60] H. Zhang, T. Kuila, N. H. Kim, D. S. Yu, and J. H. Lee, "Simultaneous reduction, exfoliation, and nitrogen doping of graphene oxide via a hydrothermal reaction for energy storage electrode materials," *Carbon,* vol. 69, pp. 66-78, 2014.

[61] Z. Lin, Y. Liu, Y. Yao, O. J. Hildreth, Z. Li, K. Moon, and C.-p. Wong, "Superior capacitance of functionalized graphene," *The Journal of Physical Chemistry C,* vol. 115, pp. 7120-7125, 2011.

[62] J. Xia, F. Chen, J. Li, and N. Tao, "Measurement of the quantum capacitance of graphene," *Nature nanotechnology,* vol. 4, p. 505, 2009.

[63] Y. Zhu, S. Murali, M. D. Stoller, K. Ganesh, W. Cai, P. J. Ferreira, A. Pirkle, R. M. Wallace, K. A. Cychosz, and M. Thommes, "Carbon-based supercapacitors produced by activation of graphene," *science,* vol. 332, pp. 1537-1541, 2011.

[64] Y. Xu, Z. Lin, X. Zhong, X. Huang, N. O. Weiss, Y. Huang, and X. Duan, "Holey graphene frameworks for highly efficient capacitive energy storage," *Nature communications,* vol. 5, p. 4554, 2014.

[65] L. L. Zhang, Z. Xiong, and X. Zhao, "Pillaring chemically exfoliated graphene oxide with carbon nanotubes for photocatalytic degradation of dyes under visible light irradiation," *Acs Nano,* vol. 4, pp. 7030-7036, 2010.

[66] J. Liu, J. Tang, and J. J. Gooding, "Strategies for chemical modification of graphene and applications of chemically modified graphene," *Journal of Materials Chemistry,* vol. 22, pp. 12435-12452, 2012.

[67] Z.-K. Wu, Z. Lin, L. Li, B. Song, C.-C. Tuan, Z. Li, K.-s. Moon, S.-L. Bai, and C.-P. Wong, "Capacitance enhancement by electrochemically active benzene derivatives for graphene-based supercapacitors," *RSC Advances,* vol. 5, pp. 84113-84118, 2015.

[68] K. Zhang, L. Mao, L. L. Zhang, H. S. O. Chan, X. S. Zhao, and J. Wu, "Surfactant-intercalated, chemically reduced graphene oxide for high performance supercapacitor electrodes," *Journal of Materials Chemistry,* vol. 21, pp. 7302-7307, 2011.

[69] S. Cho, M. Kim, and J. Jang, "Screen-printable and flexible RuO2 nanoparticle-decorated PEDOT: PSS/graphene nanocomposite with enhanced electrical and electrochemical performances for high-capacity supercapacitor," *ACS applied materials & interfaces,* vol. 7, pp. 10213-10227, 2015.

[70] N. A. Kumar, H.-J. Choi, Y. R. Shin, D. W. Chang, L. Dai, and J.-B. Baek, "Polyaniline-grafted reduced graphene oxide for efficient electrochemical supercapacitors," *ACS nano,* vol. 6, pp. 1715-1723, 2012.

[71] B. Song, J. Zhao, M. Wang, J. Mullavey, Y. Zhu, Z. Geng, D. Chen, Y. Ding, K.-s. Moon, and M. Liu, "Systematic study on structural and electronic properties of diamine/triamine functionalized graphene networks for supercapacitor application," *Nano Energy,* vol. 31, pp. 183-193, 2017.

[72] S. Stankovich, R. D. Piner, S. T. Nguyen, and R. S. Ruoff, "Synthesis and exfoliation of isocyanate-treated graphene oxide nanoplatelets," *Carbon,* vol. 44, pp. 3342-3347, 2006.

[73] J. R. Lomeda, C. D. Doyle, D. V. Kosynkin, W.-F. Hwang, and J. M. Tour, "Diazonium functionalization of surfactant-wrapped chemically converted graphene sheets," *Journal of the American Chemical Society,* vol. 130, pp. 16201-16206, 2008.

[74] Z.-F. Li, H. Zhang, Q. Liu, Y. Liu, L. Stanciu, and J. Xie, "Covalently-grafted polyaniline on graphene oxide sheets for high performance electrochemical supercapacitors," *Carbon,* vol. 71, pp. 257-267, 2014.

[75] J. An, J. Liu, Y. Zhou, H. Zhao, Y. Ma, M. Li, M. Yu, and S. Li, "Polyaniline-grafted graphene hybrid with amide groups and its use in supercapacitors," *The Journal of Physical Chemistry C,* vol. 116, pp. 19699-19708, 2012.

[76] G. G. Jang, B. Song, L. Li, J. K. Keum, Y. Jiang, A. Hunt, K.-s. Moon, C.-P. Wong, and M. Z. Hu, "Microscopic vertical orientation of nano-interspaced graphene architectures in deposit films as electrodes for enhanced supercapacitor performance," *Nano Energy,* vol. 32, pp. 88-95, 2017.

[77] B. Song, C.-C. Tuan, X. Huang, L. Li, K.-S. Moon, and C.-P. Wong, "Sulfonated polyaniline decorated graphene nanocomposites as supercapacitor electrodes," *Materials Letters,* vol. 166, pp. 12-15, 2016.

[78] J. Han, L. L. Zhang, S. Lee, J. Oh, K.-S. Lee, J. R. Potts, J. Ji, X. Zhao, R. S. Ruoff, and S. Park, "Generation of B-doped graphene nanoplatelets using a solution process and their supercapacitor applications," *ACS nano,* vol. 7, pp. 19-26, 2012.

[79] H. M. Jeong, J. W. Lee, W. H. Shin, Y. J. Choi, H. J. Shin, J. K. Kang, and J. W. Choi, "Nitrogen-doped graphene for high-performance ultracapacitors and the importance of nitrogen-doped sites at basal planes," *Nano letters,* vol. 11, pp. 2472-2477, 2011.

[80] B. Song, J. I. Choi, Y. Zhu, Z. Geng, L. Zhang, Z. Lin, C.-c. Tuan, K.-s. Moon, and C.-p. Wong, "Molecular level study of graphene networks functionalized with phenylenediamine monomers for supercapacitor electrodes," *Chemistry of Materials,* vol. 28, pp. 9110-9121, 2016.

[81] G. Wang, L. Zhang, and J. Zhang, "A review of electrode materials for electrochemical supercapacitors," *Chemical Society Reviews,* vol. 41, pp. 797-828, 2012.

[82] M. Armand, F. Endres, D. R. MacFarlane, H. Ohno, and B. Scrosati, "Ionic-liquid materials for the electrochemical challenges of the future," *Nature materials,* vol. 8, p. 621, 2009.

[83] T. Tsuda and C. L. Hussey, "Electrochemical applications of room-temperature ionic liquids," *Interface-Electrochemical Society,* vol. 16, pp. 42-49, 2007.

[84] F. Endres, A. Abbot, and D. MacFarlane, "Electrodeposition from Ionic Liquids, Wiley-VCH," *Electrodeposition from Ionic Liquids, Wiley-VCH,* 2008.

[85] B. Song, K.-S. Moon, and C.-P. Wong, "Recent developments in design and fabrication of graphene-based interdigital micro-supercapacitors for miniaturized energy storage devices," *IEEE Transactions on Components, Packaging and Manufacturing Technology,* vol. 6, pp. 1752-1765, 2016.

[86] B. Song, F. Wu, Y. Zhu, Z. Hou, K.-s. Moon, and C.-P. Wong, "Effect of polymer binders on graphene-based free-standing electrodes for supercapacitors," *Electrochimica Acta,* vol. 267, pp. 213-221, 2018.

[87] H. Zhao, Z. Wang, P. Lu, M. Jiang, F. Shi, X. Song, Z. Zheng, X. Zhou, Y. Fu, and G. Abdelbast, "Toward practical application of functional conductive polymer

binder for a high-energy lithium-ion battery design," *Nano letters*, vol. 14, pp. 6704-6710, 2014.

[88] G. Zhang, W. Li, K. Xie, F. Yu, and H. Huang, "A One-Step and Binder-Free Method to Fabricate Hierarchical Nickel-Based Supercapacitor Electrodes with Excellent Performance," *Advanced Functional Materials*, vol. 23, pp. 3675-3681, 2013.

[89] N. Jäckel, D. Weingarth, M. Zeiger, M. Aslan, I. Grobelsek, and V. Presser, "Comparison of carbon onions and carbon blacks as conductive additives for carbon supercapacitors in organic electrolytes," *Journal of Power Sources*, vol. 272, pp. 1122-1133, 2014.

[90] Z.-S. Wu, X. Feng, and H.-M. Cheng, "Recent advances in graphene-based planar micro-supercapacitors for on-chip energy storage," *National Science Review*, vol. 1, pp. 277-292, 2014.

[91] S. Chalasani and J. M. Conrad, "A survey of energy harvesting sources for embedded systems," in *Southeastcon, 2008. IEEE*, 2008, pp. 442-447.

[92] Y. K. Tan and S. K. Panda, "Energy harvesting from hybrid indoor ambient light and thermal energy sources for enhanced performance of wireless sensor nodes," *Industrial Electronics, IEEE Transactions on*, vol. 58, pp. 4424-4435, 2011.

[93] Z. L. Wang and W. Wu, "Nanotechnology-Enabled Energy Harvesting for Self-Powered Micro-/Nanosystems," *Angewandte Chemie International Edition*, vol. 51, pp. 11700-11721, 2012.

[94] Z. L. Wang, "Towards self-powered nanosystems: from nanogenerators to nanopiezotronics," *Advanced Functional Materials*, vol. 18, pp. 3553-3567, 2008.

[95] J.-H. Sung, S.-J. Kim, and K.-H. Lee, "Fabrication of microcapacitors using conducting polymer microelectrodes," *Journal of power sources*, vol. 124, pp. 343-350, 2003.

[96] A. Saleem, R. Andersson, V. Desmaris, B. Song, and C. Wong, "On-Chip Integrated Solid-State Micro-Supercapacitor," in *Electronic Components and Technology Conference (ECTC), 2017 IEEE 67th*, 2017, pp. 173-178.

[97] M. Beidaghi and Y. Gogotsi, "Capacitive energy storage in micro-scale devices: recent advances in design and fabrication of micro-supercapacitors," *Energy & Environmental Science*, vol. 7, pp. 867-884, 2014.

[98] Y. Gogotsi and P. Simon, "True performance metrics in electrochemical energy storage," *Science Magazine*, vol. 334, pp. 917-918, 2011.

[99] J. Chmiola, C. Largeot, P.-L. Taberna, P. Simon, and Y. Gogotsi, "Monolithic carbide-derived carbon films for micro-supercapacitors," *Science,* vol. 328, pp. 480-483, 2010.

[100] D. Pech, M. Brunet, H. Durou, P. Huang, V. Mochalin, Y. Gogotsi, P.-L. Taberna, and P. Simon, "Ultrahigh-power micrometre-sized supercapacitors based on onion-like carbon," *Nature nanotechnology,* vol. 5, pp. 651-654, 2010.

[101] J. H. Lim, D. J. Choi, H.-K. Kim, W. I. Cho, and Y. S. Yoon, "Thin film supercapacitors using a sputtered RuO2 electrode," *Journal of The Electrochemical Society,* vol. 148, pp. A275-A278, 2001.

[102] Y. Honda, T. Haramoto, M. Takeshige, H. Shiozaki, T. Kitamura, and M. Ishikawa, "Aligned MWCNT sheet electrodes prepared by transfer methodology providing high-power capacitor performance," *Electrochemical and Solid-State Letters,* vol. 10, pp. A106-A110, 2007.

[103] S. W. Lee, B.-S. Kim, S. Chen, Y. Shao-Horn, and P. T. Hammond, "Layer-by-layer assembly of all carbon nanotube ultrathin films for electrochemical applications," *Journal of the American Chemical Society,* vol. 131, pp. 671-679, 2008.

[104] M. Singh, H. M. Haverinen, P. Dhagat, and G. E. Jabbour, "Inkjet printing—process and its applications," *Advanced materials,* vol. 22, pp. 673-685, 2010.

[105] W. W. Liu, Y. Q. Feng, X. B. Yan, J. T. Chen, and Q. J. Xue, "Superior Micro-Supercapacitors Based on Graphene Quantum Dots," *Advanced Functional Materials,* vol. 23, pp. 4111-4122, 2013.

[106] Y. Wang, S. Xiang, M. R. Pulugurtha, H. Sharma, B. Williams, and R. Tummala, "All-Solution Thin-film Capacitors and Their Deposition in Trench and Through-Via Structures," *Components, Packaging and Manufacturing Technology, IEEE Transactions on,* vol. 3, pp. 688-695, 2013.

[107] K. Wang, W. Zou, B. Quan, A. Yu, H. Wu, P. Jiang, and Z. Wei, "An All-Solid-State Flexible Micro-supercapacitor on a Chip," *Advanced Energy Materials,* vol. 1, pp. 1068-1072, 2011.

[108] Z. Niu, L. Zhang, L. Liu, B. Zhu, H. Dong, and X. Chen, "All-Solid-State Flexible Ultrathin Micro-Supercapacitors Based on Graphene," *Advanced Materials,* vol. 25, pp. 4035-4042, 2013.

[109] P. Yang, X. Xiao, Y. Li, Y. Ding, P. Qiang, X. Tan, W. Mai, Z. Lin, W. Wu, and T. Li, "Hydrogenated ZnO core–shell nanocables for flexible supercapacitors and self-powered systems," *ACS nano,* vol. 7, pp. 2617-2626, 2013.

[110] S. Hashmi, S. Suematsu, and K. Naoi, "All solid-state redox supercapacitors based on supramolecular 1, 5-diaminoanthraquinone oligomeric electrode and polymeric electrolytes," *Journal of power sources,* vol. 137, pp. 145-151, 2004.

[111] C. Meng, C. Liu, L. Chen, C. Hu, and S. Fan, "Highly flexible and all-solid-state paperlike polymer supercapacitors," *Nano letters,* vol. 10, pp. 4025-4031, 2010.

[112] G. Prajapati, R. Roshan, and P. Gupta, "Effect of plasticizer on ionic transport and dielectric properties of PVA–H 3 PO 4 proton conducting polymeric electrolytes," *Journal of Physics and Chemistry of Solids,* vol. 71, pp. 1717-1723, 2010.

[113] G. Ma, M. Dong, K. Sun, E. Feng, H. Peng, and Z. Lei, "A redox mediator doped gel polymer as an electrolyte and separator for a high performance solid state supercapacitor," *Journal of Materials Chemistry A,* vol. 3, pp. 4035-4041, 2015.

[114] J. Le Bideau, L. Viau, and A. Vioux, "Ionogels, ionic liquid based hybrid materials," *Chemical Society Reviews,* vol. 40, pp. 907-925, 2011.

[115] J. Feng, X. Sun, C. Wu, L. Peng, C. Lin, S. Hu, J. Yang, and Y. Xie, "Metallic few-layered VS2 ultrathin nanosheets: high two-dimensional conductivity for in-plane supercapacitors," *Journal of the American Chemical Society,* vol. 133, pp. 17832-17838, 2011.

[116] S. Wang, B. Hsia, C. Carraro, and R. Maboudian, "High-performance all solid-state micro-supercapacitor based on patterned photoresist-derived porous carbon electrodes and an ionogel electrolyte," *Journal of Materials Chemistry A,* vol. 2, pp. 7997-8002, 2014.

[117] Y. Yoon, K. Lee, C. Baik, H. Yoo, M. Min, Y. Park, S. M. Lee, and H. Lee, "Anti-Solvent Derived Non-Stacked Reduced Graphene Oxide for High Performance Supercapacitors," *Advanced materials,* vol. 25, pp. 4437-4444, 2013.

[118] W. Ai, X. Cao, Z. Sun, J. Jiang, Z. Du, L. Xie, Y. Wang, X. Wang, H. Zhang, and W. Huang, "Redox-crosslinked graphene networks with enhanced electrochemical capacitance," *Journal of Materials Chemistry A,* vol. 2, pp. 12924-12930, 2014.

[119] H. N. Tien, N. T. M. Hien, E.-S. Oh, J. Chung, E. J. Kim, W. M. Choi, B.-S. Kong, and S. H. Hur, "Synthesis of a highly conductive and large surface area graphene oxide hydrogel and its use in a supercapacitor," *Journal of Materials Chemistry A,* vol. 1, pp. 208-211, 2013.

[120] Z.-Y. Sui, Y. Cui, J.-H. Zhu, and B.-H. Han, "Preparation of three-dimensional graphene oxide–polyethylenimine porous materials as dye and gas adsorbents," *ACS applied materials & interfaces,* vol. 5, pp. 9172-9179, 2013.

[121] W. Wan, L. Li, Z. Zhao, H. Hu, X. Hao, D. A. Winkler, L. Xi, T. C. Hughes, and J. Qiu, "Ultrafast fabrication of covalently cross-linked multifunctional graphene oxide monoliths," *Advanced Functional Materials,* vol. 24, pp. 4915-4921, 2014.

[122] W.-S. Hung, C.-H. Tsou, M. De Guzman, Q.-F. An, Y.-L. Liu, Y.-M. Zhang, C.-C. Hu, K.-R. Lee, and J.-Y. Lai, "Cross-linking with diamine monomers to prepare composite graphene oxide-framework membranes with varying d-spacing," *Chemistry of Materials,* vol. 26, pp. 2983-2990, 2014.

[123] J. P. Perdew, K. Burke, and M. Ernzerhof, "Generalized gradient approximation made simple," *Physical review letters,* vol. 77, p. 3865, 1996.

[124] B. Delley, "From molecules to solids with the DMol3 approach," *The Journal of chemical physics,* vol. 113, pp. 7756-7764, 2000.

[125] W. Gao, L. B. Alemany, L. Ci, and P. M. Ajayan, "New insights into the structure and reduction of graphite oxide," *Nature chemistry,* vol. 1, pp. 403-408, 2009.

[126] B. Song, L. Li, Z. Lin, Z.-K. Wu, K.-s. Moon, and C.-P. Wong, "Water-dispersible graphene/polyaniline composites for flexible micro-supercapacitors with high energy densities," *Nano Energy,* vol. 16, pp. 470-478, 2015.

[127] W. Chen, L. Yan, and P. Bangal, "Chemical reduction of graphene oxide to graphene by sulfur-containing compounds," *The Journal of Physical Chemistry C,* vol. 114, pp. 19885-19890, 2010.

[128] Z.-K. Wu, Z. Lin, L. Li, B. Song, K.-s. Moon, S.-L. Bai, and C.-P. Wong, "Flexible micro-supercapacitor based on in-situ assembled graphene on metal template at room temperature," *Nano Energy,* vol. 10, pp. 222-228, 2014.

[129] K. Zhang, L. L. Zhang, X. Zhao, and J. Wu, "Graphene/polyaniline nanofiber composites as supercapacitor electrodes," *Chemistry of Materials,* vol. 22, pp. 1392-1401, 2010.

[130] I. K. Moon, J. Lee, R. S. Ruoff, and H. Lee, "Reduced graphene oxide by chemical graphitization," *Nature communications,* vol. 1, p. 73, 2010.

[131] B. Song, C. Sizemore, L. Y. Li, X. G. Huang, Z. Y. Lin, K. S. Moon, and C. P. Wong, "Triethanolamine functionalized graphene-based composites for high performance supercapacitors," *Journal of Materials Chemistry A,* vol. 3, pp. 21789-21796, 2015.

[132] K. Tasaki, "Poly (oxyethylene)-water interactions: a molecular dynamics study," *Journal of the American Chemical Society,* vol. 118, pp. 8459-8469, 1996.

[133] J. H. Lee, N. Park, B. G. Kim, D. S. Jung, K. Im, J. Hur, and J. W. Choi, "Restacking-inhibited 3D reduced graphene oxide for high performance supercapacitor electrodes," *ACS nano,* vol. 7, pp. 9366-9374, 2013.

[134] H. Li, Y. Wang, Y. Shi, J. Li, L. He, and H. Y. Yang, "Large scale synthesized sulphonated reduced graphene oxide: a high performance material for electrochemical capacitors," *RSC Advances,* vol. 3, pp. 14954-14959, 2013.

[135] Y. Yu, Y. Sun, C. Cao, S. Yang, H. Liu, P. Li, P. Huang, and W. Song, "Graphene-based composite supercapacitor electrodes with diethylene glycol as inter-layer spacer," *Journal of Materials Chemistry A,* vol. 2, pp. 7706-7710, 2014.

[136] X. Li, J. Rong, and B. Wei, "Electrochemical behavior of single-walled carbon nanotube supercapacitors under compressive stress," *ACS nano,* vol. 4, pp. 6039-6049, 2010.

[137] R. Lin, P.-L. Taberna, J. Chmiola, D. Guay, Y. Gogotsi, and P. Simon, "Microelectrode study of pore size, ion size, and solvent effects on the charge/discharge behavior of microporous carbons for electrical double-layer capacitors," *Journal of the Electrochemical Society,* vol. 156, pp. A7-A12, 2009.

[138] W.-w. Liu, X.-b. Yan, J.-w. Lang, C. Peng, and Q.-j. Xue, "Flexible and conductive nanocomposite electrode based on graphene sheets and cotton cloth for supercapacitor," *Journal of Materials Chemistry,* vol. 22, pp. 17245-17253, 2012.

[139] G. P. Hao, A. H. Lu, W. Dong, Z. Y. Jin, X. Q. Zhang, J. T. Zhang, and W. C. Li, "Sandwich-Type Microporous Carbon Nanosheets for Enhanced Supercapacitor Performance," *Advanced Energy Materials,* vol. 3, pp. 1421-1427, 2013.

[140] S. Vivekchand, C. S. Rout, K. Subrahmanyam, A. Govindaraj, and C. Rao, "Graphene-based electrochemical supercapacitors," *Journal of Chemical Sciences,* vol. 120, pp. 9-13, 2008.

[141] Y. Chen, X. Zhang, H. Zhang, X. Sun, D. Zhang, and Y. Ma, "High-performance supercapacitors based on a graphene–activated carbon composite prepared by chemical activation," *RSC Advances,* vol. 2, pp. 7747-7753, 2012.

[142] Z. Xu, Z. Li, C. M. Holt, X. Tan, H. Wang, B. S. Amirkhiz, T. Stephenson, and D. Mitlin, "Electrochemical supercapacitor electrodes from sponge-like graphene nanoarchitectures with ultrahigh power density," *The journal of physical chemistry letters,* vol. 3, pp. 2928-2933, 2012.

[143] J. Wang, B. Ding, X. Hao, Y. Xu, Y. Wang, L. Shen, H. Dou, and X. Zhang, "A modified molten-salt method to prepare graphene electrode with high capacitance and low self-discharge rate," *Carbon,* vol. 102, pp. 255-261, 2016.

[144] Q. Zhang, J. Rong, D. Ma, and B. Wei, "The governing self-discharge processes in activated carbon fabric-based supercapacitors with different organic electrolytes," *Energy & Environmental Science,* vol. 4, pp. 2152-2159, 2011.

[145] B. E. Conway, W. Pell, and T. Liu, "Diagnostic analyses for mechanisms of self-discharge of electrochemical capacitors and batteries," *Journal of Power Sources,* vol. 65, pp. 53-59, 1997.

[146] Q. Zhang, C. Cai, J. Qin, and B. Wei, "Tunable self-discharge process of carbon nanotube based supercapacitors," *Nano Energy,* vol. 4, pp. 14-22, 2014.

[147] L. Chen, Y. Chen, J. Wu, J. Wang, H. Bai, and L. Li, "Electrochemical supercapacitor with polymeric active electrolyte," *Journal of Materials Chemistry A*, vol. 2, pp. 10526-10531, 2014.

[148] M. Jisha, Y. J. Hwang, J. S. Shin, K. S. Nahm, T. P. Kumar, K. Karthikeyan, N. Dhanikaivelu, D. Kalpana, N. Renganathan, and A. M. Stephan, "Electrochemical characterization of supercapacitors based on carbons derived from coffee shells," *Materials Chemistry and Physics*, vol. 115, pp. 33-39, 2009.

[149] M. F. El-Kady and R. B. Kaner, "Scalable fabrication of high-power graphene micro-supercapacitors for flexible and on-chip energy storage," *Nature communications*, vol. 4, p. 1475, 2013.

[150] A. C. Ferrari and J. Robertson, "Interpretation of Raman spectra of disordered and amorphous carbon," *Physical review B*, vol. 61, p. 14095, 2000.

[151] M. Iqbal, A. K. Singh, M. Iqbal, and J. Eom, "Raman fingerprint of doping due to metal adsorbates on graphene," *Journal of Physics: Condensed Matter*, vol. 24, p. 335301, 2012.

[152] S. Niyogi, E. Bekyarova, M. E. Itkis, H. Zhang, K. Shepperd, J. Hicks, M. Sprinkle, C. Berger, C. N. Lau, and W. A. Deheer, "Spectroscopy of covalently functionalized graphene," *Nano letters*, vol. 10, pp. 4061-4066, 2010.

[153] Z. Lin, G. Waller, Y. Liu, M. Liu, and C. P. Wong, "Facile Synthesis of Nitrogen-Doped Graphene via Pyrolysis of Graphene Oxide and Urea, and its Electrocatalytic Activity toward the Oxygen-Reduction Reaction," *Advanced Energy Materials*, vol. 2, pp. 884-888, 2012.

[154] O. C. Compton, D. A. Dikin, K. W. Putz, L. C. Brinson, and S. T. Nguyen, "Electrically Conductive "Alkylated" Graphene Paper via Chemical Reduction of Amine-Functionalized Graphene Oxide Paper," *Advanced Materials*, vol. 22, pp. 892-896, 2010.

[155] H. Zhang, K. Wang, X. Zhang, H. Lin, X. Sun, C. Li, and Y. Ma, "Self-generating graphene and porous nanocarbon composites for capacitive energy storage," *Journal of Materials Chemistry A*, vol. 3, pp. 11277-11286, 2015.

[156] X. Liu, P. Shang, Y. Zhang, X. Wang, Z. Fan, B. Wang, and Y. Zheng, "Three-dimensional and stable polyaniline-grafted graphene hybrid materials for supercapacitor electrodes," *Journal of Materials Chemistry A*, vol. 2, pp. 15273-15278, 2014.

[157] W. S. V. Lee, M. Leng, M. Li, X. L. Huang, and J. M. Xue, "Sulphur-functionalized graphene towards high performance supercapacitor," *Nano Energy*, vol. 12, pp. 250-257, 2015.

[158] Z. Wen, X. Wang, S. Mao, Z. Bo, H. Kim, S. Cui, G. Lu, X. Feng, and J. Chen, "Crumpled Nitrogen-Doped Graphene Nanosheets with Ultrahigh Pore Volume for High-Performance Supercapacitor," *Advanced materials,* vol. 24, pp. 5610-5616, 2012.

[159] D. S. Yu, T. Kuila, N. H. Kim, P. Khanra, and J. H. Lee, "Effects of covalent surface modifications on the electrical and electrochemical properties of graphene using sodium 4-aminoazobenzene-4′-sulfonate," *Carbon,* vol. 54, pp. 310-322, 2013.

[160] P. Du, H. C. Liu, C. Yi, K. Wang, and X. Gong, "Polyaniline-modified oriented graphene hydrogel film as the free-standing electrode for flexible solid-state supercapacitors," *ACS applied materials & interfaces,* vol. 7, pp. 23932-23940, 2015.

[161] H. P. De Oliveira, S. A. Sydlik, and T. M. Swager, "Supercapacitors from free-standing polypyrrole/graphene nanocomposites," *The Journal of Physical Chemistry C,* vol. 117, pp. 10270-10276, 2013.

[162] L. Lai, H. Yang, L. Wang, B. K. Teh, J. Zhong, H. Chou, L. Chen, W. Chen, Z. Shen, and R. S. Ruoff, "Preparation of supercapacitor electrodes through selection of graphene surface functionalities," *ACS nano,* vol. 6, pp. 5941-5951, 2012.

[163] T. Liu, L. Finn, M. Yu, H. Wang, T. Zhai, X. Lu, Y. Tong, and Y. Li, "Polyaniline and polypyrrole pseudocapacitor electrodes with excellent cycling stability," *Nano letters,* vol. 14, pp. 2522-2527, 2014.

[164] Z. Jin and B. L. Lucht, "Poly-p-phenylene phosphine/polyaniline alternating copolymers: Electronic delocalization through phosphorus," *Journal of the American Chemical Society,* vol. 127, pp. 5586-5595, 2005.

[165] F. Marken, A. Blythe, R. G. Compton, S. D. Bull, and S. G. Davies, "Sulfide accumulation and sensing based on electrochemical processes in microdroplets of N 1-[4-(dihexylamino) phenyl]-N 1, N 4, N 4-trihexyl-1, 4-phenylenediamine," *Chemical Communications,* pp. 1823-1824, 1999.

[166] Y. Yan, T. Kuila, N. H. Kim, S. H. Lee, and J. H. Lee, "N-doped carbon layer coated thermally exfoliated graphene and its capacitive behavior in redox active electrolyte," *Carbon,* vol. 85, pp. 60-71, 2015.

[167] J. Stejskal, "Polymers of phenylenediamines," *Progress in Polymer Science,* vol. 41, pp. 1-31, 2015.

[168] Z. Liu, H. Zhou, Z. Huang, W. Wang, F. Zeng, and Y. Kuang, "Graphene covalently functionalized with poly (p-phenylenediamine) as high performance electrode material for supercapacitors," *Journal of materials chemistry. A, Materials for energy and sustainability,* vol. 1, pp. 3454-3462, 2013.

[169] I. R. Shapiro, S. D. Solares, M. J. Esplandiu, L. A. Wade, W. A. Goddard, and C. P. Collier, "Influence of elastic deformation on single-wall carbon nanotube atomic force microscopy probe resolution," *Journal of Physical Chemistry B,* vol. 108, pp. 13613-13618, Sep 9 2004.

[170] A. K. Rappe, C. J. Casewit, K. S. Colwell, W. A. Goddard, and W. M. Skiff, "Uff, a Full Periodic-Table Force-Field for Molecular Mechanics and Molecular-Dynamics Simulations," *Journal of the American Chemical Society,* vol. 114, pp. 10024-10035, Dec 2 1992.

[171] W. G. Hoover, "Canonical Dynamics - Equilibrium Phase-Space Distributions," *Physical Review A,* vol. 31, pp. 1695-1697, 1985.

[172] S. Nose, "A Unified Formulation of the Constant Temperature Molecular-Dynamics Methods," *Journal of Chemical Physics,* vol. 81, pp. 511-519, 1984.

[173] A. K. Rappe and W. A. Goddard, "Charge equilibration for molecular dynamics simulations," *The Journal of Physical Chemistry,* vol. 95, pp. 3358-3363, 1991/04/01 1991.

[174] S. Plimpton, "Fast Parallel Algorithms for Short-Range Molecular-Dynamics," *Journal of Computational Physics,* vol. 117, pp. 1-19, Mar 1 1995.

[175] P. E. Blochl, "Projector Augmented-Wave Method," *Physical Review B,* vol. 50, pp. 17953-17979, Dec 15 1994.

[176] G. Kresse and D. Joubert, "From ultrasoft pseudopotentials to the projector augmented-wave method," *Physical Review B,* vol. 59, pp. 1758-1775, Jan 15 1999.

[177] J. P. Perdew, K. Burke, and M. Ernzerhof, "Generalized gradient approximation made simple," *Physical Review Letters,* vol. 77, pp. 3865-3868, Oct 28 1996.

[178] G. Kresse and J. Furthmuller, "Efficient iterative schemes for ab initio total-energy calculations using a plane-wave basis set," *Physical Review B,* vol. 54, pp. 11169-11186, Oct 15 1996.

[179] G. Kresse and J. Furthmuller, "Efficiency of ab-initio total energy calculations for metals and semiconductors using a plane-wave basis set," *Computational Materials Science,* vol. 6, pp. 15-50, Jul 1996.

[180] H. J. Monkhorst and J. D. Pack, "Special Points for Brillouin-Zone Integrations," *Physical Review B,* vol. 13, pp. 5188-5192, 1976.

[181] S. Grimme, J. Antony, S. Ehrlich, and S. Krieg, "A consistent and accurate ab initio parametrization of density functional dispersion correction (dft-d) for the 94 elements H-Puc," *J. Chem. Phys,* vol. 132, 2010c.

[182] C.-M. Chen, Q. Zhang, X.-C. Zhao, B. Zhang, Q.-Q. Kong, M.-G. Yang, Q.-H. Yang, M.-Z. Wang, Y.-G. Yang, and R. Schlögl, "Hierarchically aminated graphene honeycombs for electrochemical capacitive energy storage," *Journal of Materials Chemistry*, vol. 22, pp. 14076-14084, 2012.

[183] G. Erdenedelger, T. Lee, T. D. Dao, J. S. Kim, B.-S. Kim, and H. M. Jeong, "Solid-state functionalization of graphene with amino acids toward water-dispersity: implications on a composite with polyaniline and its characteristics as a supercapacitor electrode material," *Journal of Materials Chemistry A*, vol. 2, pp. 12526-12534, 2014.

[184] H.-L. Ma, H.-B. Zhang, Q.-H. Hu, W.-J. Li, Z.-G. Jiang, Z.-Z. Yu, and A. Dasari, "Functionalization and reduction of graphene oxide with p-phenylene diamine for electrically conductive and thermally stable polystyrene composites," *ACS applied materials & interfaces*, vol. 4, pp. 1948-1953, 2012.

[185] Y. Wang, X. Yang, L. Qiu, and D. Li, "Revisiting the capacitance of polyaniline by using graphene hydrogel films as a substrate: the importance of nano-architecturing," *Energy & Environmental Science*, vol. 6, pp. 477-481, 2013.

[186] H. Bai, Y. Xu, L. Zhao, C. Li, and G. Shi, "Non-covalent functionalization of graphene sheets by sulfonated polyaniline," *Chemical Communications*, pp. 1667-1669, 2009.

[187] H. Mi, J. Zhou, Q. Cui, Z. Zhao, C. Yu, X. Wang, and J. Qiu, "Chemically patterned polyaniline arrays located on pyrolytic graphene for supercapacitors," *Carbon*, vol. 80, pp. 799-807, 2014.

[188] M. Kim, C. Lee, and J. Jang, "Fabrication of Highly Flexible, Scalable, and High-Performance Supercapacitors Using Polyaniline/Reduced Graphene Oxide Film with Enhanced Electrical Conductivity and Crystallinity," *Advanced Functional Materials*, vol. 24, pp. 2489-2499, 2014.

[189] L. Li, B. Song, L. Maurer, Z. Lin, G. Lian, C.-C. Tuan, K.-S. Moon, and C.-P. Wong, "Molecular engineering of aromatic amine spacers for high-performance graphene-based supercapacitors," *Nano Energy*, vol. 21, pp. 276-294, 2016.

[190] R. Rathore, S. Lindeman, and J. Kochi, "Charge-transfer probes for molecular recognition via steric hindrance in donor-acceptor pairs," *Journal of the American Chemical Society*, vol. 119, pp. 9393-9404, 1997.

[191] Y. Lu, F. Zhang, T. Zhang, K. Leng, L. Zhang, X. Yang, Y. Ma, Y. Huang, M. Zhang, and Y. Chen, "Synthesis and supercapacitor performance studies of N-doped graphene materials using o-phenylenediamine as the double-N precursor," *Carbon*, vol. 63, pp. 508-516, 2013.

[192] L. Lai, L. Chen, D. Zhan, L. Sun, J. Liu, S. H. Lim, C. K. Poh, Z. Shen, and J. Lin, "One-step synthesis of NH 2-graphene from in situ graphene-oxide reduction and its improved electrochemical properties," *Carbon,* vol. 49, pp. 3250-3257, 2011.

[193] Y. Cui, Q.-Y. Cheng, H. Wu, Z. Wei, and B.-H. Han, "Graphene oxide-based benzimidazole-crosslinked networks for high-performance supercapacitors," *Nanoscale,* vol. 5, pp. 8367-8374, 2013.

[194] L. Zhao, L. Z. Fan, M. Q. Zhou, H. Guan, S. Qiao, M. Antonietti, and M. M. Titirici, "Nitrogen-Containing Hydrothermal Carbons with Superior Performance in Supercapacitors," *Advanced materials,* vol. 22, pp. 5202-5206, 2010.

[195] J. Shen, A. Liu, Y. Tu, G. Foo, C. Yeo, M. B. Chan-Park, R. Jiang, and Y. Chen, "How carboxylic groups improve the performance of single-walled carbon nanotube electrochemical capacitors?," *Energy & Environmental Science,* vol. 4, pp. 4220-4229, 2011.

[196] J.-H. Sung, S.-J. Kim, S.-H. Jeong, E.-H. Kim, and K.-H. Lee, "Flexible micro-supercapacitors," *Journal of power sources,* vol. 162, pp. 1467-1470, 2006.

[197] X. Xue, P. Deng, B. He, Y. Nie, L. Xing, Y. Zhang, and Z. L. Wang, "Flexible Self-Charging Power Cell for One-Step Energy Conversion and Storage," *Advanced Energy Materials,* vol. 4, 2014.

[198] W. Gao, N. Singh, L. Song, Z. Liu, A. L. M. Reddy, L. Ci, R. Vajtai, Q. Zhang, B. Wei, and P. M. Ajayan, "Direct laser writing of micro-supercapacitors on hydrated graphite oxide films," *Nature Nanotechnology,* vol. 6, pp. 496-500, 2011.

[199] M. Beidaghi and C. Wang, "Micro-Supercapacitors Based on Interdigital Electrodes of Reduced Graphene Oxide and Carbon Nanotube Composites with Ultrahigh Power Handling Performance," *Advanced Functional Materials,* vol. 22, pp. 4501-4510, 2012.

[200] Z. S. Wu, K. Parvez, X. Feng, and K. Müllen, "Graphene-based in-plane micro-supercapacitors with high power and energy densities," *Nature communications,* vol. 4, 2013.

[201] H. Bai, Y. Xu, L. Zhao, C. Li, and G. Shi, "Non-covalent functionalization of graphene sheets by sulfonated polyaniline," *Chem. Commun.,* pp. 1667-1669, 2009.

[202] M. Beidaghi and C. Wang, "Micro-supercapacitors based on three dimensional interdigital polypyrrole/C-MEMS electrodes," *Electrochimica Acta,* vol. 56, pp. 9508-9514, 2011.

[203] C. Yu, P. Ma, X. Zhou, A. Wang, T. Qian, S. Wu, and Q. Chen, "All-solid-state flexible supercapacitors based on highly dispersed polypyrrole nanowire and reduced graphene oxide composites," *ACS applied materials & interfaces,* vol. 6, pp. 17937-17943, 2014.

[204] W. Liu, X. Yan, J. Chen, Y. Feng, and Q. Xue, "Novel and high-performance asymmetric micro-supercapacitors based on graphene quantum dots and polyaniline nanofibers," *Nanoscale,* vol. 5, pp. 6053-6062, 2013.

[205] Z. Li, B. Song, Z. Wu, Z. Lin, Y. Yao, K.-S. Moon, and C. Wong, "3D porous graphene with ultrahigh surface area for microscale capacitive deionization," *Nano Energy,* vol. 11, pp. 711-718, 2015.

[206] M. D. Stoller, S. Park, Y. Zhu, J. An, and R. S. Ruoff, "Graphene-based ultracapacitors," *Nano letters,* vol. 8, pp. 3498-3502, 2008.

[207] S. Stankovich, D. A. Dikin, G. H. Dommett, K. M. Kohlhaas, E. J. Zimney, E. A. Stach, R. D. Piner, S. T. Nguyen, and R. S. Ruoff, "Graphene-based composite materials," *Nature,* vol. 442, pp. 282-286, 2006.

[208] H. Gómez, M. K. Ram, F. Alvi, P. Villalba, E. L. Stefanakos, and A. Kumar, "Graphene-conducting polymer nanocomposite as novel electrode for supercapacitors," *Journal of Power Sources,* vol. 196, pp. 4102-4108, 2011.

[209] H. Wang, Q. Hao, X. Yang, L. Lu, and X. Wang, "A nanostructured graphene/polyaniline hybrid material for supercapacitors," *Nanoscale,* vol. 2, pp. 2164-2170, 2010.

[210] Z.-F. Li, H. Zhang, Q. Liu, L. Sun, L. Stanciu, and J. Xie, "Fabrication of high-surface-area graphene/polyaniline nanocomposites and their application in supercapacitors," *ACS applied materials & interfaces,* vol. 5, pp. 2685-2691, 2013.

[211] S. Ito, K. Murata, S. Teshima, R. Aizawa, Y. Asako, K. Takahashi, and B. M. Hoffman, "Simple synthesis of water-soluble conducting polyaniline," *Synthetic Metals,* vol. 96, pp. 161-163, 1998.

[212] Y. Cao, A. Andreatta, A. J. Heeger, and P. Smith, "Influence of chemical polymerization conditions on the properties of polyaniline," *Polymer,* vol. 30, pp. 2305-2311, 1989.

[213] M. F. El-Kady, V. Strong, S. Dubin, and R. B. Kaner, "Laser scribing of high-performance and flexible graphene-based electrochemical capacitors," *Science,* vol. 335, pp. 1326-1330, 2012.

[214] I. Jung, D. A. Field, N. J. Clark, Y. Zhu, D. Yang, R. D. Piner, S. Stankovich, D. A. Dikin, H. Geisler, and C. A. Ventrice Jr, "Reduction kinetics of graphene oxide determined by electrical transport measurements and temperature programmed desorption," *The Journal of Physical Chemistry C,* vol. 113, pp. 18480-18486, 2009.

[215] Z. Lin, Y. Yao, Z. Li, Y. Liu, Z. Li, and C.-P. Wong, "Solvent-assisted thermal reduction of graphite oxide," *The Journal of Physical Chemistry C,* vol. 114, pp. 14819-14825, 2010.

[216] J. Yan, T. Wei, B. Shao, Z. Fan, W. Qian, M. Zhang, and F. Wei, "Preparation of a graphene nanosheet/polyaniline composite with high specific capacitance," *Carbon,* vol. 48, pp. 487-493, 2010.

[217] X. Li, H. Wang, J. T. Robinson, H. Sanchez, G. Diankov, and H. Dai, "Simultaneous nitrogen doping and reduction of graphene oxide," *Journal of the American Chemical Society,* vol. 131, pp. 15939-15944, 2009.

[218] L. Ruangchuay, J. Schwank, and A. Sirivat, "Surface degradation of α-naphthalene sulfonate-doped polypyrrole during XPS characterization," *Applied surface science,* vol. 199, pp. 128-137, 2002.

[219] J.-C. Chiang and A. G. MacDiarmid, "'Polyaniline': protonic acid doping of the emeraldine form to the metallic regime," *Synthetic Metals,* vol. 13, pp. 193-205, 1986.

[220] H.-P. Cong, X.-C. Ren, P. Wang, and S.-H. Yu, "Flexible graphene–polyaniline composite paper for high-performance supercapacitor," *Energy & Environmental Science,* vol. 6, pp. 1185-1191, 2013.

[221] Q. Wu, Y. Xu, Z. Yao, A. Liu, and G. Shi, "Supercapacitors based on flexible graphene/polyaniline nanofiber composite films," *ACS nano,* vol. 4, pp. 1963-1970, 2010.

[222] J. J. Yoo, K. Balakrishnan, J. Huang, V. Meunier, B. G. Sumpter, A. Srivastava, M. Conway, A. L. Mohana Reddy, J. Yu, and R. Vajtai, "Ultrathin planar graphene supercapacitors," *Nano letters,* vol. 11, pp. 1423-1427, 2011.

[223] B. Song, Y. Chen, K.-S. Moon, and C. Wong, "Design of Miura Folding-Based Micro-Supercapacitors as Foldable and Miniaturized Energy Storage Devices," in *Electronic Components and Technology Conference (ECTC), 2017 IEEE 67th*, 2017, pp. 2027-2032.

[224] J. P. Gardner, J. C. Mather, M. Clampin, R. Doyon, M. A. Greenhouse, H. B. Hammel, J. B. Hutchings, P. Jakobsen, S. J. Lilly, and K. S. Long, "The james webb space telescope," *Space Science Reviews,* vol. 123, pp. 485-606, 2006.

[225] K. Miura, "Map fold a la Miura style, its physical characteristics and application to the space science," ed: KTK Scientific Publishers, Tokyo, Japan, 1994, pp. 77-90.

[226] B. Y. Ahn, D. Shoji, C. J. Hansen, E. Hong, D. C. Dunand, and J. A. Lewis, "Printed origami structures," *Advanced Materials,* vol. 22, pp. 2251-2254, 2010.

[227] K. Kuribayashi, K. Tsuchiya, Z. You, D. Tomus, M. Umemoto, T. Ito, and M. Sasaki, "Self-deployable origami stent grafts as a biomedical application of Ni-rich TiNi shape memory alloy foil," *Materials Science and Engineering: A,* vol. 419, pp. 131-137, 2006.

[228] Q. Cheng, Z. Song, T. Ma, B. B. Smith, R. Tang, H. Yu, H. Jiang, and C. K. Chan, "Folding paper-based lithium-ion batteries for higher areal energy densities," *Nano letters,* vol. 13, pp. 4969-4974, 2013.

[229] M. Inagaki, H. Konno, and O. Tanaike, "Carbon materials for electrochemical capacitors," *Journal of power sources,* vol. 195, pp. 7880-7903, 2010.

[230] D. Drobny, S. Tychyna, Y. A. Maletin, N. Stryzhakova, and S. Zelinskyi, "Methods for Manufacturing Carbon Electrodes for Supercapacitors: Pros and Cons," in *Proceedings of the international conference Nanomaterials: applications and properties*, 2013, pp. 04NEA17-04NEA17.

[231] B. Fang and L. Binder, "A novel carbon electrode material for highly improved EDLC performance," *The Journal of Physical Chemistry B,* vol. 110, pp. 7877-7882, 2006.

[232] B. Dyatkin, V. Presser, M. Heon, M. R. Lukatskaya, M. Beidaghi, and Y. Gogotsi, "Development of a green supercapacitor composed entirely of environmentally friendly materials," *ChemSusChem,* vol. 6, pp. 2269-2280, 2013.

[233] V. Ruiz, C. Blanco, M. Granda, R. Menéndez, and R. Santamaría, "Influence of electrode preparation on the electrochemical behaviour of carbon-based supercapacitors," *Journal of applied electrochemistry,* vol. 37, pp. 717-721, 2007.

[234] T. M. Higgins, S.-H. Park, P. J. King, C. Zhang, N. McEvoy, N. C. Berner, D. Daly, A. Shmeliov, U. Khan, and G. Duesberg, "A commercial conducting polymer as both binder and conductive additive for silicon nanoparticle-based lithium-ion battery negative electrodes," *Acs Nano,* vol. 10, pp. 3702-3713, 2016.

[235] B.-H. Park and J.-H. Choi, "Improvement in the capacitance of a carbon electrode prepared using water-soluble polymer binder for a capacitive deionization application," *Electrochimica Acta,* vol. 55, pp. 2888-2893, 2010.

[236] B. Lestriez, S. Bahri, I. Sandu, L. Roué, and D. Guyomard, "On the binding mechanism of CMC in Si negative electrodes for Li-ion batteries," *Electrochemistry Communications,* vol. 9, pp. 2801-2806, 2007.

[237] J. Li, R. Lewis, and J. Dahn, "Sodium carboxymethyl cellulose a potential binder for Si negative electrodes for Li-ion batteries," *Electrochemical and Solid-State Letters,* vol. 10, pp. A17-A20, 2007.

[238] W.-R. Liu, M.-H. Yang, H.-C. Wu, S. Chiao, and N.-L. Wu, "Enhanced cycle life of Si anode for Li-ion batteries by using modified elastomeric binder," *Electrochemical and Solid-State Letters,* vol. 8, pp. A100-A103, 2005.

[239] S. Kumagai, K. Mukaiyachi, and D. Tashima, "Rate and cycle performances of supercapacitors with different electrode thickness using non-aqueous electrolyte," *Journal of Energy Storage,* vol. 3, pp. 10-17, 2015.

[240] L. Kouchachvili, N. Maffei, and E. Entchev, "Novel binding material for supercapacitor electrodes," *Journal of Solid State Electrochemistry,* vol. 18, pp. 2539-2547, 2014.

[241] M. Aslan, D. Weingarth, P. Herbeck-Engel, I. Grobelsek, and V. Presser, "Polyvinylpyrrolidone/polyvinyl butyral composite as a stable binder for castable supercapacitor electrodes in aqueous electrolytes," *Journal of Power Sources,* vol. 279, pp. 323-333, 2015.

[242] A. Varzi and S. Passerini, "Enabling high areal capacitance in electrochemical double layer capacitors by means of the environmentally friendly starch binder," *Journal of Power Sources,* vol. 300, pp. 216-222, 2015.

[243] M. Aslan, D. Weingarth, N. Jäckel, J. Atchison, I. Grobelsek, and V. Presser, "Polyvinylpyrrolidone as binder for castable supercapacitor electrodes with high electrochemical performance in organic electrolytes," *Journal of Power Sources,* vol. 266, pp. 374-383, 2014.

[244] R. López-Chavéz and A. Cuentas-Gallegos, "The Effect of Binder in Electrode Materials for Capacitance Improvement and EDLC Binder-free Cell Design," *Journal of New Materials for Electrochemical Systems,* vol. 16, pp. 197-202, 2013.

[245] A. Banerjee, P. S. Kumar, and A. Shukla, "Influence of binder solvent on carbon-layer structure in electrical-double-layer capacitors," *Journal of Chemical Sciences,* vol. 125, pp. 1177-1183, 2013.

[246] L. Li, Z. P. Wu, H. Sun, D. Chen, J. Gao, S. Suresh, P. Chow, C. V. Singh, and N. Koratkar, "A Foldable Lithium–Sulfur Battery," *ACS nano,* vol. 9, pp. 11342-11350, 2015.

[247] S. Komaba, K. Shimomura, N. Yabuuchi, T. Ozeki, H. Yui, and K. Konno, "Study on polymer binders for high-capacity SiO negative electrode of Li-ion batteries," *The Journal of Physical Chemistry C,* vol. 115, pp. 13487-13495, 2011.

[248] Z. Wu, L. Li, Z. Lin, B. Song, Z. Li, K.-S. Moon, C.-P. Wong, and S.-L. Bai, "Alternating current line-filter based on electrochemical capacitor utilizing template-patterned graphene," *Scientific reports,* vol. 5, p. 10983, 2015.

[249] J. Jiang, Y. Li, J. Liu, X. Huang, C. Yuan, and X. W. D. Lou, "Recent advances in metal oxide-based electrode architecture design for electrochemical energy storage," *Advanced materials,* vol. 24, pp. 5166-5180, 2012.

[250] A. S. Arico, P. Bruce, B. Scrosati, J.-M. Tarascon, and W. Van Schalkwijk, "Nanostructured materials for advanced energy conversion and storage devices," *Nature materials,* vol. 4, p. 366, 2005.

[251] Z. Sun, D. K. James, and J. M. Tour, "Graphene chemistry: synthesis and manipulation," *The Journal of Physical Chemistry Letters,* vol. 2, pp. 2425-2432, 2011.

[252] D. R. Rolison, J. W. Long, J. C. Lytle, A. E. Fischer, C. P. Rhodes, T. M. McEvoy, M. E. Bourg, and A. M. Lubers, "Multifunctional 3D nanoarchitectures for energy storage and conversion," *Chemical Society Reviews,* vol. 38, pp. 226-252, 2009.

[253] J. R. Miller, R. Outlaw, and B. Holloway, "Graphene double-layer capacitor with ac line-filtering performance," *Science,* vol. 329, pp. 1637-1639, 2010.

[254] Z. L. Wang, "Self-powered nanosensors and nanosystems," *Advanced Materials,* vol. 24, pp. 280-285, 2012.